Evaluation of aerial thermography to discriminate loft insulation in residential housing

by David Allinson BEng(Hons) MSc(Eng)

Thesis submitted to the University of Nottingham
for the degree of Doctor of Philosophy

May 2007

"It is difficult to say what is impossible, for the dream of yesterday is the hope of today and the reality of tomorrow."

Robert Goddard

Acknowledgements

The Author wishes to thank Benachir Medjdoub and Robin Wilson of the School of the Built Environment at the University of Nottingham for their guidance, help and support throughout the 36 months of this study.

Gillian Tidy of the Nottingham Energy Partnership provided all of the initial drive behind the project while the support of Phil Angus was invaluable to its completion.

Stuart Marsh, Gisela Ager and Rhonda Newsham of the British Geological Survey, Keyworth provided the data, gave their time, much useful help and advice and excellent training in GIS software.

Paul Gray and Mike Etridge of Infoterra provided invaluable background and technical information on their thermal infrared line scanner.

Paul Flowers of Nottingham City Council Housing Energy Team demonstrated an encyclopaedic knowledge of housing in Nottingham and provided most the housing data. Sarah Watson of Nottingham City Councils Housing Strategy was also of great assistance.

The advice of Robert Madding, co-founder of the Thermosense Conference and director of the Infrared Training Centre and Jack Kleinfield, president of Kleinfield Technical Services was beneficial to the development of this project.

Graeme Loudon of the Meteorological Office was efficient and helpful in providing meteorological data.

Though my laboratory time was short, the technicians in the School of the Built Environment, lead by Robert Clarke, were helpful and accommodating at all times.

Abstract

This thesis examines the use of aerial thermography data to discriminate loft (attic) insulation levels in residential housing, with ventilated pitched roofs, in the UK. Quantitative techniques from the fields of remote sensing, GIS, building physics and atmospheric science were used to develop a methodology and analyse survey data flown over Nottingham in 2001.

The quantitative techniques were applied to real survey data using the most up to date atmospheric propagation models. A new model of the heat loss through the ceiling, loft and roof was developed for this study, based on the most recent methods. The limitations of these techniques were explored. A complete methodology, valid for any future study, was defined.

It was found that, measuring roof surface temperature from the thermal image was complicated by roof material properties, the intervening atmosphere and the surrounding topography. Relating roof surface temperature to insulation thickness was further complicated by loft space ventilation and the outside surface heat balance. The additional data, needed to quantify the results, produced inaccuracies caused by measurement error. Analysis of the uncertainties, by simulation, indicated that loft insulation level could not be discriminated by aerial thermography. This was confirmed by comparing the results, calculated from the survey data, with the actual insulation level for a number of houses in test areas of the city.

Table of Contents

List of Tables

1 Introduction

This thesis examines the use of aerial thermography data to discriminate loft (attic) insulation level in residential housing with ventilated pitched roofs. Quantitative remote sensing techniques were applied to survey data using the most up to date atmospheric propagation model. Existing techniques, from the literature, were combined in a new and unique way in an attempt to provide the most sophisticated and complete analysis to date. A new model of the heat loss through the ceiling, loft and roof was developed for this study, based on some of the most recent methods. The limitations of these techniques were explored and the errors in the input were investigated and analysed. The finding that aerial thermography data could not be used to discriminate loft insulation level was supported by the analysis of existent thermography data flown over Nottingham. To the author's knowledge, this is the first time a quantitative methodology has been applied to UK house styles and meteorological conditions. The general methodology presented here will be valid in any future study of aerial thermography or building heat loss through the roof.

1.1 Background

For over thirty years, aerial infrared thermography has been adopted as a tool for energy conservation in the built environment. Instinctively it makes sense: a poorly insulated building will appear warmer as heat, better used for warming the occupants, warms the roof. The technique was first used in the USA as a reaction to the 1973 oil crisis [1] when OPEC doubled the price of its exports and imposed an embargo on the USA. After falling out of favour, it reamerged in the UK as a reaction to the 1995 Home Energy Conservation Act and was targeted at Local Authorities (e.g. [2, 3]), obliged to tackle energy conservation in private sector housing.

The Nottingham Energy Partnership (NEP) [4] was established in 1988 to work in an education and advisory role, to promote energy efficiency and to combat Nottingham's contribution to climate change. In 2001, in collaboration with the British Geological Survey

(BGS) [5], they commissioned an aerial thermography survey of the city of Nottingham. Their objective was to use these data to identify thermally inefficient buildings.

Aerial thermography is a remote sensing technique that displays the apparent temperatures of objects in a scene. Infoterra [6], a leading geographic information provider, carried out the survey using a digital thermal line scanner operating in the 8-14μm (infrared) wavelength range. Data were acquired during the winter heating season from 760m above ground level, on both an evening (20.30 to 23.00) and a morning (02.30 to 06.00).

The BGS created a Geographical Information System (GIS) layer from the evening data [7] such that the average radiance from the roof of each building in the city of Nottingham could be displayed on a colour-coded map. Qualitative analysis of these data was inconclusive and produced anomalies [8, 9].

The NEP approached the School of the Built Environment at the University of Nottingham to carry out a quantitative analysis. This thesis is the culmination of a 36 month study, funded by the Engineering and Physical Sciences Research Council (EPSRC) and NEP.

1.2 Infrared thermography

Infrared radiation, part of the electromagnetic spectrum, was discovered by Sir William Herschel, a German born, British astronomer in 1800. Infrared thermography involves the measurement and visualisation of this infrared radiation. The first prototype infrared line-scanner, incorporating an infrared detector, was developed for military applications in 1946. By the 1960s, the technology was declassified and commercially available [10].

During the energy crisis of the 1970s, infrared thermography, though not yet a mature technology, provided convenient visual images of ‘heat loss’ that helped to promote energy conservation [1]. All instruments of this period had a single detector but rotating mirrors or prisms were used to scan a line or scene. The resultant analogue signal was typically

recorded on tape and could be post-processed to form a thermogram on photographic paper. The sensors had to be cooled using compressed gases.

Analysis software and electrical cooling systems (Stirling cycle refrigeration) were developed in the 1980s while focal plane array (staring array) instruments followed in the 1990s [1]. The focal plane array negated the need for mechanical scanning as the image was formed from a two dimensional matrix of sensor elements. Today, sensors with arrays of up to 640x512 pixels are available [11].

Infrared sensors typically operate in the short wave (3-5μm) or long wave (8-14μm) portions of the infrared spectrum, which relate to windows of reduced atmospheric absorption. The sensor simply converts incoming infrared radiation into an electrical signal. The relationship between the magnitude of this signal and the magnitude of the incoming radiation depends on the type of detector and the optics, filters and electronics that comprise the sensor. This is further described in Chapter 3.

The use of thermography in aeroplanes to produce images of the ground is part of the wider field of remote sensing (see [12, 13] for an introduction to remote sensing). This aerial thermography has a number of modern applications which are discussed in more detail in the literature review in Chapter 2. The sensor used for collection of the Nottingham aerial thermography survey in 2001 is described in detail in Chapter 3.

1.3 Justification

The Home Energy Conservation Act of 1995 puts a duty on local authorities to develop strategies to improve energy efficiency in all public and private sector housing in order to tackle fuel poverty and reduce carbon dioxide emissions [14]. Fuel poverty occurs when a household cannot afford to keep adequately warm at reasonable cost and is linked to increased mortality, ill health and lower quality of life. The factors that influence fuel poverty include household income, fuel costs and energy efficiency of the home [15]. Energy efficiency is the best way to reduce carbon dioxide emissions in the short term and, in 2003,

the Energy Saving Trust claimed that the average household could avoid around 2 tonnes of carbon dioxide emissions (and save around £200) a year [16].

Insulating buildings to reduce heat loss through the building fabric is becoming increasingly important as space heating accounts for 26% of final energy consumption by end use in the UK [17]. In 2003 the percentage of households with no insulation was only 11%, however, a mere 14% had full insulation and loft insulation was less than 100mm thick in 40% of households [18]. Installing 250mm of loft insulation can save up to 25% of household heating costs, according top the Energy Saving Trust [16].

An important aspect of energy conservation programs is identifying those households where saving can be made. This is problematic due to the large number of houses in each local authority area. In 2006, Nottingham City Council itself had 32,241 properties and 7,547 Social Landlords, there were 58,751 privately owned properties in the city and 19,274 privately rented [19]. At April 2006, the vast majority (83.3%) of Council owned properties were insulated to 200-250mm with the remaining tenants refusing insulation [19] (mainly because it prevented boarding out/storage in the loft space). It was officially estimated that 56.8% of privately owned properties had more than 150mm of loft insulation, 11.87% had between 50mm and 150mm and 31.3% had under 50mm [19].

Currently, free or discounted loft insulation is available to homeowners through a number of schemes. Nottingham's Housing Energy Team have used annual mail drops to encourage upgrading and recorded increasing levels of participation [19] but cannot identify those most in need. If aerial thermography could be used to identify houses with inadequately insulated lofts the owners could be targeted directly with energy efficiency advice and guidance. By taking effective action, the occupants could benefit from lower energy bills and improved health and quality of life. This would also reduce carbon dioxide emissions, help tackle fuel poverty and, by periodically re-flying surveys to monitor progress, aid Nottingham City Council to meet the objectives of the Home Energy Conservation Act.

If the cost of a quantitative aerial thermography survey of Nottingham city, with analysis, was in the region of £50,000, the cost per household would be less than 50p. However, costs vary and a recent survey over Reims in France, which has a slightly smaller population than Nottingham, cost €185,000 [20] or more than £125,000. By way of comparison a thermography survey of a house on the ground would cost between around £50 for a single image of the front elevation to over £1700 for a full survey including the roof, according to one UK company [21]. Aerial thermography, therefore, appears to offer very good value for money. However, if insulation level cannot be discriminated from these data, the money spent on these surveys may be better used elsewhere.

1.4 Aims and objectives

The aim of this work was to develop and test a methodology for measuring the thickness of loft insulation in residential buildings using aerial thermography with the Nottingham dataset as a case study.

The key objectives were to develop techniques to measure roof surface temperature from the thermal image, relate that roof surface temperature to insulation thickness and test the accuracy of the results.

To meet these objectives, a substantial review of the literature was carried out (see Chapter 2) and the required steps of the methodology defined (see Chapter 3). Numerical models were developed to calculate the roof surface temperature from the thermal image (see Chapter 4) and to relate roof surface temperature to insulation level (see Chapter 5). A number of different heat balance methods were considered for the roof surface and the loft space and the most suitable chosen for this work (see Chapter 6). Similarly, methods defining the important atmospheric properties: upwelled radiance, atmospheric transmission, downwelled radiance and broadband sky temperature were chosen (see Chapter 7). The physical properties of test buildings, needed for the analysis, were determined from a combination of ground surveys, electronic maps, laboratory based emissivity measurements and a number of methods for determining sky view factor were compared (see Chapter 8).

The effect of errors in the input parameters was assessed by sensitivity analysis and uncertainty analysis (see Chapter 9) and the results for houses in a number of test areas of the city of Nottingham were analysed and compared with the known insulation level (see Chapter 10).

Only the evening survey data were analysed, as heating systems were more likely to be active in residential houses at that time and internal temperatures higher. The analysis was limited to the loft insulation as roofs were the only part of each house reliably imaged by the aerial survey. Flat roofs were ignored as the vast majority of residential houses in the city had pitched ventilated roofs.

2 Literature review

This chapter comprises a review of the relevant and wider field literature relating to aerial thermography for energy conservation in the built environment, and an overview of some of the other applications of thermal imaging. More detailed and specific reviews are included in the relevant chapters.

2.1 Aerial thermography for energy conservation

Aerial thermography has been used to examine heat loss from buildings for over thirty years. Initially, analysis of the thermal image was purely qualitative but increasingly attempts were made to quantify the results. In recent years, a number of surveys have been carried out for local authorities in the UK, including Nottingham. These are discussed further below.

2.1.1 Qualitative analysis

Thermal images were first used, qualitatively, to compare grey scale levels of building roofs in the scene. The analysis was, relatively, quick, cheap and simple, as no additional data were needed.

American utility companies faced widespread customer dissatisfaction as energy prices rose in the 1970s. A number of them funded aerial thermography surveys to develop positive publicity and improve public perception [22-24]. The thermal image was used to generate public interest while the real work of public relations and energy efficiency education was carried out through the media, at dissemination centres and during home audits. The results were successful in that the companies received good publicity and there was a significant reduction in energy use. When the State of Minnesota invested in a survey and dissemination scheme, the additional tax raised on the sale of retrofit insulating and draft exclusion materials was reported to have more than covered their costs [25]. The US department of Energy's 'Aerial Infrared Users manual' recommended using only qualitative analysis (as it was cheaper), stressed the importance of enthusiastic dissemination and deemed the survey a

means to stimulate the public's interest and participation in energy conservation schemes [26].

In the late 1970s and throughout the 1980s, it was reported that patches of faulty insulation and water damage on flat roofs could be identified from aerial thermography data but insulation level could not be inferred [27-30]. It was thought that the insulation level of identical roofs could be compared using a skilled interpreter if the meteorological conditions at the time of collection were suitable [31-35] and some energy audits used these results [36]. Additionally, some success was claimed with detecting steam pipe leaks using these data [27, 35] but this was complicated by the line size, spacing, insulation, depth of burial and back fill material [32].

Roof moisture surveys [37-43] and district heating pipeline surveys [44-49] were developed in their own right and separately from heat loss surveys. The ASHRAE handbook of fundamentals states that while aerial thermography is suitable for identifying patches of wet insulation on flat roofs, it should not be used to rank roofs according to their thermal resistance [50].

Aerial heat loss surveys provided a cheap way to gather data over large areas of the built environment, very quickly. Qualitative analysis of these data did engage the public in energy conservation programs and provided positive publicity for their sponsors, however, the scientific basis of this analysis was questionable and insulation level could not be inferred reliably. Engineers and scientists started trying to model the data collection and the heat loss through a building roof to aid understanding, prove qualitative analysis was misleading and develop a successful quantitative technique.

2.1.2 Quantitative analysis

The development of quantitative analysis techniques started, in part, as a reaction to what was seen as the misuse of aerial thermography for energy conservation surveys [1].

Goldstein [51] defined both, the measurement of roof surface temperature by the sensor and the heat transfer through the roof of the building, as numerical models. The senor model included surface emissivity, sky view factor, downwelled radiance from the sky and the spectral response of the sensor but a number of simplifying assumptions were (explicitly) made. Atmospheric transmission and upwelled radiance were ignored and emissivity was assumed the same in all directions to the surface. The sensor was assumed to be ideal within the wavelength band (i.e. all of the incident radiation was sensed) and a simplified solution of Planck's Law used. The results were shown to be very sensitive to errors in emissivity.

For the building model, Goldstein considered both flat roofs and ventilated pitched roofs. Sky view factor, broadband sky temperature and background temperature were included in the radiative heat exchange at the surface. The surface temperature depression, where the roof cools below ambient air temperature on cold, clear, windless nights, and the effect of this on the convection coefficient, were discussed. Equations for calculating the broadband sky temperature were given but no method for calculating sky view factor. Analysis of the building model with assumed values demonstrated that wind speed, sky temperature and ventilation could all have more effect on roof surface temperature than the thermal resistance of the roof structure.

Goldstein concluded that aerial thermography could not quantify loft insulation but roofs with low thermal resistance might be identifiable if wind speeds were low and the emissivity and microclimate of each roof was known. While this was the first study to introduce all of the elements required for quantitative analysis, techniques to define all of the relevant parameters were not given and a number of simplifying assumptions used instead.

The Canada Centre for Remote Sensing, which had an active role in trying to develop a methodology [31], identified many of the limitations, especially relating to ventilated pitched roofs [52], and developed a model for calculating the heat loss from a pitched ventilated roof and a method for calculating sky view factor [53]. They sought to develop an empirical relationship between loft insulation level and the apparent roof surface temperature measured

by the sensor for three surveys carried out, over a residential housing area, under different weather conditions [54].

The sensor model included the reflected components of background temperature and sky temperature but ignored atmospheric transmission and upwelled radiance. The building model included ventilation of the loft cavity but the roof surface radiant heat exchange was modelled using ambient air temperature in the place of sky and background temperatures. This, therefore, would not have modelled the surface temperature depression.

Houses were divided into classes based on type (e.g. bungalow, two-storey) as significant temperature differences were found between types. Plotting the apparent roof surface temperature against the known insulation level for a number of the houses indicated that insulation level had only a small effect on roof surface temperature. They concluded that it might be impossible to estimate loft insulation levels from aerial thermography data. This was thought to be mainly due to variations in attic ventilation and the effect of local topography on wind circulation.

The National Bureau of Standards also investigated comparative roof surveys [55, 56]. A simplified sensor model, that ignored sky view factor and background radiation, was developed. The building model included a steady state heat balance for the loft space that accounted for infiltration through the ceiling and ventilation to the outside air. The resulting equations were solved iteratively for surfaces and air space temperatures. From the model, it was predicted that the discrimination of insulation levels would be masked by the effect of variations in emissivity, wind speed and ambient air temperature. They suggested that dew formation on the roof, caused by the surface temperature depression on the cold, clear windless nights most suitable for data collection, might be a problem. Their model of the pitched ventilated roof was the most complete of all the aerial thermography studies reviewed.

Calspan/Rochester Institute of Technology made the most significant advances in the field. Their work defined all of the principles of the technology [57], mapped the developments [58,

59], developed the quantitative methods [60] and raised awareness of the limitations [61]. They reported the first successful quantitative survey in the early 1980s and the second in the 1990s. These are, to the author's knowledge, the only aerial thermography surveys to discriminate insulation level successfully.

The first survey was flown over three communities in New York while concurrent ground surface temperature measurements were taken [62]. The sensor model included all of the radiation paths and losses. Atmospheric transmission, upwelled radiance and downwelled radiance were calculated from profile flights, background radiance from the thermal image, sky view factor from the geometric properties of the roof and surroundings, and spectral emissivity from look up tables based on roof material [63]. The spectral response of the sensor was not included and the effect of line of sight angle on emissivity judged small enough to ignore. The building model was also comprehensive, though the effect of loft space ventilation was judged small and ignored. A numerical model was used to determine the broad band sky temperature, broad band emissivity was assumed to be the same as the spectral emissivity, background temperature was derived from the thermal image, and the convection coefficient was based on the roof material type and wind speed [64]. Wind speed and ambient air temperature were obtained from the local meteorological station. The results were classified into five levels of heat loss and compared with detailed ground survey data for 100 houses. The quantitative method correctly classified the result 63% of the time and was only significantly wrong 1% of the time. This was a great improvement over qualitative analysis with 36% correct and 21% significantly wrong.

The second survey was flown over a single New York community using a similar methodology with the addition of an empirical relationship between emissivity and line of sight angle. The uncertainty in the result was propagated by simulation and surface temperature measurements, taken on the ground at the time of the survey, used to reduce bias in the temperatures calculated by the sensor model. To reduce the bias in the building model results, the broadband sky temperature and the convection coefficient were set so that the mean heat flow matched that predicted from the known insulation level for 32 houses. Results

for these houses were classified into two levels based on an R-11 (ft²°Fh/Btu) thermal resistance threshold, which equated to about 60mm of loft insulation. While 79% were correctly classified, the sample was small and possibly biased as only 56% of those with less than R-11 were correctly classified compared with 87% with more than R-11. Uniquely, the aerial survey was combined with a mobile ground thermography survey of the outside of the house. Only the owners of houses that appeared to be performing badly were targeted with follow up advice and face-to-face survey analysis. The results reportedly cost less than detailed ground surveys and provided stronger motivation to the owners to make changes.

Evans [65-67] helped define the most suitable meteorological conditions for surveys to be carried out (cold, clear skies, little wind), highlighted micrometeorology effects (cold air pooling in valleys) and introduced the concept of 'freeze-out' were roofs remained at 0°C while surface water changed phase. He also described how trees, overlooking houses, would warm the roofs.

At Ohio State University experiments were carried out using an electrically heated reference pad [68, 69] to calibrate the thermal image. It was used on flat roofs with no overlooking buildings or trees, so that heat exchange only occurred with the sky. Limited precision (± 0.5°C) was quoted and the system would not be applicable to pitched ventilated residential housing.

In the UK, the Atomic Energy Research Establishment [70] made attempts to develop quantitative techniques by numerical methods for flat roofs with no non-sky backgrounds. Atmospheric transmission and upwelled radiance were ignored for the sensor model. The convective heat transfer coefficient, sky temperatures and emissivity measurement were identified as significant sources of error and investigated further. Langmuir's equation was chosen for modelling convection, Swinbank's method was used for the broad band sky temperature (see Goldstein [51]) and it was recommended that spectral sky temperature was measured. It was estimated that the overall error in the heat loss was 15% but this was not

verified as it was found difficult to calculate or measure the thermal conductance of roofs in situ.

Work by the University of Dundee [71] described the limitations of quantitative aerial thermography and provided numerical methods for estimating atmospheric transmission and upwelled radiance but this was not applied to real survey data. A consortium of local interests sponsored an aerial thermography survey of Aberdeen City in 1984, but the meteorological conditions at the time of the survey were recognised to be warmer, windier and more humid than ideal and the analysis of building heat loss not attempted [72]. A number of more recent surveys were flown for local authorities in the UK.

2.1.3 UK local authorities

Companies offering aerial thermography surveys in the UK include Infoterra [2], Horton Levi [3] and Thermal Survey (formerly DHR consultancy, formerly Sight Unseen) [73]. They have flown a number of aerial thermography surveys for local authorities in the UK in recent years, including (dates given where known): Nottingham Energy Partnership (2001), Sandwell Metropolitan Council (1996), Chester City Council (1996), The London Borough of Brent Council, Stockport Council [9]; Hampshire County Council, London Borough of Havering, Aberdeen City Council (2001), Birmingham City Council (2002) [74]; The London Borough of Greenwich (2006) [75]; Chester-le-Street Borough Council, City of London and the 32 Boroughs [76]; and Norwich City Council, Stafford Borough Council [77].

Of the above, several authorities are known to have used their data, though none quantitatively. Sandwell Metropolitan Council found the survey generated interest when introduced to businesses and through schools, though they resorted to door to door enquiries to determine insulation level as they recognised the lack of quantitative information in the data [9]. Chester City Council struggled to generate public interest with their survey and ultimately used GIS to identify the houses that appeared the warmest on the thermal image and hand delivered information packs containing the a copy of the thermogram alongside energy efficiency advice and discounts for insulation upgrades [9]. This was reported to have resulted

in 300 grants compared with 150 to 200 in other years [74]. Aberdeen City Council used their survey extensively as a publicity tool and provided public access through the internet, but its effectiveness has not been quantified [74]. Birmingham City Council found their survey data was not being used and commissioned a report to explore what they could do with it. The report concluded that the survey was limited to being a publicity tool though it would need additional support and the fuel rich, rather than the fuel poor, would be the main benefactors of such a scheme [74]. The London Borough of Greenwich used their survey for a public open day (provided by Thermal Survey) and planned to add these data to their GIS [75]. Of the remaining surveys, some authorities were dissatisfied with the results and/or had no plans to use the data [9, 74].

Data collection and primary analysis of the Nottingham survey were reported by the BGS [7]. The results comprised 30 overlapping flight lines of line scanner data for each of the two surveys. The BGS geometrically corrected and registered the evening data to a map coordinate system and created a GIS building layer representing the average sensor response (0-255 DN), for every building within the city. The geometric correction process was extremely arduous, as it had to be done by hand for every building in the city. Because of this, the morning data were not processed. Their main caveat was the accuracy of the geometric correction and they suggested that the averaged sensor response for a roof might actually have included values that were not from that roof.

Geography students at the University of Nottingham [8] carried out qualitative analysis of the resulting thermal image and GIS building layer. The root mean square error (RMSE) of the geometric correction was found to be ± 2.3m on the y-axis and ± 3.25m on the x-axis, though this was calculated using only 45 points spread across the image. Statistical analysis of the thermal image using electronic height data for the city, showed sensor output increased (got ‘warmer’) with elevation. Using the Nottingham city council housing database (of council owned property in Nottingham), an analysis of construction type, number of floors, position of building, council branch, age of building and number of bedrooms was carried out. Houses of ‘concrete no fines’ and ‘concrete (PRC)’ were found have the highest average sensor output

and the number of floors and number of bedrooms were found to increase with average sensor output. Comparing two very similar housing estates, one of which appeared much 'warmer' on the thermal image, the houses in the 'colder' estate were observed to have a lower pitch roof. No correlation was found between SAP energy ratings and the observed sensor output. Creating a 3.5m buffer zone around a building to compensate for the RMSE was found to reduce the range of pixel values within that roof, suggesting an improvement in accuracy, but the buffer zone could not be used for smaller buildings as it completely covered them. The early morning data were found to have less contrast and overall lower average sensor output.

Thompson [9] carried out further qualitative analysis of the data, studying four estates in detail. Some common factors, linking buildings with a high averaged sensor output were found. These included exposure to the prevailing wind direction, adjacency to open ground and main roads and reduced housing density. It was reported that many well-insulated buildings showed a high averaged sensor output.

From this review, it appears that, while new 'building heat loss' surveys were being flown, little was done with the existing data. Thermography is used more successfully in a number of different applications.

2.2 Other applications of thermography

Thermography has many applications both from the air and on the ground.

2.2.1 Aerial thermography

Outside of building heat loss studies, aerial thermography, flown from a helicopter or a fixed wing aircraft, has a number of commercial applications. These include pipeline surveys, identifying geothermal activity, identifying buried archaeology, monitoring landfill, finding unexploded ordnance, examining forest or large building fires, monitoring self-heating in peat or coal stock piles, identifying pollution of waterways, counting animals, search and rescue (people and animals), detecting electrical faults on overhead high voltage distribution lines

and roof moisture surveys [78-87]. Quantitative temperature measurements are not required in any of these applications and the purely qualitative analysis of these data is adequate.

2.2.2 Building thermography

Building thermography is a well-developed technology in common usage in the UK and around the world. Ground based surveys, from inside or outside of a building, have been successfully used to detect missing or damaged insulation, hidden structural elements or faults, air leaks, damp and even pests. Thermography has been used to examine building services including electrical mains circuitry (poor connections will appear as hot spots), for locating buried heating pipes and inspecting air conditioning vents. Qualitative analysis of the thermogram to identify anomalies in the apparent surface temperature is sufficient for the majority of applications. There are numerous sources of information on the internet and a number of conferences on the topic.

2.2.3 Non destructive testing

Subsurface defects in components and samples can be detected using thermographic techniques. Quantitative temperature measurements are not used as only differential heating rates caused by subsurface inhomogeneity are of interest. Typically, the component is heated actively or passively and the time-dependant and/or frequency-dependant effects on the surface temperature are analysed to reveal the location and depth of the defect. Ibarra-Castanedo [88] or Maldague [89] offer excellent introductions to the topic.

2.2.4 Medical

In medicine, infrared thermography is used to image the temperature patterns on the surface of the human body or during surgery. Temperature anomalies, typically caused by restrictions in blood flow, indicate problems such as tumours, arthritis and muscle damage (see, for example, [90-92]). Absolute temperature measurement is not required.

2.3 Conclusions

The use of aerial thermography data to discriminate insulation thickness has been a contentious subject since it was used to promote energy conservation programs in America thirty years ago. Several studies have shown that variations in the appearance of roofs in a thermal image may be due to the roof type, the roof material, the building type, the surroundings and the microclimate, as well as the insulation level. The development of numerical models demonstrated that roof surface temperature must be calculated with considerable accuracy and a great deal of additional data was needed for the analysis.

Few attempted this quantitative analysis and of those that did, only the work of Calspan/Rochester Institute of Technology was successful. Their success was based in part on a low threshold of discrimination (about 60mm of insulation), relied on ground truth data taken at the time of the survey to 'tune' the results and used a small sample of housing to validate them.

In the UK, many local authorities have purchased survey data in recent years but its use has been limited to generating publicity and results have been mixed. To date, qualitative analysis of the Nottingham survey data has been inconclusive.

The use of infrared thermography, from the air and on the ground, has been much more successful in other applications where accurate surface temperature measurements are not required.

A methodology for discriminating loft insulation thickness by aerial thermography, developed from the literature review, is introduced in the next chapter.

3 An overview of the methodology

Guided by the review of the literature, in Chapter 2, a methodology was devised for quantifying the loft insulation thickness of houses using aerial thermography. This Chapter has been divided into the data collection, carried out before this study was started, an introduction to the data analysis, which forms the core of this thesis and a summary of the additional data that were needed for that analysis.

For any successful survey, dissemination of the results in a useable form and to the relevant parties is an essential part of the methodology. A high level of automation would be required to analyse data for a whole city as well as a custom user interface and report generator. The system would have to be benchmarked against the known level of insulation in independently selected houses. Other than being mentioned here for completeness, dissemination is beyond the scope of this thesis.

3.1 Data collection

The Nottingham survey took place on the 15th February 2001 between 2030hrs and 2300hrs. The sensor that was used, the weather conditions at the time of the survey and geometric correction of the thermal image are considered.

3.1.1 Sensor

The survey was flown by Infoterra, from a fixed wing aircraft at 760m (2,500 feet) above the ground. This is the lowest allowable altitude for flights over built up areas of the UK. The sensor used was a military UK Thermal Imaging Common Modules (TICM) Class 2 imager, which was designed as a night vision system for Chieftain and Challenger tanks [93]. The detector was a Cadmium Mercury Teluride (CMT) Sprite, cooled to 80K using either a Stirling engine or liquid Nitrogen. It had been modified to line scan and give a digital output using an 8-bit analogue to digital converter. With line scanning, a sensor detects thermal radiation from a point on the ground, a rotating mirror moves this point from side to side and forward motion of the aircraft advances the scan line, as illustrated in Figure 3-1.

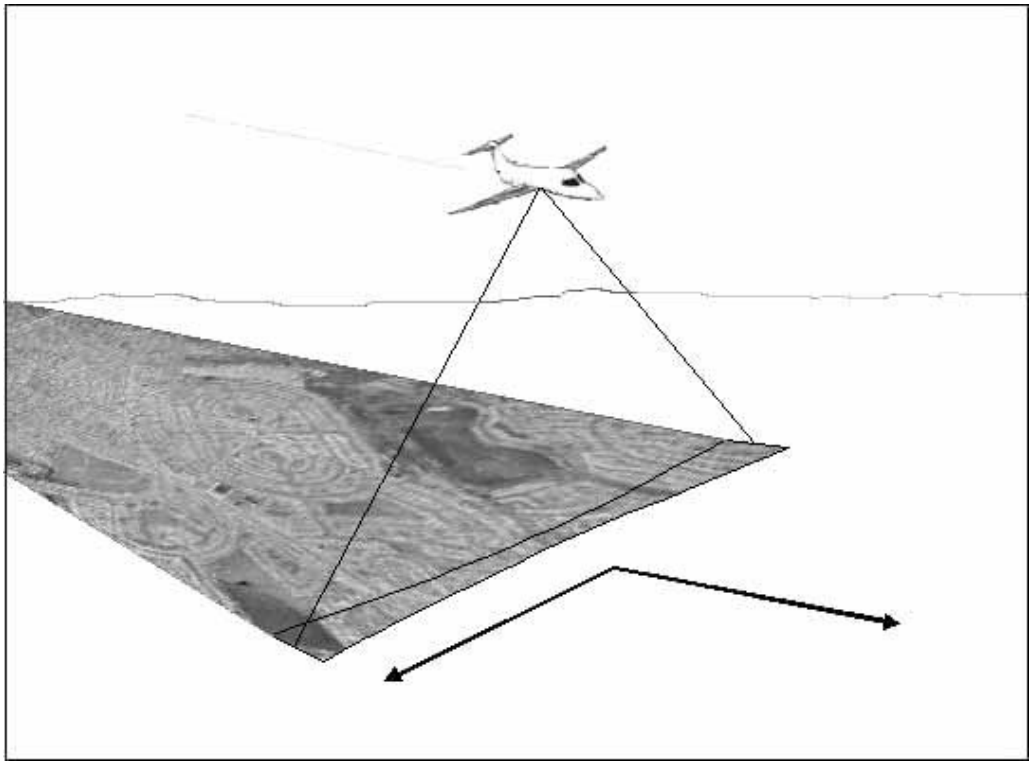

Figure 3-1: Line scanning from a fixed wing aircraft

'S-bend' correction was applied to the image by varying the digitisation rate across each scanned line and a gyroscopic mounting used to reduce distortions caused by aircraft roll. The scan angle was 60° ± 10° roll correction giving an average swath of 878m at 760m altitude and a pixel size of approximately 1m x 1m. Thermal resolutions of 0.2°C were claimed, under ideal conditions. The sensor was operating in the long wave (8-14μm) thermal band that coincides with the peak emittance of objects at typical terrestrial temperatures and is a window of reduced atmospheric attenuation.

3.1.2 Weather conditions

The literature contained a number of references that specified the most suitable meteorological conditions for data collection. These conditions can be summarised as [31, 52, 54, 67, 70-72, 94, 95]:

- selecting a period at least four hours after sunset to reduce the effects of daytime solar heating

- clear skies to prevent unpredictable variations in sky temperature
- calm winds to reduce ventilation and convective heat loss from the roof and prevent thermal shadows in sheltered areas
- dry roofs as heat will be lost by evaporation from a wet roof and water affects the emissivity of the surface
- good visibility to reduce atmospheric attenuation
- low ambient air temperature to maximize the temperature difference between the inside and outside of the building
- avoiding roof temperatures around 0°C where temperatures will stabilise as water freezes
- low humidity and roof surface temperatures above the dew point to avoid condensation

Absolute values of these parameters varied between references. The Nottingham survey was started approximately 3¼ hours after sunset (sunset was at 17.16hrs [96]) and it was assumed that any residual heating from daytime solar radiation had dissipated. For this study, weather data were purchased from the Meteorological Office for the 15th February 2001 in the form of hourly readings from the nearest weather station at Watnall, Nottinghamshire as shown in Table 3-1.

The average air temperature was reasonably low at 4.5°C, air temperatures were not changing rapidly and there had been no rain in the previous 24 hours. Mean wind speed was 4.7 knots (2.4m/s) reducing convective and ventilation heat loss effects. Clear skies prevented unpredictable variations in sky temperature. At 93%, the relative humidity would have increased the atmospheric attenuation due to water vapour in the air and condensation may have formed on roof surfaces if their temperature dropped below the dew point. While the former can be modelled, the effect of the latter is unknown. The dew point temperature was about 3.5°C and roof surface temperatures were calculated to be below this value (see Chapter 10).

Table 3-1: Hourly weather readings at Watnall on 15th February 2001

NOTTINGHAM, WATNALL
NGR = 4503E 3457N
Altitude = 117 metres
Latitude = 53:01 N Longitude = 01:25 W

Date	Time (GMT)	Temperature dry bulb (°C)	Relative humidity (%)	Rain amount (mm)	Wind mean direction (degrees)	Wind mean speed (knots)	Visibility (m)	Radiation global (kJ/m^2)
15/02/2001	00:00	2.1	92.5	0.0	210	3	10000	0
15/02/2001	01:00	2.2	90.8	0.0	270	4	8000	0
15/02/2001	02:00	2.8	89.2	0.0	260	5	10000	0
15/02/2001	03:00	1.8	92.4	0.0	270	4	8000	0
15/02/2001	04:00	0.7	98.0	0.0	250	3	6000	0
15/02/2001	05:00	-0.2	95.7	0.0	250	1	4300	0
15/02/2001	06:00	0.5	97.9	0.0	240	5	4600	0
15/02/2001	07:00	0.3	96.0	0.0	220	3	3200	0
15/02/2001	08:00	0.6	98.1	0.0	260	6	4000	32
15/02/2001	09:00	2.4	92.7	0.0	270	5	7000	191
15/02/2001	10:00	4.4	86.6	0.2	260	5	7000	702
15/02/2001	11:00	6.6	79.0	0.0	260	4	9000	1152
15/02/2001	12:00	8.3	72.1	0.0	260	3	10000	1354
15/02/2001	13:00	10.5	58.6	0.0	300	3	15000	1444
15/02/2001	14:00	11.2	49.3	0.0	350	3	24000	1361
15/02/2001	15:00	11.5	53.3	0.0	10	2	23000	1112
15/02/2001	16:00	10.7	57.7	0.0	340	3	17000	702
15/02/2001	17:00	7.6	76.9	0.0	60	4	9000	151
15/02/2001	18:00	5.6	85.7	0.0	70	3	5000	0
15/02/2001	19:00	5.3	88.7	0.0	360	3	7000	0
15/02/2001	20:00	4.4	91.6	0.0	310	4	6000	0
15/02/2001	21:00	4.2	93.2	0.0	320	5	6000	0
15/02/2001	22:00	4.5	93.2	0.0	360	4	6000	0
15/02/2001	23:00	4.8	93.5	0.0	360	5	60000	0
Average 21:00-23:00		**4.5**	**93.3**	**0.0**	**346.7**	**4.7**	**24000.0**	**0.0**

3.1.3 Geometric correction

Data collection by line scanning produces distorted images due to unwanted aircraft movement (roll, pitch and yaw), scanning geometry and ground topography. The Nottingham survey consisted of 30 overlapping flight lines of raw data. The BGS registered these data to a map coordinate system and geometrically corrected the position of buildings [7]. This was achieved by a rubber sheet correction of the individual flight line strips to 1:1250 Ordnance Survey Landline data using a large number of control points placed by hand on building corners. The flight line strips were then merged to produce the composite thermogram as a raster layer suitable for use in GIS software. The geometric correction was complicated by the poor image contrast, which was partly a result of the 8-bit digitisation and partly because of the meteorological conditions at the time of the survey.

An improved survey system has been reported by Wilson [97] that used a cruciform of GPS antennae, mounted on the aircraft, to provide absolute position in space along with roll, pitch and yaw. Combined with a Digital Elevation Model (DEM), geometric correction may automatically be applied in post processing. The system also provided 16-bit digitisation. The BGS had used data from this system on a separate investigation and found geometric correction simpler [98], though without a high resolution DEM, the tops of tall buildings were displaced when viewed off nadir.

It was observed by the BGS that flight line strips, from the Nottingham survey, did not join seamlessly. This was most noticeable where pixels from overlapping strips had different values for the same spot on the ground. This may have been due to either changing meteorological conditions during the survey or sensor drift. The BGS altered the contrast of entire strips to avoid an obviously striped image. While this is perfectly acceptable for qualitative analysis, it is problematic for quantitative analysis, as the pixels have lost their true values.

Sensor drift has been compensated for in other studies by using two black bodies, of known temperature, within the sensor that are imaged at the start and end of each scan line to provide a unique calibration for that scan [52, 54, 70-72, 97-100]. Some sensors also monitor the temperature of their optics and offset the errors caused by temperature change.

For the Nottingham survey, a contrast enhancement algorithm (contrast stretch), had been applied to the thermal image, within the GIS software, to improve discrimination of buildings. This was removed before the analysis for this study was carried out. The entire thermal image of the city is shown in Figure 3-2 along with a close up of one small area and the same area with the building polygons overlaid. Several of the limitations of the thermal image are evident. The location of buildings is not easy to identify, there are gaps where no data exists as flight lines did not always overlap or even join and roads do not appear straight as only the buildings were geometrically corrected.

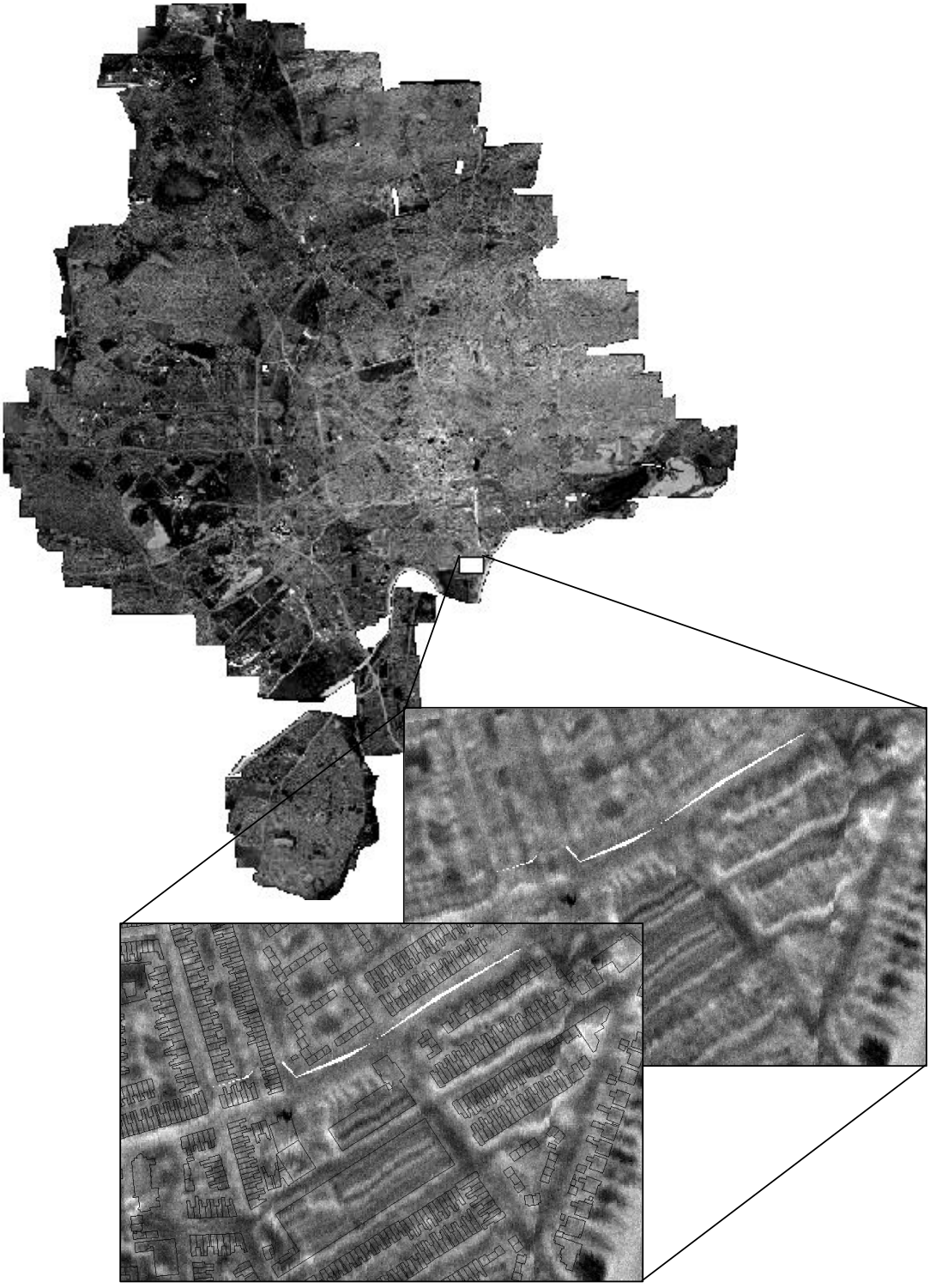

Figure 3-2: Thermal image of the city of Nottingham, close up of one area and the same area with building polygons overlaid (contrast adjusted for graphical reproduction)

3.2 Introduction to the data analysis

The quantitative analysis of the aerial thermography data forms the core of this thesis. From other studies (see Chapter 2.2.2), the key steps to this analysis were calculating the roof surface temperature from the thermal image, relating this temperature to insulation level and assessing the accuracy of the results.

The spatial analysis was carried out using ArcSoft's ArcMap Geographical Information System (GIS) software and the numerical models were programmed in MathSoft's Matlab software using Microsoft Excel spreadsheets for the input data for each house and manipulation and graphing of the outputs.

3.2.1 Calculating roof surface temperature

A sensor model was developed for this study to calculate roof surface temperature from the thermal image. This is a remote sensing application and the problems have been well defined (e.g. [101]). Primarily, the observed roof surfaces are not perfect emitters of infrared radiation and infrared radiation is absorbed by the atmosphere.

Thermal radiation is emitted by all objects, with a temperature above absolute zero, in a spectrum of wavelengths. The amount of radiation emitted by a blackbody, at any one wavelength, is described by the spectral blackbody emissive power distribution or Planck's Law, which may be written as Equation 3-1.

$$E_{b\lambda} = \frac{2\pi hc^2}{10^6 \lambda^5 (\exp(hc/\lambda KT) - 1)} \qquad \textbf{(3-1)}$$

$E_{b\lambda}$	spectral emissive power of a blackbody	$[W/m^2\mu m]$
c	velocity of light = 3.0×10^8	[m/s]
h	Planck's constant = 6.63×10^{-34}	[Js]
K	Boltzmann's constant = 1.38×10^{-23}	[J/K]
λ	wavelength	[μm]
T	surface temperature	[K]

Planck's Law

Plotting the spectral emissive power for a blackbody against wavelength for a number of temperatures produces a series of curves, known as Planck's curves, as shown in Figure 3-3.

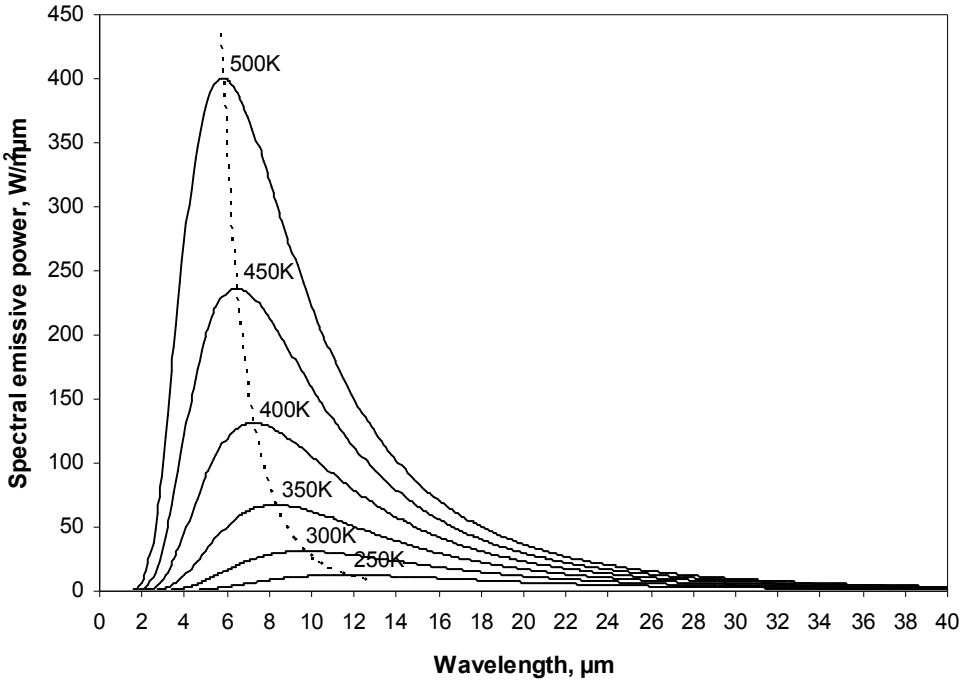

Figure 3-3: Planck's curves

The total emissive power can be found by integrating Planck's law across all wavelengths, which gives us the area under the curve for a particular temperature and is known as the Stefan-Boltzmann law as shown in Equation 3-2.

$$\int_0^\infty E_{b\lambda}\, d\lambda = E_b = \sigma T^4 \qquad \textbf{(3-2)}$$

$E_{b\lambda}$	spectral emissive power of a blackbody	$[W/m^2\mu m]$
E_b	total emissive power of a black body	$[W/m^2]$
T	surface temperature	[K]
σ	Stefan-Boltzmann constant = 5.670×10^{-8}	$[W/m^2 K^4]$

Stefan-Boltzmann law

The thermography sensor only operates in the 8-14μm wavelength band and this is accounted for by weighting the results by the sensors spectral response function as detailed in Section 4.5.

Real surfaces are not perfect emitters of thermal radiation and the ratio of the emissive power of a surface to the emissive power of a black surface at the same temperature is known as the emissivity as shown in Equation 3-3.

$$\varepsilon = \frac{E}{E_b} \qquad \textbf{(3-3)}$$

ε	emissivity	
E	emissive power of a surface	$[W/m^2]$
E_b	emissive power of a black body at the same temperature as the surface	$[W/m^2]$

Definition of emissivity

A blackbody absorbs all of the incident radiation at any given temperature and wavelength. Real surfaces, however, absorb and reflect thermal radiation and may transmit thermal radiation as shown in Figure 3-4.

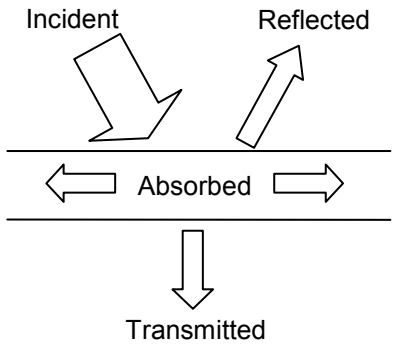

Figure 3-4: Absorption, reflection and transmission of incident thermal radiation

The proportions of radiation absorbed, reflected and transmitted by a surface are described by the fractions absorptivity, α, reflectivity, ρ and transmissivity, τ such that $\alpha+\rho+\tau=1$. Roof surfaces are typically opaque to infrared radiation and so the transmissivity, $\tau=0$. Kirchoff's law dictates that the amount of radiative energy emitted by a surface must equal the amount

of radiative energy absorbed by that surface, i.e. $\varepsilon = \alpha$. The reflectivity of a roof surface may therefore be defined by $\rho=(1-\varepsilon)$.

During an aerial thermography survey, the infrared sensor in the aeroplane, when viewing the roof of a house, detects some of the radiance emitted by the roof and some of the incident radiation reflected from the roof. This incident radiation may originate from the very cold night sky or the warmer surroundings. Additionally, the column of air between the roof and the sensor, while having a relatively high transmissivity in the 8 to 14μm wavelength band, still absorbs some of the radiation originating at the roof and emits some radiation as a function of its own temperature that is detected by the sensor. Only by accounting for these radiation paths and losses, shown in Figure 3-5, can roof surface temperature can be calculated with any certainty.

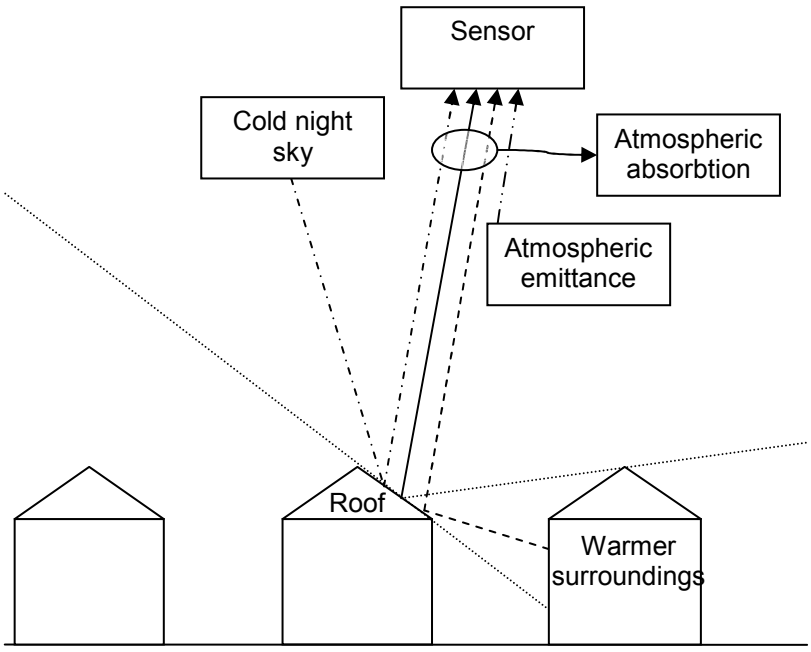

Figure 3-5: Radiation paths and losses

The sensor model, detailed in Chapter 4, describes the infrared radiation in terms of radiance rather than emissive power. Radiance is simply the directional emissive power per solid angle (steradian) and, assuming the surfaces are Lambertian (i.e. the radiance is the same in all

directions) the relationship between emissive power and radiance is described by Equation 3-4.

$$L = \frac{E}{\pi} \quad \textbf{(3-4)}$$

L	radiance	$[W/m^2sr]$
E	emissive power of a surface	$[W/m^2]$

Relationship between emissive power and radiance

3.2.2 Relating roof surface temperature and insulation thickness

A building model was developed for this study, to examine the relationship between insulation thickness and roof surface temperature. It was assumed that the building, its roof and the surroundings had reached a point of thermal equilibrium and that steady state conditions applied. This assumption is reasonable if daytime solar thermal loading of the building fabric has had time to dissipate, the heating system is providing a constant inside temperature and the outside air temperatures are not changing rapidly.

As illustrated in Figure 3-6, heat from the inside of the house is lost through the ceiling and insulation layer by conduction into the loft space. The loft space exchanges heat with the roof surface by conduction through the outer fabric of the roof and, as loft spaces are normally ventilated to prevent condensation in the cavity, heat exchange occurs through ventilation. The outside surface of the roof exchanges heat with its environment through radiation and convection.

Roof surface temperature depends on the meteorological conditions, roof construction and the buildings surroundings as well as insulation level. Insulation level can only be inferred from roof surface temperature if all of the heat paths are quantified. The building model, developed for this study, is detailed in Chapter 5. A number of different heat balance methods for the loft space and the outside surface were found in the literature and these were compared, as presented in Chapter 6, so that the most accurate techniques were chosen for this study.

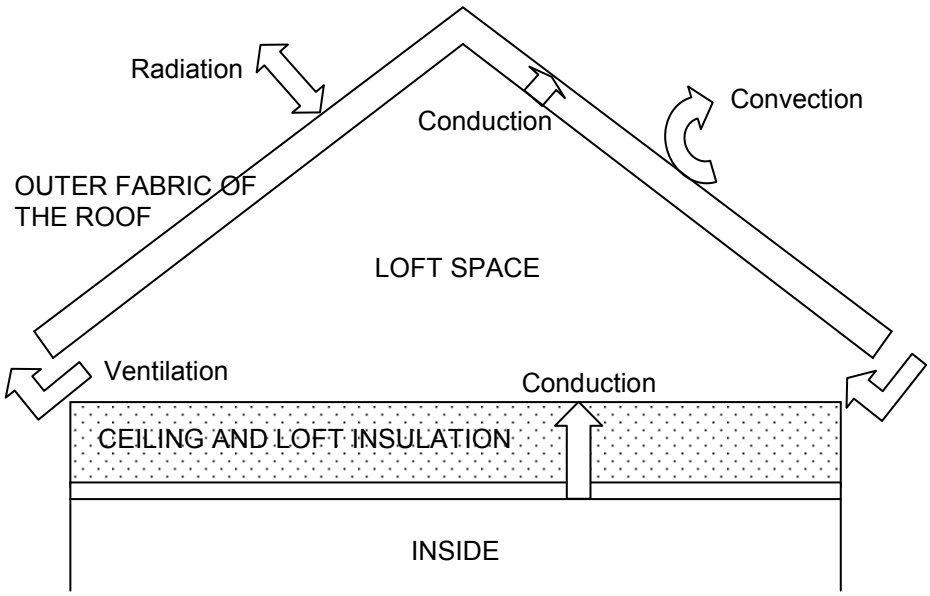

Figure 3-6: Heat exchange between the building and its environment through the roof

3.2.3 Assessing the accuracy of the results

The sensor and building models introduced a considerable level of complexity and included assumptions and simplifications. A large number of additional parameters were needed for the analysis and it was not possible to know the value of each of these parameters exactly. These errors were investigated and quantified by an error analysis (Chapter 9) and using a case study of houses in trial areas of the Nottingham survey.

The sensor model was used to measure roof surface temperature from the thermal image and the building model was used to relate the roof surface temperature to insulation level for any building on the ground. These two temperatures were then analysed and compared in the accuracy assessment for a number of buildings in this study. This process is shown as a flowchart in Figure 3-7.

Initially a number of test buildings were defined (see Section 9.2), based on those used for the Nottingham case study. The parameter sets for these buildings were used to investigate the sensitivity of the results of the models to error in each of the input parameters in turn. This was achieved by a one-at-a-time sensitivity analysis, which is detailed in Section 9.3.

Additional effort was put into defining those parameters to which the result was most sensitive.

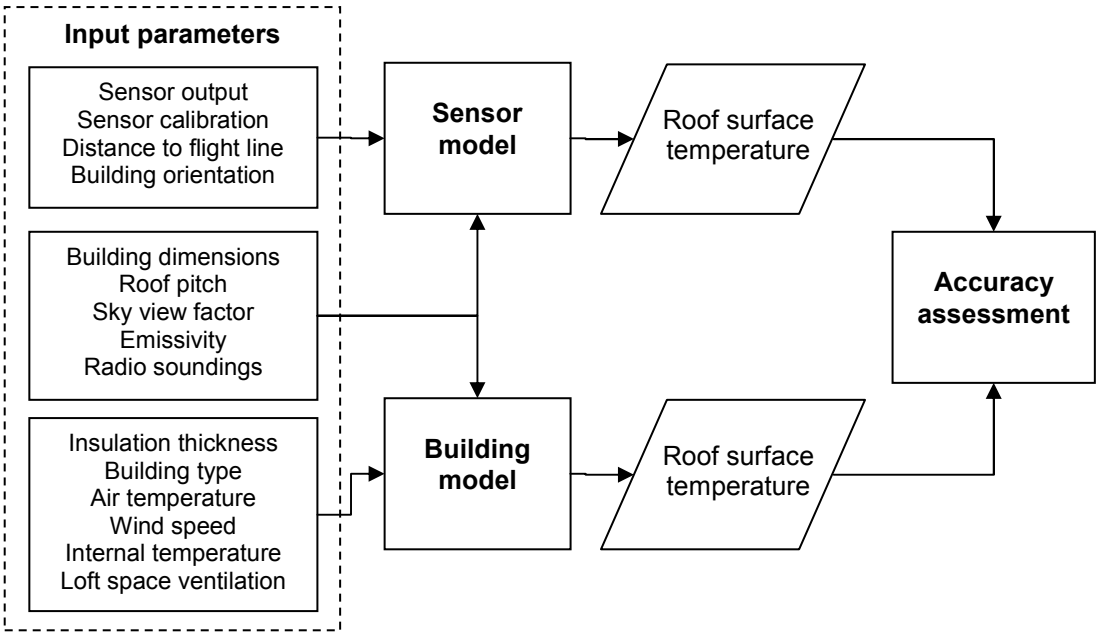

Figure 3-7: Process flowchart

The same test building parameters were used to calculate the overall uncertainty in the results. This necessitated defining the standard uncertainty of each input parameter, after the British Standard Institute's guide to measurement uncertainty [102]. These uncertainties were then propagated by simulation using a Monte Carlo technique as detailed in Section 9.4.

A case study of 98 council owned houses in the City of Nottingham was chosen to complete this study. The actual thickness of loft insulation for each house was taken from the values recorded in Nottingham City Council's housing database. The roof surface temperature of each house was calculated from the thermal image using the sensor model and from this, the thickness of insulation using the building model. These two temperatures were compared and a confusion matrix was used to determine the accuracy of using aerial thermography to discriminate insulation level, for the 98 houses. The results of the analysis of this case study are given in Chapter 10.

3.3 Additional data

To complete the quantitative analysis, large amounts of data, in addition to the thermal image, were collected, or determined, for this study. These parameters, and where they were sourced, are summarised in Table 3-2. Further details are contained in the relevant chapter.

Table 3-2: Additional data with source

Parameter	Source
Building ground plan/position	Ordnance Survey Landline data in GIS
Building length (along ridge)	Ordnance Survey Landline data in GIS
Building width	Ordnance Survey Landline data in GIS
Distance from flight line	Ordnance Survey Landline data in GIS
Orientation to flight line	Ordnance Survey Landline data in GIS
Roof pitch	Site survey
Building type	Site survey
Sky view factor	GIS/Site survey/Rayman software
Roof material/emissivity	Site survey/laboratory testing
Ambient air temperature	Meteorological Office historical data
Wind speed	Meteorological Office historical data
Building internal temperature	Assumed 18°C
Roof construction	Building Surveyor/guesstimates
Loft space air changes	Assumed 2 per hour
Loft insulation thickness	Council housing database
Atmospheric radio soundings	University of Wyoming web site
Sensor calibration	Assumed from back calibration
Sensor spectral response	Typical response data from Infoterra

Within the GIS, the Ordnance Survey Landline data were used to define the extents of each building. The ground plan of the buildings, represented in these data as two-dimensional polygons, was overlaid on the thermal image to determine the pixels relating to each house

(see Section 4.2). Building length and width were also measured from these data (see Section 8.2.1). Flight lines were drawn onto a new GIS layer, at the centre of each strip, to calculate the sensor angle and roof orientation for each house (see Section 8.2.3).

Site surveys of the test areas were carried out to identify the roof pitch (see Section 8.2.2) and determine the building type (end or mid-terrace see Section 5.4.2) for each house in the case study. Sky view factor was determined from simplistic three-dimensional models of the areas using a combination of GIS measurements and site survey (see Section 8.4). The roof surface material was identified for each house from the site survey and the emissivity of a similar material measured in the laboratory (see Section 8.3).

Wind speed and ambient air temperature measurements were needed and in the absence of local measurements, historical hourly weather from the Meteorological Office was procured (see Section 3.1.2). These data were observed at the nearest meteorological station at Watnall, Nottinghamshire, which is about 10km northeast of the city centre. The areas chosen for the case study were also to the North and North East of the city.

Additional data required for the building model included the internal temperature below the insulated ceiling, details of the roof construction (see Section 5.2) and the number of air changes per hour in the loft air space (see Section 6.3). These were guesstimated or based on the advice of a Nottingham City Council surveyor [103]. The thickness of loft insulation for each building was taken from the Council's housing database. This was an extremely useful resource as, for the first Calspan/Rochester Institute of Technology survey, staff resorted to door-to-door enquiries to try and find out the insulation level of sufficient houses to check their results and reported widespread 'homeowner enmity' [62].

Atmospheric radio soundings were needed to characterise the atmosphere above the city at the time of the survey (see Chapter 7). Fortunately these data were also available from the weather station at Watnall and were obtained freely on the internet via the University of Wyoming [104].

The sensor used for the Nottingham survey was not calibrated and the data was therefore back calibrated. As there were no surfaces of known temperature in the thermal image, (unsuccessful attempts were made to get historical temperature data for the River Trent which appears at the southern edge of the image) the sensor model was back calibrated against the temperatures calculated by the building model, for a test area of the case study (see Section 4.2). The spectral response of the sensor was also unknown, and Infoterra provided these data for a similar instrument (see Section 4.4).

3.4 Conclusions

A methodology for discriminating insulation level from aerial thermography was developed for this study. While the data collection had already being carried out, the sensor used, weather conditions at the time of the survey and geometric correction of the data were all considered.

The analysis of the data necessitated developing a sensor model to calculate roof surface temperature from the thermal image (Chapter 4) and a building model to relate roof surface temperature to insulation level (Chapters 5 and 6). The accuracy of these models was investigated and assessed by sensitivity analysis and uncertainty analysis (Chapter 9) and a confusion matrix used to classify the results for the houses in the Nottingham case study (Chapter 10).

A large amount of additional data had to be sourced for the quantitative analysis and a number of atmospheric properties (Chapter 7) and physical properties (Chapter 8) had to be derived. This would not always be available or easy to accomplish for an entire city. Existing techniques from the literature were combined in a new and unique way in an attempt to provide the most sophisticated and complete analysis to date. Theses techniques are described in more detail in the following chapters, starting with the development of the sensor model.

4 Developing of the sensor model

This chapter describes the sensor model that was introduced in Chapter 3. It was developed for this study to calculate the roof surface temperature of houses, from their thermal image pixel values.

A simplified process flow chart is shown in Figure 4-1. The calculation of at-sensor radiance, roof blackbody radiance and roof surface temperature are described below along with the sensor's spectral response function, which is a key input to each of these processes.

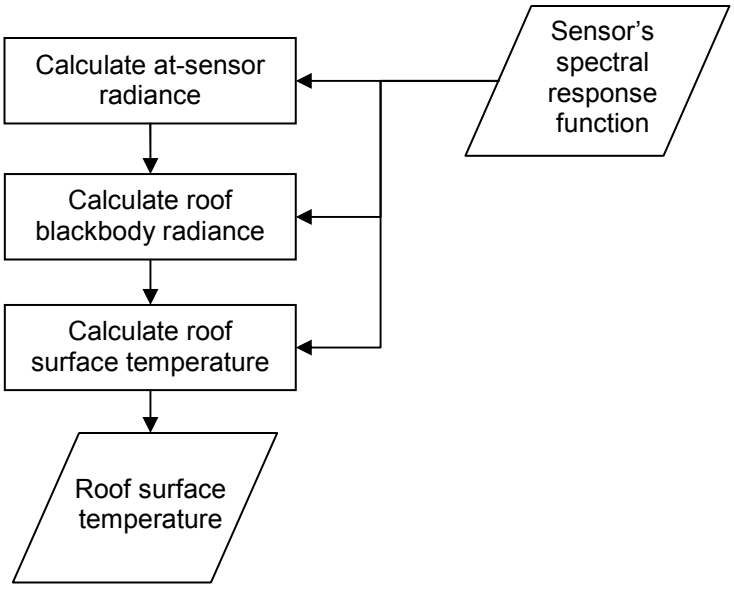

Figure 4-1: The sensor model process flowchart

4.1 At-sensor radiance

The at-sensor radiance is that radiance detected by the sensor when viewing a particular roof. This is not the same as the radiance originating from that roof. It was calculated by averaging the thermal image pixel values for the roof of each house and then applying a sensor calibration.

4.1.1 Averaging pixel values

GIS software was used to average those thermal image pixels with centres inside the building polygon representing each house. To avoid sampling pixels outside of the building, and to allow for some error in the geometric correction process, a 1.1m buffer was used inside of each building polygon as shown Figure 4-2. This followed the recommendations Adepoju et al. [8].

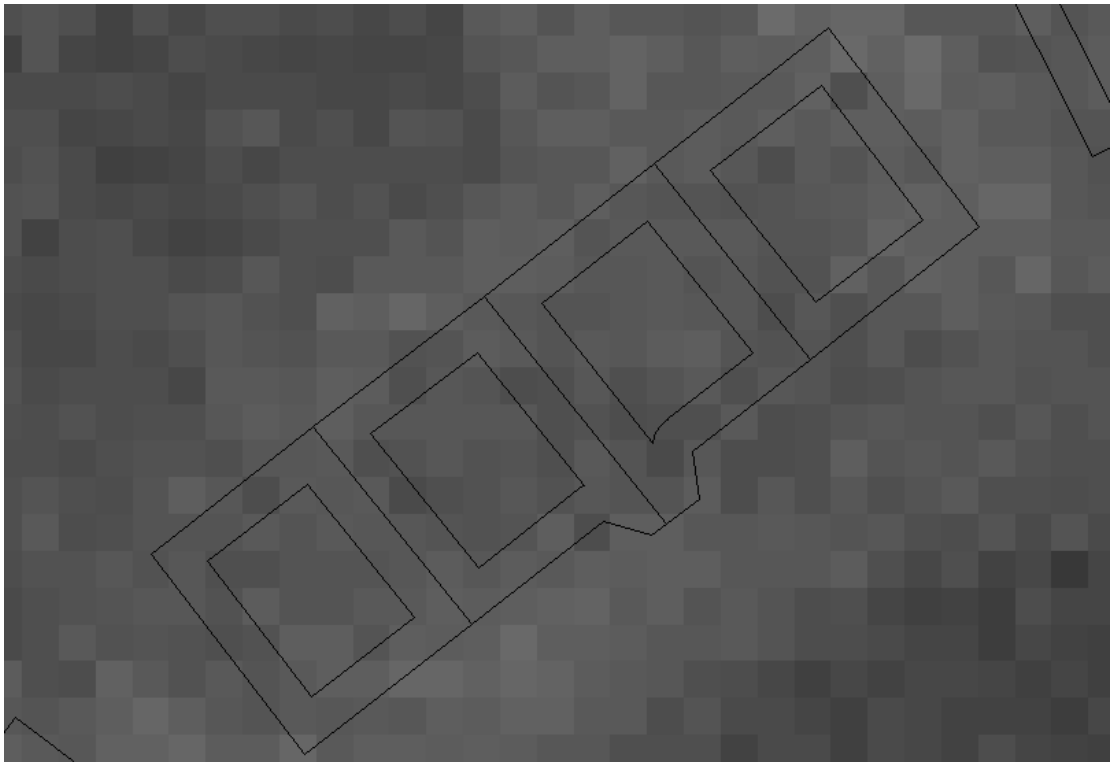

Figure 4-2: 1.1m buffer within each building

The sensor output was in the form of an eight-bit digital number (0-255) for each pixel of the thermal image. Pixels were approximately 1m square and between 12 and 19 pixels were averaged in total for the roof of each house.

The uncertainty in the roof averaged sensor output was determined for the uncertainty analysis in Section 9.4. The standard uncertainty in the mean pixel value was calculated by dividing the standard deviation of the pixel values, within the buffer of each house, by the square root of the number of pixels, after the method set out by BSI [102] as shown in Equation 4-1.

$$u(\bar{x}) = \frac{s(x)}{\sqrt{N}} \quad \textbf{(4-1)}$$

$u(\bar{x})$ standard uncertainty of the mean pixel values within building buffer

$s(x)$ standard deviation of the pixel values within building buffer

N number of pixels

Standard uncertainty of the mean pixel value within a building buffer

The average of the standard uncertainties calculated for all of the Council owned houses in the Northwood Crescent and Eltham Drive test areas (see Chapter 10.2) was 1.3. This standard uncertainty was used in the absence of any other data to characterise the sensor's accuracy.

4.1.2 Sensor calibration

A sensor calibration was used to calculate the at-sensor radiance from the mean pixel value. Thermal infrared sensors are designed to give a linear response with observed radiance as shown in Equation 4-2 after Schott [99].

$$DN = m\left[\int_0^\infty L_\lambda R'(\lambda)d\lambda\right] + c \quad \textbf{(4-2)}$$

DN averaged sensor output

m system gain including optics and electronics

c system bias including radiometric and electronic offset

L_λ monochromatic radiance at wavelength, λ [$W/m^2 sr \mu m$]

$R'(\lambda)$ peak normalised spectral response function of the sensor

Sensor linear response after Schott [99]

Utilising this linear response, the average pixel value for each building was converted to at-sensor radiance using Equation 4-3 after Singh [105].

$$L = \frac{(L_{max} - L_{min})}{255} \times DN + L_{min} \quad \textbf{(4-3)}$$

L	at-sensor radiance	[W/m^{2}sr]
L_{max}	radiance at DN=255	[W/m^{2}sr]
L_{min}	radiance at DN=0	[W/m^{2}sr]
DN	average radiance for the roof of interest	

Calculation of at-sensor radiance after Singh [105]

The values of L_{max} and L_{min} were not known and there was no formal calibration for the sensor but it was operating in a 20K temperature window [106]. By estimating the value of the minimum temperature in the range, values of L_{min} and L_{max} were calculated from a numerical solution of the Planck equation weighted by the spectral response function of the sensor as shown in Equation 4-4.

$$L_{min} = \int_0^{\infty} 2hc^2\lambda_i^{-5} \times \left[\exp\left(hc / \lambda_i kT_{min} \right) - 1\right]^{-1} \times R'(\lambda)d\lambda$$
$$L_{max} = \int_0^{\infty} 2hc^2\lambda_i^{-5} \times \left[\exp\left(hc / \lambda_i k(T_{min} + 20)\right) - 1\right]^{-1} \times R'(\lambda)d\lambda \quad \textbf{(4-4)}$$

T_{min}	minimum brightness temperature of the temperature window	[K]
h	Planck constant = 6.6262 x 10^{-34}	[Js]
c	speed of light in a vacuum = 299792458	[m/s]
λ	wavelength	[m]
k	Boltzmann constant = 1.3807×10^{-23}	[J/K]

Calculation of radiance range from apparent temperature range

The value of T_{min} was found by matching the output of the sensor model with the output from the building model. The average roof surface temperature of 63 houses on the Fenwick Road test area (see Chapter 10.2) was calculated from their known insulation thickness using the building model (see Chapter 4). The roof surface temperature was then determined for the same 63 houses using the sensor model and an estimate of T_{min}. The estimate of T_{min} was adjusted until the average roof surface temperature calculated by the sensor model was the same as that calculated by the building model.

4.2 Roof blackbody radiance

The roof surface emits radiance as a function of its temperature and emissivity. The roof blackbody radiance is the equivalent radiance emitted by a blackbody at the same temperature as the roof. Its calculation is an important step towards finding roof surface temperature and requires consideration of the radiation paths and losses between a point on the roof and the sensor shown in Figure 4-3. The radiance reaching the sensor (at-sensor radiance) was expressed as Equation 4-5, after Schott [101].

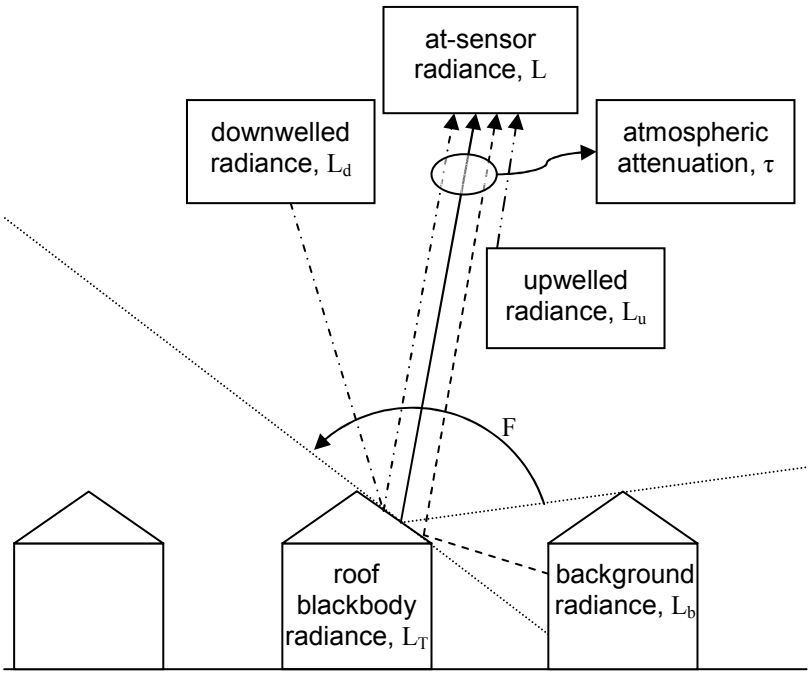

Figure 4-3: Paths and losses of radiation reaching the sensor

$$L = \{\varepsilon L_T + (1-\varepsilon)(F L_d + (1-F) L_b)\}\tau + L_u \qquad \textbf{(4-5)}$$

L	at-sensor radiance	$[W/m^2sr]$
L_T	roof blackbody radiance	$[W/m^2sr]$
L_d	downwelled radiance from the atmosphere	$[W/m^2sr]$
L_b	average background radiance	$[W/m^2sr]$
L_u	upwelled radiance due to the atmosphere	$[W/m^2sr]$
ε	is the emissivity of the roof	
τ	is the transmittance of the atmosphere	
F	is the sky view factor of the roof	

At-sensor radiance after Schott [101]

This approximation relies on the wavelength dependant terms being reasonably constant over the spectral band pass of the sensor [101] as ε and τ are average values. The radiance terms, L_T, L_b, L_d and L_u, are effective radiances and are all weighted by the peak normalised spectral response function of the sensor as shown in Equation 4-6.

$$L_{eff} = \int_0^{\infty} L_\lambda R'(\lambda) d\lambda \qquad \textbf{(4-6)}$$

L_{eff}	effective radiance in the sensor's band pass	[W/m^{2}sr]
L_λ	monochromatic radiance at wavelength, λ	[W/m^{2}srμm]
R'(λ)	peak normalised spectral response function of the sensor	

Effective radiance in the sensors band pass

The roof blackbody radiance was calculated by rearranging Equation 4-5 and assuming that the background radiance was the same (i.e. L_T=L_{bg}) as shown in Equation 4-7.

$$L_T = \frac{(L - L_u)/\tau - (1-\varepsilon)FL_d}{\varepsilon + (1-\varepsilon)(1-F)} \qquad \textbf{(4-7)}$$

L	at-sensor radiance	[W/m^{2}sr]
L_T	roof blackbody radiance	[W/m^{2}sr]
Ld	downwelled radiance from the atmosphere	[W/m^{2}sr]
Lu	upwelled radiance due to the atmosphere	[W/m^{2}sr]
ε	is the emissivity of the roof	
τ	is the transmittance of the atmosphere	
F	is the sky view factor of the roof	

Solving Equation 4-5 for the roof blackbody radiance

The assumption that the background radiance was the same as the roof blackbody radiance was made in the absence of any other data. The background radiance may have originated from cold surrounding roofs, which are viewed on the thermal image, warmer building walls, which are not, as well as ground surfaces, trees and any other objects in the vicinity. It was therefore difficult to ascertain a true background temperature. This issue is discussed further in Section 6.2 and considered during the sensitivity analysis in Section 9.3.

The derivation of emissivity and sky view factor are given in Chapter 8 and downwelled radiance and upwelled radiance in Chapter 7.

4.3 Calculating surface temperature

The relationship between the roof blackbody radiance and its surface temperature was described by the Planck law weighted by the peak normalised spectral response function of the sensor as shown in Equation 4-8.

$$L_T = \int_0^{\infty} 2hc^2\lambda^{-5} \times \left[\exp\left(hc / \lambda k T_{surface} \right) - 1\right]^{-1} \times R'(\lambda) d\lambda \qquad \textbf{(4-8)}$$

L_T	roof blackbody radiance	[W/m^{2}sr]
h	Planck constant = 6.6262 x 10^{-34}	[Js]
c	speed of light in a vacuum = 299792458	[m/s]
k	Boltzmann constant = 1.3807×10^{-23}	[J/K]
λ	wavelength of emitted radiation	[m]
$T_{surface}$	roof surface temperature	[K]
R'(λ)	peak normalised spectral response function of the sensor	

Planck law weighted by the peak normalised spectral response function

L_T was calculated by a numeric solution of Equation 4-8 for temperatures $T_{min} \leq T_{surface} \leq T_{max}$ in 0.1K intervals. T_{min} and T_{max} were the same minimum and maximum temperatures of the sensor operating window ($T_{max}=T_{min}+20$, see Section 4.1). Linear regression of $\ln(L_T)$ with $1/T_{surface}$ gave the straight line described by the regression coefficients a and b in Equation 4-9. This is the Singh approximation [105], as used by Snyder and Schott [95] for Calspan/Rochester Institute of Technology.

$$\ln(L_T) = a + b\frac{1}{T_{surface}} \qquad \textbf{(4-9)}$$

L_T	roof blackbody radiance	[W/m^{2}sr]
$T_{surface}$	roof surface temperature	[K]
a	regression coefficient	
b	regression coefficient	

The Singh approximation [105]

The roof surface temperature, $T_{surface}$ was then calculated for any value of L_T from Equation 4-10.

$$T_{surface} = \frac{b}{\ln(L_T) - a} \quad \textbf{(4-10)}$$

L_T	roof blackbody radiance	[W/m^{2}sr]
$T_{surface}$	roof surface temperature	[K]
a	regression coefficient from Equation 4-9	
b	regression coefficient from Equation 4-9	

Calculation of roof surface temperature from roof blackbody radiance

4.4 Spectral response function of the sensor

The peak normalised spectral response function of the sensor was used to relate the radiance emitted by any surface to that measured by the sensor. The spectral response function was described by Schott [101] as the signal output per unit flux incident on the sensor at each wavelength, as shown in Equation 4-11.

$$R(\lambda) = \frac{dS}{d\Phi(\lambda)} \quad \textbf{(4-11)}$$

$R(\lambda)$	spectral response function of the sensor	[V/W]
S	signal output	[V]
Φ	flux incident on the detector	[W]

Spectral response function of the sensor after Schott [101]

The peak normalised spectral response function was also defined after Schott [101], as shown in Equation 4-12.

$$R'(\lambda) = \frac{R(\lambda)}{R(\lambda)_{max}} \quad \textbf{(4-12)}$$

$R'(\lambda)$	peak normalised spectral response function of the sensor	
$R(\lambda)$	spectral response function of the sensor	[V/W]
$R(\lambda)_{max}$	maximum value (or peak) of the spectral response function	[V/W]

Peak normalised spectral response function after Schott [101]

There was no spectral calibration for the sensor used for the Nottingham data set. Post calibration of the instrument was too expensive for the purposes of this study. Infoterra supplied a typical calibration data set for a similar instrument in the form of tables of percentage transmission for the lens and cut-on filter and percentage response for the detector [106]. The total responsivity of the sensor in this study was defined from these data by Equation 4-13 as plotted in Figure 4-4.

$$R(\lambda) = R_{lens}(\lambda) \times R_{filter}(\lambda) \times R_{detector}(\lambda) \quad \textbf{(4-13)}$$

$R(\lambda)$ spectral response function of the sensor

$R_{lens}(\lambda)$ spectral transmission of the lens

$R_{filter}(\lambda)$ spectral transmission of the cut-on filter

$R_{detect}(\lambda)$ spectral response of the detector

Total responsivity of the sensor

The response was then peak-normalised as shown in Figure 4-5. The response of an "ideal sensor" operating in the 8-14μm wavelength range was included for comparison. It can be seen that an ideal sensor would detect more of the incident radiation, especially above 12μm. The radiance emitted by any object is a function of wavelength, as shown in Section 3.3.1, and it is therefore important to include the spectral response in all the sensor model radiance calculations.

As the transmission and response values supplied by Infoterra had irregular wavelength intervals, they were re-sampled to give a wavelength interval of 0.1μm across the range. The results were smoothed using a 3-point moving average and are given in Appendix 1.

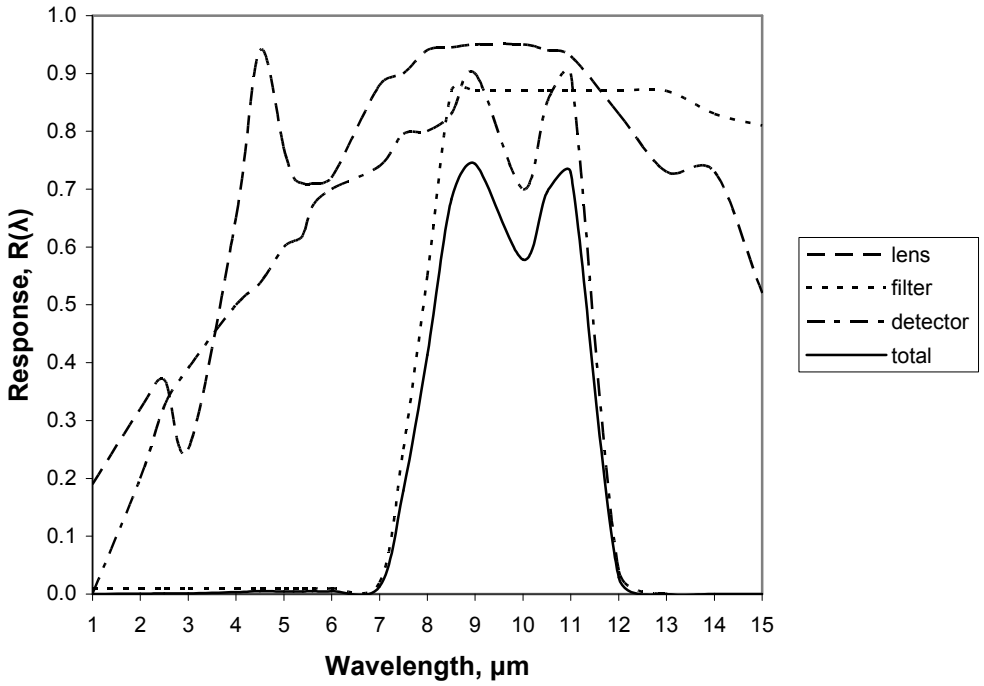

Figure 4-4: Response data for a typical sensor

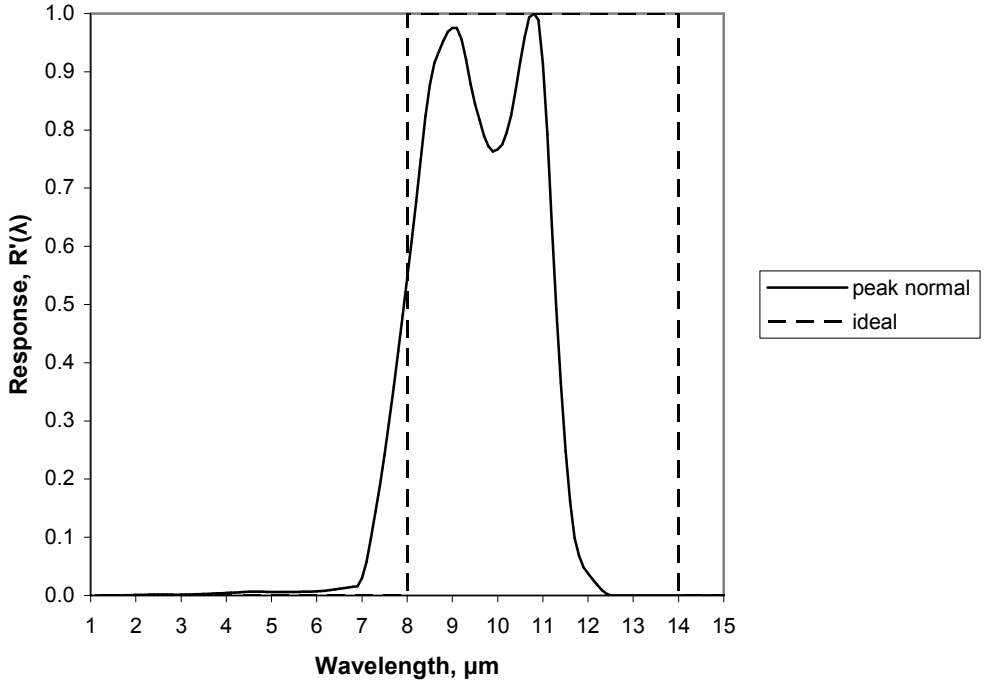

Figure 4-5: Peak normalised spectral response function

4.5 Conclusions

The sensor model was developed for this study, to determine roof surface temperature from the thermal image. The at-sensor radiance was calculated from the averaged sensor output of each roof using an assumed calibration. The roof blackbody radiance was then calculated by accounting for the atmospheric attenuation, upwelled radiance and the reflected sky and background radiance. All the radiance terms were weighted by the peak normalised spectral response function of the sensor and the roof surface temperature calculated from a numerical, inverse solution of Planck's Law.

The next chapter considers the building model used to relate roof surface temperature to insulation level.

5 Developing the building model

This chapter describes the building model that was introduced in Chapter 3. It was developed for this study to calculate the roof surface temperature of houses from their loft insulation thickness. It was assumed that the roof and its surroundings had reached a state of thermal equilibrium and that steady state conditions applied. A simplified process flow chart of this model is shown in Figure 5-1.

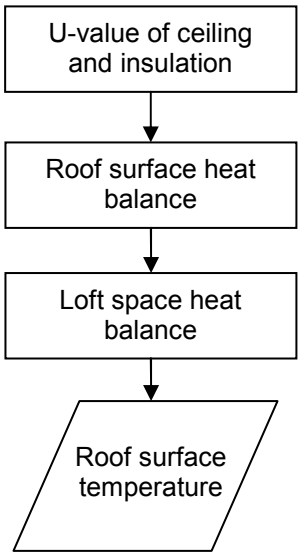

Figure 5-1: The building model process flowchart

Each of these processes is described below. While the calculation of the U-value of the ceiling and insulation layer was by an established method, numerous methods existed for the roof surface heat balance and the loft space heat balance. These methods were compared in Chapter 6, and those deemed to provide the most accurate results were chosen for this study.

It would have been useful to be able to calculate the loft insulation level directly from the roof surface temperature measurement derived from the sensor model for a given house. This was not possible as the relationship was non-linear. An iterative solution was not appropriate as very small temperature changes produced large increases in insulation level, especially for well insulated houses, up to a maximum temperature for infinite insulation. There was also a

minimum temperature relating to no insulation, beyond which the calculated insulation level was negative. Roof surface temperature was therefore calculated from insulation level.

5.1 U-value of the ceiling and loft insulation

The thermal conductance (U-value) of the ceiling and loft insulation was calculated so that the heat lost from the inside of the house and into the loft space, by conduction of heat through these layers as shown in Figure 5-2, could be quantified.

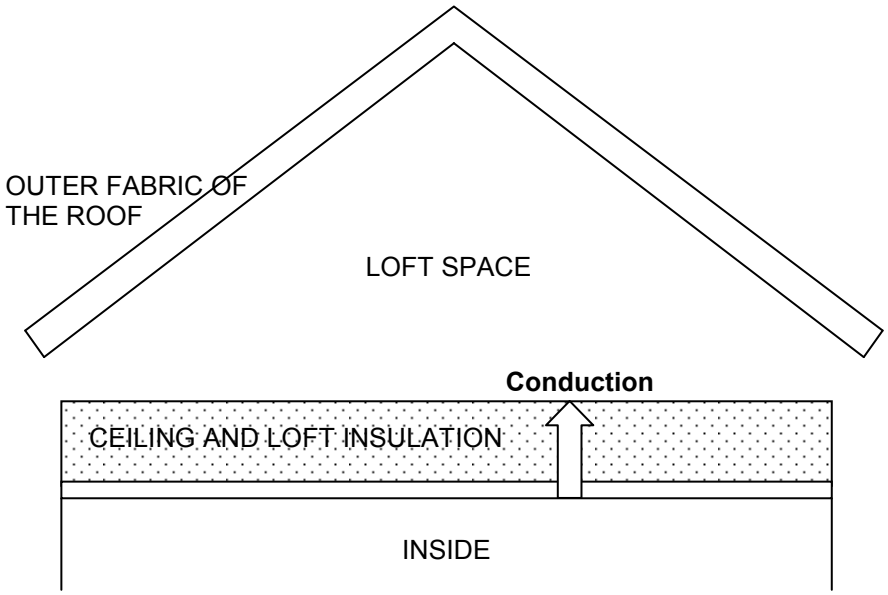

Figure 5-2: Conduction of heat through the ceiling and loft insulation

Based on information provided by a Nottingham City Council Building Surveyor [103], for a typical house in the case study area, the ceiling consisted of (see Figure 5-3) 13mm plasterboard and skim, 100mm x 50mm ceiling joists at 600mm centres, up to 100mm of mineral wool quilt between joists and up to 150mm of mineral wool quilt over joists (for total thicknesses greater than 100mm). The thermal resistance (R) of each material was calculated from design thermal conductivity values in the CIBSE guide [107].

The U-value was calculated by Equation 5-1 using the proportional area method, from the CIBSE Guide [107], for the ceiling joist bridges. The thermal resistance at the surface of the mineral wool quilt insulation layer was ignored as it was accounted for in the loft space heat

balance. Values of thermal conductance, calculated by Equation 5-1, for various insulation levels are shown in Table 5-1.

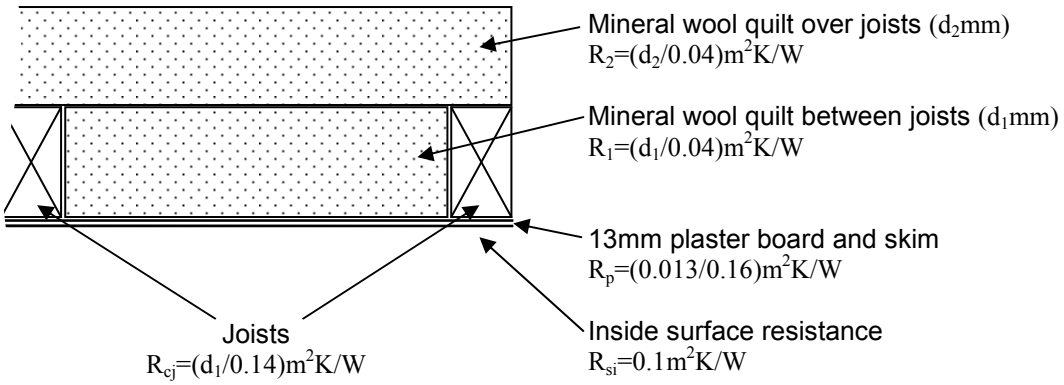

Figure 5-3: Cross section through the ceiling and loft insulation

$$U_{ceiling} = \frac{P_{cj}}{R_2 + R_{cj} + R_p + R_{si}} + \frac{(1 - P_{cj})}{R_2 + R_1 + R_p + R_{si}} \qquad \textbf{(5-1)}$$

$U_{ceiling}$	thermal conductance of the ceiling and loft insulation	[W/m^{2}K]
P_{cj}	proportion of the ceiling area that is ceiling joist (=50mm/600mm)	
R_2	thermal resistance of mineral wool quilt over joists	[m^{2}K/W]
R_1	thermal resistance of mineral wool quilt between joists	[m^{2}K/W]
R_p	thermal resistance of the plaster board and skim	[m^{2}K/W]
R_{si}	thermal resistance of the inside surface	[m^{2}K/W]
R_{cj}	thermal resistance of ceiling joist	[m^{2}K/W]

U-value of the ceiling and loft insulation

Table 5-1: U-value of the ceiling and loft insulation calculated by Equation 5-1

Insulation level mm	Thermal conductance, $U_{ceiling}$ W/m^{2}K
0	5.52
50	0.80
100	0.43
150	0.27
200	0.20
250	0.16

There were a number of potential limitations to this calculation. Loft insulation that is ill fitting, damp or dirty will affect the U-value as would items stored in the loft space, cold water tanks and services penetrating the plasterboard (e.g. mains electrical wiring and plumbing). Also, the actual thermal resistance of the insulation and plaster board may not be the same as the published figures. At the Building Research Establishment, Doran [108] reported an investigation into the thermal performance of a number of wall and ceiling constructions in the UK. Measuring the as built U-value he found it was typically larger than that calculated by BS EN ISO 6948 [109] by an average of around 20% or 0.1W/m^{2}K for walls and room-in-roof, sloping ceilings. These variations were attributed to both the calculation methodology and construction defects.

BS EN ISO 6948 [109] provides a correction for air gaps in insulation which may be appropriate where insulation is poorly fitted. This accounts for an increase in the U-value of about 0.01W/m^{2}K for houses in this study and is equivalent to about 10mm of insulation. Assuming the 90% confidence interval is ±10mm, the standard uncertainty calculated from Equation 5-2, after the method set out by BSI [102], was 6mm (k=1.64 for 90%). This conservative estimate of uncertainty was used for the uncertainty analysis in Section 9.4.

$$u(x) = \frac{U(x)}{k} \qquad \textbf{(5-2)}$$

U(x)	expanded uncertainty (confidence interval)	
u(x)	standard uncertainty	
k	statistical coverage factor	

Standard uncertainty calculated from expanded uncertainty after BSI [102]

The conduction through the ceiling and loft insulation was described by Equation 5-3.

$$q_{ceiling} = U_{ceiling}\left(T_{inside} - T_{tin}\right) \qquad \textbf{(5-3)}$$

$q_{ceiling}$	conduction through the ceiling and loft insulation	[W/m^2]
$U_{ceiling}$	thermal conductance of the ceiling and loft insulation	[W/m^{2}K]
T_{inside}	building internal temperature	[K]
T_{tin}	surface temperature at the top surface of the insulation	[K]

Conduction through ceiling and loft insulation

An interior temperature of 18°C was assumed, based on the bedroom temperature for central heating design [107]. The 99% confidence interval of this measurement was assumed to be ± 2°C (based on a thermal comfort range of 16 to 20°C) giving a standard uncertainty, for Section 9.4, of 0.8 as calculated by Equation 5-2 (k=2.58 for 99%).

5.2 Roof surface heat balance

The roof surface heat balance was used to calculate the net heat lost by the external surface of the roof to the surrounding environment. Heat exchange occurs at the roof surface by radiation and convection as shown in Figure 5-4 and described by Equation 5-4. The resulting heat balance is shown in Equation 5-5.

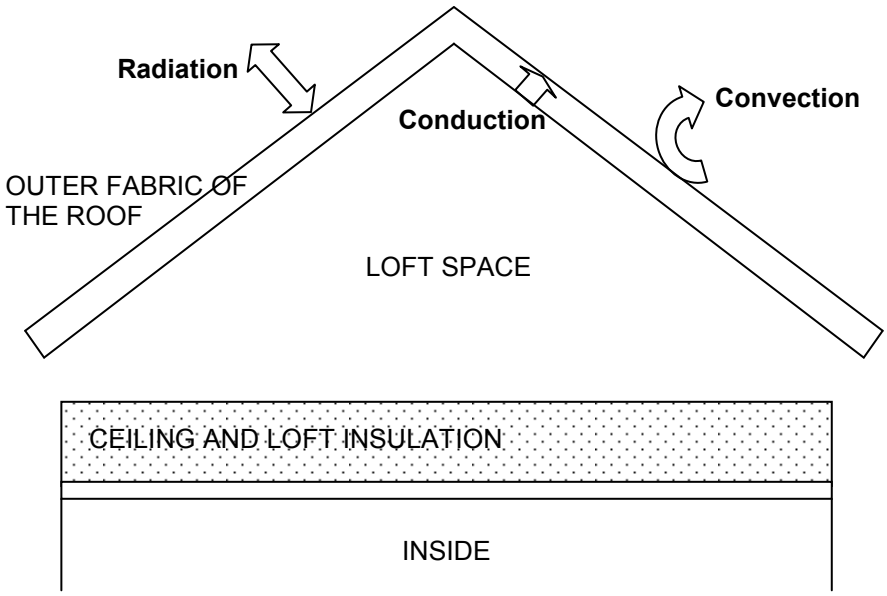

Figure 5-4: Radiative and convective heat exchange at the roof surface

$$q_{conduction} = q_{radiation} + q_{convection} \quad \textbf{(5-4)}$$

$q_{conduction}$ conductive heat loss through the outer fabric of the roof $[W/m^2]$

$q_{radiation}$ roof surface radiative heat exchange $[W/m^2]$

$q_{convection}$ roof surface convective heat exchange $[W/m^2]$

Heat loss at the roof surface

$$U_{roof}\left(T_{surface}-T_{uor}\right)=F\sigma\varepsilon\left(T_{surface}^{4}-T_{sky}^{4}\right)+h_{co}\left(T_{surface}-T_{air}\right) \quad \textbf{(5-5)}$$

U_{roof}	thermal conductance of the outer fabric of the roof	[W/m^{2}K]
$T_{surface}$	roof surface temperature	[K]
T_{uor}	surface temperature of the underside of the outer fabric of the roof	[K]
T_{sky}	broad band sky temperature	[K]
T_{air}	ambient air temperature	[K]
F	sky view factor	
σ	Steffan-Boltzmann constant	[W/m^{2}K^4]
ε	broad band emissivity of the roof surface	
h_{co}	convection coefficient of the roof surface	[W/m^{2}K]

Roof surface heat balance

The full derivations of the radiation and convection elements of the roof surface heat balance, including the radiation and convection heat transfer coefficients, are given in Section 6.2. The derivation of the sky view factor is given in Section 8.4, the emissivity in Section 8.3 and the broadband sky temperature in Section 7.4. The ambient air temperature was taken from the Nottingham weather station at Watnall (see Section 3.2). The roofs in this study were finished with single lap tiles and no felt [103] giving a thermal resistance of 0.12m^{2}K/W based on the value for a tile hung wall given in the CIBSE guide [107]. This excludes the surface resistances, which were included in the surface heat balances.

5.3 Loft space heat balance

The loft space heat balance was used to calculate the net heat transfer from the top of the insulation layer to the underside of the outer fabric of the roof. There are a number of heat paths within the loft space as shown in Figure 5-5. The inside surfaces of the loft space exchange heat with each other by radiation, the loft space air exchanges heat with each inside surface by convection and loft space air is being replaced by outside air through ventilation.

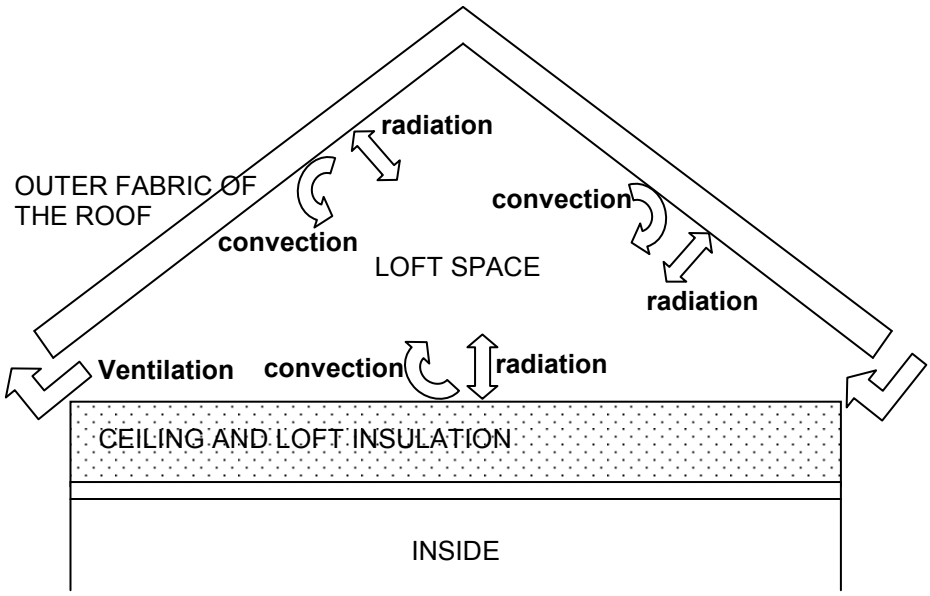

Figure 5-5: Radiation, convection and ventilation in the loft space

In an attempt to simplify the calculations, the loft space was initially considered to be part of a thermally homogenous roof having an overall effective U-value. These results were then compared with those from a more complex loft space heat balance that was developed for this study to determine if the simpler method was appropriate.

5.3.1 Thermally homogenous roof

If the roof is considered to be thermally homogenous with an effective U-value, the total heat lost at the roof surface can be described by Equation 5-6. Here the effective U-value includes the ceiling and loft insulation, the loft space and the outer fabric of the roof combined.

$$q_{roof} = U\left(T_{inside} - T_{surface}\right) \quad \textbf{(5-6)}$$

q_{roof}	total heat lost at roof surface (see Equation 5-4)	[W/m^2]
U	effective U-value of the roof	[W/m^2K]
T_{inside}	building internal temperature	[K]
$T_{surface}$	roof surface temperature	[K]

Total heat lost at the roof surface

Relationships between effective U-value and insulation thickness were determined, for this study, using both the elemental calculation methods given in British Standard BS EN ISO 6946:1997 [109] and the CIBSE guide [107].

British Standard BS EN ISO 6946:1997 [109] gave a thermal resistance value for the ventilated space and pitched roof construction combined of 0.06m^2K/W for a tiled roof with no boards. The effective U-value of the roof was therefore calculated by Equation 5-7.

$$U = \frac{1}{0.06 + 1/U_{ceiling}} \quad \textbf{(5-7)}$$

U	effective U-value of the roof	$[W/m^2K]$
$U_{ceiling}$	U-value of the ceiling and insulation	$[W/m^2K]$

Effective U-value of the roof calculated by BS EN ISO 6946:1997 [109]

The CIBSE guide [107] gave the thermal resistance of the loft space as 0.18m^2K/W for a pitched roof lined with felt or building paper (there was no value for an unlined roof). The U-value of the outer fabric of the roof must be measured in the plane of the ceiling and is corrected as shown in Equation 5-8. A value of 0.12m^2K/W was used for the thermal resistance of the outer fabric of the roof.

$$U = \frac{1}{R_{roof}\cos\theta + 0.18 + 1/U_{ceiling}} \quad \textbf{(5-8)}$$

U	effective U-value of the roof	$[W/m^2K]$
R_{roof}	resistance of the outer fabric of the roof = 0.12	$[m^2K/W]$
θ	roof pitch	[radians]
$U_{ceiling}$	U-value of the inner layer of the roof	$[W/m^2K]$

Effective U-value of the roof calculated by the CIBSE guide [107]

The heat loss at the roof surface (Equation 5-6) was expanded, as shown in Equation 5-9, using the radiation heat transfer coefficient shown in Equation 5-10. This was solved for roof surface temperature as shown in Equation 5-11. As the convective and radiative heat transfer coefficients at the outside surface (derived in Section 6.2) are functions of the roof surface temperature, a simple iterative scheme was used for this study. The results converged quickly to over 4 decimal places within 10 iterations, using an initial value of $T_{surface}$ = 273.15K.

$$h_{co}\left(T_{surface} - T_{air}\right) + h_{ro}\left(T_{surface} - T_{sky}\right) = U\left(T_{inside} - T_{surface}\right) \quad \textbf{(5-9)}$$

h_{co}	roof surface convection heat transfer coefficient	[W/m^{2}K]
h_{ro}	roof surface radiation heat transfer coefficient	[W/m^{2}K]
U	effective u-value of the roof	[W/m^{2}K]
$T_{surface}$	roof surface temperature	[K]
T_{air}	ambient air temperature	[K]
T_{sky}	broadband sky temperature	[K]
T_{inside}	building interior temperature	[K]

Expanded roof surface heat balance

$$h_{ro} = F\sigma\varepsilon\left(T_{surface}^2 + T_{sky}^2\right)\left(T_{surface} + T_{sky}\right) \quad \textbf{(5-10)}$$

h_{ro}	roof surface radiation heat transfer coefficient	[W/m^{2}K]
F	sky view factor of the roof	
σ	Steffan-Boltzmann constant	[W/m^{2}K^4]
ε	broad band emissivity of the roof material	
$T_{surface}$	roof surface temperature	[K]
T_{sky}	broadband sky temperature	[K]

Radiation heat transfer coefficient

$$T_{surface} = \frac{UT_{inside} + h_{co}T_{air} + h_r T_{sky}}{h_{co} + h_r + U} \quad \textbf{(5-11)}$$

h_{co}	roof surface convection heat transfer coefficient	[W/m^{2}K]
h_{ro}	roof surface radiation heat transfer coefficient	[W/m^{2}K]
U	effective u-value of the roof	[W/m^{2}K]
$T_{surface}$	roof surface temperature	[K]
T_{air}	ambient air temperature	[K]
T_{sky}	broadband sky temperature	[K]
T_{inside}	building interior temperature	[K]

Calculation of roof surface temperature

The roof surface temperature was generally lower than the ambient air temperature and the convective heat exchange was therefore a heat gain. This is probably the norm on calm, cold clear nights as the radiative heat exchange with the cold night sky dominates. The relationships between roof surface temperature and insulation thickness, calculated by both the British Standard and CIBSE methods, are shown in Figure 5-6 for a 1:1 pitched roof house typical to this study (see Section 9.2). The shape of the curves demonstrates the diminishing returns of increasing insulation thickness.

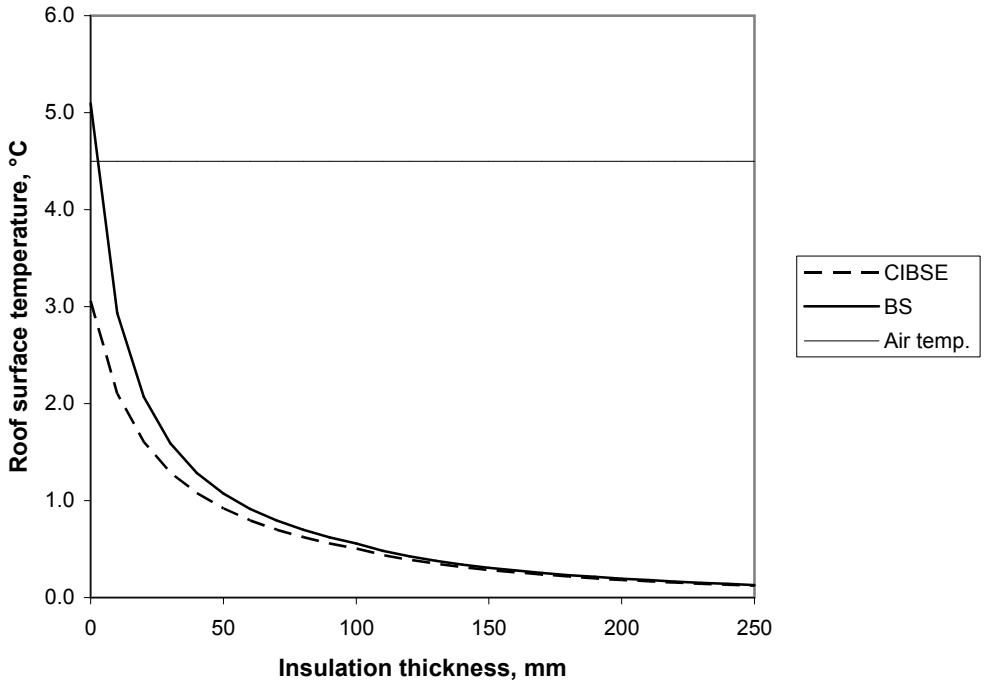

Figure 5-6: The relationships between roof surface temperature and insulation thickness calculated by British Standard and CIBSE methods

5.3.2 Loft space heat balance

For comparison with the simple methods described above, a loft space heat balance was developed for this study, based on the work of Parker [110], Pedersen et al. [111] and Burch [55] as detailed in Section 6.3. Additional heat from flues or hot water pipes passing through the loft space and infiltration through the ceiling were ignored and the air in the loft space was assumed to be well mixed and not stratified. An iterative solution was used, calculating the temperatures of the roof surfaces, the inside surfaces of the loft space and the air in the loft space at each iteration. The overall scheme is shown in Figure 5-7.

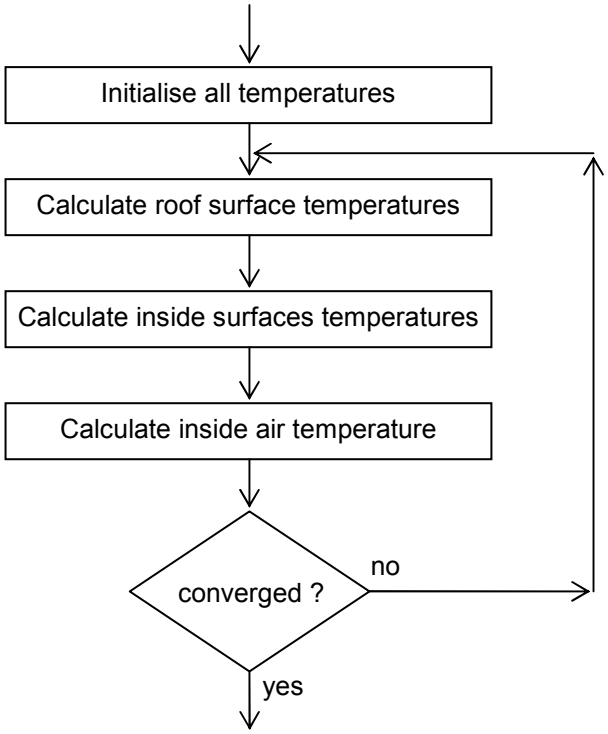

Figure 5-7: Iterative scheme for roof heat balance

The resulting seven equations in seven unknown temperatures were expressed as shown in Equation 5-12 for the outside surface heat balance, Equation 5-13 for the five inside surfaces heat balance (i = 1 to 5) and Equation 5-14 for the airspace heat balance.

$$T_{surface} = \frac{h_{ro} T_{sky} + h_{co} T_{air} + U_{roof} T_{uor}}{h_{ro} + h_{co} + U_{roof}} \qquad \textbf{(5-12)}$$

h_{ro}	roof surface radiation heat transfer coefficient	[W/m^{2}K]
h_{co}	roof surface convective heat transfer coefficient	[W/m^{2}K]
U_{roof}	thermal conductance of the outer leaf of the roof	[W/m^{2}K]
$T_{surface}$	roof surface temperature	[K]
T_{sky}	broad band sky temperature	[K]
T_{air}	ambient air temperature	[K]
T_{uor}	temperature of the underside of the outer fabric of the roof	[K]

Outside surface heat balance

$$T_i = \frac{h_{radi} T_{MRT} + h_{ci} T_{as} + U_i T_{oi}}{h_{radi} + h_{ci} + U_i} \quad \textbf{(5-13)}$$

U_i	thermal conductance of surface i	[W/m^{2}K]
h_{radi}	radiation heat transfer coefficient of surface i	[W/m^{2}K]
h_{ci}	convection heat transfer coefficient of surface i	[W/m^{2}K]
T_{as}	temperature of the loft space air	[K]
T_i	inside surface temperature of surface i	[K]
T_{MRT}	mean radiant temperature	[K]
T_{oi}	outside surface temperature for surface i	[K]

Inside surfaces heat balance

$$T_{as} = \frac{\sum (A_i h_{ci} T_i) + \rho n V c_p T_{air}}{\sum (A_i h_{ci}) + \rho n V c_p} \quad \textbf{(5-14)}$$

A_i	area of surface i	[m^2]
h_{ci}	convection heat transfer coefficient of surface i	[W/m^{2}K]
T_{as}	temperature of the loft space air	[K]
T_i	inside surface temperature of surface i	[K]
ρ	density of air in the loft space ≈ 1.29	[kg/m^3]
n	number of loft space air changes per second	[s^{-1}]
V	volume of the loft space	[m^3]
c_p	specific heat capacity of the air in the loft space ≈ 1000	[J/kgK]

Loft space air heat balance

Surface temperatures were initialised at 0°C and the air in the loft space at 0.75°C. The solution converged to better than 2 decimal places within 100 iterations.

Two styles of roof, with different surface configurations, were modelled for this study (mid-terrace and end-terrace) as illustrated in Figure 5-8.

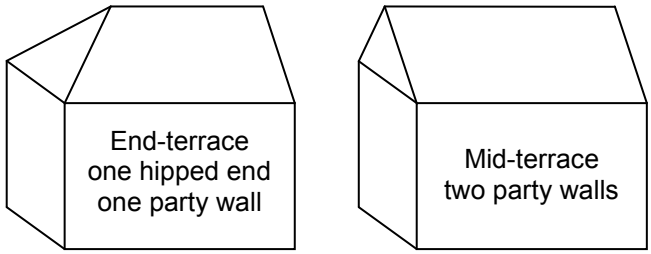

Figure 5-8: End-terrace and mid-terrace roof styles

The loft space of the mid-terrace consisted of the surfaces at the top of the insulation layer, the two insides of the roof and the two party walls. It was assumed that there was no conduction through the party walls and that the two roof surfaces had the same sky view factor and therefore temperature. The loft space of the end-terrace consisted of the surfaces at the top of the insulation layer, the two insides of the roof, the inside of the roof at the hipped end and the party wall. It was again assumed that there was no conduction through the party wall. The three outside faces of the roof were assumed to have the same sky view factor (see Section 8.4) but as the hipped end had a smaller area, the surface temperature was different to the other two faces. The resulting overall roof surface temperature was calculated from an area weighted average as shown in Equation 5-15.

$$T_{surface} = \frac{\sum_{i=1}^{3} T_i A_i}{\sum_{i=1}^{3} A_i} \qquad \textbf{(5-15)}$$

$T_{surface}$	average roof surface temperature	[K]
T_i	surface temperature of the ith roof face	[K]
A_i	surface area of the ith roof face	[m^2]

Area weighted average for roof surface temperature

The ventilation rate of the loft space was not known for the houses in this study and so results were calculated for air change rates of between zero and ten per hour as shown in Figure 5-9 for end-terrace, and Figure 5-10 for a mid-terrace, houses with a 1:1 pitched roof typical to this study (see Section 9.2).

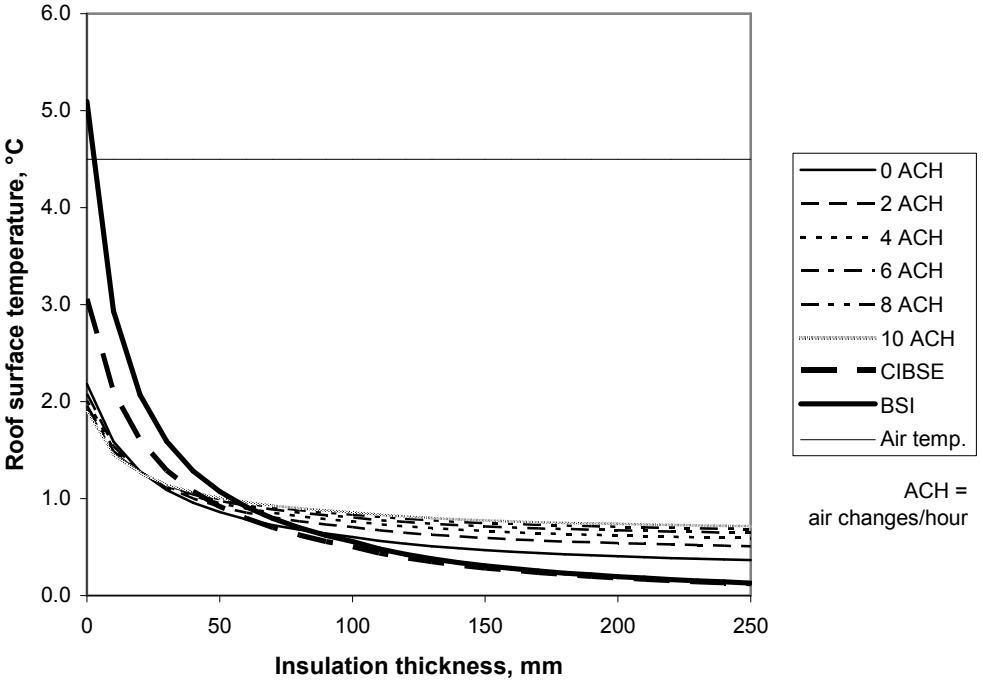

Figure 5-9: Calculated roof surface temperature for 1:1 pitch, end-terrace

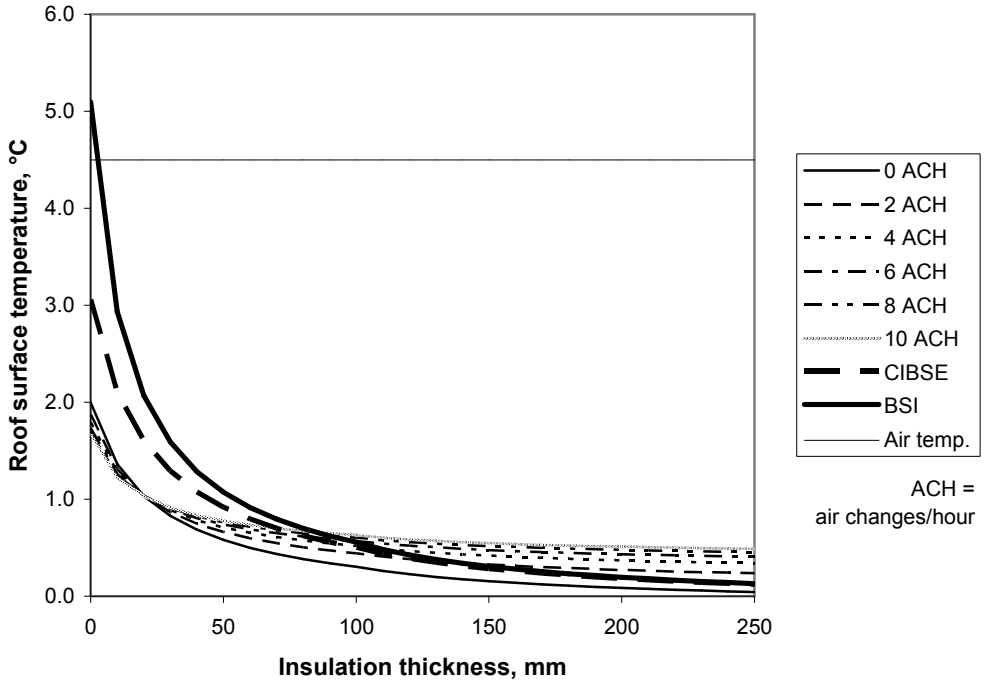

Figure 5-10: Calculated roof surface temperature for 1:1 pitch, mid-terrace

From these graphs it can be seen that increasing ventilation, for houses with more than about 25mm of loft insulation, warms the roofs and end-terraces have warmer roofs than mid-terraces. While the results of the BS and CIBSE methods were similar to those from the loft space heat balance for a mid-terraced house with 200-250mm of insulation and about 1 loft space air change per hour, the agreement between results diminished outside of these parameters. Without further validation of these results it is impossible to determine which of the models is the most accurate. The BS and CIBSE methods ignored the effects of ventilation and were insensitive to the shape of the roof (mid-terrace compared with end-terrace). The loft space heat balance was therefore chosen for this study.

A loft ventilation rate of 2 per hour was chosen based on the assumptions of Burch [55]. For the uncertainty analysis (see Section 9.4), the 99% confidence interval of this measurement was estimated to be ± 2 per hour giving a standard uncertainty of 0.8 as calculated by Equation 5-2.

From the completed model, temperatures and the values of radiative, convective and ventilation heat loss for each surface and for the airspace were calculated for a mid-terrace house with a 1:1 pitched roofs and 150mm of insulation, typical to this study (see Section 9.2). The results are shown in Table 5-2 where negative heat losses describe heat gains.

Table 5-2: Temperature and heat loss for surfaces and air space

Surface	Temperature °C	Heat loss, W			
		Ventilation	Radiation	Convection	Net
Roof outsides	0.32	n/a	1892.17	-1624.74	267.43
Undersides of roof	0.91	n/a	-159.85	-107.58	-267.43
Party walls	1.78	n/a	8.43	-8.43	0
Top of insulation	2.43	n/a	151.42	10.96	162.38
Loft space air	2.15	-105.06	n/a	105.06	0

From the table it can be seen that the loft space air was colder than the ambient air temperature (4.5°C) and so ventilation produced a heat gain into the air space. Heat transfer from the top of the insulation to the underside of the roof was predominantly by radiation. The

temperature difference between the surface and the underside of the roof was small compared with the temperature difference between the underside of the roof and the top of the insulation. The total heat lost by the outside surface of the roof was equal to the sum of the net heat lost at the top surface of the loft insulation and the heat gained by the loft air space by ventilation. The net heat lost by the top of the insulation was equal to the heat gained through the ceiling and insulation layer by conduction.

The roof surface temperatures of end-terrace and mid-terrace houses with 1:1 pitched roofs and varying insulation levels, typical to this study (see Section 9.2) was then calculated. The roof surface temperature of each inadequately insulated house was compared to that for a house with the recommended 250mm of loft insulation as shown Table 5-3.

Table 5-3: Roof surface temperatures for houses with different insulation levels and the difference compared with one that has the recommended 250mm of insulation

Insulation level	End-terrace		Mid-terrace	
	°C	Difference	°C	Difference
0mm	2.08	+1.57	1.87	+1.64
50mm	0.92	+0.41	0.66	+0.43
100mm	0.71	+0.20	0.44	+0.20
150mm	0.59	+0.08	0.33	+0.09
200mm	0.54	+0.03	0.27	+0.03
250mm	0.51	-	0.24	-

These temperature differences are relatively small. It can be seen that the roof of a poorly insulated house with 50mm of insulation is only about 0.4°C warmer than the well insulated one. A house with 150mm of insulation would be considered in need of upgrading but the roof surface temperature is less than 0.1°C warmer than the well insulated example. These temperatures would be difficult to discriminate using instrumentation on the ground (a basic thermocouple will measure to an accuracy of ± 0.5°C).

The difference between end and mid-terraces with the same insulation level is about 0.25°C and so the type of roof had a significant effect on the roof surface temperature as may many of the other parameters. This will be considered in the accuracy assessment in Chapter 9.

Both the accuracy of the temperature measurement by aerial thermography and the accuracy of the building model itself will determine if these temperature differences are detectable and if insulation thickness can be quantified.

5.4 Conclusions

The building model, introduced in Chapter 3, was developed for this study to calculate the roof surface temperature of houses from their loft insulation level. The U-value of the ceiling and insulation layer was calculated, based on a mineral wool quilt over plasterboard and joists, so that the heat lost from the inside of the house and into the loft space could be quantified. The roof surface heat balance considered the heat conducted through the outer fabric of the roof and the net heat loss by radiation and convection. Convection was found to be a heat gain as roof surfaces dropped below ambient air temperature on cold, clear, calm nights and radiative losses to the cold night sky dominated. The loft space heat balance developed for this study included radiative and convective heat exchange at the inside surfaces, and ventilation of the air. Ventilation was found to be a heat gain, under the conditions at the time of the Nottingham survey, for all but the most poorly insulated houses modelled. Radiative heat exchange dominated the heat transfer in the loft space.

Calculations for end-terrace and mid-terrace properties with 1:1 pitched roofs, typical to this study (see Section 9.2) showed that the temperature difference between well insulated and poorly insulated roofs was very small, suggesting that accuracies better than 0.1°C may be needed to discriminate insulation levels. The uncertainty in the insulation level, the interior temperature of the building and the loft space ventilation rate were estimated for the uncertainty analysis in Section 9.3.

The methods for the roof surface and loft space heat balances used in this study were selected from a number of different models detailed in the literature. The next chapter describes these models and how they were compared to determine the most accurate.

6 Examining heat balance methods

The methods for representing the roof surface and loft space heat balances were developed from a review of the relevant literature. In this chapter, these heat balance methods are compared and the most suitable chosen for the building model that was developed in Chapter 5. Detailed calculations for the radiation and convection heat transfer coefficients, at each surface, are included.

Many different models, applicable to the roof surface heat balance and the loft space heat balance, were described in the literature and these are summarised below.

In other aerial heat loss studies, Goldstein [51], the Canada Centre for Remote Sensing [53, 54] and the National Bureau of Standards [55] considered heat transfer, of a roof with its surroundings, by radiation, convection and ventilation. Calspan/Rochester Institute of Technology [64, 95] ignored ventilation, and Ohio/Delaware [68], Atomic Energy Research Establishment [70] and University of Dundee [71] only considered flat roofs with no ventilated air cavity.

In addition to these works, a large number of building energy-performance simulation programs have been developed over the years (Crawley et al. [112] contrasts twenty of the most recent). The algorithms used for the calculations were not always transparent or freely available. Of notable exception were the University of Strathclyde's ESP-r [113] along with Clarke [114] which details the theory and structure, and the US Department of Energy's EnergyPlus [115], both of which are free to download and use and have detailed documentation.

Furthermore, cooling load calculation procedures have been developed for HVAC system designers and published by CIBSE [107] in the UK and ASHRAE [111, 116] in North America as compared by Spitler and Rees [117, 118]. The CIBSE admittance method [107] and the ASHRAE radiant time series method [116] are not as detailed as the ASHRAE heat balance

method [111] and it was reported that they did not perform as well in comparative studies due to their simplifications [118]. The ASHRAE heat balance method is similar to methods used in EnergyPlus and the models used are well documented [119, 120]. While the method was developed for pseudo non-steady state calculations, the instantaneous heat balances at surfaces are valid for the steady state case.

6.1 Roof surface heat balance

As seen in Section 5.3, the roof surface exchanges heat with the environment by radiation and convection. These are considered separately, below.

6.1.1 Radiative heat exchange

In common with all other studies, the net radiative heat exchange between each roof and its surroundings was described by the Steffan-Boltzmann law as shown in Equation 6-1.

$$q_{radiation} = \sigma\varepsilon T_{surface}^4 - F\sigma\varepsilon T_{sky}^4 - (1-F)\sigma\varepsilon T_{bg}^4 \quad \textbf{(6-1)}$$

$q_{radiation}$	net radiative heat exchange, roof to surroundings	$[W/m^2]$
σ	Steffan-Boltzmann constant	$[W/m^2K^4]$
$T_{surface}$	roof surface temperature	[K]
ε	broadband emissivity	
F	sky view factor	
T_{sky}	broadband sky temperature	[K]
T_{bg}	background temperature	[K]

Steffan-Boltzmann law for radiative heat exchange

Derivation of emissivity and sky view factor are given in Sections 8.3 and 8.4, and the broadband sky temperature in Section 7.4.

A simple background temperature was not easy to ascertain as the non-sky background could include the ground (possibly grass, asphalt or concrete), the walls of other buildings, the roofs of other buildings and vegetation such as trees. Goldstein [51] suggested a special case were

the background temperature was the same as the roof surface temperature, simplifying the radiative heat exchange as shown in Equation 6-2.

$$q_{radiation} = F\sigma\varepsilon\left(T_{surface}^4 - T_{sky}^4\right) + (1-F)\sigma\varepsilon\left(T_{surface}^4 - T_{bg}^4\right)$$
$$q_{radiation} = F\sigma\varepsilon\left(T_{surface}^4 - T_{sky}^4\right) \quad \textbf{(6-2)}$$

$q_{radiation}$	net radiative heat exchange, roof to surroundings	[W/m^2]
σ	Steffan-Boltzmann constant	[W/m^{2}K^4]
$T_{surface}$	roof surface temperature	[K]
ε	broadband emissivity	
F	sky view factor	
T_{sky}	broad band sky temperature	[K]
T_{bg}	background temperature	[K]

Simplification of radiant heat exchange when $T_{background}$=$T_{surface}$ after Goldstein [51]

For the Canada Centre for Remote Sensing, the model of Brown et al. [54] assumed that the background temperature was the same as the ambient air temperature, even though wind speed was low and the sky temperature very cold (215K). For the Atomic Energy Research Establishment, Haigh and Pritchard [70] only considered flat roofs and, along with Burch [55] for the National Bureau of Standards, did not include heat exchange with non-sky surroundings. Anderson and Wilson for University of Dundee [71] simply estimated the temperature of the background in their study. For Calspan/Rochester Institute of Technology, Schott and Wilkinson [64] measured the background temperature from the thermal image, though this would not have included the contribution of the walls of surrounding buildings as they are not seen on the thermal image.

For ESP-r, Clarke [114] suggested that the temperature of the surface being analysed was used for the background temperature as a general rule for building modelling. EnergyPlus [115] and ASHRAE [119] used the ground temperature as the background temperature and assumed it was the same as the ambient air temperature, however, the problems with this technique are spelt out by McClellan and Pedersen [119] who suggested that it should be estimated on a case by case basis. Cole [121] also highlighted problems with assuming the

surroundings were at ambient air temperature but provided no alternative. These methods are more generally applicable to building walls and not the roof specifically.

In the absence of a better solution the background temperature was assumed to be the same as the roof surface temperature, using Equation 6-2 after Goldstein [51]. The sensitivity of the calculated roof surface temperature to the value of the background temperature is explored in the sensitivity analysis in Section 9.3.

The radiative losses, calculated from Equation 6-2 for houses typical to this study (see Section 9.2) are given in Table 6-1. The roof surface temperature was assumed the same for each house and was set to 0.35°C for demonstration purposes.

Table 6-1: Radiative heat losses calculated from Equation 6-2

Radiation heat loss W/m^2 for roof pitch		
1:1	**1:2**	**1:3**
39.74	44.07	45.05

It can be seen from Table 6-1 that radiative heat loss increases with roof pitch as the sky view factor increases and more heat is lost to the relatively cold sky.

6.1.2 Convective heat exchange

Convective heat exchange at the roof surface occurs as the boundary layer of air exchanges heat with that surface by conduction before natural buoyancy effects (natural convection) and bulk air movement (forced convection) displace the air in a continuous process. It is commonly calculated using a convection coefficient, h_c as shown in Equation 6-3.

$$q_{convection} = h_c (T_{surface} - T_{air}) \quad \textbf{(6-3)}$$

$q_{convection}$	convective heat exchange, roof to surroundings	[W/m^2]
h_c	convection coefficient	[W/m^{2}K]
$T_{surface}$	roof surface temperature	[K]
T_{air}	ambient air temperature	[K]

Calculation of convective heat exchange using a convection coefficient

Goldstein [51] formulated a natural convection coefficient, for low wind speed scenarios, for a flat roof that is warmer than the ambient air temperature as given in Equation 6-4. A factor of 24% of this value was stated for a flat roof that was colder than the air and, for a sloping roof, a factor of 96% when the roof was warmer than the air or 56% when the roof was colder than the air.

$$h_n = 2(\Delta T)^{1/3} \quad \textbf{(6-4)}$$

h_n	natural convection coefficient	[W/m^{2}K]
ΔT	temperature difference between surface and ambient air	[K]

Natural convection coefficient after Goldstein [51]

For higher wind speeds, Goldstein predicted a forced convection coefficient based on turbulent forced convection over a smooth flat surface, as shown im Equation 6-5. He noted that the rough surfaces of roofs could increase the convection coefficient by as much as a factor of two and that the natural and forced convection coefficients should be added at low wind speeds.

$$h_f \cong 6.25 v^{4/5} L^{-1/5} \quad \textbf{(6-5)}$$

h_f	forced convection coefficient	[W/m^{2}K]
v	wind speed	[m/s]
L	surface length	[m]

Turbulent forced convection coefficient after Goldstein [51]

For the Atomic Energy Research Establishment, Haigh and Pritchard [70] identified the convective heat transfer model as one of the primary sources of inaccuracy in their roof heat loss survey. They found that, at low wind speeds, Langmuir's equation (Equation 6-6) gave results closer to those from the equations for forced convection in turbulent flow (Equation 6-8) than the IHVE guide equation (Equation 6-7) and no characteristic length for the roof was needed. A factor of 20% was stated for roofs colder than the ambient air temperature.

$$q_{convection} = 1.9468\left(T_{surface} - T_{air}\right)^{1.25}\left(\frac{v + 0.35}{0.35}\right)^{0.5} \quad \textbf{(6-6)}$$

$q_{convection}$	convective heat exchange, roof to surroundings	[W/m^2]
v	wind speed	[m/s]
$T_{surface}$	roof surface temperature	[K]
T_{air}	ambient air temperature	[K]

Langmuir's equation for convective heat exchange (see [70])

$$q_{convection} = \left(5.8 + 4.1v\right)\left(T_{surface} - T_{air}\right) \quad \textbf{(6-7)}$$

$q_{convection}$	convective heat exchange, roof to surroundings	[W/m^2]
v	wind speed	[m/s]
$T_{surface}$	roof surface temperature	[K]
T_{air}	ambient air temperature	[K]

IHVE guide equation for convective heat exchange (see [70])

$$q_{convection} = \left(T_{surface} - T_{air}\right)\frac{6.04}{l}\left(vl\right)^{0.8} \quad \textbf{(6-8)}$$

$q_{convection}$	convective heat exchange, roof to surroundings	[W/m^2]
v	wind speed	[m/s]
$T_{surface}$	roof surface temperature	[K]
T_{air}	ambient air temperature	[K]
l	surface length	[m]

Forced convection in turbulent flow equations for convective heat exchange (see[70])

For the National Bureau of Standards, Burch [55] used an equation, similar to the IHVE guide, based on data for a concrete surface as shown in Equation 6-9.

$$q_{convection} = \left(2.8 + 4.8v\right)\left(T_{surface} - T_{air}\right) \quad \textbf{(6-9)}$$

$q_{convection}$	convective heat exchange, roof to surroundings	[W/m^2]
v	wind speed	[m/s]
$T_{surface}$	roof surface temperature	[K]
T_{air}	ambient air temperature	[K]

Equation for convective heat exchange used by Burch [55]

For the work of CALSPAN/Rochester Institute of Technology, Snyder and Schott [95] used an adaptation of Langmuir's equation, the details of which are not given. The error in the convection coefficient was found to be a significant contributor to the overall error and the

authors 'tuned' the convection coefficient, along with the sky temperature, to match predictions, by setting it to 4.5 W/m^{2}K.

For ESP-r, Clarke [114] gave the convection coefficient at external surfaces as Equation 6-10, based on early copper plate flow experiments made at wind speeds below 4.88m/s. The case where roof surface temperature is lower than air temperature was not dealt with.

$$h_c = 5.678\left[1.09 + 0.23\left(\frac{294.26v}{0.3048T_{air}}\right)\right] \quad \textbf{(6-10)}$$

h_c	convection coefficient	[W/m^{2}K]
v	wind speed	[m/s]
T_{air}	ambient air temperature	[K]

Forced convection coefficient described by Clarke [114]

EnergyPlus [115] offers a choice of six algorithms, many the same as those described by McClellan and Pederesen [119] for ASHRAE. The 'detailed algorithm' was deemed the most applicable to this study as it explicitly accounted for the pitch of the roof and surfaces that were colder than the ambient air temperature.

The total convection coefficient was determined from separate forced and natural coefficients as shown in Equation 6-11.

$$h_c = h_f + h_n \quad \textbf{(6-11)}$$

h_c	convection coefficient	[W/m^{2}K]
h_f	forced convection coefficient	[W/m^{2}K]
h_n	natural convection coefficient	[W/m^{2}K]

Overall convection coefficient as described by ASHRAE [119]

The forced convection coefficient was calculated from surface geometry, surface roughness and wind speed as shown in Equation 6-12.

$$h_f = 2.537 \cdot W_f R_f \sqrt{\frac{P v_z}{A}} \quad \textbf{(6-12)}$$

h_f	forced convection coefficient	[W/m^{2}K]
W_f	surface orientation =1 for windward surfaces	
R_f	roughness index =1.67 for rough	
P	perimeter measurement of the roof	[m]
v_z	local wind speed	[m/s]
A	surface area of the roof	[m^2]

Forced convection coefficient after ASHRAE [119]

Local wind speed was reduced for the urban environment as per the ASHRAE handbook [50] and shown in Equation 6-13.

$$v_z = v_{met}\left(\frac{\delta_{met}}{z_{met}}\right)^{a_{met}}\left(\frac{z}{\delta}\right)^{a} \quad \textbf{(6-13)}$$

v_z	wind speed at the roof	[m/s]
z	height of the roof surface centroid	[m]
δ	layer thickness = 460 for cities	[m]
a	exponent = 0.33 for cities	
v_{met}	measured wind speed	[m/s]
z_{met}	height of the measurement mast = 10	[m]
δ_{met}	layer thickness = 270 for flat open country	[m]
a_{met}	exponent = 0.14 for flat open country	

Local wind speed calculation after ASHRAE [119]

The natural convection coefficient was described by Equation 6-14, for upward heat flow (roof is warmer than the ambient air temperature), and Equation 6-15, for downward heat flow (roof is colder than the ambient air temperature).

$$h_n = 9.482 \cdot \frac{\sqrt[3]{\left|T_{surface} - T_{air}\right|}}{7.238 - \left|\cos(\phi)\right|} \quad \textbf{(6-14)}$$

h_n	natural convection coefficient	[W/m^{2}K]
$T_{surface}$	roof surface temperature	[K]
T_{air}	ambient air temperature	[K]
ϕ	angle between roof normal and ground normal	[radians]

Natural convection, upward heat flow, after ASHRAE [119]

$$h_n = 1.810 \cdot \frac{\sqrt[3]{|T_{surface} - T_{air}|}}{1.382 + |\cos(\phi)|} \quad \textbf{(6-15)}$$

h_n	natural convection coefficient	[W/m^{2}K]
$T_{surface}$	roof surface temperature	[K]
T_{air}	ambient air temperature	[K]
ϕ	angle between roof normal and ground normal	[radians]

Natural convection, downward heat flow, after ASHRAE [119]

Other work has dealt with convection and wind flow around buildings. Cole and Sturrock [122] review the early attempts, including the IHVE guide, concluding that there is much work to be done in the field. Sharples [123] and Loveday and Taki [124] carried out full scale experimental analysis of the convection coefficient on the façade of buildings but neglected the roof. Clear et al. [125] devised an empirical convective heat transfer coefficient based on measurements on the flat roofs of two commercial buildings in Northern Carolina, USA but ignored all data when roof surface temperature dropped below ambient air temperature.

The EnergyPlus/ASHRAE detailed method [119] was chosen for this case study as it was the most recent and dealt explicitly with both sloping faces and surface temperatures below ambient air temperature. The calculation of local wind speed in Equation 6-13 was not used as the ASHRAE handbook of fundamentals [50] stated that it was only for wind speeds greater than 9mph (4m/s) as it was based on surface roughness. The average wind speed during the Nottingham survey was only 2.4m/s (see Section 3.3.2). During these calmer periods, the local wind speed will depend more on the terrain. Wind will be channelled along valleys, increasing its speed at the crests of a hills and dropping off in their lee. Cooler air will run down valley sides and settle in valley bottoms, while buoyant warm air will rise over the city pulling cooler air along the ground from all directions.

A 99% confidence interval of ± 50% (1.2 to 3.6m/s) in the wind speed, as indicated by the ASHRAE handbook of fundamentals [50], was used for the uncertainty analysis of the building model in Section 9.4. This gave a standard uncertainty of 0.5m/s after the method set out by BSI [102] (see Equation 5-2, k=2.58 for 99%).

The convective heat losses, calculated by a number of methods, for houses typical to this study (see Section 9.2) are given in Table 6-2. Ambient air temperature was 4.5°C and wind speed 2.4m/s. The roof surface temperature was assumed the same for each house and was set to 0.35°C for demonstration purposes. Considerable differences between the values calculated by these methods are evident.

Table 6-2: Comparison of convection heat loss by different methods.

Method	Convection heat loss W/m^2 for roof pitch		
	1:1	1:2	1:3
Goldstein* [51]	-78.36	-75.10	-74.31
Langmuir [70]	-32.32	-32.32	-32.32
IHVE Guide [70]	-64.91	-64.91	-64.91
Forced convection [70]	-37.22	-39.01	-39.47
Burch [55]	-59.43	-59.43	-59.43
ESP-r [114]	-70.91	-70.91	-70.91
ASHRAE detailed* [119]	-29.74	-30.99	-31.35
* Calculation compensated for downward heat flow (roof surface, colder than air)			

Under low wind, clear sky conditions, cities like Nottingham are prone to developing an urban heat island, with an associated rise in boundary layer temperatures [126]. As the observations of ambient air temperature were taken at the Meteorological station at Watnall, located outside of the city, approximately 10km to the north west of the centre, elevated temperatures across the city may be expected. In addition, the topography of the city may promote the sinking of cold air into valley bottoms, displacing warmer air upwards. As a conservative estimate, a 99% confidence interval of ±1°C in the ambient air temperature was used for the uncertainty analysis of the building model in Section 9.4. This gave a standard uncertainty of 0.4°C after the method set out by BSI [102] (see Equation 5-2, k=2.58 for 99%) .

6.2 Loft space heat balance

In other studies, a number of different techniques have been employed for the loft space heat balance. These are reviewed below and the method developed for this study is detailed.

6.2.1 Review of loft space heat balance methods

Goldstein [51] considered a loft space with a fixed number of air changes and a simple heat balance to equate the heat flow through the ceiling to the combined heat flow through the roof and by ventilation as shown Equation 6-16. Calculations of the roof surface temperature, for air change rates from 0 to 10 per hour, demonstrated that ventilation of the loft space decoupled the roof surface temperature from the loft insulation level.

$$U_{ceiling}\left(T_{inside} - T_{as}\right) = U_{roof}\left(T_{as} - T_{surface}\right) + c_p H n \rho \left(T_{as} - T_{air}\right) \quad \textbf{(6-16)}$$

$U_{ceiling}$	thermal conductance of the ceiling	[W/m^2K]
U_{roof}	thermal conductance of the roof (omitting outside surface resistance)	[W/m^2K]
T_{inside}	building internal temperature	[K]
T_{as}	temperature of air in the loft space (average temperature)	[K]
T_{air}	ambient air temperature	[K]
$T_{surface}$	roof surface temperature	[K]
c_p	specific heat capacity of air in the loft space	[J/kgK]
V	volume of the loft space	[m^3]
H	height of the loft space	[m]
n	number of loft space air changes per second	[s^{-1}]
ρ	density of air in the loft space	[kg/m^3]

Loft space heat balance after Goldstein [51]

The work of the Canada Centre for Remote Sensing [54] used a similar method to Goldstein but included temperature stratification of the air in the loft space as shown in Equation 6-17. The temperature difference between the underside of the roof and the top of the insulation was found to be approximately 0.5°C from measurements made in real buildings [53]. While air changes of only 0.75 per hour were calculated to be adequate to prevent condensation in the very cold (-23°C) Canadian winter, measurements on a test house found ventilation rates between 5 and 10 per hour, increasing with wind speeds above 2.8m/s to over 25 per hour [54]. Brown concluded that airspace ventilation was a “major contributing factor” in determining roof surface temperature but that the local microclimate and variations in roof air vents made it “impossible” to model [54].

$$U_{ceiling}\left(T_{inside} - T_{as1}\right) = U_{roof}\left(T_{as2} - T_{surface}\right) + c_p Vn\left(T_{as} - T_{air}\right) \quad \textbf{(6-18)}$$

$U_{ceiling}$	thermal conductance of the ceiling	[W/m^2K]
U_{roof}	thermal conductance of the roof (omitting outside surface resistance)	[W/m^2K]
T_{inside}	building internal temperature	[K]
T_{as1}	temperature of air in the loft space, just above the ceiling	[K]
T_{as2}	temperature of air in the loft space, just below the roof	[K]
T_{as}	temperature of air in the loft space (average temperature)	[K]
T_{air}	ambient air temperature	[K]
$T_{surface}$	roof surface temperature	[K]
c_p	specific heat capacity of air in the loft space	[J/kgK]
V	volume of the loft space	[m^3]
n	number of loft space air changes per second	[s^{-1}]

Loft space heat balance after Brown [54]

For the National Bureau of Standards, Burch [55] developed a more complex model, using a loft space air heat balance along with an interior surface heat balance, and included infiltration through the ceiling and heat loss through the soffit region and roof space end walls. The loft space heat balance equated the heat gains of attic floor convection and air infiltration through the ceiling, with conduction through the soffit and end walls, convection to the roof and ventilation as shown in Equation 6-18. The U-value of the soffit and end walls included air film (surface) resistance. The surface heat balance at the floor of the airspace is given in Equation 6-19, at the underside of the roof in Equation 6-20 and at the roof surface in Equation 6-21.

The four equations were solved iteratively for the surface temperatures at the top of the insulation, the underside of the roof, the roof surface and the airspace. The air change rate was assumed to be two per hour and infiltration through the ceiling $1.3x10^{-4}m^3/sm^2$. The radiation coefficients were expressed in the form shown in Equation 6-22. A convection coefficient was calculated for the underside of the roof and the floor of the airspace as shown in Equation 6-23.

For the roof construction investigated it was found that increasing ventilation from 2 to 4 changes per hour had little effect on roof surface temperature as radiation exchange between the loft space floor and the underside of the roof was the dominant factor. This contradicted

the findings of Brown, above. The sensitivity of the building model, developed for this study, to variations in ventilation rate was examined in the sensitivity analysis in Section 9.3.

$$A_{ceiling} h_{ctin} (T_{tin} - T_{as}) + V_{inf} A_{ceiling} c_p \rho (T_{inside} - T_{as}) = A_{roof} h_{cusr} (T_{as} - T_{usr}) + A_{soffit} U_{soffit} (T_{as} - T_{air}) + A_{wall} U_{wall} (T_{as} - T_{air}) + \rho c_p V n (T_{as} - T_{air}) \quad \textbf{(6-18)}$$

$A_{ceiling}$	area of the ceiling	[m^2]
A_{roof}	area of the roof	[m^2]
A_{soffit}	area of the soffit	[m^2]
A_{wall}	area of the end wall	[m^2]
T_{as}	loft space air temperature	[K]
T_{tin}	surface temperature at the top surface of the insulation	[K]
T_{usr}	surface temperature of the underside of the outer fabric of the roof	[K]
T_{inside}	building internal temperature	[K]
T_{air}	ambient air temperature	[K]
h_{ctin}	convection coefficient of the top surface of the insulation	[W/m^2K]
h_{cusr}	convection coefficient of the underside of the outer fabric of the roof	[W/m^2K]
U_{soffit}	thermal conductance of the soffit	[W/m^2K]
U_{wall}	thermal conductance of the end wall	[W/m^2K]
V_{inf}	rate of air infiltration through the ceiling per unit ceiling area	[m^3/m^2s]
c_p	specific heat capacity of air in the loft space	[J/kgK]
ρ	density of air in the loft space	[kg/m^3]
V	volume of the loft space	[m^3]
n	number of loft space air changes per second	[s^{-1}]

Loft space heat balance after Burch [55]

$$(T_{inside} - T_{tin}) U_{ceiling} = h_{ctin} (T_{tin} - T_{as}) + h_{rusr} (T_{tin} - T_{usr}) \quad \textbf{(6-19)}$$

T_{inside}	building internal temperature	[K]
T_{tin}	surface temperature at the top surface of the insulation	[K]
T_{as}	loft space air temperature	[K]
T_{usr}	surface temperature of the underside of the outer fabric of the roof	[K]
$U_{ceiling}$	thermal conductance of the ceiling omitting upper surface resistance	[W/m^2K]
h_{ctin}	convection coefficient of the top surface of the insulation	[W/m^2K]
h_{rusr}	radiation coefficient of the underside of the outer fabric of the roof	[W/m^2K]

Surface heat balance at the floor of the airspace after Burch [55]

$$(T_{usr} - T_{surface})U_{roof} = h_{cusr}(T_{as} - T_{usr}) + h_{rusr}(T_{tin} - T_{usr}) \quad \textbf{(6-20)}$$

T_{usr}	surface temperature of the underside of the outer fabric of the roof	[K]
$T_{surface}$	roof surface temperature	[K]
T_{as}	loft space air temperature	[K]
T_{usr}	surface temperature of the underside of the outer fabric of the roof	[K]
T_{tin}	surface temperature at the top surface of the insulation	[K]
U_{roof}	thermal conductance of the roof omitting surface resistances	[W/m^{2}K]
h_{cusr}	convection coefficient of the underside of the outer fabric of the roof	[W/m^{2}K]
h_{rusr}	radiation coefficient of the underside of the outer fabric of the roof	[W/m^{2}K]

Surface heat balance at the underside of the roof after Burch [55]

$$(T_{usr} - T_{surface})U_{roof} = h_c(T_{surface} - T_{sky}) + h_r(T_{surface} - T_{sky}) \quad \textbf{(6-21)}$$

T_{usr}	surface temperature of the underside of the outer fabric of the roof	[K]
$T_{surface}$	roof surface temperature	[K]
T_{sky}	broad band sky temperature	[K]
U_{roof}	thermal conductance of the roof omitting surface resistances	[W/m^{2}K]
h_{co}	outside surface convection coefficient	[W/m^{2}K]
h_{ro}	outside surface radiation coefficient	[W/m^{2}K]

Roof surface heat balance after Burch [55]

$$h_r = \varepsilon\sigma(T_1^2 + T_2^2)(T_1 + T_2) \quad \textbf{(6-22)}$$

h_r	radiation coefficient	[W/m^{2}K]
ε	emissivity of the underside of the outer fabric of the roof	
σ	Steffan-Boltzmann constant	[W/m^{2}K^4]
T_1 T_2	exchanging surface temperatures	[K]

Radiation coefficient after Burch [55]

$$h_c = 1.5(\Delta T)^{0.33} \quad \textbf{(6-23)}$$

h_c	convection coefficient	[W/m^{2}K]
ΔT	absolute temperature difference between surface and loft space air	[K]

Convection coefficient for loft space surfaces after Burch [55]

The most up to date studies were in the field of building simulation. For the Florida Solar Energy Centre, Parker [110] carried out a comprehensive literature review of attic thermal simulations, evaluating the models used, and found that, in particular, calculation of convection coefficients, accurate determination of material properties (such as emissivity) and

knowledge of loft space ventilation were critical to the development of an effective model. For ASHRAE, Pedersen et al. [111] outlined their iterative heat balance method and an examination of the inside surface heat balance was reported by Liesen and Pedersen [120]. More details of these methods are given below.

6.2.2 Loft space heat balance method developed for this study

The loft space heat balance method developed for this study employed a combination of the methods described by Parker [110], Pedersen et al.[111] and Burch [55]. The model consisted of an outside surface heat balance, a heat balance for each inside surface and one air heat balance as shown in Figure 6-1.

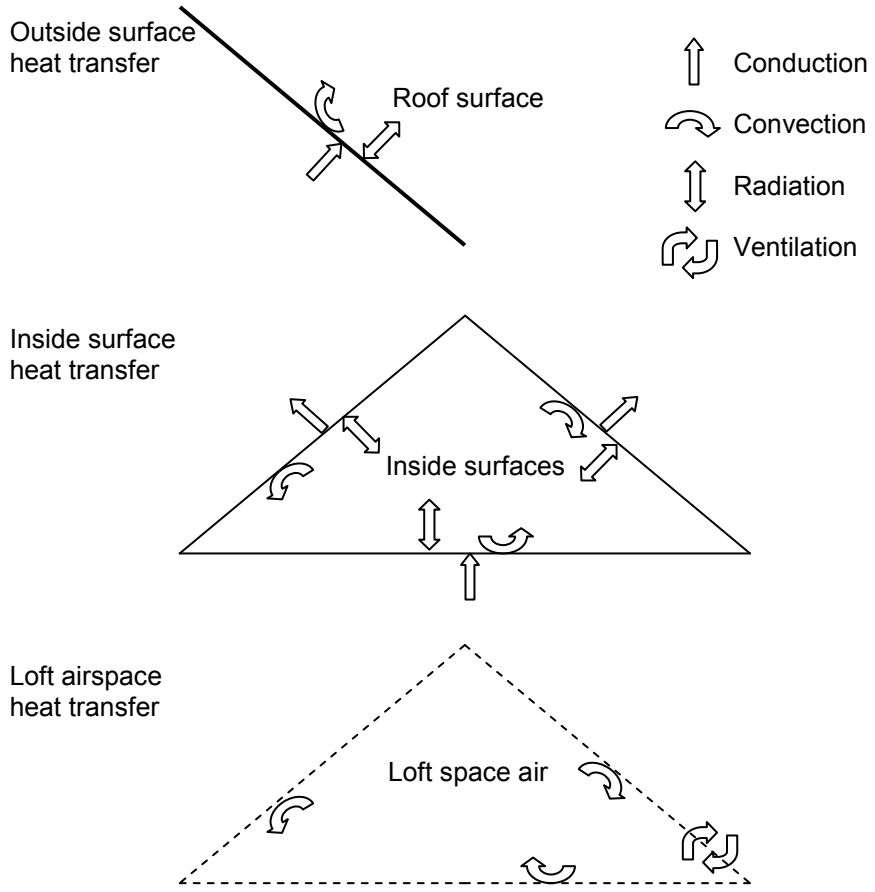

Figure 6-1: Heat balances

The solution was achieved by iteration, repeatedly calculating the temperature of each surface and the air inside the roof space, until each result converged. The resulting seven

equations in seven unknown temperatures were expressed in Equation 5-12 for the outside surface heat balance (described in Section 6.2), Equation 5-13 for the five inside surfaces heat balance and Equation 5-14 for the airspace heat balance given in Chapter 5.

At each of the inside surfaces, conduction, convection and radiation were balanced as shown in Equation 6-24.

$$q_{conduction} + q_{radiation} + q_{convection} = 0 \quad \textbf{(6-24)}$$

$q_{conduction}$	conduction heat exchange through the fabric	$[W/m^2]$
$q_{radiation}$	net radiative heat exchange at the surface	$[W/m^2]$
$q_{convection}$	convective heat exchange at the surface	$[W/m^2]$

Inside surface heat balance

Heat transfer by conduction was calculated from U-value and temperature difference as shown in Equation 6-25. For the party walls, it was assumed that the surface temperature was the same at each side and no net conduction occurred through them.

$$q_{conduction} = U_i \left(T_i - T_{oi}\right) \quad \textbf{(6-25)}$$

$q_{conduction}$	conduction heat exchange through the fabric (floor, roof or wall)	$[W/m^2]$
U_i	thermal conductance of the fabric	$[W/m^2K]$
T_i	temperature of the inner surface of the fabric	[K]
T_{oi}	temperature of the outer surface of the fabric	[K]

Conduction heat loss

For the radiation heat transfer it was assumed that all the internal surfaces could be represented by grey bodies with an even temperature distribution. The transmission and self-emission of radiation in the air of the loft space was ignored. While Parker [110] used the script-F technique to calculate a radiant heat transfer coefficient, the ‘mean radiant temperature network’ method was used for this case study after Caroll (see Liesen and Pedersen [120]). This technique avoided the calculation of radiation view factors for each surface, which was complicated due to the geometry of the loft space.

The mean radiant temperature network simplified the calculations as it allowed heat transfer coefficients to be used along with a mean radiant temperature, as shown in Equation 6-26.

$$q_{radiation} = h_{ri}\left(T_i - T_{MRT}\right) \quad \textbf{(6-26)}$$

$q_{radiation}$	net radiative heat exchange at the surface	$[W/m^2]$
h_{ri}	radiation heat transfer coefficient at the i^{th} surface	$[W/m^2K]$
T_i	temperature of the i^{th} surface	[K]
T_{MRT}	mean radiant temperature	[K]

Radiation heat transfer using radiation coefficients

The radiation heat transfer coefficients accounted for the radiation view factor by including F_i factors, which were independent of temperature and were calculated as shown in Equation 6-27. A simple iterative algorithm was used with F_i initially set to 1. Only 15 iterations were needed for convergence of the factors to better than 4 decimal places.

$$F_i = \frac{1}{1 - \frac{A_i F_i}{\sum A_i F_i}} \quad \textbf{(6-27)}$$

F_i	F_i factor for the i^{th} surface	
A_i	area of the i^{th} surface	$[m^2]$

Calculation of the F_i factor

The radiation heat transfer coefficient, which included the surface emissivity, was initialised as shown in Equation 6-28. The emissivity of all the surfaces in the roof space was assumed to be 0.9, as a typical value for the building materials (e.g. [127]), and the base temperature, T_{base} was initialised at an arbitrary 0°C.

$$h_{radi}^{init} = \frac{4\sigma T_{base}^3}{\left(\frac{1}{F_i} + \frac{1-\varepsilon_i}{\varepsilon_i}\right)} \quad \textbf{(6-28)}$$

h_{radi}^{init}	initial heat transfer coefficient	[W/m^{2}K]
σ	Steffan-Boltzmann constant	[W/m^{2}K^4]
T_{base}	Base temperature	[K]
F_i	F_i factor for the ith surface	
ε_i	emissivity of the ith surface	

Initialisation of the radiation heat transfer coefficient

The heat transfer coefficient was adjusted for each surface, depending on its temperature (see Equation 6-29) and the mean radiant temperature of the roof space was calculated from the surface temperatures (see Equation 6-30). The heat transfer coefficient was adjusted again using the mean radiant temperature (see Equation 6-31) and the final mean radiant temperature was calculated (see Equation 6-32). These values of radiation heat transfer coefficient and mean radiant temperature were then used in the surface heat balance equations. This process was repeated at each iteration.

$$h'_{radi} = \left(a + \frac{T_i}{b}\right) h_{radi}^{init} \quad \textbf{(6-29)}$$

h'_{radi}	temperature adjusted heat transfer coefficient of the ith surface	[W/m^{2}K]
a	constant = -0.5	
b	constant = 200	
T_i	temperature of the ith surface	[K]
h_{radi}^{init}	initial heat transfer coefficient of the ith surface	[W/m^{2}K]

Heat transfer coefficient adjusted for temperature

$$T'_{MRT} = \frac{\sum h'_{radi} A_i T_i}{\sum h'_{radi} A_i} \quad \textbf{(6-30)}$$

T'_{MRT}	initial mean radiant temperature of the roof space	[K]
h'_{radi}	temperature adjusted heat transfer coefficient of the ith surface	[W/m^{2}K]
A_i	area of the ith surface	[m^2]
T_i	temperature of the ith surface	[K]

Mean radiant temperature is calculated

$$h_{radi} = \left(a + \frac{T'_{MRT}}{b} \right) h'_{radi} \quad \textbf{(6-31)}$$

h_{radi}	readjusted heat transfer coefficient of the i^{th} surface	[W/m^2K]
a	constant = -0.5	
b	constant = 200	
T'_{MRT}	initial mean radiant temperature of the roof space	[K]
h'_{radi}	temperature adjusted heat transfer coefficient of the i^{th} surface	[W/m^2K]

Heat transfer coefficient adjusted again

$$T_{MRT} = \frac{\sum h_{radi} A_i T_i}{\sum h_{radi} A_i} \quad \textbf{(6-32)}$$

T_{MRT}	mean radiant temperature of the roof space	[K]
h_{radi}	readjusted heat transfer coefficient of the i^{th} surface	[W/m^2K]
A_i	area of the i^{th} surface	[m^2]
T_i	temperature of the i^{th} surface	[K]

Final mean radiant temperature calculated

For the convective heat transfer within the loft space, a simple convection coefficient was used after Burch [55] as shown in Equation 6-33.

$$h_{ci} = 1.5(\Delta T)^{0.33} \quad \textbf{(6-33)}$$

h_{ci}	convection coefficient of the i^{th} surface	[W/m^2K]
ΔT	absolute temperature difference between i^{th} surface and loft space air	[K]

Convection coefficient after Burch [55]

The convection coefficients described by Parker [110] were more detailed but were not chosen for this study as they depended on the heat flow direction. As temperatures and flow directions were liable to change during iterations, the solution would not have converged in some circumstances. The inside surface convection coefficient formulations by Fisher and Pedersen [128], for ASHRAE, did not apply to the relatively cold and draughty loft space as they were defined empirically for a heated interior room. The Burch simplification was acceptable as radiation was found to be the dominant heat transfer mechanism in the loft space (see Section 5.4.2) and the difference in convection coefficient had little effect on the calculated roof surface temperature.

The heat balance for the loft space air included convection at each surface and ventilation of the airspace as shown in Equation 6-34.

$$\sum A_i h_{ci} (T_{as} - T_i) + \rho n V c_p (T_{as} - T_{air}) = 0 \quad \textbf{(6-34)}$$

A_i	area of the i^{th} surface	$[m^2]$
h_{ci}	convection coefficient of the i^{th} surface	$[W/m^2K]$
T_{as}	loft space air temperature	[K]
T_i	temperature of the i_{th} surface	[K]
T_{air}	ambient air temperature	[K]
ρ	density of air in the loft space	[kg/m3]
n	loft space air change rate	$[s^{-1}]$
V	volume of the loft space	$[m^3]$
c_p	specific heat capacity of air in the loft space	[J/kgK]

Loft space air heat balance

6.3 Conclusions

The methods for the roof surface and loft space heat balances, used in the building model, were developed for this study, based on a review of the relevant literature.

The roof surface exchanged heat with its environment by radiation and convection. For the radiative heat exchange, it was assumed that the non-sky background temperature was the same as the roof surface temperature as a simple background temperature was not easy to ascertain. For the convective heat exchange, forced and natural convection coefficients were defined that accounted for both the temperature inversion (roof surface colder than ambient air temperature) and the roof pitch.

An iterative scheme was developed for the loft space heat balance that accounted for the outside surface heat balance, a heat balance for each inside surface and a loft space air heat balance. The inside surface heat balance considered radiative heat transfer, using a mean radiative temperature network method, and convective heat transfer using a simple convection coefficient as radiative heat transfer was dominant.

The next two chapters describe how the atmospheric and physical properties, needed for the sensor and building models, were derived.

7 Deriving the atmospheric properties

Certain properties of the atmosphere, above the survey area and at the time of the survey, were required inputs for the sensor and building models developed for this study (see Chapters 4 and 5). These were, for the sensor model, the upwelled radiance, atmospheric transmission and downwelled radiance and for the building model, the broadband sky temperature. As they were not measured at the time of the survey, they had to be derived from available historical meteorological data. The literature was reviewed, a number of different methods were compared and the most accurate developed for this study.

7.1 Upwelled radiance and atmospheric transmission

Upwelled radiance is that emitted by the atmosphere between the roof and the sensor as a function of its temperature. Atmospheric transmission is the fraction of the radiance originating from the roof (self emitted and reflected) that reaches the sensor. Both of these terms are expressed within the spectral band pass of the sensor. They were ignored in some aerial heat loss studies. Goldstein [51] assumed no absorption or emission in the air layer between the roof and the sensor. For the Canada Centre for Remote Sensing, Brown et al. [54] claimed this was acceptable on account of the short path lengths involved and for the Atomic Energy Research Establishment, Haigh and Pritchard [70] claimed that atmospheric effects could be ignored on cold dry nights. For the National Bureau of Standards, Burch [55] omitted these properties.

Other studies deemed the atmospheric properties to be important and developed methods for their calculation. For the University of Dundee, Anderson and Wilson [71] derived an equation for atmospheric transmission as a function of wavelength for the water vapour in the atmosphere, assuming a homogenous atmosphere and for path lengths less than 1km. For upwelled radiance, the variation in air temperature with height was incorporated. These simple models ignored other constituent gases and aerosols in the atmosphere. Wilson and Anderson [129] went on to look at using LOWTRAN computer code for calculating atmospheric transmission. The LOWTRAN model of the atmosphere included water vapour

along with other gases and aerosols. Their result for atmospheric transmission compared well with their ground measurements of 0.976 ± 0.006, at 0.974.

Much of Schott's earlier work for Calspan/Rochester Institute of Technology stressed the importance of measuring atmospheric transmission and upwelled radiance [57]. Byrnes and Schott [130] compared two calibration flight techniques and LOWTRAN computer code results with ground temperature measurements. The calibration flights were carried out at the beginning of the survey. The profile calibration technique required viewing targets on the ground at a number of altitudes while the angular calibration technique required viewing targets on the ground at two distinct angles but a single altitude. They found that LOWTRAN and the profile calibration gave similar results for atmospheric transmission and upwelled radiance, producing errors in surface temperature of 0.7°C. Results for the angular calibration were worse, at around 2°C for a typical survey altitude.

In their key study, Snyder and Schott [95] calculated upwelled radiance and atmospheric transmission from profile calibration flights, carried out just before their survey. To reduce the overall error, the upwelled radiance was adjusted so that calculations from the thermal image matched temperature measurements taken for a test surface on the ground. Schott [101] further defined these techniques in his text book and introduced the MODTRAN computer code which superseded LOWTRAN, increased the spectral resolution and improved the accuracy.

As no calibration flights were carried out at the time of the Nottingham survey, the most recent version of the MODTRAN software, MODTRAN 4 [131], was used to estimate the downwelled radiance and atmospheric transmission for this study. The method used was after Schott [101] but extended for this study to include a cubic polynomial fit to model the relationship between atmospheric transmission, upwelled radiance and sensor angle. Atmospheric radio soundings taken at the time of the survey were used to characterise the atmosphere. These observations, given in Appendix 2, were made from the Nottingham weather station at

Watnall, at 2400hrs on the day of the survey. All of the inputs to MODTRAN were in the form of a text file called a 'tape 5' input card, given in Appendix 3.

The MODTRAN computer code was developed by the United States Air Force for predicting atmospheric transmission and radiance. Calculations are done on a $2cm^{-1}$ spectral resolution and the atmosphere modelled as a number of discrete layers described by altitude, pressure, temperature and absorber (gases and aerosols) density. The code uses the atmospheric radio sounding data, of temperature, pressure and relative humidity, to estimate the density of the gases and aerosols, and thereby the transmission and emission, for each atmospheric layer based on a typical urban, winter environment. The height and view angle of the sensor are used to determine the path through these layers and the overall effect calculated.

The spectral radiance output from MODTRAN plotted against wavelength is shown in Figure 7-1 for a sensor at 760m viewing a surface temperature of 273.15K at nadir. The dashed line indicates the radiance from the same surface with no intervening atmosphere. It can be seen that the overall affect of the atmosphere was to increase the radiance received by the sensor, in this situation.

The output from MODTRAN, for thermal radiation, in radiance mode was approximated by Schott [101] as Equation 7-1. For this study, the effective radiance reaching the sensor was calculated by numeric integration of the spectral radiance output weighted by the spectral response function of the sensor, as shown in Equation 7-2, after Schott [101].

This was calculated for temperatures -5°C to 5°C in steps of 2°C at a fixed sensor angle, θ=0 and sensor height, h=760m. Emissivity was set to unity. The effective radiance reaching the sensor with no intervening atmosphere, $L(0)$, was then calculated for the same temperatures by numeric integration of the Planck function weighted by the spectral response function of the sensor, as shown in Equation 7-3.

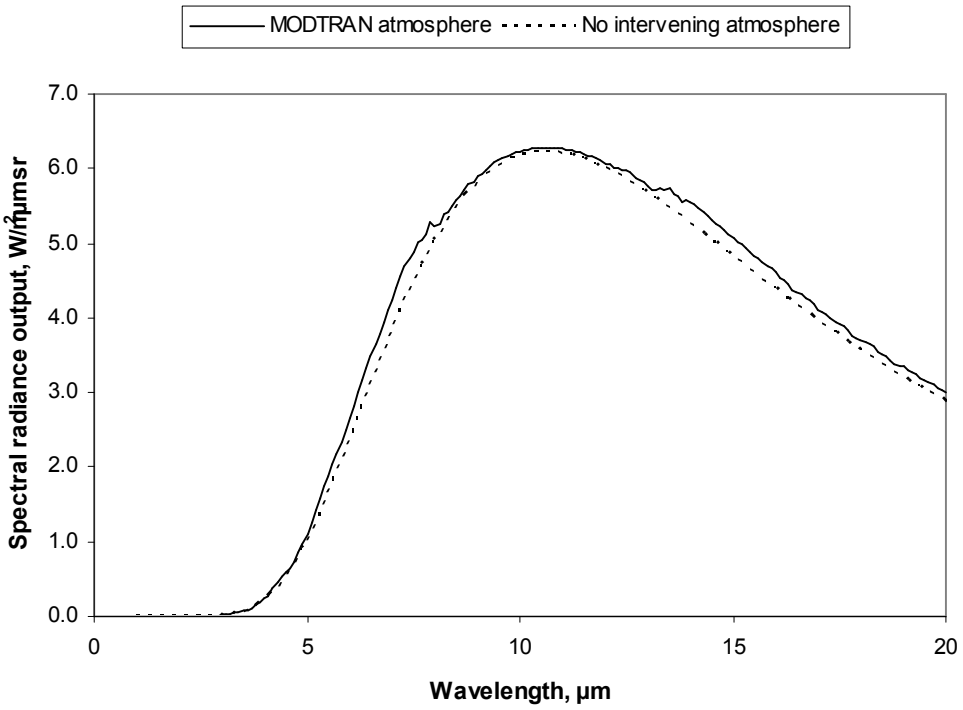

Figure 7-1: Spectral radiance vs. wavelength

$$L_\lambda = \varepsilon L_{T\lambda}\tau_\lambda(h,\theta) + L_{u\lambda}(h,\theta) \qquad \textbf{(7-1)}$$

L_λ	spectral radiance output	[W/m^{2}srµm]
ε	emissivity of the surface	
$L_{T\lambda}$	spectral blackbody radiation from a surface at temperature T	[W/m^{2}srµm]
$\tau_\lambda(h, \theta)$	transmission at sensor height, h and view angle θ	
$L_{u\lambda}(h, \theta)$	upwelled radiance at sensor height, h and view angle θ	[W/m^{2}srµm]

MODTRAN output after Schott [101]

$$L(h,\theta) = \int R'(\lambda) L_\lambda \, d\lambda \qquad \textbf{(7-2)}$$

$L(h, \theta)$	effective radiance reaching the sensor at sensor height, h and view angle θ	
$R'(\lambda)$	normalised spectral response function of the sensor	
L_λ	spectral radiance output from **Error! Reference source not found.**	[W/m^{2}sr]

Effective radiance reaching the sensor through the atmosphere after Schott [101]

$$L(0) = \int_0^{\infty} 2hc^2 \lambda_i^{-5} \times \left[\exp\left(hc / \lambda_i kT \right) - 1\right]^{-1} \times R'(\lambda) d\lambda \quad \textbf{(7-3)}$$

L(0)	effective radiance reaching the sensor with no intervening atmosphere	
T	temperature	[K]
h	Planck constant = 6.6262 x 10^{-34}	[Js]
c	speed of light in a vacuum = 299792458	[m/s]
λ	wavelength	[μm]
k	Boltzmann constant = 1.3807 × 10^{-23}	[J/K]
R'(λ)	peak normalised spectral response function of the sensor	

Effective radiance reaching the sensor with no intervening atmosphere

A linear regression of $L(0)$ with $L(h, \theta)$, shown graphically in Equation 7-2 for $\theta = 0$, produced Equation 7-4, after Schott [101], where the gradient of the line was the atmospheric transmission and the intercept upwelled radiance.

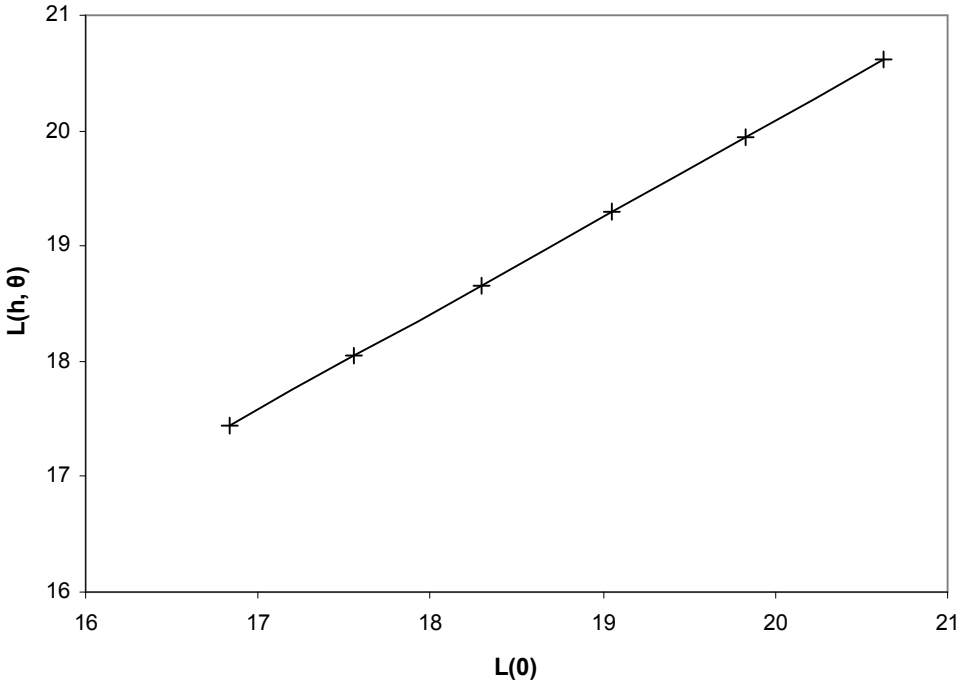

Figure 7-2: Linear regression of L(0) with L(h, θ)

$$L(h,\theta) = \tau(h,\theta)L(0) + L_u(h,\theta) \quad \textbf{(7-4)}$$

$L(h, \theta)$	effective radiance reaching the sensor at sensor height, h and view angle θ	
$L(0)$	effective radiance with no intervening atmosphere	$[W/m^2sr]$
$\tau(h, \theta)$	atmospheric transmission (gradient of the line)	
$L_u(h, \theta)$	upwelled radiance (intercept of the line)	$[W/m^2sr]$

Linear regression of $L(0)$ with $L(h,\theta)$ after Schott [101]

This was repeated for a number of sensor angles, $0° \leq \theta \leq 30°$, in steps of 2°. Results, plotted against sensor angle are shown in Figure 7-3 for atmospheric transmission and in Figure 7-4 for upwelled radiance. From these figures, it can be seen that atmospheric transmission decreased and the upwelled radiance increased as the atmospheric path length increased with sensor angle.

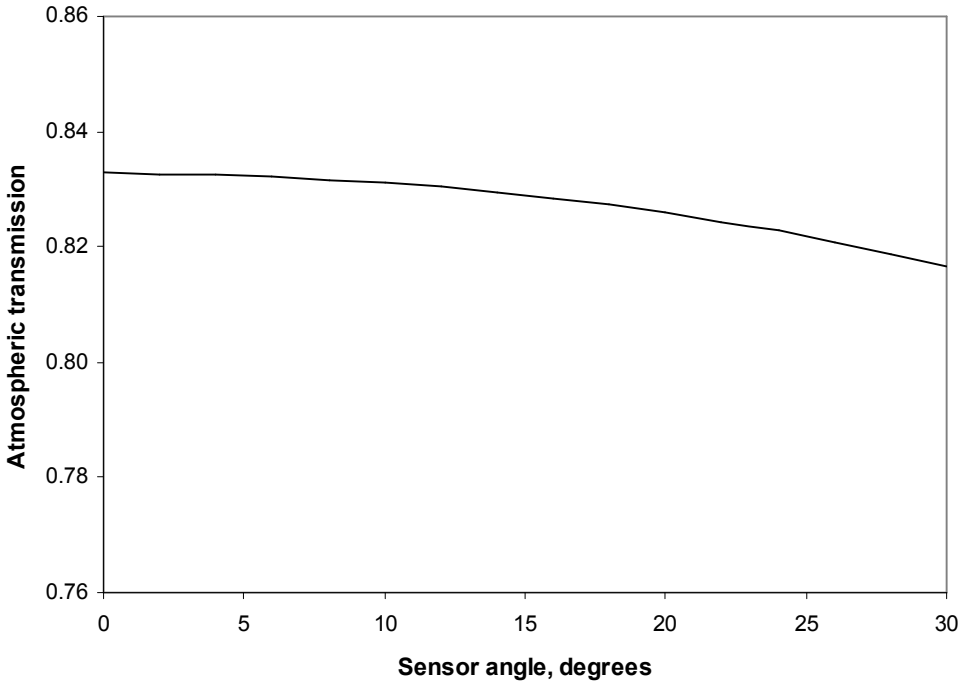

Figure 7-3: Plot of atmospheric transmission against sensor angle

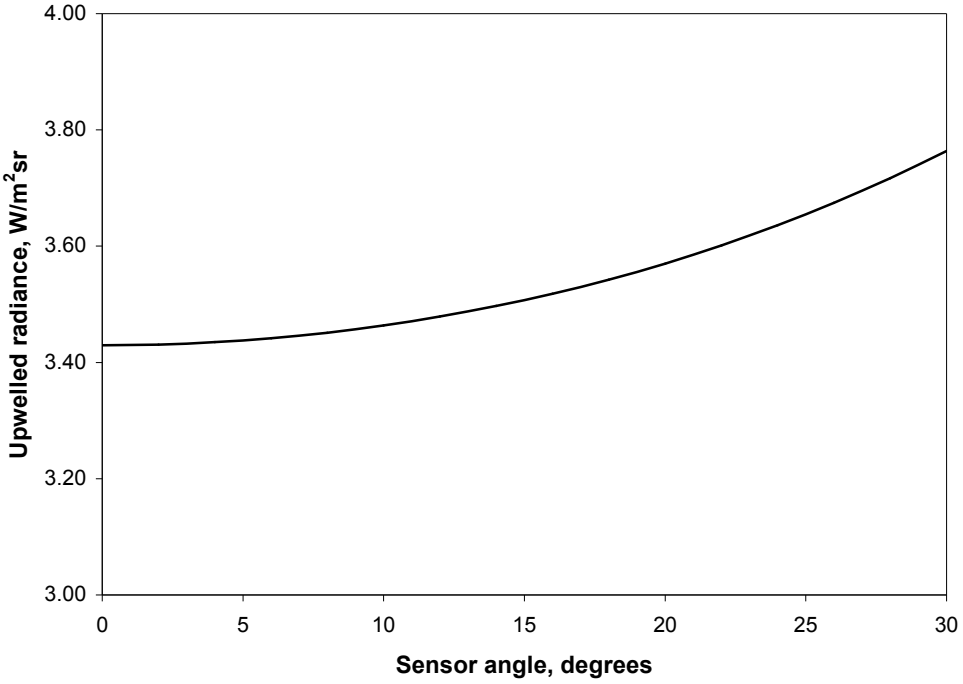

Figure 7-4: Plot of upwelled radiance against sensor angle

To enable atmospheric transmission and upwelled radiance to be calculated at any sensor angle, cubic polynomials were introduced for this study. They described the curves in Figure 7-3 and Figure 7-4 as shown in Equation 7-5 and Equation 7-6.

$$\tau(h,\theta) = a_1\theta^4 + a_2\theta^3 + a_3\theta^2 + a_4\theta + a_5 \qquad \textbf{(7-5)}$$

$\tau(h,\theta)$ atmospheric transmission

$a_1..a_5$ polynomial coefficients

θ sensor angle

Cubic polynomial for atmospheric transmission with angle

$$L_u(h,\theta) = b_1\theta^4 + b_2\theta^3 + b_3\theta^2 + b_4\theta + b_5 \qquad \textbf{(7-6)}$$

$L_u(h, \theta)$ upwelled radiance $[W/m^2sr]$

$b_1..b_5$ polynomial coefficients

θ sensor angle

Cubic polynomial for upwelled radiance with angle

The standard uncertainties in atmospheric transmission and upwelled radiance were estimated for the uncertainty analysis in Section 9.4. The accuracy of MODTRAN is stated as

5%. Based on this, the 99% confidence intervals were calculated to be ± 0.17 W/m^{2}sr in upwelled radiance and ± 0.04 in atmospheric transmission. This gave standard uncertainties of 0.07 and 0.016 respectively after the methods set out by BSI [102] (see Equation 5-2, k=2.58 for 99%).

7.2 Downwelled radiance

Downwelled radiance is that emitted by the entire sky dome, above the roof, as a function of its temperature within the spectral band pass of the sensor. It is often represented by the spectral sky temperature, which is the equivalent blackbody temperature of the sky. This is lower than the broadband sky temperature as the atmosphere absorbs less radiation in the 8-14μm band pass and therefore emits less.

Downwelled radiance was widely acknowledged in other heat loss surveys, though methods for its calculation were less prevalent. Goldstein [51], while recognising the importance of spectral sky temperature did not give any method for calculating it. For the Canada Centre for Remote Sensing, Brown et al. [54] defined the spectral sky temperature as being about -60°C, set it at 215K for their calculations, but gave no indication of its derivation. Burch [55], also gave no derivation of spectral sky temperature for the work of the National Bureau of Standards. For the Atomic Energy Research Establishment, Haigh and Pritchard [70] estimated the spectral sky temperature as 250.2K for a cold clear night but recommended that it was measured using a large reflecting plate on the ground, viewed by the sensor as the aircraft flew over. For Calspan/Rochester Institute of Technology, Byrnes and Schott [130] used a numerical integration of LOWTRAN results over the hemisphere of the sky, though no temperature values were given. This method was further defined by Schott [101].

For this study, downwelled radiance was calculated using MODTRAN 4 [131] software using the method defined by Schott [101]. Atmospheric radio soundings taken at the time of the survey were used to characterise the atmosphere. These observations, given in Appendix 2, were made from the Nottingham weather station at Watnall, at 2400hrs on the day of the

survey. All of the inputs to MODTRAN were in the form of a text file called a 'tape 5' input card, given in Appendix 3.

The MODTRAN sensor was modelled on the ground ($h=0$), looking into space, and the directional downwelled radiance, $L_d(\theta,\phi)$ was calculated for a declination angle of θ from the zenith and azimuth angle, ϕ. Repeated runs of MODTRAN for multiple declination angles 0° to 90° in steps of 1° were carried out and the total downwelled radiance calculated by numerical integration, assuming no azimuthal variations in the sky. The integration is shown in Equation 7-7.

$$L_d = 2\int_{\theta=0}^{\frac{\pi}{2}} L_d(\theta,\phi)\cos\theta\sin\theta d\theta \qquad \textbf{(7-7)}$$

L_d	downwelled radiance	$[W/m^2sr]$
θ	declination angle	
ϕ	azimuth angle	

Integration of downwelled radiance after Schott [101]

The standard uncertainty in the downwelled radiance was estimated for the uncertainty analysis in Section 9.4. The accuracy of MODTRAN is stated as 5%. Based on the detected downwelled radiance of 7.41W/m^2, this gave a 99% confidence interval of ± 0.37W/m^2, which equated to a sky temperature of 234.21K ± 1.77K. The standard uncertainty was calculated to be 0.14W/m^2 after the methods set out by BSI [102] (see Equation 5-2, k=2.58 for 99%).

7.3 Broadband sky temperature

The broadband sky temperature is the blackbody sky temperature of the entire sky dome, above the roof, which was used for the radiative heat exchange at the roof surface. It is different from the downwelled radiance as it is not restricted to the sensor's spectral band pass.

A useful overview of simple models based on ambient air temperature and atmospheric water was given by Cole [121], including work by pioneers Ångström, Brunt and Swinbank along with others. These models were typically for clear skies but included models for overcast skies as did Goforth et al. [132]. Clouds produced a significant increase in the sky temperature but a less predictable temperature distribution and surveys are carried out under clear skies for this reason.

For the work of the Canada Centre for Remote Sensing, Brown [53] used ambient air temperature as the baseline temperature of the roof of an unheated house for the calculation of radiative heat loss. This ignored the temperature depression that occurs on cold, clear, windless nights. Goldstein [51] gave two versions of Swinbank's formula for a clear (cloudless) sky as shown in Equation 7-8.

$$T_{sky} = \left(-3.014\times10^{9} + 1.195T_{air}^{4}\right)^{1/4} \qquad \textbf{(7-8)}$$

$$T_{sky} = 0.05532T_{air}^{1.5}$$

T_{sky}	sky temperature	[K]
T_{air}	ambient air temperature	[K]

Swinbank's formula for clear skies, after Goldstein [51]

The work by the National Bureau of Standards [55] and the University of Dundee [71] used Swinbank's equation as did the Atomic Energy Research Establishment [70] who gave the error as ±1.5K. For Calspan/Rochester Institute of Technology, Snyder and Schott [95] used Brunt's formula as shown in Equation 7-9. This reportedly produced a large bias error in the results and was 'tuned' along with the coefficient of convection until the calculated mean effective U-value equalled the predicted mean calculated from surveys of buildings on the ground. The ESP-r software [114] also used Swinbank's equation while the ASHRAE method [119] gave a number of models with the Brown sky model, given in Equation 7-10, deemed the most accurate.

The above models were developed for situations were detailed knowledge of the atmosphere was unavailable.

$$T_{sky} = T_{air}\left[0.61 + 0.05 p_v^{0.5}\right]^{1/4} \quad \textbf{(7-9)}$$

T_{sky}	sky temperature	[K]
T_{air}	ambient air temperature	[K]
p_v	partial pressure of water vapour	[mb]

Brunt's formula from Calspan/RIT [95]

$$T_{sky} = T_{air}\left[0.65 + 0.41 p_v^{0.9} \exp\left(-0.01033 T_r - 6.060\times10^{-4} T_r^2 + 6.121\times10^{-6} T_r^3\right)\right]^{1/4} \quad \textbf{(7-10)}$$

T_{sky}	sky temperature	[K]
T_{air}	ambient air temperature	[K]
T_r	reference temperature = T_{air} – 240	[K]
p_v	partial pressure of water vapour	[kPa]

The Brown sky model from ASHRAE [119]

Dilley and O'Brien [133] developed new methods for calculating clear sky irradiance, one based on a physical model (Equation 7-11) and one based on Swinbank's equation (Equation 7-12). Both used the air temperature but also included the precipitable water pressure. This is the pressure of the column of water, which could be condensed from moisture above the surface, and can be obtained from radio sounding data.

They compared the results with those derived from LOWTRAN computer code in the 100cm^{-1} to 300cm^{-1} wave number range using standardised atmospheres and found standard deviations in the residual errors of approximately 5W/m^2 in radiance terms. Results were more accurate than calculated by Swinbank's equation, which gave a standard deviation of nearly 19W/m^2 in their trial. Sky temperature can be calculated from these irradiance values by Equation 7-13.

$$E_{sky} = \{1 - \exp(-D\tau)\}\sigma T_{air}^4$$
$$\tau = \alpha + \beta(T_{air}/T_*) + \gamma\sqrt{\omega/\omega_*} \quad \textbf{(7-11)}$$

E_{sky}	irradiance from the sky	[W/m^2]
D	'diffusivity parameter' = 1.66	
τ	'grey-body optical thickness'	
σ	Steffan-Boltzmann constant	[W/m^{2}K^4]
T_{air}	ambient air temperature	[K]
T_*	reference temperature = 273.16	[K]
ω	water vapour	[kg/m^2]
ω_*	reference water vapour = 25	[kg/m^2]
α	parameter = 2.232	
β	parameter = -1.875	
γ	parameter = 0.7356	

For calculating clear sky irradiance based on a physical model [133]

$$E_{sky} = \alpha + \beta(T_{air}/T_*)^6 + \gamma\sqrt{\omega/\omega_*} \quad \textbf{(7-12)}$$

E_{sky}	irradiance from the sky	[W/m^2]
T_{air}	ambient air temperature	[K]
T_*	reference temperature = 273.16	[K]
ω	precipitable water	[kg/m^2]
ω_*	reference precipitable water = 25	[kg/m^2]
α	parameter = 59.38	
β	parameter = 113.7	
γ	parameter = 96.96	

For calculating clear sky irradiance based on Swinbank [133]

$$E_{sky} = \sigma T_{sky}^4$$
$$T_{sky} = \left[\frac{E_{sky}}{\sigma}\right]^{1/4} \quad \textbf{(7-13)}$$

E_{sky}	irradiance from the sky	[W/m^2]
T_{sky}	sky temperature	[K]
σ	Steffan-Boltzmann constant	[W/m^{2}K^4]

Calculating sky temperature from irradiance

For this study, the sky temperature was calculated using the MODTRAN 4 [131] software with atmospheric radio soundings, taken at the time of the survey, to characterise the atmosphere.

The method was similar to that used to calculate the downwelled radiance (see Chapter 7.2), as described by Schott [101] but over a wider frequency band width (100cm^{-1} to 300cm^{-1}) as Dilley and O'Brien [133] did using LOWTRAN.

The MODTRAN sensor was positioned on the ground, looking into space. The directional downwelled radiance L(φ,θ) was then calculated for a declination angle of θ from the zenith and azimuth angle, φ. Repeated runs of MODTRAN for multiple declination angles 0° to 90° in steps of 1° were used to integrate the total downwelled radiance assuming no azimuth variations in the sky. The MODTRAN 'tape5' input files are given in Appendix 3.

The variation in radiance with angle from the vertical is shown in Figure 7-5. Radiance increased with angle from the vertical due to the increasing length of the atmospheric path closer to the horizon.

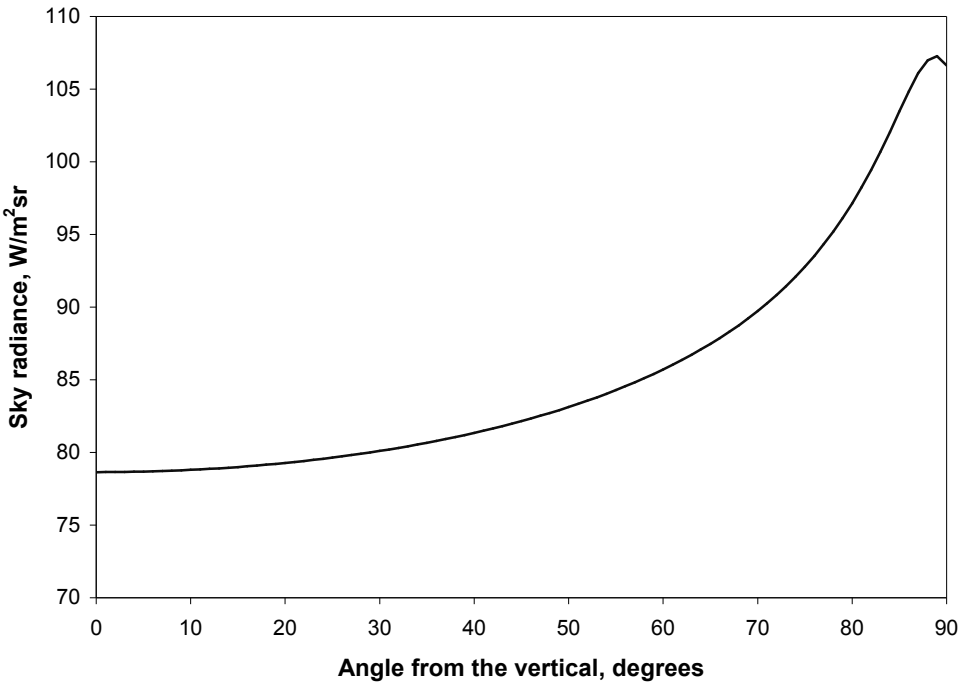

Figure 7-5: Variation in broadband sky radiance with angle as calculated by MODTRAN

Total irradiance from the sky was calculated by a numerical solution of Equation 7-14 and sky temperature was calculated from the irradiance by the Steffan-Boltzmann law as shown in Equation 7-15.

$$E_{sky} = 2\pi \int_{\theta=0}^{\frac{\pi}{2}} L(\theta,\phi)\cos\theta \sin\theta d\theta \qquad \textbf{(7-14)}$$

E_{sky}	irradiance from the sky	[W/m^2]
θ	declination angle from the zenith	[radians]
ϕ	azimuthal angle	[radians]

Integration of the radiance from the sky after Schott [101]

$$T_{sky} = \left(\frac{E_{sky}}{\sigma}\right)^{1/4} \qquad \textbf{(7-15)}$$

T_{sky}	sky temperature	[K]
E_{sky}	irradiance from the sky	[W/m^2]
σ	Steffan-Boltzmann constant	[W/m^2K^4]

Solving the Steffan-Boltzmann Law for sky temperature

The results from each of the methods described above, using the radio sounding data observed at the Nottingham weather station, Watnall at 2400hrs on the day of the survey, are given in Table 7-1. The radio sounding data are given in Appendix 2. On the ground, air temperature was 4.4°C, air pressure was 101.8kPa, partial pressure of water vapour was 0.7668kPa (calculated from the mixing ratio 4.65g/kg) and the precipitable water was 9.24kg/m^2 (mm H_2O).

It can be seen from Table 7-1 that there were large variations in the sky temperature calculated by the different methods. The Brown result agreed well with the MODTRAN result and was much simpler but MODTRAN was deemed the most accurate and more widely recognised method.

Table 7-1: Comparison of sky temperature results calculated by different methods

Method	Reference	Sky temperature, K
Swinbank (1)	Goldstein [51]	252.7
Swinbank (2)	Goldstein [51]	255.8
Brunt	Snyder and Schott [95]	258.2
Brown	McClellan and Pedersen [119]	260.7
Dilley and O'Brien (1)	Dilley and O'Brien [133]	256.0
Dilley and O'Brien (2)	Dilley and O'Brien [133]	256.0
MODTRAN 4	AFRL [131]	261.0

The standard uncertainty in the broadband sky temperature was estimated for the uncertainty analysis in Section 9.4. The accuracy of MODTRAN is stated as 5%. Based on the irradiance result of 263 W/m^2, this gave a 99% confidence interval of ± 3.2K. While this was slightly better than the 5W/m^2 standard deviation quoted by Dilley and O'Brien [133] it suggested that the ±1.5K quoted by the Atomic Energy Research Establishment [70], using Swinbank's equation, was underestimated. The standard uncertainty was calculated to be 1.2K after the methods set out by BSI [102] (see Equation 5-2, k=2.58 for 99%).

7.4 Conclusions

Methods for defining the atmospheric properties of upwelled radiance, atmospheric transmission, downwelled radiance and broadband sky temperature were defined and calculated for the Nottingham case study. Upwelled radiance and atmospheric transmission were estimated using MODTRAN 4 software with local radio soundings, taken at the time of the survey, used to characterise the atmosphere. Cubic polynomials were used to describe their relationship with sensor angle. Downwelled radiance and broadband sky temperature were also calculated using MODTRAN 4 with the radio sounding data. For each parameter, the directional downwelled radiance, in declination angles 0° to 90° and in the appropriate band pass, was numerically integrated assuming no azimuthal variations in the sky.

8 Determining the physical property parameters

The input parameters for the sensor and building models (see Chapters 4 and 5) included a number of physical properties. For this study, the roof and sensor geometry were determined for each house. A method for experimental emissivity measurement was developed and carried out on two representative roofing materials. A number of methods, for calculating the sky view factor, were compared and the most suitable chosen for this study.

8.1 Roof and sensor geometry

Roof and sensor geometry were determined, for each house in this study, from a combination of site visits, Ordnance Survey Landline data and the thermal image. During site visits, building types, ridge directions and house numbers were recorded and digital camera images were taken of typical buildings.

8.1.1 Building dimensions

The length and width of each building was measured from the Ordnance Survey Landline data, using the measure tool, in the GIS software. Length was defined as the along the ridge dimension. For the uncertainty analysis in Section 9.4, the 99% confidence interval of this measurement was estimated to be ± 0.1m giving a standard uncertainty of 0.04 after the method set out by BSI [102] (see Equation 5-2, k=2.58 for 99%).

8.1.2 Roof pitch, θ

The roof pitch was determined from the digital photographs taken during site visits. Images of a typical building of each style, taken end on, where imported, as bitmaps, in to AutoCAD. Roof pitch was then measured by overlaying lines along the gutter and slope and using the angle dimension tool. The 99% confidence interval in this measurement was estimated as ± 2° giving a standard uncertainty of 0.8 after the method set out by BSI [102] (see Equation 5-2, k=2.58 for 99%).

8.1.3 Line of sight angle, α

Line of sight angle is the angle between the sensor and the roof normal. At nadir and for a flat roof the line of sight angle is 0°, while for a 1/1 pitched roof the line of sight angle is 45°. As the sensor angle increases beyond the nadir, line of sight angle depends on the sensor angle, the roof pitch (see Figure 8-1), and the orientation of the roof to the flight line. It was calculated for each house by Equation 8-1, which was determined from geometry for this study.

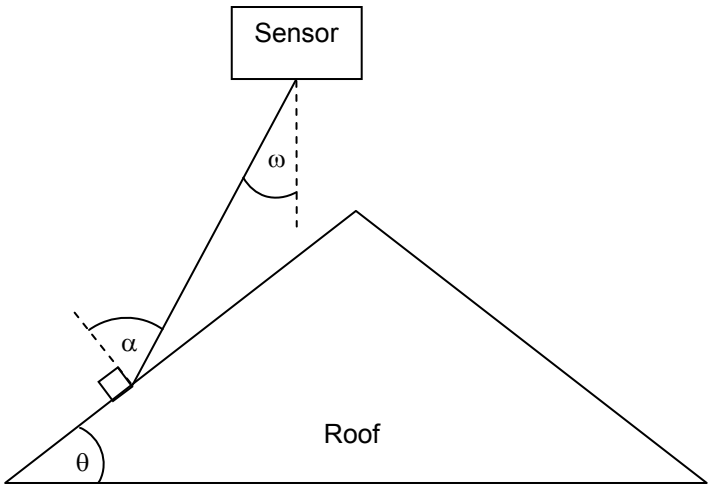

Figure 8-1: Line of sight angle

$$\alpha = \cos^{-1}\left(\cos(90-\omega)\cdot\left(\cos(\beta)\cdot\cos(90-\theta)\right)+\cos(\omega)\cdot\cos(\theta)\right) \quad \textbf{(8-1)}$$

α	line of sight angle between sensor and roof normal	[radians]
ω	sensor angle	[radians]
β	building orientation to flight line	[radians]
θ	roof pitch	[radians]

Line of sight angle between the sensor and the roof normal

The orientation of the roof to the flight line was measured by importing the building and flight line maps, generated by the GIS, into AutoCAD and using the angle dimension tool. A satisfactory way of measuring the angle in the GIS was not found.

While most roofs have more than one face, only the line of sight angle to that face nearest the flight line was calculated. The implications of this decision are discussed in Section 8.3.

8.1.4 Sensor angle, ω

For this study, the sensor angle was calculated, by simple geometry, from the height of the sensor (flight altitude=760m) and the distance of each house from the flight line. Distance from the flight line was measured using the GIS software and the Ordnance Survey Landline data. This necessitated creating a new GIS layer and adding flight line vectors, drawn at the centre of each flight strip. A raster layer, representing the distance of each pixel from the flight line, was then generated using the GIS and averaged within each building outline. This produced a database of the average distance of each building from the flight line.

8.2 Emissivity

Roof surfaces are not perfect emitters of infrared radiation. Emissivity describes the radiation emitted by the roof as a fraction of that emitted by a blackbody at the same temperature (see Equation 8-2).

$$\varepsilon = \frac{L_{roof}}{L_{bb}} \qquad \textbf{(8-2)}$$

ε	emissivity	
L_{roof}	radiance emitted by the roof	$[W/m^2sr]$
L_{bb}	radiance emitted by a blackbody at the same temperature	$[W/m^2sr]$

Emissivity as a ratio

This is the total or broad band emissivity used for calculating the radiative heat exchange of the roof surface with its environment (building model). For infrared sensor calculations, because emissivity is a function of wavelength and the sensor operates in a narrow wavelength band, the effective emissivity over the spectral band pass of the sensor is described by Equation 8-3.

$$\varepsilon_{eff} = \frac{\int_0^{\infty} \varepsilon(\lambda) L_\lambda R'(\lambda) d\lambda}{\int_0^{\infty} L_\lambda R'(\lambda) d\lambda} \quad \textbf{(8-3)}$$

ε_{eff}	effective emissivity in the spectral band pass of the sensor	
$\varepsilon(\lambda)$	emissivity function	
L_λ	monochromatic radiance	[$W/m^2 sr \mu m$]
$R'(\lambda)$	peak normalised spectral response function of the sensor	

Effective emissivity

While the difference is commonly recognised, the two are often assumed to be the same and of an arbitrary value in other studies. This is probably because emissivity is difficult to measure and the effective emissivity depends on the instrument used and the temperature of the sample [134]. Where emissivity data do appear in the literature there is often much discrepancy [135].

In some studies, attempts have been made to determine the emissivity of all the roofs in a large area of the built environment [136, 137]. These aerial surveys used two infrared sensors, operating in different wavelength bands, and equated the measurements to calculate the emissivity. The technique assumes that the emissivity of each roof is the same in each wavelength band and the different spectral response of each sensor is ignored. These assumptions are problematic and it is more usual to take measurements on the ground, either in the field or in a laboratory. While professional laboratories can provide emissivity spectra for samples of materials measured under stringent conditions [138, 139] the service was prohibitively expensive for this study.

For the Atomic Energy Research Establishment, Haigh and Pritchard [70] suggested using a quantitative radiometer to measure the emissivity of roof materials in situ. The radiometer housing was placed flush with the roof so that all reflected radiation came from the temperature controlled cavity. They stated that the error in the measurement was ± 0.02.

Salvaggio and Miller introduced detailed methodologies for the collection of emissivity spectra in the field using a portable spectrometer [140] and compared their results with those measured in the laboratory [141]. Errors were found to be 1 to 2%.

ASTM E 1933-99a [142] provided two simple test methods for measuring emissivity using an infrared camera. The contact method used a thermocouple (or similar) attached to the specimen, while the non-contact method used a surface modifying material of known emissivity (typically a paint or adhesive tape). For both methods the temperature of the specimen must be at least 10°C warmer or cooler than the ambient temperature and these temperatures stable. Also the infrared camera must have a function for inputting the emissivity and the background temperature (to compensate for reflected radiance).

Madding [143] presented equations for calculating emissivity from infrared camera measurements using reference emitter (as ASTM non-contact method), reference temperature (as ASTM contact method) and two temperature techniques. Calculations of the uncertainty in the emissivity measurement demonstrated that the accuracy improved as the temperature difference between target and background increased.

Avdelidis and Moropoulou [144] compared the results of using the method set out in ASTM E 1933-99a [142] with Madding's [143] reference emitter technique to measure the emissivity of a number of historic building materials. They found the results to be in good agreement in the 8-14μm wavelength band at a sample temperature of 48.8°C.

Johnson et al. [145] compared the emissivity of sand blasted aluminium plates, determined using three different methods. The bi-reference method used a blackbody at the same temperature as the sample and a highly reflective reference plate to determine the background contribution. The bi-temperature method used a coating of known emissivity on the sample and measurements at two different but unknown temperatures. The bi-background method again used a coating of known emissivity on the sample but took

measurements at two different, but unknown, background temperatures. They reported to an accuracy of ± 0.02 emissivity units.

For Calspan/Rochester Institute of Technology, Schott and Wilkinson [63, 64] used a three temperature technique to measure the emissivity of roofing material in the 8-14μm band pass. Measurements were made at three surface temperatures, with a constant background temperature, using a radiometer and a large constant temperature cavity. The same tests were carried out with a surface of known emissivity and the ratio of the results gave the ratio of the emissivity values. The measurement error was estimated as ± 0.02. Variations due to weathering and ageing were found to be insignificant compared with the measurement error. Some of their results are shown in Table 8-1. The emissivity of slate was found to vary significantly (i.e. greater than measurement error) with line of sight angle.

Table 8-1: Emissivity of roofing materials (8-14μm) from Schott and Wilkinson [64]

Type	Description	Emissivity
Asphalt shingles	white	0.93
	grey	0.89
Asbestos shingles	white	0.90
	grey	0.89
Slate shingles	grey	0.85
	red	0.84
Miscellaneous	wood shingle	0.82
	heavy felt with tar	0.88
	heavy weight roofing felt	0.87
	light weight roofing felt	0.92
	red clay tile	0.82

Further to this work, Schott [146] developed a complex mechanism with two rotating choppers of known emissivity and two constant temperature cavities, to measure emissivity normal to the surface with a precision of ± 0.007. These results were then used in the large constant temperature cavity with the radiometer at an angle to the specimen's surface. The emissivity at any angle was calculated from the radiance at that angle based on the radiance measured normal to the specimen and the precise emissivity measurement.

Snyder and Schott [95] developed an empirical relationship (see Equation 8-4) between emissivity and line of sight angle based on laboratory measurements of roofing asphalt. A plot of this relationship is given in Figure 8-2 for an emissivity normal to the surface of 0.9. At 30 degrees the emissivity is 0.891 and at 50°, 0.873.

$$\varepsilon_\alpha = \varepsilon_0 \left(\frac{1}{0.9^{0.07}} \right) [0.9 \cos(\alpha)]^{0.07} \qquad \textbf{(8-4)}$$

ε_α emissivity at angle, α

ε_0 emissivity normal to the surface

Emissivity variation with angle after Snyder and Schott [95]

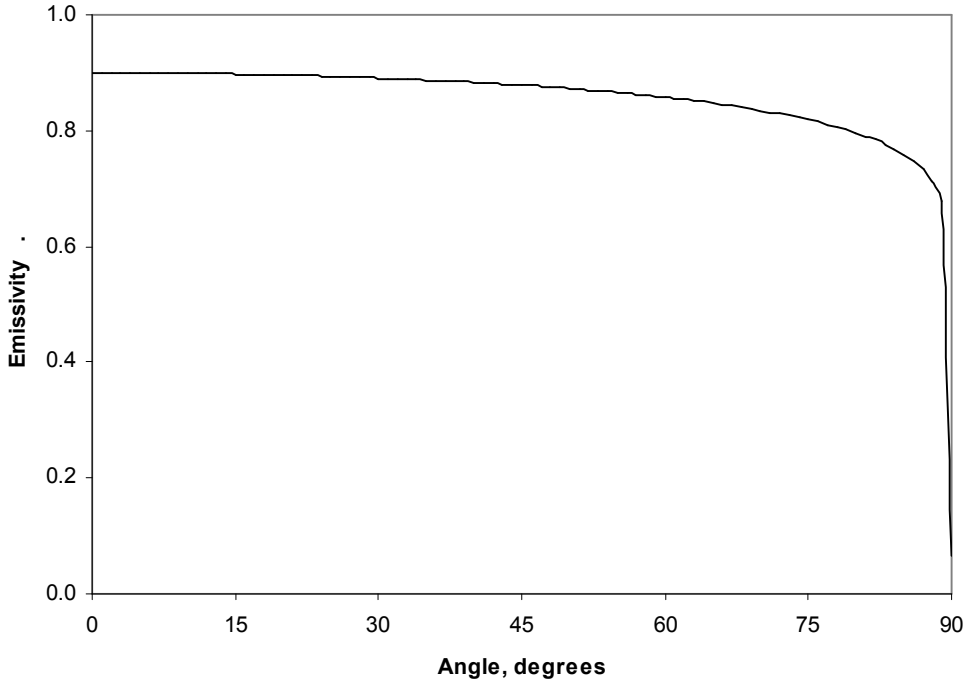

Figure 8-2: Graphical representation of Equation 8-4 for $\varepsilon_0 = 0.9$

They propagated errors in the result by simulation and estimated the precision and bias in emissivity, for a value of 0.92, to have standard deviations of 0.018 and 0.011 respectively. The uncertainty is larger than in other studies.

While most other aerial thermography studies ignored the variation of emissivity with angle, Burch [55], for the National Bureau of Standards, suggested that emissivity had only a weak

dependence on line of sight angle until that angle exceeded 60°. Daryabeigi et al. [147] developed a technique to measure the directional emissivity of samples using a commercially available imager in the 7.5 to 14um wavelength band. They found the results compared well with electromagnetic theory and directional reflectance measurements. Electromagnetic theory showed that emissivity remained relatively constant for angles less than 60 degrees and then dropped sharply to zero as shown in Figure 8-3, reproduced from the text.

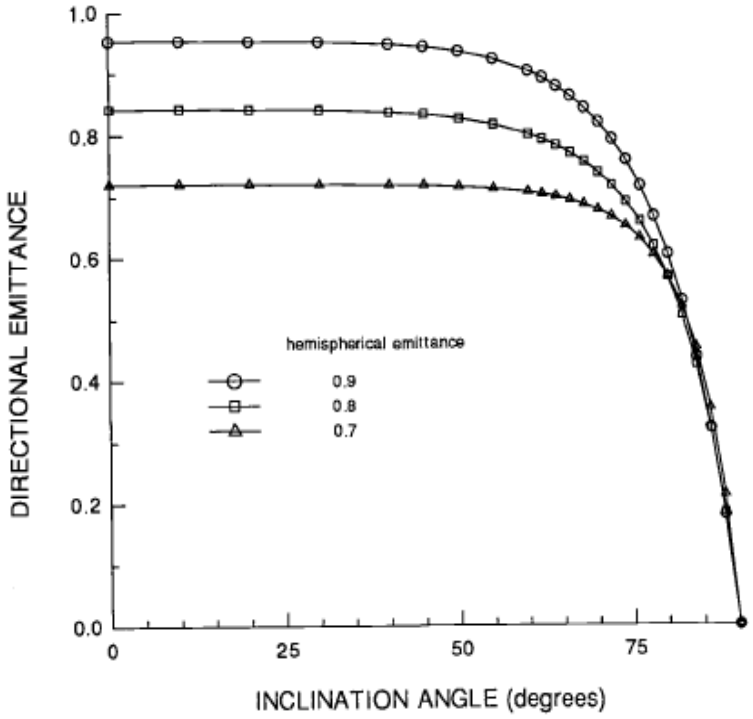

Figure 8-3: Variation in emissivity with angle to normal by electromagnetic theory reproduced from Daryabeigi et al. [147]

Their measurements were taken using an infrared camera imaging a temperature controlled sample, mounted on a rotating mechanism. The entire apparatus was surrounded by white cardboard to help provide a uniform background temperature. The emissivity at each angle was calculated from the emissivity normal to the senor, the relative spectral response of the imager, the ambient temperature, the target temperature, and the measured apparent temperature. Differences between measured values and electromagnetic theory predictions were in the order of 0.01. These results support the findings of Snyder and Schott [95] .

Two types of roofing material were identified for the houses in this study (see Section 10.2): a natural slate tile and a red clay tile. Experimental measurements of representative materials (see Figure 8-4) were made for this study, using a thermal imaging camera, operating in the 8-14μm wavelength range.

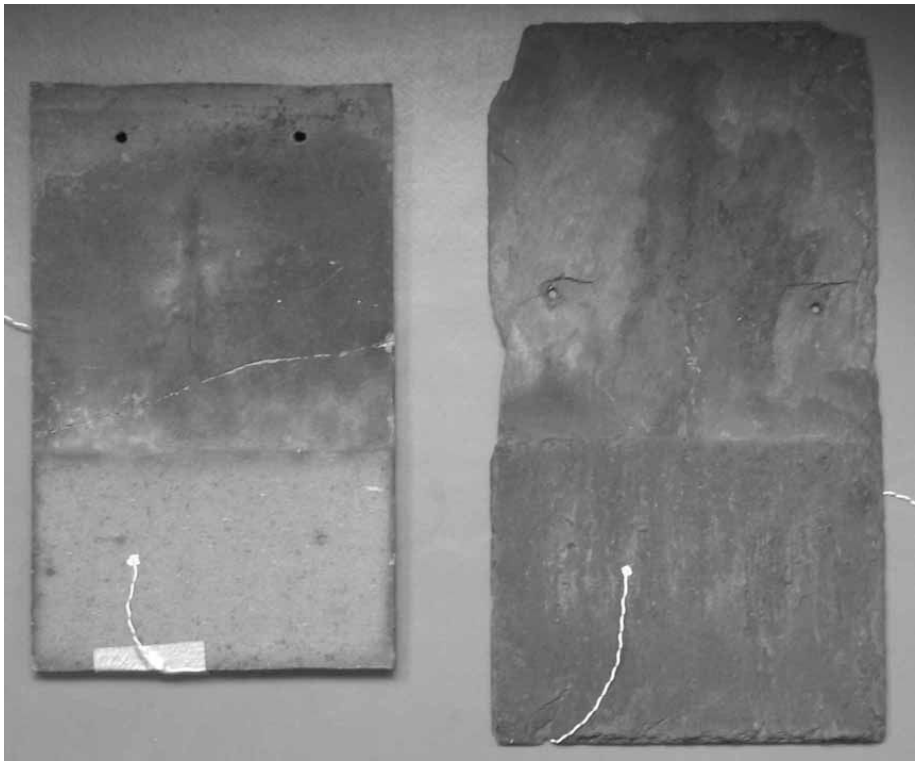

Figure 8-4: Clay roofing tile and Slate roofing tile

The experimental method used was based on the contact thermometer method of ASTM, E 1933-99a [142], using a thermocouple to measure the sample temperature, but heating the sample using an oven after Madding [143] and Avdelidis and Moropoulou [144]. Each sample had a thermocouple attached to its surface using a small piece of reflecting tape. The sample was heated in an oven at approximately 50°C, removed and placed in a cardboard enclosure, and viewed through an aperture using a FLIR ThermoVision A20M infrared camera connected to a video monitor. The enclosure was designed to limit variations in the background temperature. The camera was set to display the temperature of an averaging box positioned on the image close to the site of the thermocouple on the specimen. Thermocouples were used to continually monitor the temperatures of the specimen, the inner surface of the enclosure (background temperature) and the air temperature inside the

enclosure using a data logger linked to a PC. The difference between surface temperature and background temperature was typically 20°C. The experimental set up is shown in Figure 8-5.

Figure 8-5: Experimental set up for emissivity measurement

Measurement was performed by simultaneously 'freezing' the image on the infrared camera and the thermocouple readout. The humidity in the room and distance between the specimen and the camera were entered using the camera's on-board controls. The background temperature, air temperature and emissivity settings on the camera were then adjusted so that all the temperatures matched those of the thermocouples. All the values were recorded. This was repeated ten times for each sample and the average emissivity taken. The results are given in Table 8-2.

Table 8-2: Results of the emissivity measurements

Sample	Emissivity	Standard deviation	Standard uncertainty
Clay tile	0.881	0.007	0.002
Slate tile	0.925	0.009	0.003

In each case, the emissivity is an average of ten measurements although the methodologies that were followed recommended fewer measurements. The standard deviation of the measurements is shown along with the standard uncertainty of the average, which was calculated after the method set out by BSI [102] (see Equation 4-1) for the uncertainty analysis in Section 9.4. This was an optimistic estimate as it ignored experimental factors,

which may have caused a bias error and only recorded the uncertainty in the precision of the results collected under those conditions. Any difference in spectral response function between the thermal imaging camera and the sensor used for the Nottingham case study was ignored.

For the Nottingham case study the maximum line of sight angle was around 50 degrees and the empirical relationship, for variation in emissivity with angle, determined by Snyder and Schott [95] was used (see Equation 8-4). The additional uncertainty of this model was not included. The line of sight angle was only calculated for the face of the roof nearest the flight line (see Section 8.2.3) but if the sensor viewed any face that was sloping away from the flight line, larger line of sight angles would be possible. This would reduce the emissivity for that part of the roof and therefore the averaged sensor output and at-sensor radiance. By ignoring this phenomenon, the calculated roof surface temperature is lower than if corrected. However, the individual faces of roofs on the thermal image could not be distinguished and were too small to determine using more than one buffer (see Figure 4-2). Analysis of several roofs showed no statistically significant difference in averaged sensor output or pixel values for different roof faces.

Variations in material used on the surface of a roof and chimneys, flashing, windows and vents (see Figure 8-6), will alter the effective emissivity as might moisture, dirt and other surface contamination. The effective value for each roof will be difficult to determine with any certainty.

In the absence of any other data the spectral band pass emissivity, used for the sensor model, and the total broadband emissivity, used for the building model, were assumed the same.

Figure 8-6: Variations in roof material and windows can make the effective emissivity difficult to determine with any certainty

8.3 Sky view factor

The sky view factor (SVF) of each roof dictates both the radiative heat exchange at the surface (building model) and how much of the reflected radiation received by the sensor is derived from the relatively cold sky (sensor model). It can be described as the fraction of the surface area of a hemispherical surface (the sky dome) that can be seen from the roof. It is shown schematically in Figure 8-7, for a single point and in two dimensions.

The SVF is an average value for the roof surface and is a function of the 3-dimensional geometry of the building roof and its surroundings, including buildings, ground and trees. Various techniques have been suggested for its calculation.

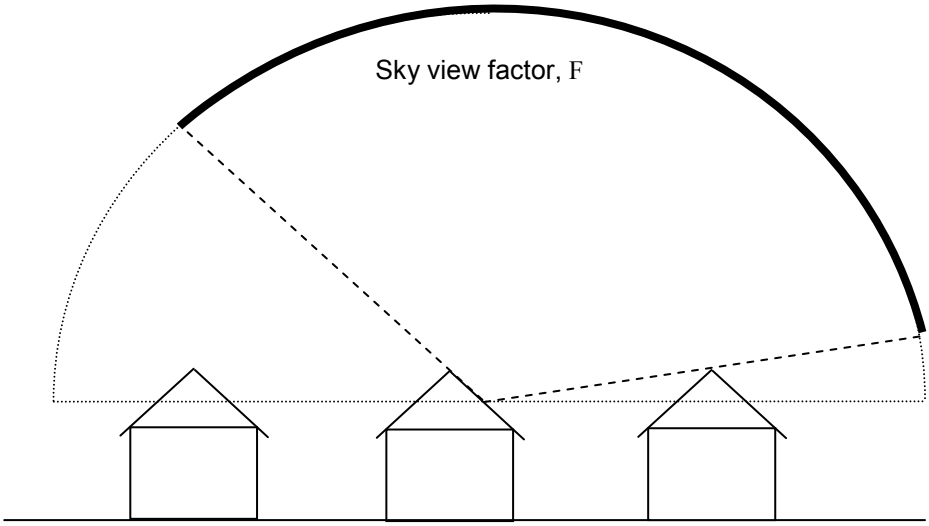

Figure 8-7: Sky view factor of a roof

While Goldstein [51] included the SVF, he gave no method for its calculation. The Canada Centre for Remote Sensing [54] calculated the SVF for a pitched roof, based on two identical buildings, from their distance apart, width and roof pitch. A hemispherical integration [53] was applied at both the ridge and gutter level of the slope of the roof and averaged. For the work of Calspan/Rochester Institute of Technology, Snyder and Schott [95] did not describe how they calculated the SVF but Schott and Wilkinson [64] gave a technique that used the building width, peak to peak distance to the neighbouring house, the height difference to the neighbouring house and the roof slope. Their method simply calculated the angle, from the midpoint of the roof, between a line to the ridge and a line to the ridge of a neighbouring building and divided it by 180° as shown in Figure 8-8. This may overestimate the sky view factor as it does not account for the hemispherical surface of the sky dome, which has proportionally more area near the horizon.

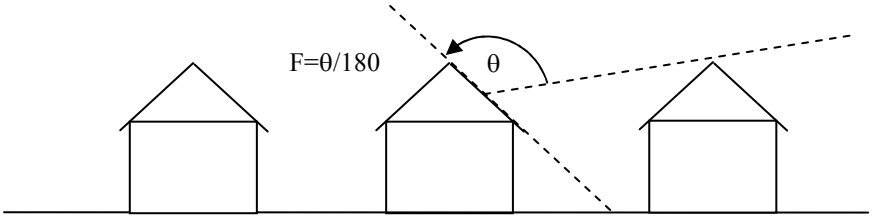

Figure 8-8: Angle calculated by Schott and Wilkinson [64] to determine sky view factor

Schott [101] gave a more thorough treatment for a pitched roof based on a hemispherical integration as shown in Equation 8-5.

$$F = 1 - \frac{1}{2}\cos\left(\frac{\pi}{2} - \theta\right) \quad \textbf{(8-5)}$$

F	sky view factor	
θ	roof pitch	[°]

Sky view factor calculation after Schott [101]

Work by the Atomic Energy Research Establishment [70] only considered flat roofs and, along with the work of the National Bureau of Standards [55], implicitly assumed the SVF was unity. The work by the University of Dundee [70] acknowledged the role of SVF but gave no guidance for its calculation other than that it may be estimated geometrically. The ESP-r software used three view factors for external surfaces: surface to sky, surface to ground and surface to surroundings [114]. A table of example values was given for these view factors under a number of different circumstances, as shown in Table 8-3.

Table 8-3: Representative radiation view factors from Clarke [114]

Location	F_{sky}	F_{ground}	$F_{surround}$
City centre: surrounding buildings same height, vertical surface	0.36	0.36	0.28
City centre: surrounding buildings higher, vertical surface	0.15	0.33	0.52
Urban site: vertical surface	0.41	0.41	0.18
Rural site: vertical surface	0.45	0.45	0.10
City centre: sloping roof	0.50	0.20	0.30
Urban site: sloping roof	0.50	0.30	0.20
Rural site: isolated	0.50	0.50	0.00

EnergyPlus and the ASHRAE heat balance method also used three view factors after Walton (see [148] and [119]): surface to sky, surface to air and surface to ground. They were estimated from the angle of the surface of interest (the roof pitch in our case) as given in Equation 8-6. However, it was noted that if the building is in an urban area, where surrounding buildings may dominate the view, the view factor should be approximated based on those surroundings.

$$F_{sky} = \left[\frac{(1+\cos\theta)}{2}\right]\cos\left(\frac{\theta}{2}\right)$$
$$F_g = (1-\cos\theta)/2 \qquad \textbf{(8-6)}$$
$$F_a = 1 - F_g - F_{sky}$$

F_{sky}	view factor of surface to sky	
F_g	view factor of surface to ground	
F_a	view factor of surface to air	
θ	surface tilt (roof pitch)	[°]

Radiation view factors and ASHRAE heat balance method [119]

Other techniques for calculating the SVF have been used, particularly in researching the 'urban heat island' (e.g. Oke [126]). These have included optical methods such as analysing a fish-eye photographs [149] and simple geometry models [150] but were developed for use in the 'urban canyon', typified by a road with buildings on either side.

The Rayman [151] software included a tool for calculating the SVF from a point. A three dimensional model of the building and its surroundings was needed for the analysis. A simple model comprising identical roofs in a large grid was generated for this study, as shown in Figure 8-9. The resultant polar diagram generated by the software is shown in Figure 8-10 for a roof pitch of 1/1. The pitched roofs were modelled from centroid height upwards in a typical street arrangement.

While the Rayman results were deemed accurate for any configuration modelled, it would not be possible to model every roof within a city, as the level of computing required would be excessive. Additionally the software did not account for variations in surface topography.

Using a computer to analyse three dimensional city models on a lager scale is an emerging technology. Ratti [152] proposed a novel technique for analysing raster based digital elevation models on a pixel by pixel basis based on a shadow casting algorithm. The SVF was estimated by computing the shadows for each of a large number of light sources distributed evenly over the sky dome and then calculating the number of times a particular pixel was in light as a fraction of the total number of light sources. While this technique is very well suited

to calculations on a citywide scale, the analysis is based on a relatively coarse pixel size and would not represent the sloping surface of a residential house's pitched roof easily.

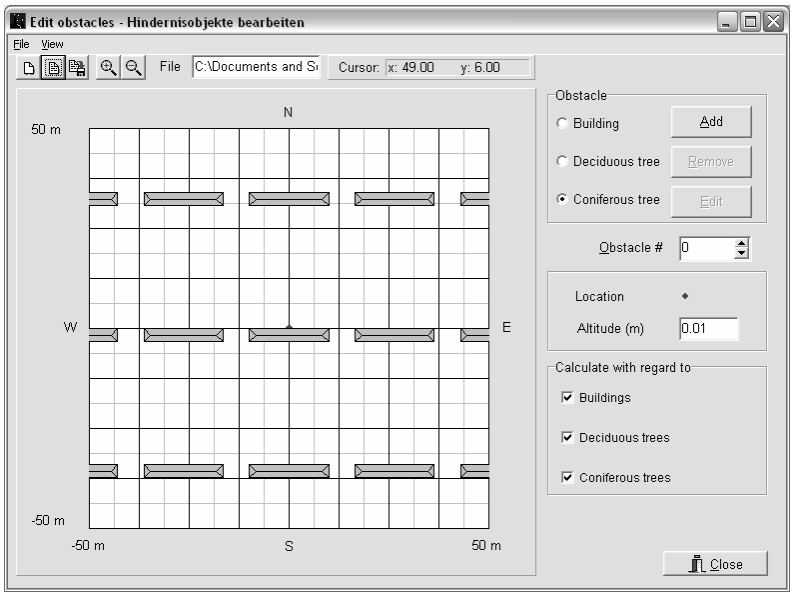

Figure 8-9: Simple 3D model in Rayman [151]

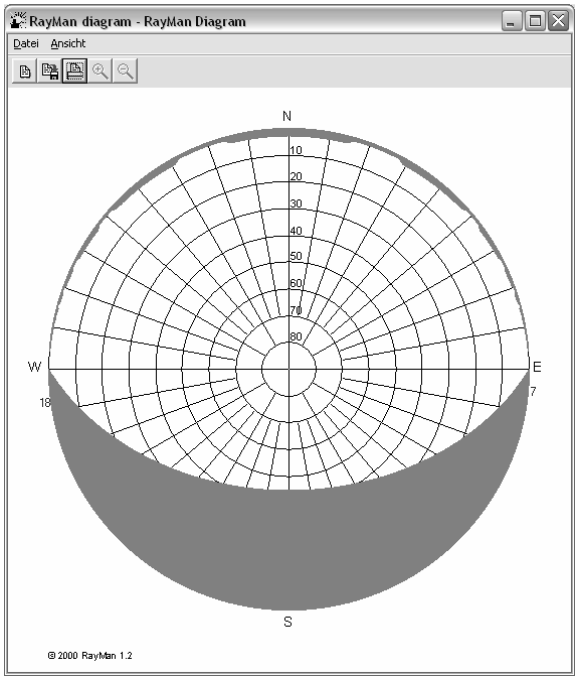

Figure 8-10: Rayman [151] polar diagram for 1/1 roof pitch

While the Arc GIS [153] 3D Analyst tool has a function for computing line of site visibility on a three dimensional surface it will not calculate sky view factor directly. However, Beesley [154]

and Souza et al. [155] independently developed GIS extensions for computing the sky view factor within ArcGIS. Both were based on finding the skyline from the maximum angle between a point and its surroundings at a number of positions around the compass. While Beesley [154] simply calculated the fraction of visible sky represented by each angle as a percentage of 90°, Souza et al. [155] performed a more complex projection of the buildings onto the hemispherical sky vault. Both techniques were only applied to urban canyons.

A three-dimensional model of the city of Nottingham, including the terrain elevations and building geometry, does not exist. However, models have been created for many cities around the world [156] and it is understood that a model of Nottingham may be available in the future. Automated generation of 3d city models is possible using LiDAR remote sensing and building extraction software [157, 158]. In the short term, these techniques will have a significant cost associated.

The sky view factor calculated by different methods, for a building width of 6.5m, peak to peak distance of 34m and a pitch of 1/1, 1/2 and 1/3, surrounded by identical buildings in an urban setting, were compared as shown in Table 8-4. It can seem that none of the methods reproduce the Rayman results and the discrepancies are significant. The Rayman results were repeated with a 1.5m diameter coniferous tree, with height 1m above the roof centroid placed 3m in front of the building. It can be seen from Table 8-4 that this has a noticeable effect on the results.

Table 8-4: Sky view factor as calculated by different methods

Method	Sky view factor		
	1/1	1/2	1/3
CCRS [54]	0.714	0.840	0.891
Calspan/RIT [64]	0.717	0.836	0.886
Schott [101]	0.646	0.776	0.842
ESP-r [114] (see Table 8-3)	'0.50'	'0.50'	'0.50'
Energy plus [148] and ASHRAE [119]	0.789	0.922	0.962
Rayman [151]	0.734	0.812	0.832
Rayman with tree	0.713	0.788	0.806

For this study, the sky view factor was determined using the simple Rayman results and based on the roof pitch alone. The roofs had more than one face and it was assumed that the sky view factor was the same for each.

The standard uncertainty in the sky view factor was calculated for the uncertainty analysis in Section 9.4. A 90% confidence interval of ± 0.02 was estimated, to approximate a tree in the garden or different surrounding buildings. This gave a standard uncertainty of 0.012 after the method set out by BSI [102] (see Equation 5-2, k=1.64 for 90%). This is a conservative estimate of the uncertainty as the geometry of the roof and the surrounding topography are often more complex than considered here (see Figure 8-11).

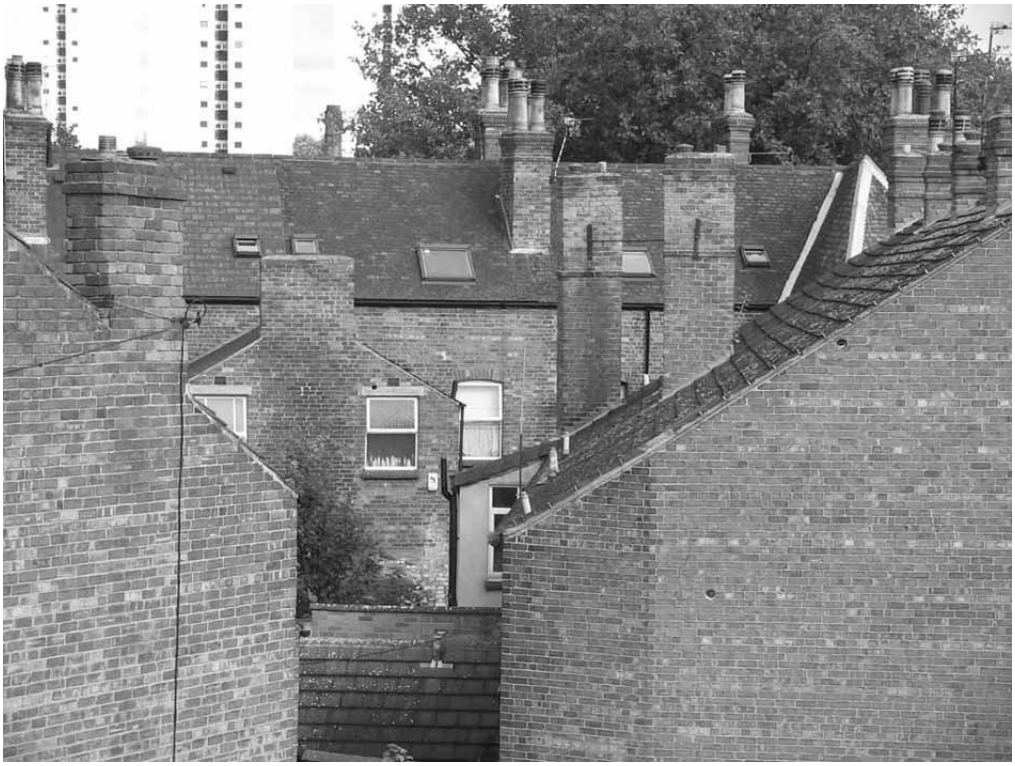

Figure 8-11: Complex geometry can make sky view factor difficult to calculate

8.4 Conclusions

Methods for defining the roof and sensor geometry were developed and values calculated for each house in this study. The building dimensions were measured in the GIS software, the roof pitch was measured from photographs taken on site and the line of sight angle was

calculated from the roof pitch, building orientation and sensor angle. Sensor angle was calculated from the altitude of the flight and the distance of the house from the flight line.

A technique to measure the emissivity roof tiles, using an infrared camera and thermocouples in the laboratory, was developed for this study. Measurements were made on two representative materials.

While other studies have typically used numerical methods, the sky view factor was derived for each house in this study using the Rayman software. The houses were modelled as a grid of identical roofs at each pitch.

Conservative estimates of the standard uncertainty in each of these parameters were made. The accuracy of the results of the sensor and building models is considered in the next chapter.

9 Simulating the errors

Errors represent the difference between the value of an input parameter specified for this study and its actual (true) value as well as the difference between the results of the models developed for this study and the actual (true) roof surface temperature. The errors in each input parameter will produce an error in the roof surface temperature calculated by the sensor and building models.

How close the results of these models are to true values defines the accuracy. Accuracy will determine the ability of aerial thermography to discriminate poorly insulated roofs from those that are well insulated. This chapter describes the techniques that were used to explore that accuracy by analysing the errors in the input parameters.

The magnitude of the error in the results of the sensor and building models may depend on the initial value of all the input parameters. Therefore, parameter sets were defined for 'test houses' that were representative of those analysed in the Nottingham case study in Chapter 10. The effect of error in individual parameters, on the roof surface temperature calculated by the building and sensor models, was examined by a one-at-a-time sensitivity analysis. The magnitude of the total error was predicted by an uncertainty analysis, propagating the errors by simulation using a Monte Carlo method.

9.1 Test houses

The houses in the Nottingham case study in Chapter 10 comprised similar blocks of two story houses with two different styles of roof: a high (1:1) pitched clay-tiled roof and a lower (1:3) sloped slate-tiled roof. There were both end and mid terraced properties, of each style. Parameter sets were created to represent examples of each of these houses with insulation thicknesses of 50mm (poorly insulated), 150mm, and 250mm (well insulated). This produced 12 distinct test houses for which the roof surface temperature, shown in Table 9-1, was calculated using the building model.

Table 9-1: Roof surface temperature of the 12 test houses

Insulation level	Calculated roof surface temperature, °C			
	1:1 pitch, clay tiles		1:3 pitch, slate tiles	
	End-terrace	Mid-terrace	End-terrace	Mid-terrace
50mm	0.932	0.679	0.680	0.393
150mm	0.598	0.331	0.236	-0.081
250mm	0.512	0.240	0.119	-0.205

The averaged sensor output was determined by iteration such that the sensor model produced the same roof surface temperature as the building model for each test house. The averaged sensor output for each house is shown in Table 9-2.

Table 9-2: Averaged sensor output for the 12 test houses

Insulation level	Averaged sensor output, (digital number)			
	1:1 pitch, clay tiles		1:3 pitch, slate tiles	
	End-terrace	Mid-terrace	End-terrace	Mid-terrace
50mm	104.32	101.87	113.94	111.07
150mm	101.21	98.65	109.66	106.52
250mm	100.40	97.80	108.52	105.31

All the test houses were modelled at zero distance and angle to the flight line and with typical building dimensions of 5.9m in the ridge direction and 6.5m width as shown in Figure 9-1.

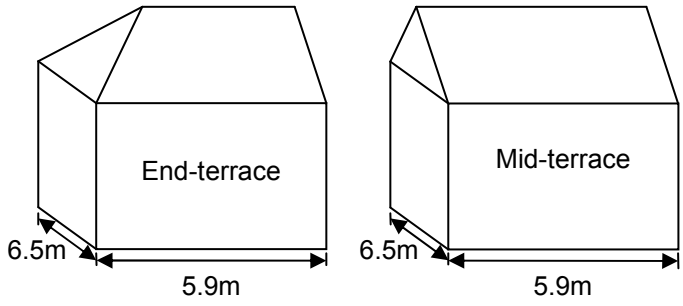

Figure 9-1: Building dimensions of the end and mid-terraced houses

All other parameters were the same as those for the Nottingham case study. The ambient air temperature was 4.5°C and the wind speed 2.4m/s. The broadband sky temperature was calculated as -12.15°C (261K). Building internal temperature was set to 18°C and the loft

space ventilation at 2 air changes per hour. For the high slope (1:1), clay tiled roof the pitch was 45°, the sky view factor 0.734 and the emissivity 0.881. For the low slope (1:3), slate tiled roof the pitch was 18.43°, the sky view factor 0.832 and the emissivity 0.925. The roof of the end terrace houses had a hipped end with the same pitch as the main roof.

The relationship between roof surface temperature and insulation thickness for the four building styles, as calculated by the building model, is shown in Figure 9-2. It can be seen that higher pitched roofs are generally warmer than the lower ones as they exchange less heat with the cold night sky. In addition, end-terraces are generally warmer than mid-terraces due to a smaller net heat loss at the roof surface resulting from higher radiative losses but proportionally larger convective gains for the half-hipped roof shape.

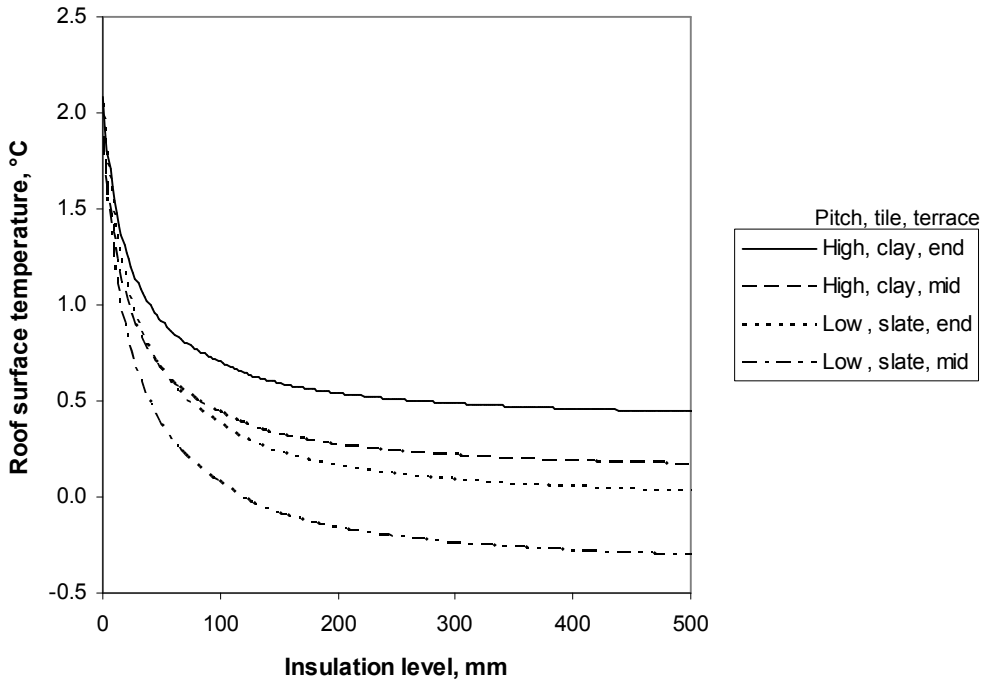

Figure 9-2: Relationship between roof surface temperature and insulation thickness for the four building styles as calculated by the building model

9.2 Sensitivity analysis

The sensitivity of the output of the sensor and building models to error in each of the input parameters was explored using a one-at-a-time sensitivity analysis. These results were used to identify those parameters to which the models were most sensitive and provided an indication of the level of accuracy required when defining each parameter.

Sensitivity analysis has been used in other aerial thermography studies. Goldstein [51] determined the important parameters from his model by examining the effect on the results of changing each parameter in turn. He concluded that for any building, roof surface temperature might be more sensitive to local wind speed, broadband sky temperature and ventilation of the loft space than to the insulation level. He also noted that measurement of the roof surface temperature by the sensor was particularly sensitive to the spectral emissivity. He concluded that uncertainty in these inputs made discrimination of insulation levels impossible.

For the Canada Centre for Remote Sensing, Brown et al. [54] found, by plotting the effect of varying each in turn, that their models for the sensor and the building were very sensitive to roof pitch and loft space ventilation respectively. This lead to the conclusion that insulation level could not be determined from aerial thermography as ventilation rates could not be quantified accurately enough for each building.

For the Atomic Energy Research Establishment, Haigh and Pritchard [70] concentrated on errors in calculating the convective heat transfer at the surface, determining broad band sky temperature and measuring emissivity. They concluded that the broadband sky temperature should be measured at the time of the survey to reduce the effect of error in that parameter.

For the National Bureau of Standards, Burch [55] plotted the effect of varying input parameters in turn. He found the results were more sensitive to emissivity, local wind speed and ambient air temperature than to insulation thickness. The effect was greater for pitched ventilated roofs than it was for flat roofs but ventilation rate had little effect on the result.

There was some discrepancy in the most sensitive parameters between studies, which may be due to differences in the weather at the time of each survey and different types of buildings. This confirms that the sensitivity analysis should be carried out for each building type and for the conditions under which the data was collected.

For this study, the sensitivity analysis was undertaken by making repeated runs of the model, altering each input parameter in turn (one-at-a-time) while all other parameters maintained their initial value. The sensor model and the building model were considered separately and the sensitivity of both models to background temperature was explored further.

9.2.1 Sensor model

The input parameters of atmospheric transmission (τ), emissivity (ε), upwelled radiance (L_u), averaged sensor output (DN), background temperature (T_{bg}), sky view factor (F), downwelled radiance (L_d) and roof slope (θ) were considered for the sensitivity analysis of the sensor model. Standard units were used with temperatures in degrees Celsius and angles in degrees. These input parameters are shown in relation to the process flowchart of the sensor model in Figure 9-3.

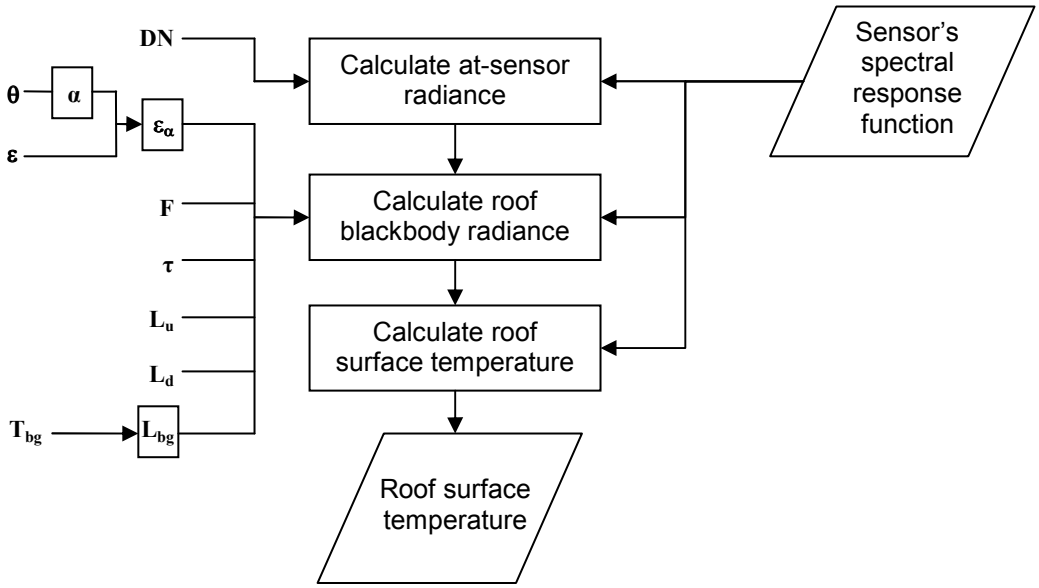

Figure 9-3: The sensor model process flowchart with input parameters

The at-sensor radiance was calculated from the averaged sensor output by Equation 4-3. The roof slope was used to determine the line of sight angle by Equation 8-1 and this was used to determine the emissivity variation with angle (ε_α) by Equation 8-4. Background radiance (L_{bg}) was calculated from the background temperature using a numerical integration of Planck's law, weighted by the spectral response function of the sensor as per Equation 4-6.

The newly calculated at sensor-radiance, emissivity and background radiance, and the remaining input parameters were then used to determine the roof blackbody radiance by solving Equation 4-5. Finally, roof surface temperature was calculated by Equation 4-10. For each test house, each parameter, in turn, was perturbed in 2% steps to ± 10% of its original value, while all the other parameters maintained their original value and the roof surface temperature recalculated, for each step, by the sensor model.

The graphical results for change in roof surface temperature (°C) against fraction of the input variable, for low and high sloped, end terraces, with different insulation thicknesses are shown in Figure 9-4 for the six most sensitive parameters. The graphs demonstrate that the effect of the perturbation in each parameter was to produce a change in the calculated roof surface temperature, the response was approximately linear in each case and the gradient of the line depended upon the roof type and insulation thickness to a varying degree. The roof type was dominant in most cases, as can be seen clearly for background temperature where the higher sloped roof is more sensitive. The steeper the gradient of the line, the greater the sensitivity of the output (roof surface temperature) was to error in that parameter.

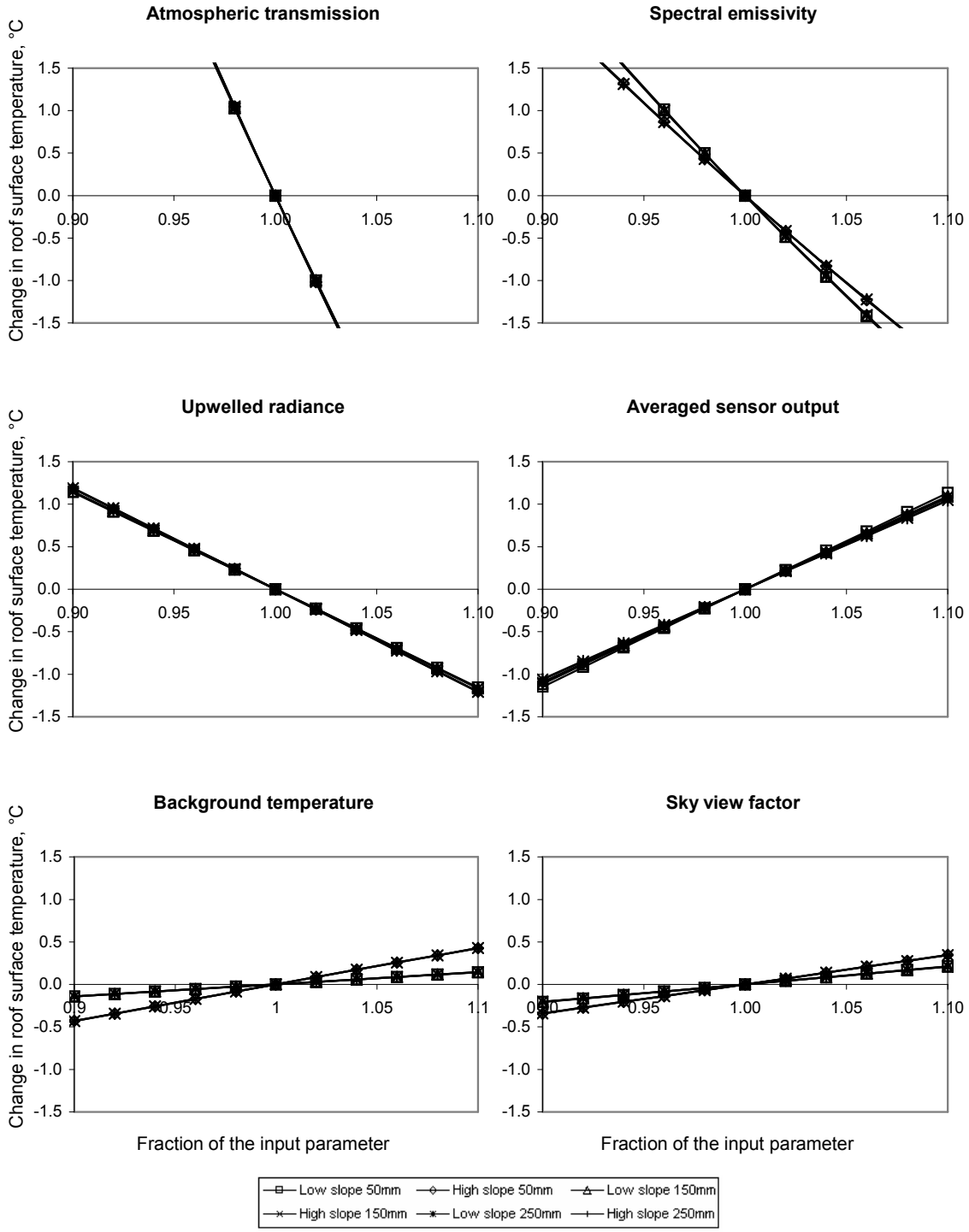

Figure 9-4: Graphical results for sensitivity of the sensor model

The results are summarised in Table 9-3, for the high slope (1:1 pitch), clay tiled roof houses and Table 9-4 for the low slope (1:3 pitch), slate tiled roof houses, as change in roof surface temperature (°C) per 1% error in that parameter. These values were calculated from the gradient of the lines in Figure 9-4. Negative values indicate an inverse relationship such that the roof surface temperature decreased as the value of that parameter increased.

The results are ranked in order with the parameter the result is most sensitive to being listed first. While the type of roof (slope and material) has some effect on the results, there is very little difference between the results for a mid-terrace and an end-terrace and between the results for different insulation levels. It can be seen that roof slope alone has little effect on the result (it caused a change in the spectral emissivity due to a change in the line of sight angle) but the effects of emissivity and sky view factor are much more significant.

One of the drawbacks of a simple sensitivity analysis is that it ignores the interrelationships between parameters (e.g. roof slope and sky view factor), though it does help identify those parameters that must be determined accurately if the result is to be valid. For example, the difference in roof surface temperature between a house with 50mm of insulation and one with 250mm of insulation is only about 0.5°C (see Table 9-1). This is the equivalent of an error in atmospheric transmission of only 1% or an error in the spectral emissivity of about 2%, assuming that there are no errors in any other parameter. These variables must be known with considerable accuracy if the analysis is to be possible.

Table 9-3: Sensitivity of the sensor model results for a high slope, clay tiled roof

High slope clay tiled	Temperature change per percentage error in input, °C/%						
	End-terrace			Mid-terrace			
Parameter	50mm	150mm	250mm	50mm	150mm	250mm	average
Atmospheric transmission	-0.519	-0.518	-0.518	-0.518	-0.517	-0.517	-0.52
Spectral emissivity	-0.213	-0.212	-0.211	-0.212	-0.210	-0.210	-0.21
Upwelled radiance	-0.119	-0.120	-0.120	-0.120	-0.120	-0.120	-0.12
Sensor output	0.109	0.106	0.105	0.106	0.103	0.103	0.12
Background temperature	0.043	0.043	0.043	0.043	0.043	0.043	0.04
Sky view factor	0.035	0.034	0.034	0.034	0.034	0.034	0.03
Downwelled radiance	-0.022	-0.022	-0.022	-0.022	-0.022	-0.022	-0.02
Roof slope	0.012	0.012	0.012	0.012	0.012	0.012	0.01

Table 9-4: Sensitivity of the sensor model results for low slope, slate tiled roof

Low slope slate tiled	Temperature change per percentage error in input, °C/%						
	End-terrace			Mid-terrace			
Parameter	50mm	150mm	250mm	50mm	150mm	250mm	average
Atmospheric transmission	-0.509	-0.508	-0.507	-0.508	-0.507	-0.506	-0.51
Spectral emissivity	-0.247	-0.245	-0.244	-0.246	-0.243	-0.243	-0.25
Upwelled radiance	-0.115	-0.116	-0.116	-0.115	-0.116	-0.116	-0.12
Sensor output	0.114	0.110	0.109	0.112	0.108	0.107	0.11
Background temperature	0.014	0.014	0.014	0.014	0.014	0.014	0.01
Sky view factor	0.021	0.021	0.021	0.021	0.021	0.021	0.02
Downwelled radiance	-0.014	-0.014	-0.014	-0.014	-0.014	-0.014	-0.01
Roof slope	0.002	0.002	0.002	0.002	0.002	0.002	0.002

9.2.2 Building model

The sensitivity analysis of the building model was carried out in a similar manner to that for the sensor model. The input parameters: ambient air temperature (T_{air}), emissivity (ε), sky view factor (F), broad band sky temperature (T_{sky}), wind speed (v), building dimensions (l_{bg} and w_{bg}), building internal temperature (T_{inside}), roof slope (θ), insulation thickness (d), loft

space air changes (n), and background temperature (T_{bg}); were considered. Standard units were used with °C for temperatures and degrees for angles. These input parameters are shown in relation to the process flowchart of the sensor model in Figure 9-5.

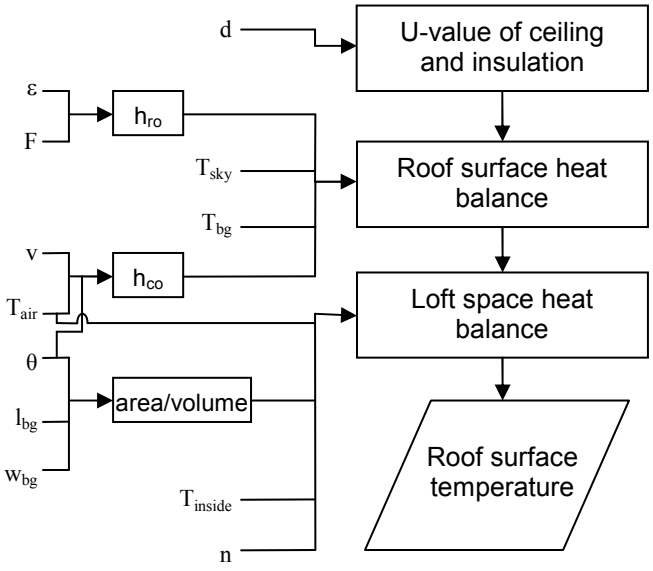

Figure 9-5: The building model process flowchart with input parameters

The U-value of the ceiling and insulation was calculated from the insulation thickness by Equation 5-1. The radiation heat transfer coefficient, at the outside surface of the roof, (h_{ro}) was calculated from the emissivity and sky view factor after Equation 5-10 and the convection coefficient (h_{co}) from the ambient air temperature, wind speed and roof slope after Equations 6-11, 6-12 and 6-15. These were then used along with the broadband sky temperature in the roof-surface heat balance as shown in Equation 5-12, which was modified from Equation 6-1 to include the background temperature. Surface areas and volumes were calculated by standard geometry from the roof slope and building dimensions. The surface areas were used to calculate the inside surface radiation coefficients in Section 6.3.2 for the inside surfaces heat balance using Equation 5-13 and the building internal temperature. The surface areas and loft space volume was then used with the ventilation rate and ambient air temperature for the loft space air heat balance using Equation 5-14. The result was calculated iteratively as described in Section 5.4.

For each test house, each parameter, in turn, was perturbed in 2% steps to ± 10% of its original value, while all the other parameters maintained their original value and the roof surface temperature recalculated, for each step, by the building model.

The graphical results for low and high sloped, end terraces, with different insulation thicknesses are shown in Figure 9-6 for the six most sensitive parameters. The graphs demonstrate that the effect of the perturbation in each parameter was to produce a change in the calculated roof surface temperature and the response was approximately linear in each case, the steeper the gradient of the line, the greater the sensitivity of the output (roof surface temperature) was to error in that parameter.

The results are summarised, in Table 9-5 for the high slope, clay tiled roof houses and Table 9-6 for the low slope, slate tiled roof houses, as change in roof surface temperature (°C) per 1% error in that parameter. These values were calculated from the gradient of the line. Negative values indicate an inverse relationship such that the roof surface temperature decreased as the value of that parameter increased. The results are ranked in order with the parameter the result is most sensitive to being listed first.

The sensitivity of the results to sky view factor and broadband emissivity were identical as the product of these parameters form part of the radiation heat transfer coefficient at the outside surface. The results do not demonstrate the same level of sensitivity seen in some of the sensor model parameters. The results are also to some extent arbitrary as the units chosen for each parameter have an effect on the calculated sensitivity coefficient. For example, the temperatures were in °C. If they had been described in K, each 1% change in temperature would have produced a larger increment. Additionally, the sensitivity to temperatures around 0°C will be small compared with the sensitivity to larger temperatures (positive or negative) as 1% of a large number will give a larger perturbation than 1% of a small number. The linearity of the curves, however, allows these sensitivity coefficients to be extrapolated to some extent. This property was used to explore the assumption made, while developing the models, that the background temperature was the same as roof surface temperature.

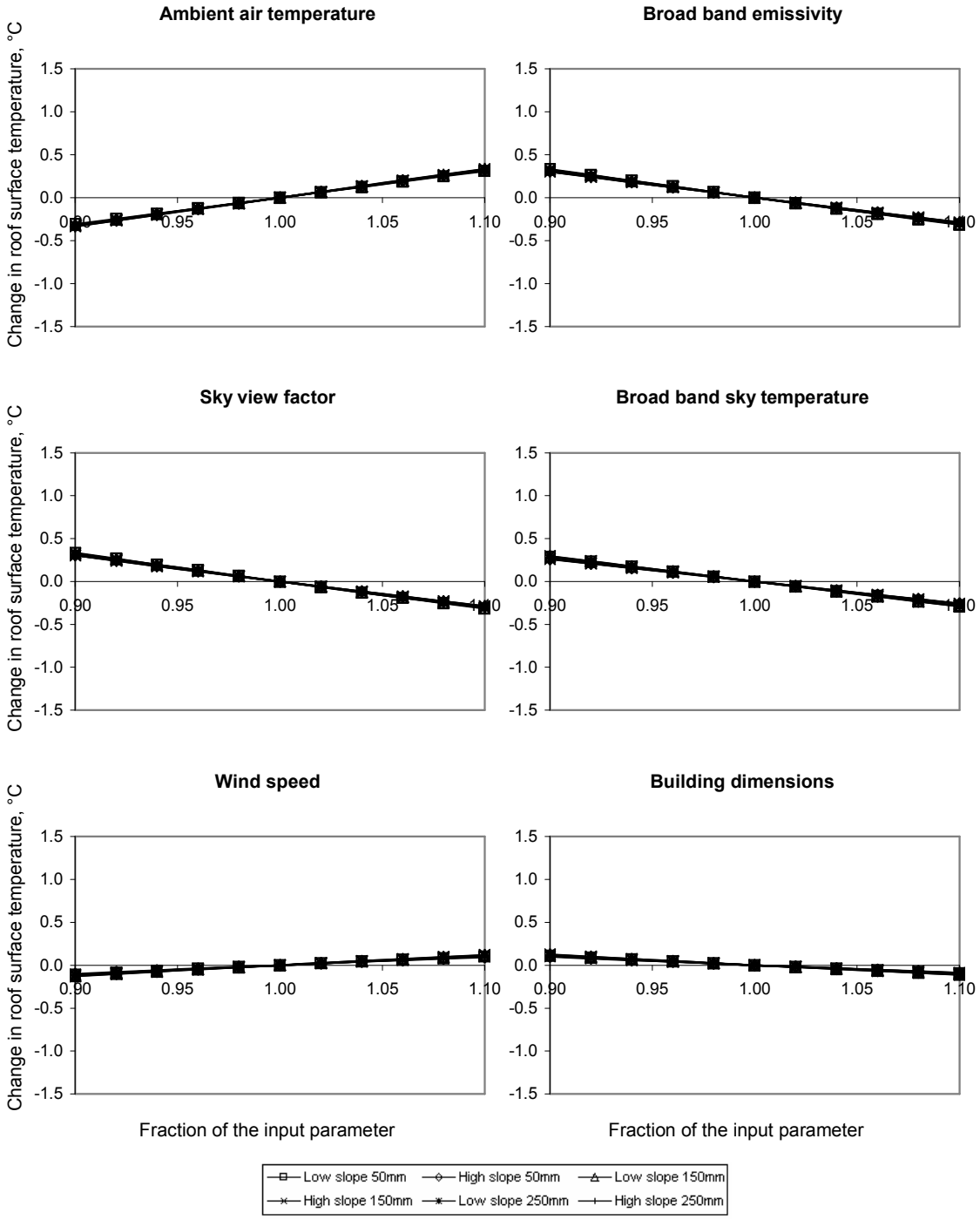

Figure 9-6: Graphical results for sensitivity of the building model

Table 9-5: Sensitivity of the building model results for a high slope, clay tiled roof

High slope clay tiled	Temperature change per percentage error in input, °C/%						
	End-terrace			Mid-terrace			
Parameter	50mm	150mm	250mm	50mm	150mm	250mm	average
Ambient air temperature	0.033	0.033	0.033	0.032	0.033	0.033	0.03
Broad band emissivity	-0.030	-0.030	-0.029	-0.031	-0.031	-0.031	-0.03
Sky view factor	-0.030	-0.030	-0.029	-0.031	-0.031	-0.031	-0.03
Broad band sky temperature	-0.026	-0.026	-0.026	-0.027	-0.028	-0.028	-0.03
Wind speed	0.010	0.011	0.011	0.010	0.011	0.011	0.01
Building dimensions	-0.009	-0.010	-0.010	-0.009	-0.009	-0.010	-0.01
Building internal temperature	0.006	0.002	0.001	0.006	0.002	0.001	0.003
Roof slope	-0.007	-0.005	-0.004	-0.007	-0.004	-0.003	-0.005
Insulation thickness	-0.004	-0.002	-0.001	-0.004	-0.002	-0.001	-0.002
Loft space air changes	0.000	0.001	0.001	0.001	0.001	0.001	0.001
Background temperature	0.0007	0.0005	0.0004	0.0006	0.0003	0.0002	0.0004

Table 9-6: Sensitivity of the building model results for a low slope, slate tiled roof

Low slope slate tiled	Temperature change per percentage error in input, °C/%						
	End-terrace			Mid-terrace			
Parameter	50mm	150mm	250mm	50mm	150mm	250mm	average
Ambient air temperature	0.031	0.032	0.032	0.030	0.031	0.031	0.03
Broad band emissivity	-0.032	-0.032	-0.032	-0.034	-0.033	-0.033	-0.03
Sky view factor	-0.032	-0.032	-0.032	-0.034	-0.033	-0.033	-0.03
Broad band sky temperature	-0.029	-0.029	-0.029	-0.031	-0.031	-0.031	-0.03
Wind speed	0.011	0.012	0.012	0.011	0.012	0.012	0.01
Building dimensions	-0.010	-0.011	-0.012	-0.010	-0.011	-0.012	-0.01
Building internal temperature	0.008	0.003	0.002	0.008	0.003	0.002	0.004
Roof slope	-0.001	0.000	0.000	-0.001	0.000	0.000	-0.001
Insulation thickness	-0.005	-0.003	-0.002	-0.005	-0.003	-0.002	-0.003
Loft space air changes	0.000	0.001	0.001	0.000	0.001	0.001	0.001
Background temperature	0.0003	0.0003	0.0003	0.0002	0.0002	0.0002	0.0003

9.2.3 Sensitivity to background temperature

The sensitivity of the result to background temperature was investigated further. The average sensitivity of the sensor and building models to background temperature was 0.04°C/% and 0.0004°C/% respectively for the high slope, clay tiled roof (see Table 9-3 and Table 9-5). If we assume that roof surface temperature is 0.5°C (somewhere between the temperatures for a mid and an end-terrace with 150mm of insulation see Table 9-1), a one percent error in background temperature produces little change in the roof surface temperature calculation. However, as we do not know the true value of background temperature, it might be much higher, due to warmer surrounding buildings. If the true effective background temperature was 1°C, which seems reasonable, the error would be 100%. Assuming the continued linearity of the sensitivity coefficients, this would produce an error in the calculated roof surface temperature of 4°C and 0.04°C for the sensor and building models, respectively.

The sensor model is obviously very sensitive to background temperature and without better knowledge of its true value it is predicted that it will be difficult to calculate roof surface temperature from the thermal image with any accuracy, for these houses and under these conditions.

The sensitivity analysis was limited in that interactions between parameters were not modelled and the results were not related to the actual error values in parameters. However, it provided an understanding of the important parameters and more effort was put into defining those parameters to which the result was most sensitive, where possible. To model the interaction between parameters using realistic error values, and to predict the overall error in the result of the models, an uncertainty analysis was carried out.

9.3 Uncertainty analysis

Uncertainty analysis was used to predict the magnitude of the total error in the results of this study using a Monte Carlo simulation method. This was achieved by repeatedly running the sensor and building models, altering each input parameter by a random function at each run. The random function was determined from the statistical uncertainty in the input parameter

and followed a Gaussian (normal) distribution. The resulting output also followed a Gaussian distribution. The advantage of the Monte Carlo method is that the model is simply a 'black box'. Only the inputs and outputs are considered and the technique is readily applied to many complex modelling situations. The simulation process is shown in Figure 9-7.

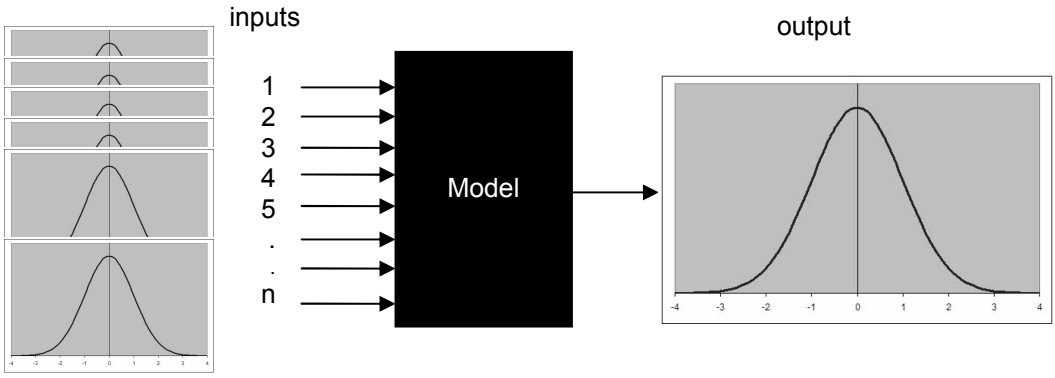

Figure 9-7: Diagram of the Monte Carlo simulation process

Uncertainty analysis has been used in other studies. For Calspan/Rochester Institute of Technology, Snyder and Schott [95] propagated errors by simulation. While the method is not described, the results demonstrated that the output was very sensitive to emissivity, external convection coefficient, broadband sky temperature, roof pitch and ambient air temperature. Steps were taken to minimise the error in those inputs. The standard deviation of the overall error was reported to be relatively constant and the results, therefore, more accurate for poorly insulated structures. In his book on remote sensing, Schott [101] describes error propagation using a calculation method, by summation of error differentials and mentions the use of Monte Carlo simulation methods.

Elsewhere, studies quantifying the uncertainty of temperature measurements by thermal infrared cameras, on the ground, were carried out. Chrzanowski et al. [159] looked at the intrinsic uncertainty of thermal cameras based on only the internal error sources. These included detector noise and non-linearity, stability of the cooling system, effect of temperature changes on optics transmission and self emission, electrical stability of the pre-amplifier, and the limited resolution and linearity of the analogue to digital converter. Parameters were defined for characterising the internal uncertainties. Calculations gave a standard uncertainty

of 0.73°C (one standard deviation) based on some assumed values for a typical camera with a measurement error of ± 1°C. Chrzanowski et al. [160] presented a mathematical model for the calculation of uncertainty of temperature measurements made with thermal infrared cameras based on the intrinsic uncertainty of the camera, and the uncertainties in the external measurement conditions of emissivity, background temperature and atmospheric transmittance.

Chrzanowski [161] reduced the number of parameters required for the intrinsic uncertainty calculation from seven to four and presented equations and a software package developed to carry out the calculation of the uncertainty of a temperature measurement made using an infrared camera. The probability distributions of the errors in the emissivity, background temperature and atmospheric transmittance were estimated from the bounds of the parameters as shown in Equation 9-1. This is the same as the rectangular distribution described in BSI [102] where there is an equal probability of the value being anywhere in the range. This gave a larger error distribution than assuming a 99% confidence interval with a Gaussian distribution where the value has a greater probability of being near the mean.

$$u(\mathrm{var}) = \frac{\Delta\,\mathrm{var}}{\sqrt{3}} \qquad \textbf{(9-1)}$$

u(var) standard uncertainty in the parameter

Δvar difference between upper bound and lower bound values of the parameter

Standard uncertainty for a rectangular distribution

The analysis of uncertainty has also been pursued in building simulation and design. MacDonald and Strachan [162] reported on applying both sensitivity analysis and Monte Carlo analysis to identify both the most important parameters and the uncertainty in the result respectively. For the sensitivity analysis, they simply used an upper and lower bound for each parameter, assuming linearity between. For the Monte Carlo analysis, they used 60 to 80 runs with each input parameter being perturbed by a random amount for each run. The probability distribution of the error was considered Gaussian for most parameters.

Wit and Augenbroe [163] examined the effect of uncertainty in building simulation on design decisions. They also assumed Gaussian distributions for the input parameters and their range was assumed to be the 95% confidence intervals or ± 2 standard deviations. Wind pressure and indoor air temperature were identified as the most important parameters by sensitivity analysis and additional effort was expended on determining their statistical distribution. Monte Carlo analysis was used to determine the uncertainty in the thermal comfort calculation for a model room using 500 runs. The uncertainty was found to be relatively large and this was deemed important to decision making in a design process. They concluded that uncertainty should be included with the results of all building analysis. Both of the above stressed the limited data available on the statistical distribution of the input parameters.

BSI's [102] published document provided a simple process for evaluating uncertainty for metrology applications. It included guidance on assessing the magnitude of the uncertainty in each input parameter and methods for calculating sensitivity coefficients, by partial derivatives or numerically, combining those coefficients analytically and expressing the resultant uncertainty with a confidence level.

For this study, the error in each of the input parameters was expressed as a standard uncertainty of a normal distribution based on BSI [102]. Two distinct scenarios were considered for the uncertainty analysis. The first scenario was the quantitative analysis of the insulation level of houses across a city where changes in the micro-climate, building materials and style lead to uncertainty in all of the input values. The second scenario was for qualitatively comparing the results of houses that are geographically close to each other and of the same style. Here the errors in the atmospheric parameters were ignored as the microclimate was assumed to be the same over the small area and absolute values are less important as the houses are being compared with each other. The standard uncertainty of each parameter is summarised in Table 9-7 for the two scenarios. Theses values were derived in the preceding Chapters.

Table 9-7: The standard uncertainty in each parameter for the two scenarios

Parameter	Standard uncertainty		Units
	Scenario 1	Scenario 2	
Sensor output	1.3	1.3	-
Distance from flight line	0.4	0.4	m
Building orientation	0.8	0.8	°
Building length	0.04	0.04	m
Building width	0.04	0.04	m
Roof slope	0.4	0.4	°
Sky view factor	0.02	0.02	-
Spectral emissivity	0.003	0.003	-
Broad band emissivity	0.003	0.003	-
Ambient air temperature	0.4	-	°C
Wind speed	0.5	-	m/s
Building internal temperature	0.8	0.8	°C
Loft space air changes	0.8	0.8	per hour
Insulation thickness	6	6	mm
Upwelled radiance	0.07	-	W/m2
Atmospheric transmission	0.016	-	-
Downwelled radiance	0.14	-	W/m2
Broadband sky temperature	1.2	-	°C

The background temperature was assumed the same as the roof surface temperature and systematic errors ignored. The relationship between ambient air temperature and the temperature of atmospheric layers for the calculation of atmospheric transmission and upwelled radiance was not modelled. All of the internal parameters (e.g. thermal conductivity of insulation) for both models were assumed exact. It was predicted that the result would give a conservative estimate of the uncertainty rather than overestimating the value.

For each run of the models, each input parameter was perturbed by a random amount of error using the 'randn' function in MATLAB. This function produced a normal distribution with a mean of zero, variance of one and standard deviation of one. Each parameter was therefore calculated from Equation 9-2.

$$var' = var + (u(x) \times randn) \quad \textbf{(9-2)}$$

var′	new value of the parameter
var	initial value of the parameter
u(x)	standard uncertainty of the input parameter
randn	MATLAB function to generate Gaussian distribution

Calculation of the new value for each variable

For each of the 12 test houses, within the two scenarios, 1000 variations of the inputs were generated and roof surface temperature calculated using both the sensor and building models to give 1000 results from each. This was found to give a reasonable normal distribution in the result for each house, as shown in the histogram in Figure 9-8, without being computationally expensive.

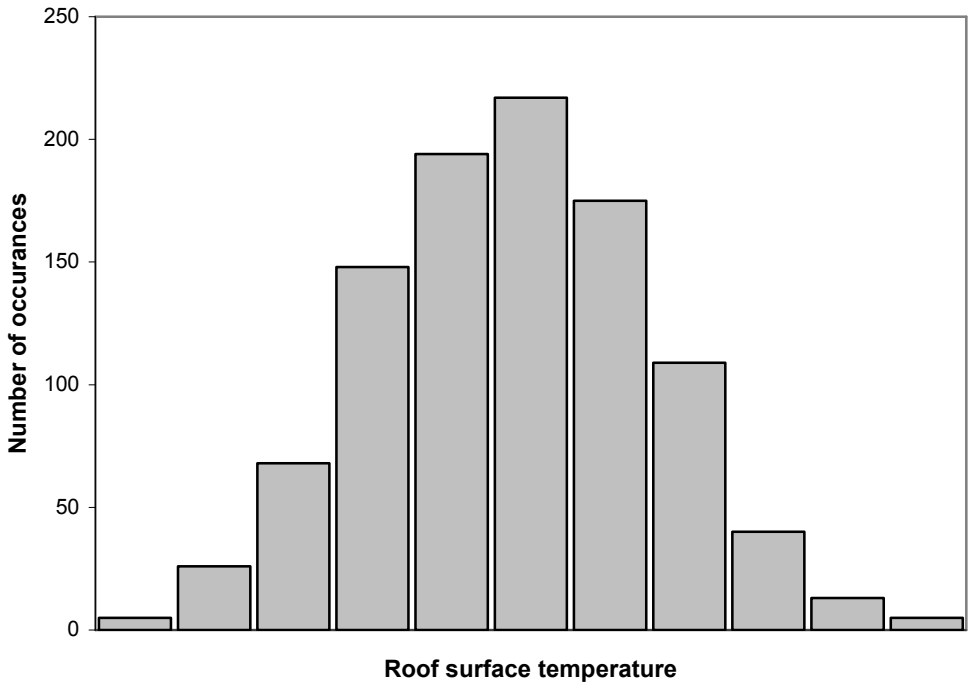

Figure 9-8: Typical frequency histogram for the sensor model output

Additionally, for each run, the difference between the sensor output and the building model output was calculated. This residual error between the two temperatures represented the potential error in a survey result based on the same incorrect data being used in both the

sensor and building models. The error in each parameter was therefore the same for each model in each run. The results for different runs were not compared as, for example, the sky view factor input to the sensor model could be at the maximum of the confidence interval while at its minimum for the building model. The standard deviations of these results was used to define the expanded uncertainty (99% confidence interval) from Equation 9-3 after BSI [102]. This expanded uncertainty gave the interval about the result in which the true value must lie with 99% confidence.

$$U(x) = ku(x) \quad \textbf{(9-3)}$$

U(x) expanded uncertainty (confidence interval)

k statistical coverage factor = 2.58 for 99% confidence interval

u(x) standard uncertainty

Expanded uncertainty

The range of possible insulation levels was then determined from the uncertainty in the residual by finding the equivalent depth of loft insulation required to give roof surface temperatures at either end of the confidence interval. For example if the roof surface temperature was 2°C and the expanded uncertainty of the residuals ± 0.5°C, the loft insulation level (mm) required to give roof surface temperatures of 1.5°C and 2.5°C was determined. The values >10^6mm and <0mm were used for thicknesses that were outside of the limits of the model. These results provided an indication of whether aerial thermography could be used to discriminate insulation level, in each scenario and for the houses considered.

9.3.1 Scenario 1

The first scenario was for the quantitative analysis of houses geographically displaced across a city where changes in the microclimate, building materials and style produced uncertainty in all of the input values. The standard error in each input parameter is given in Table 9-7 and the results are shown in Table 9-8 for the high sloped, clay tiled test houses and Table 9-9 for the low sloped, slate tiled test houses.

Table 9-8: Scenario 1- uncertainty for a high slope clay tiled roof

	Expanded uncertainty (99% confidence interval) , ± °C						
	End-terrace			Mid-terrace			
	50mm	150mm	250mm	50mm	150mm	250mm	average
Sensor model uncertainty	2.67	2.64	2.70	2.66	2.75	2.62	2.7
Building model uncertainty	1.18	1.15	1.18	1.20	1.20	1.20	1.2
Residual uncertainty	2.98	2.85	2.95	2.94	3.03	2.86	2.9
	Equivalent insulation level interval						units
Roof surface temperature	0.92	0.59	0.51	0.66	0.33	0.24	°C
Minimum insulation	< 0	< 0	< 0	< 0	< 0	< 0	mm
Maximum insulation	$> 10^6$	$> 10^6$	$> 10^6$	$> 10^6$	$> 10^6$	$> 10^6$	mm

Table 9-9: Scenario 1- uncertainty for a low slope slate tiled roof

	Expanded uncertainty (99% confidence interval) , ± °C						
	End-terrace			Mid-terrace			
	50mm	150mm	250mm	50mm	150mm	250mm	average
Sensor model uncertainty	2.62	2.58	2.64	2.61	2.64	2.64	2.6
Building model uncertainty	1.22	1.28	1.24	1.25	1.31	1.32	1.3
Residual uncertainty	2.94	2.87	2.93	2.91	2.92	3.00	2.9
	Equivalent insulation level interval						units
Roof surface temperature	0.66	0.23	0.12	0.37	-0.08	-0.21	°C
Minimum insulation	< 0	< 0	< 0	< 0	< 0	< 0	mm
Maximum insulation	$> 10^6$	$> 10^6$	$> 10^6$	$> 10^6$	$> 10^6$	$> 10^6$	mm

Based on the 99% confidence interval, the uncertainties in the sensor model, building model and residual were consistent for each test house. The uncertainty in the sensor model was ± 3°C (one significant figure), the uncertainty in the building model was ± 1.2°C and the uncertainty in the residual was ± 3°C (one significant figure). Determining the insulation level for each roof at the two extremes of temperature, based on the expanded uncertainty of the residual, produced a 99% confidence interval: 0mm > insulation level > 10^6mm. Therefore, for the Nottingham case study and for the housing style described, the uncertainty analysis predicts that aerial thermography cannot be used to determine the insulation level of houses across the city.

9.3.2 Scenario 2

The second scenario was for qualitatively comparing the results of houses that were geographically close to each and the errors in the atmospheric parameters were ignored. This would also represent the case where the local meteorological conditions have been measured precisely and the atmosphere has been characterised exactly. The standard error in each input parameter is given in Table 9-7 and the results are shown in Table 9-10 for the high sloped, clay tiled test houses and Table 9-11 for the low sloped, slate tiled houses.

Table 9-10: Scenario 2- uncertainty for a high slope clay tiled roof

	Expanded uncertainty (99% confidence interval) , ± °C						
	End-terrace			**Mid-terrace**			
	50mm	**150mm**	**250mm**	**50mm**	**150mm**	**250mm**	**average**
Sensor model uncertainty	0.41	0.43	0.42	0.41	0.42	0.43	0.4
Building model uncertainty	0.19	0.16	0.17	0.20	0.18	0.21	0.2
Residual uncertainty	0.50	0.51	0.49	0.50	0.49	0.52	0.5
	Equivalent insulation level interval						**units**
Roof surface temperature	0.92	0.59	0.51	0.66	0.33	0.24	°C
Minimum insulation	14	30	40	14	35	45	mm
Maximum insulation	1400	$> 10^6$	$> 10^6$	343	$> 10^6$	$> 10^6$	mm

Table 9-11: Scenario 2- uncertainty for a low slope slate tiled roof

	Expanded uncertainty (99% confidence interval) , ± °C						
	End-terrace			**Mid-terrace**			
	50mm	**150mm**	**250mm**	**50mm**	**150mm**	**250mm**	**average**
Sensor model uncertainty	0.40	0.40	0.41	0.40	0.40	0.40	0.4
Building model uncertainty	0.22	0.14	0.14	0.22	0.15	0.16	0.2
Residual uncertainty	0.48	0.44	0.43	0.47	0.45	0.46	0.5
	Equivalent insulation level interval						**units**
Roof surface temperature	0.66	0.23	0.12	0.37	-0.08	-0.21	°C
Minimum insulation	17	58	73	18	58	58	mm
Maximum insulation	168	$> 10^6$	$> 10^6$	158	$> 10^6$	$> 10^6$	mm

Based on the 99% confidence interval, the uncertainties in the sensor model, building model and residual were consistent for each test house. The uncertainty in the sensor model was ± 0.4°C, the uncertainty in the building model was ± 0.2°C and the uncertainty in the residual was ± 0.5°C.

Determining the insulation level for each roof at the two extremes of temperature, based on the uncertainty of the residual, demonstrated the 99% confidence interval depended on the insulation thickness. As the uncertainty was constant, the results were more accurate for poorly insulated structures. For houses with 150mm or more loft insulation, the upper limit was 10^6mm. The lower limit varied between 14mm and 73mm. For the Nottingham case study and for the housing style described, the uncertainty analysis predicts that aerial thermography cannot be used to compare the results of houses even when meteorological uncertainties are ignored, though some houses with very low insulation may be evident.

From these results, it seems unlikely that aerial thermography will be able to discriminate insulation levels, for these housing styles and under these conditions. How these results relate to the data collected for the Nottingham survey is discussed in the next chapter.

9.4 Conclusions

Parameters were defined for a number of test houses that were representative of the houses analysed for the Nottingham case study in Chapter 10. These parameter sets were used to examine the effect of input errors on the results of the building and sensor models that were developed for this study.

A one-at-a-time sensitivity analysis was carried out, varying each input parameter while all others maintained their initial value. The results were found to be linear and sensitivity coefficients were defined that described the change in the calculated roof surface temperature per one percent change in that input parameter. It was found that the sensor model was particularly sensitive to error in atmospheric transmission, emissivity of the roof material and atmospheric upwelled radiance. The sensitivity coefficients were lower for the building model.

The sensitivity analysis was limited in that relationships between variables were not considered and the sensitivity coefficient depended, to some extent, on the magnitude and units of each input parameter. However, the sensitivity of the model to background temperature suggested that assumptions made when developing the sensor model may not be valid.

An uncertainty analysis was carried out, to predict the uncertainty in the results of the sensor and building models, using a Monte Carlo simulation method. Two scenarios were considered. For quantifying the insulation level of houses of different styles and geographic locations across a city the expanded uncertainty (99% confidence interval) in the calculated roof surface temperature for any given insulation level was ± 3°C which equated to 0mm < insulation level < 10^6mm . Completely ignoring the uncertainty in the local meteorological conditions and the atmospheric parameters, the expanded uncertainty (99% confidence interval) in the calculated roof surface temperature for any given insulation level was ± 0.5°C.

As the difference in roof surface temperature between a house with only 50mm of loft insulation and a house with 250mm is only about 0.5°C, the insulation level of these houses could not be discriminated adequately. It was predicted that the uncertainty results were conservative and the actual error would be larger for a real data set.

In the next chapter, the Nottingham case study is described in more detail and the results analysed and compared.

10 Case study of Nottingham

This chapter describes the case study that was carried out for this study, using the aerial thermography data flown over Nottingham. Trial areas were selected for analysis and the results were calculated by both the sensor and building models for each Council owned house in those areas. The roof surfaces temperatures calculated from the thermal image, by the sensor model, were assessed by examining their statistical uncertainty and compared with the roof surface temperatures calculated, by the building model, from the known insulation thicknesses.

10.1 Trial areas

Council owned houses in small trial areas of the city were chosen for the Nottingham case study to determine if loft insulation level could be discriminated from the aerial thermography data. In their qualitative analysis of the Nottingham data set, Adepoju et al. [8] had identified an interesting anomaly whereby Northwood Terrace in Edwards Lane and Eltham Drive in Bells Lane had very similar housing but different appearance on the thermal image. Based on the roof averaged sensor output, Northwood Terrace appeared 'warmer' while Eltham Drive was 'colder'. The houses on North West (NW) Eltham Drive were identified as having a lower pitch roof than those on South East (SE) Eltham drive and Northwood terrace but otherwise identical construction (they also had different roof tiles). The three areas on these two roads were selected for the case study as the style of housing was also particularly prevalent in Nottingham and a suitable number of the properties were owned by the council and appeared on their database of insulation levels.

Fenwick Road, on the Broxtowe estate neighbouring Eltham Drive was also selected, as a large number of the houses were council owned, reasonably well insulated (200mm) and had the same housing style. This provided four trial areas with differences in location, roof slope, roof material and insulation thickness but otherwise similar housing. Of the 96 houses listed on the Council database, about half (54) had more than 175mm of insulation which made this

a suitable sample for classifying the results by the confusion matrix described later. The location of the three roads is shown on the composite thermal image of the city in Figure 10-1.

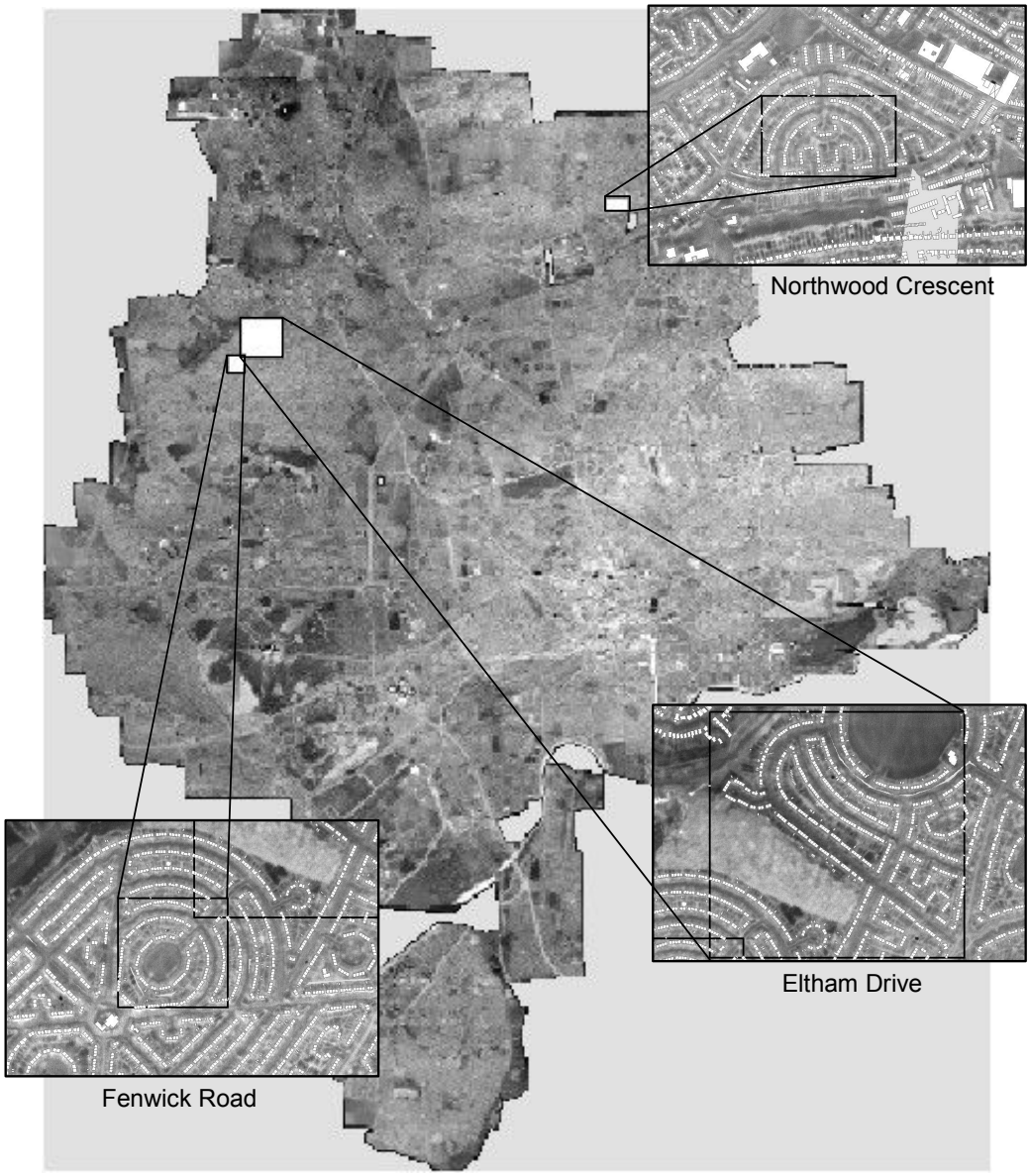

Figure 10-1: Location of the three roads on the composite thermal image of the city

From site visits, the buildings in each road were found to consist of blocks of two or four adjoined, brick built, two story houses. The roofs of the houses in NW Eltham Drive had a 1:3 pitch and slate tiles compared with the 1:1 pitch and clay tiles of the roofs in the other three areas. Photographs of typical houses are shown in Figure 10-2.

Northwood Crescent

NW Eltham Drive

SE Eltham Drive

Fenwick Road

Figure 10-2: Photographs of the housing in the four trial areas

The loft insulation thickness of council owned properties in each area was taken from the Council housing database. The characteristics of the housing in each area are summarised in Table 10-1.

Table 10-1: Characteristics of the housing in the four trial areas

Trial area	District	Number of houses	Date built	Insulation levels	Roof pitch	Tile material
Northwood Terrace	Edwards Lane	9	1936-7	75mm 100mm 150mm	1:1	Clay
NW Eltham Drive	Bells Lane	9	1933-5	150mm	1:3	Slate
SE Eltham Drive	Bells Lane	15	1933-5	150mm	1:1	Clay
Fenwick Road	Broxtowe	63	1937-9	75mm 100mm 200mm	1:1	Clay

10.2 Results

The address of each council owned house in each trial area was entered into a Microsoft Excel spreadsheet, along with data from the GIS analysis and site survey, materials properties, weather data, building data and the insulation level from the Council housing database. The inputs are summarised in Table 10-2. In addition the sensor model required a text file of the peak normalised spectral response function of the sensor, shown in Appendix 1 and the atmospheric radio sounding data in an excel spreadsheet, shown in Appendix 2.

These data were processed using MathWorks MATLAB software for the building and sensor models and MODTRAN 4.0 to calculate atmospheric properties. The results were written back to the spreadsheet and the inputs and results for each house are given in Appendix 4. Further analysis and graphing was carried out in the spreadsheet software. The results are described below, before any analysis (raw data), as roof surface temperatures calculated from the raw

data by the sensor model and as roof surface temperatures calculated from the known insulation level (recorded in the Council housing database) by the building model.

Table 10-2: Summary of the input parameters

Parameter	Units
Address	-
Average sensor output	digital number
Distance from flight line	m
Building orientation	degrees
Building length	m
Building width	m
Roof slope	degrees
Building type	1=end, 2=mid
Sky view factor	-
Spectral emissivity	-
Broadband emissivity	-
Ambient air temperature	°C
Wind speed	m/s
Building internal temperature	°C
Loft space air changes	per hour
Loft insulation thickness	mm

10.2.1 Raw data

The raw unprocessed thermal image data are shown in Figure 10-3 as, the averaged sensor output for each house (within the building buffer) against the insulation level recorded in the Council housing database. It can be seen from the graph that there was a range of averaged sensor outputs at each insulation level. As these ranges overlapped, they could not be used to infer the insulation level. The houses in NW Eltham had a noticeably lower averaged sensor output. The sensor model was used to calculate the roof surface temperature of each house from these data.

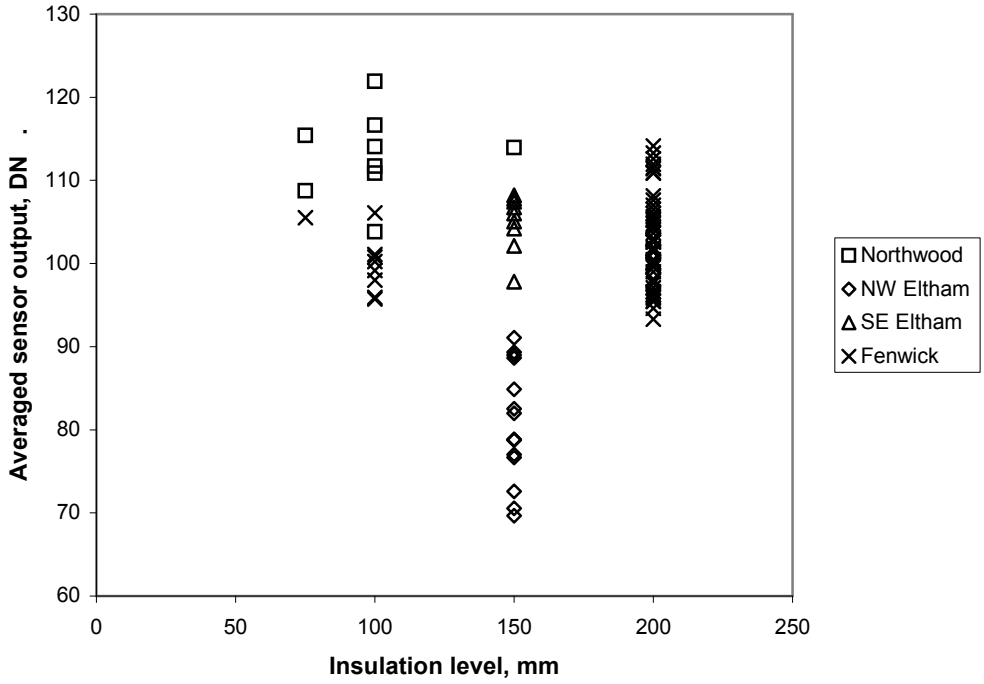

Figure 10-3: Unprocessed thermogram data- averaged sensor output against insulation level

10.2.2 Sensor model

The results for the sensor model are shown in Figure 10-4 as the roof surface temperature, calculated by the sensor model for each house, against the insulation level recorded in the Council housing database. It can be seen from the graph that there was also an overlapping range of roof surface temperatures at each insulation level for these calculated results. The houses in NW Eltham Road had a noticeably lower roof surface temperature as predicted from the raw thermal image. The building model was used to calculate the roof surface temperature for each of these houses based on the level of insulation recorded in the Council housing database.

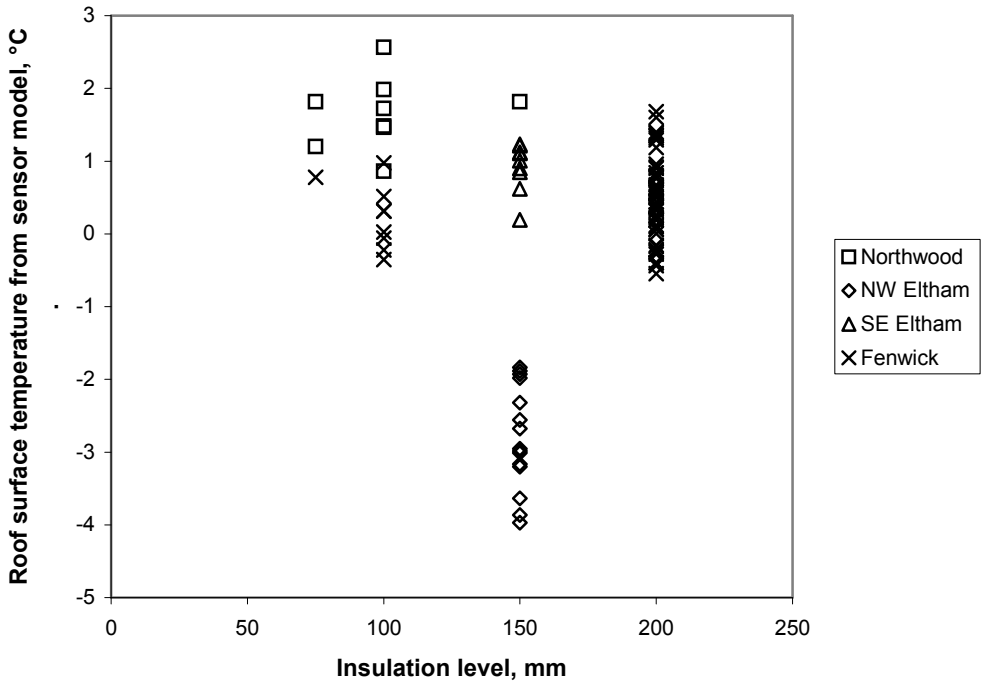

Figure 10-4: Sensor model results- roof surface temperature against insulation level

10.2.3 Building model

The results for the building model are shown in Figure 10-5 as, the roof surface temperature, calculated by the building model, for each house against the insulation level recorded in the Council housing database. It can be seen from the graph that roof surface temperature alone was not a reliable indicator of insulation level as, for example, some of the houses with 200mm of insulation had warmer roofs than those with only 100mm. The results predicted that the houses with lower pitch roofs have lower roof surface temperatures than the higher pitched roofs. However, the temperatures of these roofs were not as low as calculated from the thermal image using the sensor model.

From the results of the sensitivity analysis of the building model in Chapter 9.3.2, it was inferred that the higher sky view factor and higher emissivity of the roofs in NW Eltham Road would produce significantly lower roof surfaces temperatures, as there was more radiant heat exchange with the cold night sky. However, the lower pitch (66% lower) of these roofs acted to increase the surface temperatures. From examination of the results of the model, this was

because the surface area was smaller, resulting in less convective heat gain but reducing the radiative losses to a greater extent. The net effect of all these parameters was a small reduction in roof surface temperature. The larger reduction in roof surface temperature, seen in the sensor model results (Figure 10-4) for NW Eltham Drive, cannot be described by the results of the building model.

During the site surveys, it was noted that the NW half of Eltham drive was in a considerable ground depression. The downward slope of the road can be seen in the photographs in Figure 10-2. As cool air pools, air temperatures may be lower in this depression, convective heat gains at the surface would be lower and roof surface temperatures lower. Without on-site temperature measurements, taken during similar weather conditions, this is difficult to quantify but may explain the colder roof surface temperature calculated for houses in that area.

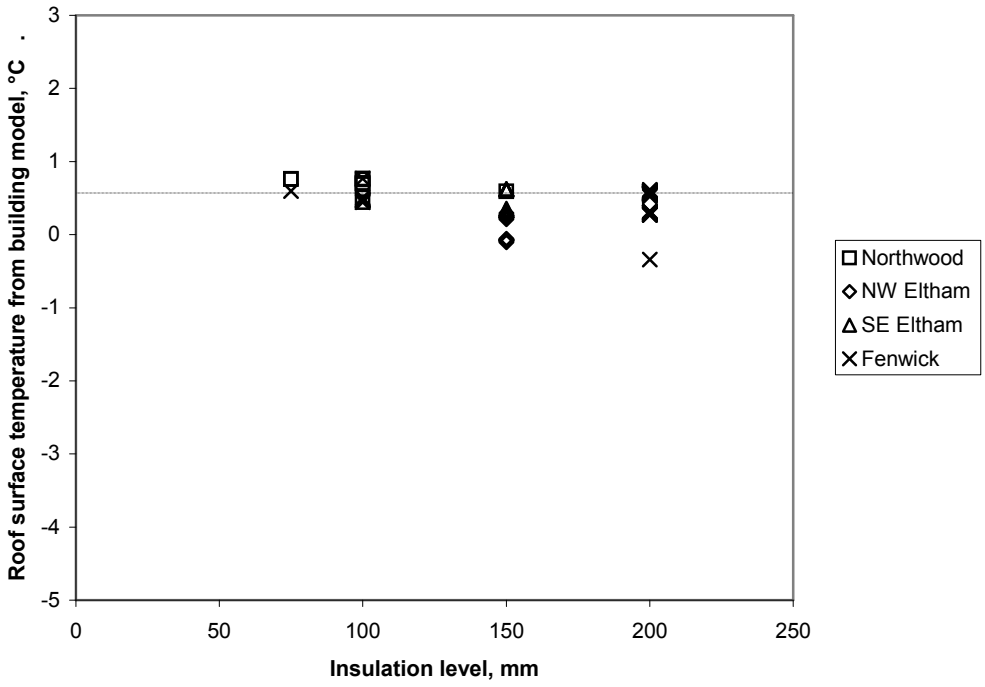

Figure 10-5: Building model results- roof surface temperature against insulation level

10.2.4 Comparison of the two models results

The results of the sensor model were plotted against those from the building model, for each house in the case study, as shown in Figure 10-6. It can be seen from the graph that there

are large discrepancies in the results. The distance of each point from the dashed line indicates the magnitude of the error for that house. These residual errors were assessed along with the overall results.

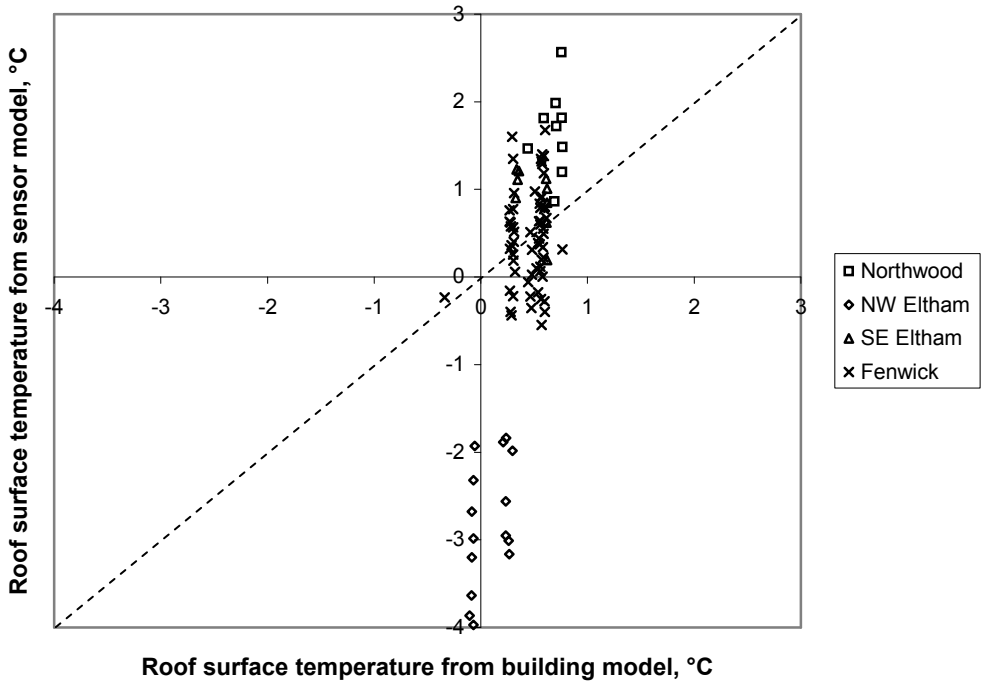

Figure 10-6: Comparison of the results from the two models

10.3 Assessment of the results

The results were assessed by their statistical uncertainty and by comparison with ground truth data of actual insulation level.

10.3.1 Uncertainty

The results were analysed to find the magnitude of the error from the difference between the roof surface temperatures calculated by the sensor and building models. The average of this residual, for each area, along with the standard uncertainty (standard deviation) and the expanded uncertainty (99% confidence interval) are shown in Table 10-3. The expanded uncertainty was calculated after the methods set out by BSI [102] as shown in Equation 9-3.

The average residual for houses on Fenwick road is zero because they were used for defining the temperature window in the back calibration of the sensor as described in Chapter 4.2. For the other areas, the average residual suggested a bias in the error. The calculated standard uncertainty for each area (and therefore the 99% confidence interval) does not consider the bias.

Table 10-3: Statistical analysis of roof surface temperatures calculated by sensor and building models

Trial area	Roof surface temperature, °C		
	Average residual	Standard uncertainty	99% confidence interval
Northwood Terrace	-0.97	0.48	± 1.3
NW Eltham Drive	2.87	0.65	± 1.7
SE Eltham Drive	-0.42	0.43	± 1.1
Fenwick Road	0.00	0.54	± 1.4
Overall	0.32	1.26	± 3.3

From the uncertainty analysis in Chapter 9, the expanded uncertainty (99% confidence interval), of the results for houses that were close together (no atmospheric uncertainties) was ± 0.5°C. From Table 10-3 the 99% confidence interval for each area is more than twice that prediction. This underestimation may be for a number of reasons. Optimistic uncertainty intervals were used for a number of parameters, as discussed in the relevant chapters. The internal temperature of empty (or overly heated) properties may fall outside of the 18 ± 2°C specified. The assumption that the background temperature was the same as the roof surface temperature reduced the sensitivity of the results to sky view factor and emissivity. There may be microclimate variations within each area, especially for long roads and those on sloping ground, as discussed in Section 10.3.3 for NW Eltham Drive.

From the uncertainty analysis in Chapter 9, the expanded uncertainty (99% confidence interval), for houses across the city, was ± 3°C as was the overall result from Table 10-3. However, as very similar styles of housing were chosen for the trial areas, this predicted uncertainty may also be optimistic. Some of the global phenomenon that were ignored

included the effect of the urban heat island on atmospheric transmission and upwelled radiation, dew formation on roof surfaces below the dew point and 'freeze out' for those roofs below the freezing point (see Section 3.2.2). In addition, the separate faces of each roof were not considered when calculating the emissivity line of sight angle, for the sensor model, and the sky view factor.

The results reinforced the conclusion that insulation level can not be discriminated from the Nottingham dataset, for this type of residential house with a ventilated pitched roof, either across the city or locally. To quantify the accuracy, the results of the sensor model were classified and compared with ground truth data using confusion matrices.

10.3.2 Confusion matrix

A confusion matrix, as shown in Figure 10-8, was used to assess the accuracy of the results by comparing them with the known insulation level of each house that was recorded in the Council housing database. The number of correct classifications, divided by the total number of houses indicated the success rate of the technique, given as a percentage.

		Calculated insulation thickness	
		<175mm	**>175mm**
Actual insulation thickness (council database)	**<175mm**	Correct	
	>175mm		Correct

Figure 10-7: Confusion matrix

This technique was used by Snyder and Schott [95], for Claspan/Rochester Institute of Technology. They reported a 79% success rate based on 32 structures and an R11 classification. The R11 threshold equates to a U-value of only about 0.5 or roughly 60mm of insulation for the houses considered in this study. To meet modern building regulations, 250mm of insulation is desirable and houses with less should be upgraded. Considering the

large uncertainty in the calculations, a threshold of 175mm was chosen for this study, as any houses with less than this amount should have their insulation upgraded.

For this study, the building model was used to calculate threshold temperatures for each house in the Nottingham case study, as if it had 175mm of loft insulation. Houses that had a roof surface temperature, calculated by the sensor model, that was warmer than their threshold temperature were classified as having less than 175mm of insulation and those that had one colder, more than 175mm.

These results were compared with the actual insulation level recorded in the Council housing database for each house using a confusion matrix for each of the four trial areas as shown in Figure 10-8. The percentage of correct classifications, shown under each matrix, varied due to the bias in the results that produced 100% correct classifications for NW Eltham Drive and 0% for Northwood Terrace. The results for Fenwick Road were not biased and produced only 57% correct classifications.

An analysis of the case study as a whole, shown in Figure 10-9, produced 54% correct classifications. This is little better than that a random classification would produce and therefore the results are indeterminate.

Calculated insulation thickness

Actual insulation thickness (council database)

	<175mm	>175mm
<175mm	0	9
>175mm	0	0

Northwood Terrace 0%

Calculated insulation thickness

	<175mm	>175mm
<175mm	15	0
>175mm	0	0

NW Eltham Drive 100%

Actual insulation thickness (council database)

	<175mm	>175mm
<175mm	1	8
>175mm	0	0

SE Eltham Drive 11%

	<175mm	>175mm
<175mm	6	3
>175mm	24	30

Fenwick Road 57%

Figure 10-8: Confusion matrices for individual areas

Calculated insulation thickness

Actual insulation thickness (council database)

	<175mm	>175mm
<175mm	22	20
>175mm	24	30

Total 54%

Figure 10-9: Confusion matrix for entire case study

10.4 Conclusions

96 houses in four trial areas were selected for the Nottingham case study. The four trial areas included houses in different locations with different roof pitch, roof material and insulation thickness, but were otherwise of a very similar style.

The roof surface temperature of each house was calculated using both the sensor and building models. Neither the raw data (averaged sensor output for each house), nor the sensor model results (roof surface temperature), could be used to infer loft insulation level.

From the building model, it was found that roof surface temperature alone was not a reliable indicator of loft insulation thickness as the roofs of well-insulated houses could be warmer than less-insulated ones.

Comparing the results of the sensor and building models for each house showed large residual errors in the roof surface temperature. From the residual for each house, expanded uncertainties (99% confidence interval) were found to be more than ± 1°C for each area in isolation and ± 3°C overall. These values confirmed the assumption that the prediction of the uncertainty analysis in Chapter 9 was optimistic and reinforced the conclusion that the insulation level of these residential houses with ventilated pitched roofs cannot be discriminated from the Nottingham dataset.

The sensor model results were classified into houses that had less than 175mm of loft insulation and those that had more. A confusion matrix was used to compare the classifications with the known insulation levels from the Council housing database. The sensor model produced only 54% correct classifications and the result was therefore indeterminate.

11 Discussion

For the Nottingham case study, it was not possible to discriminate the loft insulation level of houses with ventilated pitched roofs using aerial thermography data. In this chapter, means of reducing the uncertainty in the calculated results and the effect of the remaining errors are discussed, along with comments on applying the technique to houses in an entire city.

11.1 Reducing the uncertainty

The uncertainty in the results could be reduced by using a more accurate sensor, carrying out the survey under ideal weather conditions and measuring the local meteorological conditions at the time of the survey. These factors are discussed, and the resulting uncertainty calculated, to determine if this would enable discrimination of loft insulation level.

11.1.1 Sensor

The sensor system used for the Nottingham survey was typical of that used in other reported surveys. The digital output offered considerable advantage over analysing the brightness of photographic images as used into the 1980s but there was no calibration data (see Section 4.2.2) and the thermal image had been slightly modified by the BGS (see Section 3.2.2).

The state of the art in sensors is currently high-resolution thermal cameras with large format staring arrays. These are being used for aerial thermography roof moisture surveys in the United States with ground resolutions of around 150 mm [78]. A typical camera, the FLIR Phoenix™ 640x512 InSb camera can measure at 100 frames per second, has a noise equivalent temperature difference of better than 35milliKelvin and a 14-bit analogue to digital converter [11]. These sensors, though operating in the short wave wavelength band (1.5-5μm), offer obvious quality improvements over line scanning and may be linked with GPS, GIS and CAD systems for geographic registration and report generation [78]. The associated cost of surveys carried out with these sensors would be much higher because of the higher capital cost of the equipment and the additional overpasses needed to image an area due to the reduced image width.

11.1.2 Weather conditions

The weather conditions at the time of the survey are known to be important (see Section 3.2.2). Ambient air temperature, and wind speed, should be as low as possible to maximise heat loss, and minimise convection, at the surface, but suitable flying periods are limited. According to CIBSE [107], the average frequency of weather with wind speeds below 2m/s and temperatures below 0°C is only 1.04%, for Manchester, England. This equates to around 90 hours per year. For temperatures below -2°C, the frequency is 0.53% or only 46 hours. These may not be continuous periods or at suitable times and very few surveys could be flown under ideal weather conditions in the UK.

11.1.3 Uncertainty results

To estimate the uncertainty in the results of a survey, flown with a perfect sensor and under ideal weather conditions, the building model was run with new values of the meteorological input parameters. Ambient air temperature was set to -4°C and wind speed to 1m/s. The broadband sky temperature was calculated to be 246.5K using the ASHRAE Brown model (see Chapter 7.4) based on a partial pressure of water vapour of 0.22kPa for an assumed 50% relative humidity.

Identical mid-terraced test houses with 1:1 pitched roofs and clay tiles were defined as in Section 9.2. The houses had a range of insulation levels including 0mm (no insulation), 50mm (poorly insulated) and 250mm (well insulated). The resulting roof surface temperatures, calculated by the building model, are shown in Table 11-1. The difference in roof surface temperature between the well-insulated and poorly insulated houses was 0.83°C.

Table 11-1: Roof surface temperatures of the test houses

Insulation level	Calculated roof surface temperature, °C 1:1 pitch, clay tiles, Mid-terrace
0mm	-7.108
50mm	-9.474
100mm	-9.901
150mm	-10.126
200mm	-10.232
250mm	-10.296

The uncertainty in the results was predicted as described in Section 9.4 but with lower standard uncertainty values for the reduced wind speed and broadband sky temperature. The values for each of the input parameters are shown in Table 11-2. The expanded uncertainty (99% confidence interval) in the wind speed was ± 0.5m/s based on ± 50% as described in Section 6.2.2. The expanded uncertainty (99% confidence interval) in the broadband sky temperature was ± 5W/m^{2}K as suggested by Dilley and O'Brien [133] (see Section 7.4) which equated to ± 1.5K. The standard uncertainties, of 0.2m/s and 0.6°C respectively, were calculated after the method set out by BSI [102] (see Equation 5-2, k=2.58 for 99%).

Table 11-2: The standard uncertainty in each parameter for the ideal weather case

Parameter	Standard uncertainty	Units
Building length	0.04	m
Building width	0.04	m
Roof slope	0.4	°
Sky view factor	0.02	-
Broad band emissivity	0.003	-
Ambient air temperature	0.4	°C
Wind speed	0.2	m/s
Building internal temperature	0.8	°C
Loft space air changes	0.8	per hour
Insulation thickness	6	mm
Broadband sky temperature	0.6	°C

The uncertainty analysis was carried out for the house with 150mm of loft insulation. The standard deviation in the results of the building model was 0.44°C, which gave an expanded uncertainty (99% confidence interval) of ± 1.1°C. Therefore, the model predicts that it would not be possible to discriminate a poorly insulated (50mm) loft from a well-insulated (250mm) one with a perfect sensor and under ideal weather conditions.

To simulate the case where the broadband sky temperature was measured precisely, its standard uncertainty was set to zero and the uncertainty analysis carried out again. The resulting expanded uncertainty (99% confidence interval) in the result of the building model was still ± 1°C. Only by simulating the case where the local wind speed and air temperature were also known precisely (standard uncertainty set to zero for each) did the model predict that discrimination of a poorly insulated roof would be possible as the expanded uncertainty (99% confidence interval) in the result was ± 0.4°C. However, a roof with 100mm of insulation, which is still under-insulated, could not be discriminated, as the model predicted it would only be 0.4°C warmer (see Table 11-1).

These results suggest that an aerial thermography survey carried out with a perfect sensor and under ideal conditions with precise local meteorological measurements would not be able to discriminate insulation level beyond those houses that are very poorly insulated. As less than a third of all the homes in Nottingham have less than 50mm of insulation, and this number is falling year on year (see Section 1.2), the potential economic benefits of these results would be reduced. Households that do not have lofts (e.g. flats or room in roof lofts) and those that do not want loft insulation (~16% of council tenants refused see Section 1.2) would reduce effectiveness further.

11.2 Effect of the remaining errors

In the above example, the uncertainty in the building model results was reduced to the error in the input parameters of emissivity, sky view factor, building dimensions, building internal temperature, roof slope, insulation thickness, and the number of loft space changes. The average sensitivity coefficients for these parameters, for a 1:1 pitched, clay-tiled roof are

shown in Table 11-3, taken from the sensitivity analysis in Section 9.3. The standard uncertainty values are taken from the uncertainty analysis in Section 9.4 and the expanded uncertainty (99% confidence interval) was calculated after the methods set out by BSI [102] (see Equation 9-3, k=2.58 for 99%).

Table 11-3: Sensitivity of the building model results for a high slope, clay tiled roof

Parameter	value	sensitivity coefficient °C/%	Standard uncertainty	99% confidence interval	resulting temperature range
Broad band emissivity	0.881	-0.03	0.003	± 0.008	± 0.03°C
Sky view factor	0.734	-0.03	0.02	± 0.05	± 0.20°C
Building length	5.9m	-0.01	0.04m	± 0.1m	± 0.02°C
Building internal temperature	18°C	0.003	0.8°C	± 2°C	± 0.03°C
Roof slope	45°	-0.005	0.4°	± 1°	± 0.01°C
Insulation thickness	150mm	-0.002	6mm	± 15mm	± 0.02°C
Loft space air changes	$2hr^{-1}$	0.001	$0.8hr^{-1}$	$\pm 2hr^{-1}$	± 0.10°C

The resulting temperature error range was calculated as shown in Equation 11-1. From these results, it can be seen that the roof surface temperature calculated by the building model is especially sensitive to the error in the values of sky view factor and loft space ventilation rate. Perhaps surprisingly, the result is much less sensitive to error in the building's internal air temperature, demonstrating that the roof is thermodynamically decoupled from the inside of the house to a significant degree.

$$T_{range}(val) = \frac{CI}{val} \times 100\% \times SC \qquad \textbf{(11-1)}$$

T_{range}	resulting temperature range	[°C]
val	value of the parameter	
CI	confidence interval of the parameter	
SC	sensitivity coefficient of the parameter	[°C/%]

Calculation of the temperature range for Table 11-3

Sky view factor and loft space ventilation rate are difficult to measure precisely for the roofs of real buildings in a city. These results support the findings of Brown [54] who concluded that the difficulties in measuring ventilation rate (along with local wind speed and air temperature variations) made it impossible to model loft insulation level (see Section 6.3.1). For this study, difficulties in measuring the sky view factor of roofs and the effective background temperature (see Section 9.3.3) were also found to be significant barriers.

11.3 Application to an entire city

To apply the methods outlined in this thesis to aerial thermography data for an entire city would involve accurate data collection and a large amount of data processing. The new generation of sensors along with GPS technology and high resolution, three dimensional elevation maps could produce calibrated and geometrically corrected sensor data to a level previously unseen in this field. Simultaneous ground temperature and meteorological measurements would allow accurate calibration of the image chain. However, to relate these data to roof surface temperature and insulation level would still require a large amount of additional data for each house:

- effective emissivity of the roof surface
- effective sky view factor of the roof
- roof shape (size and geometry)
- roof construction
- loft space ventilation rate

The microclimate for each house would also be required:

- local ambient air temperature at roof level
- local wind speed at roof level
- effective background temperature
- effective sky temperature

The level of accuracy required for each of these parameters and the remaining systematic errors in the analysis may still prevent all but the most poorly insulated lofts from being

discriminated. It is suggested that, until dependable sources of these data are readily available, it would be easier (and cheaper) to measure the thickness of loft insulation in each house directly, on the ground. The council already record these data for their own housing stock and have the details of those privately owned houses that have been upgraded using grant funding.

The alternative to the quantitative analysis studied here would be to use these aerial thermography data purely quantitatively to publicise a citywide energy conservation campaign. This technique is already out of favour in the USA (see Section 2.2.1) as the technical basis of the results is questionable (see Section 2.2.2) and success depends more on the level of additional support than on the quality of the thermal image (see Section 2.2.3). The thermal image may be visually stimulating but it does not show heat loss or roof surface temperature and any reference to its analysis, even comparing similar houses, should be avoided. If the thermal image was made publicly available, problems could occur from misinterpretation, particularly if occupiers made complaints about the 'warm' appearance of the roof of their recently insulated house, for example.

11.4 Conclusions

The results of the simulation runs, carried out using the building model developed for this study, indicated that an aerial thermography survey, carried out with a perfect sensor, under ideal weather conditions and with precise measurements of local air temperature, wind speed and sky temperature, would only discriminate the most poorly insulated houses. The difficulties in measuring the sky view factor and loft space ventilation rate, in particular, were found to be significant barriers to accurately predicting roof surface temperature from the level of loft insulation.

Results could be improved by reducing the uncertainty in each of the input parameters and the systematic errors in the models used. This would mean large-scale data collection for every house in the city and to describe the local microclimate and model the atmosphere.

12 Conclusions

This thesis examined the use of aerial thermography data to discriminate loft (attic) insulation levels in residential housing with ventilated pitched roofs. The aim of this work was to develop and test a methodology for measuring insulation thickness using aerial thermography using the Nottingham dataset as a case study. To the author's knowledge, this is the first time a quantitative methodology has been applied to UK house styles and meteorological conditions.

A methodology for calculating roof surface temperature from, both, aerial thermography data and insulation level data was developed for this study. Existing techniques, from the literature, were combined in a new and unique way in an attempt to provide the most sophisticated and complete analysis to date. The methodology was tested by predicting the error in the results using a simulation and comparing results calculated from the thermal image with those calculated from the known insulation level, for houses in a case study of Nottingham. The prediction and the results of the case study supported the conclusion that the insulation level of residential houses with ventilated pitched roofs could not be discriminated from the Nottingham dataset.

Furthermore, the building model, developed for this study, was used to predict if aerial thermography could quantify insulation level in these houses under any conditions. Simulation runs indicated that a survey, carried out with a perfect sensor, under ideal weather conditions and with precise measurements of local air temperature, wind speed and sky temperature, would only discriminate the most poorly insulated houses.

Therefore, the aim of the work was accomplished. The key aspects of the methodology, the key observations made during its implementation and the inherent limitations and explicit assumptions made are summarised below along with an indication of those areas of this work that would benefit from further study in the future.

12.1 Methodology

The sensor model was developed for this study to determine roof surface temperature from the thermal image. A complete methodology was not found in the literature, but aspects were selected from different sources and combined into a complete model. That model incorporated:

- using a buffer inside building outlines to ensure only roof pixels were sampled (recommended Adepoju et al. [8])
- the Singh [105] method for calculating at-sensor radiance
- an equation for radiance reaching the sensor after Schott [101]
- assumption of background temperature after Goldstein [51]
- weighting all radiance terms by the peak normalised spectral response of the sensor after Schott [101]
- the Singh [105] approximation for relating temperature and roof blackbody radiance after Snyder and Schott [95]

The building model was developed for this study, to determine roof surface temperature from the thickness of loft insulation. Methodologies from an extensive literature review were combined, to produce an improved thermal model of the roof. The model incorporated:

- calculating the U-value of the ceiling and insulation after the method presented in the CIBSE guide [107]
- a standard radiative heat exchange, at the roof surface, with the sky and other background
- convective heat exchange, at the roof surface, using the ASHRAE detailed method as described by McClellan and Pedersen [119]
- an iterative loft space heat balance method, based on the work of Parker [110]
- radiative heat exchange at the loft space inside surfaces using a ‘mean radiant temperature network’ after Caroll (see Liesen and Pedersen [120])
- convective heat exchange at the loft space inside surfaces using a simple convection coefficient after Burch [55]
- a standard air heat balance using the loft space air change rate

To support the models:

- all the atmospheric properties were devised using an atmospheric propagation model after Schott [101]
- the emissivity of two representative roofing materials was measured
- the relationship between emissivity and line of sight angle was modelled after Snyder and Schott [95]
- sky view factor was determined, based on roof pitch
- broadband emissivity was assumed to be the same as the spectral emissivity as in many other studies

Some new methods were developed for this study:

- the sensor was back-calibrated against results of the building model and based on the brightness temperature range of the sensor
- the latest atmospheric propagation model, MODTRAN 4.0 was used in the place of the lower wavelength resolution LOWTRAN
- a cubic polynomial fit was introduced, to model the relationship between atmospheric transmission and upwelled radiance with sensor angle
- emissivity measurements were based on ASTM, E1933-99a [142] but using an oven to heat the sample after Madding [143] and a cardboard enclosure to reduce variations in background temperature after Daryabeigi [147]
- sky view factor was calculated using Rayman [151] software with the three dimensional coordinates of pitched roofs in a typical street formation
- broadband sky temperature was derived using an atmospheric propagation model after the method set out by Schott [101] for calculating downwelled radiance but over a wider frequency band after Dilley and O'Brien [133]

The results of different methods were compared, for calculating:

- convective heat exchange at the roof surface
- the loft space heat balance
- broadband sky temperature

- sky view factor

The results of the model were analysed using:

- a one-at-a-time sensitivity analysis as in many other studies
- an uncertainty analysis, by simulation as undertaken by Snyder and Schott [95], using a Monte Carlo method similar to MacDonald and Strachan [162] or Wit and Augenbroe [163]
- confusion matrices, as undertaken by Snyder and Schott [95]

For this study, the magnitude of the error in each of the input parameters was estimated for each of the input parameters and the Monte Carlo algorithm was developed from the basic principles.

12.2 Observations

A number of key observations were made during this study.

From a review of the literature, it was found that:

- in other studies, numerical models demonstrated that a great deal of additional data was needed for quantitative analysis and these data had to be known with considerable accuracy
- the only successful quantitative studies were reported by Calspan/Rochester Institute of Technology [62, 95] and their success was based, in part, on a low threshold of discrimination (about 60mm of insulation), relied on ground truth data taken at the time of the survey to 'tune' the results and used a small sample of houses to validate them

From the results of the building model developed for this study, it was found that:

- radiative losses to the cold night sky dominated the roof surface heat exchange and convection at the roof surface was a heat gain on cold, clear, calm nights

- ventilation of the loft space was found to be a heat gain to the system for all but the most poorly insulated houses modelled
- radiative heat exchange dominated the heat transfer in the loft space
- end terrace properties had warmer roofs than otherwise identical mid-terrace properties
- temperature differences between well insulated and poorly insulated ventilated pitched roofs were relatively small (0.5°C)

From an analysis of the errors by simulation, it was predicted that:

- the sensor model was particularly sensitive to error in atmospheric transmission, emissivity of the roof material and atmospheric upwelled radiance
- the sensitivity of the sensor model to background temperature indicated the assumption that background temperature was the same as roof surface temperature may not be valid
- the sensitivity coefficients were lower for the building model
- the 99% confidence interval in the calculated roof surface temperature for any given insulation level was ± 3°C, which equated to an insulation level between 0mm and 10^6mm
- therefore, insulation level could not be discriminated

Results of the Nottingham case study demonstrated that:

- neither the raw data (averaged sensor output for each house), nor the sensor model results (roof surface temperature), could be used to infer loft insulation level
- roof surface temperature alone was not a reliable indicator of loft insulation thickness as the roofs of well-insulated houses could be warmer than less-insulated ones
- there were large residual errors between the results for the sensor and building models for each house
- the expanded uncertainties (99% confidence interval) of these residuals were found to be ± 3°C overall

- this reinforced the conclusion that the insulation level of these residential houses with ventilated pitched roofs could not be discriminated from the Nottingham dataset
- the sensor model produced only 54% correct classifications and the result was therefore indeterminate

Further simulation runs carried out using the building model developed for this study, indicated that:

- an aerial thermography survey, carried out with a perfect sensor, under ideal weather conditions and with precise measurements of local air temperature, wind speed and sky temperature, would only discriminate the most poorly insulated houses
- difficulties in measuring the sky view factor and loft space ventilation rate, in particular, were found to be significant barriers to accurately predicting roof surface temperature from the level of loft insulation

To apply the technique to all the houses in a city would require:

- a large amount of additional data collection
- better understanding of the microclimate variations

There is no known source of these data at present.

12.3 Limitations and assumptions

There were a number of inherent limitations in the data collection and some explicit assumptions were made to simplify the analysis:

- weather conditions at the time of the Nottingham survey were not ideal
- the thermal image had poor contrast and geometric correction was inexact
- there was no calibration for the sensor
- weather observations and radio sounding data were taken at a weather station located 10km northeast of the city
- the effect of the urban heat island on microclimate was unknown
- the atmospheric modelling was not validated

- the background temperature was assumed to be the same as the roof surface temperature for each house
- the loft space heat balance ignored infiltration, temperature stratification and the permeable outer covering
- the models of radiative and convective heat exchange were not validated
- emissivity was determined experimentally for similar materials but using a different sensor from that used for the survey
- the effect of roof surface contaminants, on emissivity, was ignored
- sky view factor was only approximated
- the effect of any possible dew deposition on roofs was ignored

12.4 Future work

This study has raised a number of interesting avenues for further research. Development of the building model, in particular, has highlighted a number of gaps in the current understanding. Instrumenting existing buildings across the city while monitoring the microclimate would provide much needed validation data to quantify the uncertainty in, and for the development of, the models. Measurement of loft space air temperature and ventilation rate, in real houses, would do much to validate the models used in this study. Experiments aimed at investigating the porosity of the outer fabric of the roof and the convection coefficient at the surface, particularly when the roof is colder than the ambient air temperature, would also be extremely beneficial in this neglected field. For the sensor model, a simple thermal image with associated ground truth temperatures for large surfaces would do much to quantify the uncertainty in temperature measurement by the technique. Methods are yet to be developed to measure the sky view factor of pitched roofs from three-dimensional city models, efficiently and a database of emissivity values for typical roofing materials, and how those values vary with line of sight angle, is missing.

While this study has concentrated on one of the most prevalent house building styles in the city of Nottingham, numerous other styles exist. A simpler thermal model would be required for unventilated, flat roofs while more complex roof shapes and room in roof construction

would increase complexity. While greater accuracy may be possible for the flat roof, this style is uncommon for residential housing in the UK.

Perhaps, only when the results of this study are validated, would it be possible to discredit the technique. Meanwhile new development in the field may yet produce a successful quantitative heat loss survey using aerial thermography. The general methodology presented here will be valid in any future study.

12.5 Conclusions

It is clear that identifying houses that are in need of upgrading is an important aspect of energy conservation and, while aerial thermography has been sold as a tool to for this very purpose and for thirty years, the evidence does not support its use.

The numerical models, developed for this study to describe the sensor and the building roof, provided better understanding of the physical processes and allowed the results of the Nottingham survey to be quantified. However, the uncertainty in the results was significant and prevented discrimination of insulation levels.

Analysis of the model challenged some of the preconceptions about aerial thermography. In particular, a roof with a higher average sensor output may not have a higher surface temperature and a roof with a higher surface temperature may not be loosing more heat. The appearance of a roof on the thermal image will depend on the type of tiles, local microclimate, humidity and pollution levels in the atmosphere and the shape and construction of the roof and overlooking buildings, trees or hills. It will also depend on the internal temperature of the building and the amount of loft insulation to a limited extent. The raw thermal image does not identify any one of these parameters but a complex combination of them all.

The models still require validating and the thermal behaviours of the roof warrant further investigation.

References

1. R. Madding and G. Orlove, "Twenty-five years of ThermoSense: an historical and technological retrospective", *Thermosense XXV*, Orlando, Florida, USA, K.E. Cramer and X.P. Maldague, SPIE Vol. 5073, pp. 1-16, 2003.

2. Infoterra, *Geospatial solutions for local government*. Internet WWW page at: http://www.infoterra.co.uk/localgovt.htm, accessed 23/08/2006.

3. Horton Levi, *Thermal Imaging and Infra-red: H.E.C.A and Horton Levi*. Internet WWW page at: http://www.hortonlevi.co.uk/heca/default.htm, accessed 23/08/2006.

4. NEP, *Nottingham Energy Partnership- Welcome to the Nottingham Energy Partnership*. Internet WWW page at: http://nep.gngateway.org.uk/, accessed 22/08/2006.

5. BGS, *Welcome to the British Geological Survey (BGS) website*. Internet WWW page at: http://www.bgs.ac.uk/, accessed 22/08/2006.

6. Infoterra, *Remote Sensing and Geo-Information Solutions*. Internet WWW page at: http://www.infoterra.co.uk/default_no_flash.htm, accessed 22/08/2006.

7. S. Marsh and G. Ager, *Collection and primary analysis of data obtained by thermal imaging over Nottingham*, British Geological Survey (NERC) report: CR/03/132, 2003.

8. M. Adepoju, J. Harrison, A. Mohamed, A. Parkins, D. Revill, and C. Weaver, *Using thermal imagery to study heatloss in Nottingham for the BGS*, University of Nottingham report: Geography Masters Group Project, 2002.

9. W. Thompson, *An investigation into the domestic energy efficiency of the housing stock within the city of Nottingham using aerial thermal imaging*, University of Central England, M.Sc. thesis, 2004.

10. B. R. Lyon and G. Orlove, "A brief history of 25 years (or more) of infrared imaging radiometers", *Thermosense XXV*, Orlando, Florida, USA, K.E. Cramer and X.P. Maldague, SPIE Vol. 5073, pp. 17-30, 2003.

11. FLIR Systems, *Phoenix™- FLIR Systems*. Internet WWW page at: http://www.flirthermography.co.uk/cameras/camera/1064/, accessed 18/08/2006.

12. J. B. Campbell, *Introduction to remote sensing*, Taylor and Francis, London, 2002.

13. T. M. Lillesand, R. W. Kiefer, and J. W. Chipman, *Remote sensing and image interpretation*, Wiley International, 2004.

14. Great Britain, *Home Energy Conservation Act*, 1995.

15. *The UK fuel poverty strategy*, Department of Trade and Industry report: 2001.

16. EST, *Don't let your home get away with it - media facts*, Energy Savings Trust report: 2003.

17. DTI, *Our energy future - creating a low carbon economy*, Department of Trade and Industry report: 2003.

18. L. D. Shorrock and J. I. Utley, *Domestic Energy Factfile 2003*, Building Research Establishment report: BR 457, 2003.

19. P. Flowers, (Nottingham City Council, Housing Energy Team), Re: lofts. Personal communication to D. Allinson, 18/08/2006.

20. Yahoo France, *Des villes vues du ciel pour traquer les pertes d'energie de batiments- Yahoo! Actualities*. Internet WWW page at: http://fr.news.yahoo.com/26012007/202/des-villes-vues-du-ciel-pour-traquer-les-pertes-d.html, accessed 07/02/2007.

21. IRT surveys (http://www.irtsurveys.co.uk/index.html), Telephone conversation with sales manager. Personal communication to D. Allinson, 16/04/2007.

22. J. M. Lewis, "Infrared survey: Iowa utility experience", *Thermosense I: First national conference on the capabilities and limitations of thermal infrared sensing technology in energy conservation programs*, Chattanooga, Tennessee, USA, T.M. Lillesand, American Society of Photogrammetry, pp. 59-68, 1978.

23. G. W. Humphries, "Infrared: a municipal tool", *Thermosense I: First national conference on the capabilities and limitations of thermal infrared sensing technology in energy conservation programs*, Chattanooga, Tennessee, USA, T.M. Lillesand, American Society of Photogrammetry, pp. 69-72, 1978.

24. H. F. Winter, "Operation thermoscan - a utility's use of thermography for energy conservation", *Thermosense II: Second National Conference on thermal infrared sensing technology for energy conservation programs*, Albuquerque, New Mexico, USA, S.A. Morain, American Society of Photogrammetry, pp. 187-190, 1979.

25. M. K. Battles, "The dissemination of infrared imagery to 27 Minnesota communities", *Thermosense I: First national conference on the capabilities and limitations of thermal infrared sensing technology in energy conservation programs*, Chattanooga, Tennessee, USA, T.M. Lillesand, American Society of Photogrammetry, pp. 97-119, 1978.

26. F. A. Schmer, D. R. Hause, and J. C. Eidenshink, "Planning and conducting an airborne thermography survey", *Thermosense II: Second National Conference on thermal infrared sensing technology for energy conservation programs*, Albuquerque, New Mexico, USA, S.A. Morain, American Society of Photogrammetry, pp. 151-160, 1979.

27. R. H. Clawson, "Infrared thermography in a physical plant setting", *Thermosense I: First national conference on the capabilities and limitations of thermal infrared sensing technology in energy conservation programs*, Chattanooga, Tennessee, USA, T.M. Lillesand, American Society of Photogrammetry, pp. 73-91, 1978.

28. T. L. Flynn and J. E. Lukens, "Structural heat loss detection by infrared techniques", *Thermosense I: First national conference on the capabilities and limitations of thermal infrared sensing technology in energy conservation programs*, Chattanooga, Tennessee, USA, T.M. Lillesand, American Society of Photogrammetry, pp. 185-195, 1978.

29. P. A. D. Mill, "Thermography - A new tool for diagnosing building performance and quality assurance", *Thermosense II: Second National Conference on thermal infrared sensing technology for energy conservation programs*, Albuquerque, New Mexico, USA, S.A. Morain, American Society of Photogrammetry, pp. 109-143, 1979.

30. D. C. Fishburn, "Comparing the effectiveness of ground vs aerial roof thermography", *Thermosense V: Thermal Infrared Sensing Diagnostics*, Detroit, USA, G.E. Courville, SPIE Vol. 0371, pp. 177-186, 1982.

31. R. J. Brown, "Canadian experience with the use of aerial thermography", *Thermosense I: First national conference on the capabilities and limitations of thermal*

infrared sensing technology in energy conservation programs, Chattanooga, Tennessee, USA, T.M. Lillesand, American Society of Photogrammetry, pp. 121-137, 1978.

32. H. J. Monnin, "Infrared aerial surveys as an energy conservation tool", *Thermosense II: Second National Conference on thermal infrared sensing technology for energy conservation programs*, Albuquerque, New Mexico, USA, S.A. Morain, American Society of Photogrammetry, pp. 145-147, 1979.

33. J. B. Evans, "Interpretation of aerial thermograms", *Thermosense III: Thermal infrared sensing applied to energy conservation in building envelopes*, Minneapolis, USA, R.P. Madding, SPIE Vol. 254, pp. 30-34, 1980.

34. S. J. Treado and D. M. Burch, "Field evaluation of aerial infrared surveys for residential applications", *Thermosense IV: Thermal Infrared Sensing Applied to Energy Conservation in Building Envelopes*, Ottawa, Canada, R.A. Grot and J.T. Wood, SPIE Vol. 313, pp. 28-34, 1981.

35. G. Lawrence, A. Banner, and H. MacKay, "Interpretation of aerial thermographic data", *Thermosense IV: Thermal Infrared Sensing Applied to Energy Conservation in Building Envelopes*, Ottawa, Canada, R.A. Grot and J.T. Wood, SPIE Vol. 313, pp. 12-17, 1981.

36. W. R. Hazard, "Computer reduction of aerial thermograms for large scale energy audits", *Thermosense III: Thermal infrared sensing applied to energy conservation in building envelopes*, Minneapolis, USA, R.P. Madding, SPIE Vol. 254, pp. 41-49, 1980.

37. D. J. Templeton and D. E. Gay, "Thermal signatures associated with different types of moisture-damaged roofing insulation", *Thermosense VI: Thermal Infrared Sensing Diagnostics and Control*, Bellingham, Washington, USA, G.J. Burrer, SPIE, pp. 73-79, 1983.

38. C. Korhonen, W. Tobiasson, and A. Greatorex, "Comparison of aerial to on-the-roof infrared moisture surveys", *Thermosense VI: Thermal Infrared Sensing Diagnostics and Control*, Bellingham, Washington, USA, G.J. Burrer, SPIE, pp. 95-105, 1983.

39. K. B. Ouzts, "A comparison of infrared flyover, infrared walkover and visual inspection techniques for detecting roof moisture anomalies", *Thermosense VI: Thermal Infrared Sensing Diagnostics and Control*, Bellingham, Washington, USA, G.J. Burrer, SPIE, pp. 122-129, 1983.

40. Y. M. Chang and L. S. Galowin, "Aerial thermography and spot radiometer applications for detecting thermal anomalies of office buildings", *Thermosense VII: An International Conference on Thermal Infrared Sensing For Diagnostics and Control*, A.G. Kantsios, SPIE Vol. 520, pp. 178-189, 1984.

41. V. Sopko, "A discussion of the "standard practice for the location of wet insulation in roofing systems using infrared imaging" (ASTM C1153-90)", *Thermosense XIII*, Orlando, Florida, USA, G.S. Baird, SPIE Vol. 1467, pp. 83-89, 1991.

42. W. Tobiasson, "A method for conducting airborne infrared roof moisture surveys", *Thermosense X: Thermal Sensing for Diagnostics and Control*, Orlando, Florida, USA, R.D. Lucier, SPIE Vol. 934, pp. 50-61, 1988.

43. A. Knehans and J. Ledford, "The impact of aerial infrared roof moisture scans on the U.S. Army's ROOFER program", *Thermosense XV: An International Conference on Thermal Sensing and Imaging Diagnostic Applications*, L.R. Allen, SPIE Vol. 1933, pp. 67-73, 1993.

44. H. W. MacKay and G. R. Lawrence, "Application of airborn thermal infrared for steamline maintaenance", *Thermosense VI: Thermal Infrared Sensing Diagnostics and Control*, Bellingham, Washington, USA, G.J. Burrer, SPIE, pp. 106-111, 1983.

45. D. J. Templeton and M. B. Palmer, "Infrared evaluation of an underground steam distribution system", *Thermosense IX: An International Conference on Thermal Infrared Sensing for Diagnostics and Control*, Orlando, Florida, USA, R.P. Madding, SPIE Vol. 780, pp. 42-46, 1987.

46. S.-Å. Ljungberg, "Thermography for district heating network applications: operational advantages and limitations", *Thermosense X: Thermal Sensing for Diagnostics and Control*, Orlando, Florida, USA, R.D. Lucier, SPIE Vol. 934, pp. 70-77, 1988.

47. M. D. Lyberg, R. Taesler, and M. Mattsson, "Conditions for detecting malfunctions of buried heat distribution systems by thermographic methods", *Thermosense X: Thermal Sensing for Diagnostics and Control*, Orlando, Florida, USA, R.D. Lucier, SPIE Vol. 934, pp. 78-82, 1988.

48. J. E. G. Kittson, "Department of national defence use of thermography for facilities maintenance", *Thermosense XII*, Orlando, Florida, USA, S.A. Semanovich, SPIE Vol. 1313, pp. 2-5, 1990.

49. S.-Å. Ljungberg, "Aerial thermography for district heating systems application - an evaluation of commercial thermography", *Thermosense XII*, Orlando, Florida, USA, S.A. Semanovich, SPIE Vol. 1313, pp. 84-91, 1990.

50. ASHRAE, *1993 ASHRAE Handbook - Fundamentals*, American society of Heating, Refrigeration and Air-Conditioning Engineers, Inc., Atlanta, 1993.

51. R. J. Goldstein, "Application of aerial infrared thermography data to the measurement of building heat loss", *ASHRAE Transactions: Focus on Energy*, Atlanta, GA, USA, ASHRAE Vol. 84, Part 1, pp. 207-226, 1978.

52. R. J. Brown and J. Cihlar, *Introduction to aerial thermography applications in energy conservation programs*, Canada Centre for Remote Sensing report: 78-2, 1978.

53. R. J. Brown, "Infrared scanner technology applied to heat loss determination", Canadian Journal of Remote Sensing, **4**, pp. 1-9, 1978.

54. R. J. Brown, J. Cihlar, and P. M. Teillet, "Quantitative residential heat loss study", Photogrammetric Engineering and Remote Sensing, **47**(9), pp. 1327-1333, 1981.

55. D. M. Burch, "Infrared audits of roof heat loss", *ASHRAE Transactions*, Denver, Colorado, ASHRAE Vol. 86, Part 2, pp. 209-225, 1980.

56. S. J. Treado and J. M. Burch, "Applications of aerial thermography for residential energy analysis", *ASHRAE Transactions*, Washington, D.C., USA, ASHRAE Vol. 83 Part 2B, pp. 95-101, 1983.

57. J. R. Schott, "Principles of heat loss determination using infrared thermographic techniques", *Thermosense I: First national conference on the capabilities and limitations of thermal infrared sensing technology in energy conservation programs*, Chattanooga, Tennessee, USA, T.M. Lillesand, American Society of Photogrammetry, pp. 155-166, 1978.

58. J. R. Schott, "New developments in aerial thermography", *Thermosense II: Second National Conference on thermal infrared sensing technology for energy conservation programs*, Albuquerque, New Mexico, USA, S.A. Morain, American Society of Photogrammetry, pp. 227-236, 1979.

59. J. R. Schott and E. P. Wilkinson, "Trends in quantitative aerial thermography", *ASHRAE Transactions*, Washington, D.C., USA, ASHRAE Vol. 89 Part 2B, pp. 102-111, 1983.

60. J. R. Schott and E. P. Wilkinson, "Quantitative methods in aerial thermography", *Thermosense IV: Thermal Infrared Sensing Applied to Energy Conservation in Building Envelopes*, Ottawa, Canada, R.A. Grot and J.T. Wood, SPIE Vol. 313, pp. 20-27, 1981.

61. J. R. Schott, "Limitations of infrared thermography", *Thermosense V: Thermal Infrared Sensing Diagnostics*, Detroit, USA, G.E. Courville, SPIE Vol. 371, pp. 196-202, 1982.

62. J. R. Schott, J. D. Biegel, and E. Wilkinson, "Quantitative aerial survey of building heat loss", *Thermosense V: Thermal Infrared Sensing Diagnostics*, Detroit, USA, G.E. Courville, SPIE Vol. 0371, pp. 187-194, 1982.

63. J. Schott and E. Wilkinson, *Aerial measurement of heat loss: Phase I*, Calspan report: 6393-M-2, 1979.

64. J. Schott and E. Wilkinson, *Aerial measurement of heat loss: Phase II*, Calspan report: 6393-M-3, 1982.

65. J. B. Evans, "Micrometeorology and infrared measurements", *Thermosense II: Second National Conference on thermal infrared sensing technology for energy conservation programs*, Albuquerque, New Mexico, USA, S.A. Morain, American Society of Photogrammetry, pp. 103-105, 1979.

66. J. B. Evans, "Meteorology and infrared measurements", *Thermosense III: Thermal infrared sensing applied to energy conservation in building envelopes*, Minneapolis, USA, R.P. Madding, SPIE Vol. 254, pp. 21-23, 1980.

67. J. B. Evans, "Meteorology and infrared measurements", *Thermosense IV: Thermal Infrared Sensing Applied to Energy Conservation in Building Envelopes*, Ottawa, Canada, R.A. Grot and J.T. Wood, SPIE Vol. 313, pp. 9-11, 1981.

68. F. A. Kulacki, O. W. Mintzer, and L. E. Winget, "Remote sensing of building heatloss-a case study for development of methodology", *Thermosense IV: Thermal Infrared Sensing Applied to Energy Conservation in Building Envelopes*, Ottawa, Canada, R.A. Grot and J.T. Wood, SPIE Vol. 313, pp. 139-150, 1981.

69. O. W. Mintzer, "Measuring heat loss form flat-roof buildings with calibrated thermography", Photogrammetric Engineering and Remote Sensing, **49**(6), pp. 777-788, 1983.

70. G. A. Haigh and S. E. Pritchard, "Quantifying heat losses using aerial thermography", *Thermosense III: Thermal infrared sensing applied to energy conservation in building envelopes*, Minneapolis, USA, R.P. Madding, SPIE Vol. 254, pp. 91-101, 1980.

71. J. M. Anderson and S. B. Wilson, "The physical basis of current infrared remote-sensing techniques and the interpretation of data from aerial surveys", International Journal of Remote Sensing, **5**(1), pp. 1-18, 1984.

72. R. V. Birnie, P. F. S. Ritchie, G. C. Stove, and M. J. Adams, "Thermal infrared survey of Aberdeen city: data processing, analysis and interpretation", International Journal of Remote Sensing, **5**(1), pp. 47-63, 1984.

73. Thermal Survey, *Thermal imaging*. Internet WWW page at: http://www.thermal-survey.co.uk/, accessed 24/08/2006.

74. S. Roberts and G. Starling, *Making the most of Birmingham City Council's aerial thermographic study*, Centre for Sutainable Energy report: 2004.

75. Thermal survey Ltd, *Press release*. Internet WWW page at: http://www.thermal-survey.co.uk/press/index.htm, accessed 24/08/2006.

76. Horton Levi, *Horton Levi- Client List*. Internet WWW page at: http://www.hortonlevi.co.uk/clients/default.htm, accessed 24/08/2006.

77. R. Fitch, (Horton Levi), Telephone conversation. Personal communication to D. Allinson, 14/04/2005.

78. G. R. Stockton and A. Tache, "Advances in applications for aerial thermography", *Thermosense XXVIII*, Orlando, USA, SPIE Vol. 6205, pp. 2006.

79. M. Tervo and T. Kauppinen, "Supervision of self-heating in peat stockpiles by aerial thermography", *Thermosense XIII*, Orlando, Florida, USA, G.S. Baird, SPIE Vol. 1467, pp. 83-89, 1991.

80. M. Tervo, E. Kiukaanniemi, and T. Kauppinen, "The applications of aerial thermography in peat production in Finland", *Thermosense XV: An International Conference on Thermal Sensing and Imaging Diagnostic Applications*, L.R. Allen, SPIE Vol. 1933, pp. 101-109, 1993.

81. S. Björnsson and K. Árnason, "State of the art of aerial thermography in Iceland-thermography of geothermal areas during the past 20 years", *Thermosense XVII: An International Conference on Thermal Sensing and Imaging Diagnostic Applications*, Orlando, Florida, USA, S. Semanovich, SPIE Vol. 2473, pp. 2-14, 1995.

82. E. Villa-Aleman, A. J. Garret, R. J. Kurzeja, and M. M. Perdergast, "Aerial thermography studies of power plant heated lakes", *Thermosense XXII*, Orlando, Florida, USA, R.B. Dinwiddie and D.H. LeMieux, SPIE Vol. 4020, pp. 367-373, 2000.

83. L. M. West, "Commercial applications in aerial thermography: powerline inspection, research and environmental studies", *Thermosense XXII*, Orlando, Florida, USA, R.B. Dinwiddie and D.H. LeMieux, SPIE Vol. 4020, pp. 382-386, 2000.

84. G. B. Howard, "Applications of airborne thermal infared imaging for the detection of unexploded ordnance", *Thermosense XXIII*, Orlando, Florida, USA, A.E. Rozlosnik and R.B. Dinwiddie, SPIE Vol. 4360, pp. 149-160, 2001.

85. J. M. Aranda, J. Meléndez, A. J. d. Castro, and F. López, "Forest fire studies by medium infrared and thermal infrared thermography", *Thermosense XXIII*, Orlando, Florida, USA, A.E. Rozlosnik and R.B. Dinwiddie, SPIE Vol. 4360, pp. 161-168, 2001.

86. D. Campbell, W. Born, J. Beck, B. Bereska, K. Frederick, and H. Sun, "The airborne wildfire intelligence system: a decision support tool for wildland fire managers in Alberta", *Thermosense XXIV*, Orlando, Florida, USA, X.P. Maldague and A.E. Rozlosnik, SPIE Vol. 4710, pp. 159-170, 2002.

87. E. H. Castro, J. D. Pfefferman, and H. j. González, "Thermal analysis of images obtained with an airborne IR scanner in Argentina", *Thermosense XX*, Orlando, Florida, USA, J.R. Snell and R.N. Wurzbach, SPIE Vol. 3361, pp. 169-176, 1998.

88. C. Ibarra-Castanedo, D. González, M. Klein, M. Pilla, S. Vallerand, and X. Maldague, "Infrared image processing and data analysis", Infrared Physics and Technology, **46**, pp. 75-83, 2004.

89. X. Maldague, *Theory and Practice of Infred technology for non destructive testing*, John Wiley, 2001.

90. Z. Deng and J. Liu, "Mathematical modelling of temperature mapping over skin surface and its implementation in thermal disease diagnostics", Computers in biology and medicine, **34**(6), pp. 495-521, 2004.

91. M. Anbar, "Clinical thermal imaging today", IEEE Engineering in Medicine and Biology Magazine, **17**(4), pp. 25-33, 1998.

92. B. F. Jones, "A reappraisal of the use of infrared thermal image analysis in medicine", IEEE transactions on medical imaging, **17**(6), pp. 1019-1027, 1998.

93. P. Gray, (Infoterra Ltd.), RE: Aerial thermography. Personal communication to D. Allinson, 08/07/2004.

94. J. R. Jack and R. L. Bowman, "Effective Aerial thermography for energy conservation", *Thermosense II: Second National Conference on thermal infrared sensing technology for energy conservation programs*, Albuquerque, New Mexico, USA, S.A. Morain, American Society of Photogrammetry, pp. 217-225, 1979.

95. W. C. Snyder and J. R. Schott, "A combined aerial and ground technique for assessing structural heat loss", *Thermosense XVI: An International Conference on Thermal Sensing and Imaging Diagnostic Applications*, Orlando, USA, SPIE Vol. 2245, pp. 71-82, 1994.

96. Time and Date.com, *Sunrise and sunset in London - England - U.K.* Internet WWW page at: http://www.timeanddate.com/worldclock/astronomy.html?n=136&obj=sun&month=2&year=2001&day=1, accessed 2/12/2005.

97. A. K. Wilson, "An integrated data system for airborne remote sensing", International Journal of Remote Sensing, **18**(9), pp. 1889-1901, 1997.

98. S. Marsh, G. Ager, A. Wilson, and P. Purcell, *Collection and primary analysis of data obtained by thermal imaging*, British Geological Survey report: CR/02/248, 2002.

99. J. R. Schott, "Image processing of thermal infrared images", Photogrammetric Engineering and Remote Sensing, **55**(9), pp. 1311-1321, 1989.

100. R. D. Callison, P. Blake, and L. M. Anderson, "The quantitative use of airborne thematic mapper thermal infrared data", International Journal of Remote Sensing, **8**(1), pp. 113-126, 1987.

101. J. R. Schott, *Remote sensing - the image chain approach*, Oxford University Press, New York, 1997.

102. BSI, *General metrology- part4: practical guide to measurement uncertainty*, British Standards Institution report: PD 6461-4:2004, 2004.

103. S. Buil, (Nottingham City Council Building Surveyor), Telephone Conversation. Personal communication to D. Allinson, 30th March 2006.

104. University of Wyoming, *Atmospheric soundings*. Internet WWW page at: http://weather.uwyo.edu/upperair/sounding.html, accessed 21/12/2004.

105. S. M. Singh, "Brightness temperature algorithms for Landsat Thematic Mapper Data", Remote Sensing of the Environment, **24**, pp. 509-512, 1988.

106. M. Etridge, (Infoterra), Thermal system response curves. Personal communication to D. Allinson, 30/11/2004.

107. CIBSE, *Guide A: Environmental design*, CIBSE, 2006.

108. S. Doran, *Field investigations of the thermal performance of construction elements as built*, Building Research Establishment report: 78132 (Client report for DETR), 2000.

109. BSI, *Building components and building elements - Thermal resistance and thermal transmittance - calculation method*, report: BS EN ISO 6946:1997, 1997.

110. D. S. Parker, *Technical support for development of an attic simulation model for the Calafornia energy commission*, Florida Solar Energy Centre report: FSEC-CR-1526-05, 2005.

111. C. O. Pedersen, D. E. Fisher, and R. J. Liesen, "Development of a heat balance procedure for calculating cooling loads", *ASHRAE*, ASHRAE Vol. 103(2), pp. 459-468, 1997.

112. D. B. Crawley, J. W. Hand, M. Kummert, and B. T. Griffith, *Contrasting the capabilities of building energy performance simulation programs*. Internet WWW page at: http://www.eere.energy.gov/buildings/tools_directory/pdfs/contrasting_the_capabilities_of_building_energy_performance_simulation_programs_v1.0.pdf, accessed 22/02/2006.

113. University of Strathclyde, *ESP-r*. Internet WWW page at: http://www.esru.strath.ac.uk/Programs/ESP-r.htm, accessed 22/02/2006.

114. J. A. Clarke, *Energy simulation in Building design*, Butterworth-Heinemann, 2001.

115. U.S. Department of Energy, *Building technologies program: EnergyPlus*. Internet WWW page at: http://www.eere.energy.gov/buildings/energyplus/, accessed 22/02/2006.

116. J. D. Spitler, D. E. Fisher, and C. O. Pedersen, "The radiant time series cooling load calculation procedure", *ASHRAE Transactions*, Boston MA, USA, ASHRAE Vol. 103(2), pp. 503-515, 1997.

117. J. D. Spitler and S. J. Rees, "Quantitative comparison of North American and UK cooling load calculation procedures- methodology", *ASHRAE Transactions*, ASHRAE Vol. 104(2), pp. 36-46, 1998.

118. S. J. Rees, J. D. Spitler, and P. Haves, "Quantitative comparison of North American and UK cooling load calculation procedures- Results", *AHRAE Transactions*, ASHRAE Vol. 104(2), pp. 47-61, 1998.

119. T. M. McClellan and C. O. Pedersen, "Investigation of outside heat balance models for use in a heat balance cooling load calculation procedure", *ASHRAE Transaction*, Boston MA, USA, ASHRAE Vol. 103(2), pp. 469-484, 1997.

120. R. J. Liesen and C. O. Pedersen, "An evaluation of inside surface heat balance models for use in a heat balance cooling load calculation procedure", *ASHRAE Transaction*, Boston MA, USA, ASHRAE Vol. 103(2), pp. 485-502, 1997.

121. R. J. Cole, "The longwave radiative environment around buildings", Building and Environment, **11**, pp. 3-13, 1976.

122. R. J. Cole and N. S. Sturrock, "The convective heat exchange at the external surface of buildings", Building and Environment, **12**, pp. 207-214, 1977.

123. S. Sharples, "Full-scale measurements of convective energy losses from exterior building surfaces", Building and Environment, **19**(1), pp. 31-39, 1984.

124. D. L. Loveday and A. H. Taki, "Convective heat transfer coefficients at a plane surface on a full-scale building facade", International Journal of heat and mass transfer, **39**(8), pp. 1729-1742, 1996.

125. R. D. Clear, L. Gartland, and F. C. Winkelmann, "An empirical correlation for the outside convective air film coefficient for horizontal roofs", Energy and Buildings, **35**(8), pp. 797-811, 2003.

126. T. R. Oke, *Boundary Layer Climates*, Routledge, London, 1987.

127. FLIR Systems, *Thermovision A20M operators manual*, FLIR Systems, 2004.

128. D. E. Fisher and C. O. Pedersen, "Convective heat transfer in building energy and thermal load calculations", *ASHRAE transactions*, Vol. 103, pp. 137-148, 1997.

129. S. B. Wilson and J. M. Anderson, "The applicability of LOWTRAN 5 computer code to aerial thermographic data correction", International Journal of Remote Sensing, **7**(3), pp. 379-388, 1986.

130. A. E. Byrnes and J. R. Schott, "Correction of thermal imagery for atmospheric effects using aircraft measurement and atmospheric modeling techniques", Applied Optics, **25**(15), pp. 2563-2570, 1986.

131. AFRL, *AFRL/VSBM MODTRAN 4 Software*. Internet WWW page at: http://www.vs.afrl.af.mil/Division/VSBYB/modtran4.html, accessed 21/12/2004.

132. M. A. Goforth, G. W. Gilchrist, and J. D. Sirianni, "Cloud effects on thermal downwelling sky radiance", *Thermosense XXIV*, Orlando, Florida, USA, X.P. Maldague and A.E. Rozlosnik, SPIE Vol. 4710, pp. 203-213, 2002.

133. A. C. Dilley and D. M. O'Brien, "Estimating downward clear sky long-wave irradiance at the surface from screen temperature and precipitable water", Quarterly Journal of the Royal Meteorological Society, **124**(July 1998 Part A), pp. 1391-1401, 1998.

134. R. P. Madding, "Temperature dependence of the graybody approximation to emissivity for some common materials", *Thermosense XXIV*, Orlando, Florida, USA, X.P. Maldague and A.E. Rozlosnik, SPIE Vol. 4710, pp. 37-43, 2002.

135. S. J. Marshall, "We need to know more about infrared emissivity", *Thermosense IV: Thermal Infrared Sensing Applied to Energy Conservation in Building Envelopes*, Ottawa, Canada, R.A. Grot and J.T. Wood, SPIE Vol. 313, pp. 119-127, 1981.

136. D. S. Lowe, "Effects of emissivity on airborne observation of roof temperature", *Thermosense I: First national conference on the capabilities and limitations of thermal infrared sensing technology in energy conservation programs*, Chattanooga, Tennessee, USA, T.M. Lillesand, American Society of Photogrammetry, pp. 167-176, 1978.

137. D. A. Artis and W. H. Carnahan, "Survey of Emissivity Variability in Thermography of Urban Areas", Remote Sensing of Environment, **12**, pp. 313-329, 1982.

138. NPL, *Spectral and total emissivity at near ambient temperatures*. Internet WWW page at: http://www.npl.co.uk/optical_radiation/infrared_spectrometry/qd5106h.html, accessed 21/12/2004.

139. Surface Optics Corporation, *Optical Properties Library Data*. Internet WWW page at: http://www.surfaceoptics.com/brochures/SOC_Measured_Data_Doc.pdf, accessed 21/12/2004.

140. C. Salvaggio and C. J. Miller, "Methodologies and protocols for the collection of midwave and longwave infrared emissivity spectra using a portable field spectrometer", *Image exploitation and target recognition, algorithms for multispectral, hyperspectral and ultraspectral imagery VII*, SPIE Vol. 4381, pp. 2001.

141. C. Salvaggio and C. Miller, "Comparison of field and laboratory collected midwave and longwave infrared emissivity spectra/data reduction techniques", *Image exploitation and target recognition, algorithms for multispectral, hyperspectral and ultraspectral imagery VII*, SPIE Vol. 4381, pp. 2001.

142. ASTM, *E 1933-99a: Standard test methods for measuring and compensating for emissivity using infrared imageing radiometers*, 2002.

143. R. P. Madding, "Emissivity measurement and temperature correction accuracy considerations", *Thermosense XXI*, Orlando, Florida, USA, D.H. LeMieux and J.R. Snell, SPIE Vol. 3700, pp. 1999.

144. N. P. Avdelidis and A. Moropoulou, "Emissivity considerations in building thermography", Energy and Buildings, **35**(7), pp. 663-667, 2003.

145. R. B. Johnson, C. Feng, and K. D. Fehribach, "On the validity and techniques of temperature and emissivity measurement", *Thermosense X: Thermal Sensing for Diagnostics and Control*, Orlando, Florida, USA, SPIE Vol. 934, pp. 202-206, 1988.

146. J. R. Schott, "Incorporation of angular emissivity effects in longwave infrared image models", *Infrared Technology XII*, San Diego, California, SPIE Vol. 685, pp. 44-52, 1986.

147. K. Daryabeigi, R. E. Wright, C. K. Puram, and D. W. Alderfer, "Directional emittance corrections for thermal infrared imaging", *Thermosense XIV: An International Conference on Thermal Sensing and Imaging Diagnostic Applications*, Orlando, Florida, USA, J.K. Eklund, SPIE Vol. 1682, pp. 325-335, 1992.

148. U.S. Department of Energy, *EnergyPlus Energy Simulation Software- Engineering reference*. Internet WWW page at: http://www.eere.energy.gov/buildings/energyplus/pdfs/engineeringreference.pdf, accessed 23 May 2005.

149. L. Chapman, "Improved one dimensional energy balance modelling utilising sky-view factors determined from digital imagery", *10th SIRWEC conference*, Davos, Switzerland, (http://www.sirwec.org/conferences/davos2000.html), pp. 32-40, 2000.

150. C. S. B. Grimmond, S. K. Potter, H. N. Zutter, and C. Souch, "Rapid methods to estimate sky-view factors applied to urban areas", International Journal of Climatology, **21**, pp. 903-913, 2001.

151. *RayMan*. Internet WWW page at: http://www.mif.uni-freiburg.de/rayman/index.htm, accessed 17/03/2006.

152. C. Ratti, *Urban analysis for environmental prediction*, University of Cambridge, PhD thesis, 2001.

153. ESRI, *The GIS software leader*. Internet WWW page at: http://www.esri.com/, accessed 27/02/2006.

154. B. J. Beesley, *Sky viewshed modeling for GPS use in the urban environment*. Internet WWW page at: http://gis.esri.com/library/userconf/proc03/p0361.pdf, accessed 27/02/2006.

155. L. C. L. Souza, D. S. Rodrigues, and J. F. G. Mendes, "Sky view factors estimation using a 3D-GIS extension", *Building Simulation 2003*, Eindhoven, Netherlands, IBPSA, pp. 1227-1234, 2003.

156. CASA, *3D cities review*. Internet WWW page at: http://www.casa.ucl.ac.uk/research/3dcities.htm, accessed 22/12/2004.

157. F. Rottensteiner and C. Briese, "A new method for building extraction in urban areas from high resulution LIDAR data", *Photogrammetric computer vision, ISPRS commission III, symposium 2002*, Graz, Austria, ISPRS, pp. 2002.

158. A. F. Elaksher and J. S. Bethel, "Reconstructing 3D buildings from LIDAR data", *Photogrammetric computer vision, ISPRS commission III, symposium 2002*, Graz, Austria, ISPRS, pp. 2002.

159. K. Chrzanowski, J. Fischer, and R. Matyszkiel, "Testing and evaluation of thermal cameras for absolute temperature measurement", Optical Engineering, **39**(9), pp. 2535-2544, 2000.

160. K. Chrzanowski, R. Matyszkiel, J. Fischer, and J. Barela, "Uncertainty of temperature measurement with thermal cameras", Optical Engineering, **40**(6), pp. 1106-1114, 2001.

161. K. Chrzanowski, "Evaluation of thermal cameras in quality systems according to ISO9000 or EN4500 standards", *Thermosense XXIII*, SPIE Vol. 4360, pp. 387-401, 2001.

162. I. MacDonald and P. Strachan, "Practical application of uncertainty analysis", Energy and Buildings, **33**, pp. 219-227, 2001.

163. S. d. Wit and G. Augenbroe, "Analysis of uncertainty in building design evaluations and its implications", Energy and Buildings, **34**, pp. 951-958, 2002.

Appendices

Appendix 1: Spectral response of the sensor

Wavelength µm	Peak normalised response	Wavelength µm	Peak normalised response	Wavelength µm	Peak normalised response
1.4	0.000006	5.1	0.005942	8.8	0.953376
1.5	0.000017	5.2	0.005844	8.9	0.968893
1.6	0.000073	5.3	0.005798	9.0	0.975015
1.7	0.000171	5.4	0.005880	9.1	0.975356
1.8	0.000348	5.5	0.006038	9.2	0.955376
1.9	0.000574	5.6	0.006249	9.3	0.920866
2.0	0.000826	5.7	0.006436	9.4	0.879091
2.1	0.001070	5.8	0.006552	9.5	0.844582
2.2	0.001250	5.9	0.006622	9.6	0.817337
2.3	0.001385	6.0	0.006931	9.7	0.790093
2.4	0.001481	6.1	0.007540	9.8	0.771929
2.5	0.001536	6.2	0.008462	9.9	0.762848
2.6	0.001541	6.3	0.009427	10.0	0.766844
2.7	0.001484	6.4	0.010422	10.1	0.774816
2.8	0.001418	6.5	0.011444	10.2	0.795771
2.9	0.001352	6.6	0.012478	10.3	0.825654
3.0	0.001393	6.7	0.013531	10.4	0.868920
3.1	0.001543	6.8	0.014656	10.5	0.916488
3.2	0.001810	6.9	0.015873	10.6	0.959391
3.3	0.002090	7.0	0.030114	10.7	0.993155
3.4	0.002378	7.1	0.057613	10.8	1.000000
3.5	0.002674	7.2	0.099585	10.9	0.988987
3.6	0.002987	7.3	0.143947	11.0	0.913544
3.7	0.003325	7.4	0.189781	11.1	0.792674
3.8	0.003661	7.5	0.241057	11.2	0.636089
3.9	0.003983	7.6	0.296760	11.3	0.491358
4.0	0.004327	7.7	0.357844	11.4	0.365020
4.1	0.004717	7.8	0.419447	11.5	0.248126
4.2	0.005163	7.9	0.482062	11.6	0.161900
4.3	0.005626	8.0	0.545513	11.7	0.098960
4.4	0.006130	8.1	0.609505	11.8	0.068446
4.5	0.006446	8.2	0.676822	11.9	0.048256
4.6	0.006576	8.3	0.747887	12.0	0.038162
4.7	0.006492	8.4	0.823240	12.1	0.028296
4.8	0.006387	8.5	0.877993	12.2	0.018660
4.9	0.006252	8.6	0.915192	12.3	0.009254
5.0	0.006096	8.7	0.934269	12.4	0.003059

Appendix 2: Radio sounding data

03354 Nottingham Observations at 00Z 16 Feb 2001

PRES hPa	HGHT m	TEMP C	DWPT C	RELH %	MIXR g/kg	DRCT deg	SKNT knot	THTA K	THTE K	THTV K
1018.0	0	4.4	2.9	90	4.65	0	2	276.1	288.9	276.9
1016.0	28	5.6	3.7	88	4.93	1	3	277.5	291.1	278.3
1000.0	258	5.8	3.6	86	4.98	9	7	278.9	292.8	279.8
993.0	316	6.0	3.7	85	5.05	13	9	279.7	293.8	280.6
979.0	432	5.1	3.4	89	5.01	20	14	279.9	293.9	280.8
963.0	566	4.0	3.0	93	4.95	23	13	280.1	294.0	281.0
953.0	651	3.6	1.2	84	4.40	24	12	280.6	293.0	281.3
950.0	677	3.7	1.1	83	4.39	25	12	280.9	293.3	281.7
937.0	789	4.0	0.8	80	4.35	20	13	282.4	294.7	283.1
925.0	894	3.0	0.2	82	4.22	15	14	282.4	294.4	283.1
907.0	1053	1.5	-0.4	88	4.12	10	14	282.4	294.1	283.1
897.0	1142	0.6	-0.7	91	4.07	358	13	282.4	294.0	283.1
884.0	1260	1.8	-5.2	60	2.95	342	12	284.8	293.5	285.3
874.0	1351	1.0	-7.0	55	2.60	329	11	284.9	292.6	285.4
863.0	1453	1.0	-17.0	25	1.18	315	10	285.9	289.6	286.1
853.0	1547	1.4	-23.6	14	0.67	307	8	287.3	289.5	287.4
850.0	1575	1.4	-23.6	14	0.67	305	8	287.6	289.8	287.7
822.0	1844	-0.3	-28.3	10	0.45	305	7	288.6	290.1	288.6
794.0	2119	-2.4	-30.4	10	0.39	305	6	289.2	290.5	289.3
779.0	2271	-3.5	-31.5	9	0.35	295	9	289.6	290.8	289.7
768.0	2383	-3.7	-22.7	21	0.81	287	11	290.6	293.2	290.7
743.0	2644	-4.5	-26.5	16	0.59	269	15	292.4	294.4	292.6
736.0	2718	-4.3	-27.3	15	0.56	264	17	293.5	295.3	293.6
722.0	2870	-4.9	-28.9	13	0.49	253	19	294.4	296.1	294.5
711.0	2990	-5.8	-29.8	13	0.46	245	21	294.7	296.3	294.8
700.0	3112	-6.7	-30.7	13	0.43	240	23	295.0	296.5	295.1
696.0	3157	-7.1	-32.1	12	0.37	238	24	295.1	296.4	295.1
678.0	3360	-7.7	-35.5	9	0.28	230	25	296.7	297.6	296.7
677.0	3372	-7.7	-35.7	9	0.27	230	25	296.8	297.7	296.8
644.0	3758	-10.9	-29.9	19	0.50	232	27	297.4	299.1	297.5
625.0	3987	-12.3	-34.3	14	0.34	234	28	298.3	299.5	298.4
612.0	4147	-13.7	-26.7	33	0.71	235	29	298.5	300.9	298.6
609.0	4184	-14.0	-27.4	31	0.67	235	29	298.6	300.9	298.8
592.0	4399	-15.5	-31.5	24	0.47	231	32	299.3	300.9	299.4
565.0	4749	-18.1	-29.1	38	0.61	226	36	300.2	302.3	300.4
552.0	4922	-19.3	-32.3	31	0.46	223	39	300.8	302.4	300.9
542.0	5058	-20.5	-29.5	44	0.62	220	40	301.0	303.1	301.1
540.0	5085	-20.7	-29.8	44	0.60	220	41	301.1	303.1	301.2
520.0	5363	-22.3	-33.3	36	0.45	223	45	302.4	303.9	302.5
507.0	5549	-23.9	-33.4	41	0.45	225	49	302.7	304.2	302.7
502.0	5621	-24.5	-33.5	43	0.45	225	49	302.8	304.4	302.9
500.0	5650	-24.7	-33.7	43	0.45	225	49	302.9	304.4	302.9
492.0	5767	-25.7	-29.8	68	0.66	225	49	303.0	305.3	303.2
476.0	6007	-26.9	-38.9	31	0.28	225	51	304.4	305.4	304.5
464.0	6191	-28.5	-34.5	56	0.44	225	52	304.7	306.2	304.8
447.0	6457	-30.7	-34.3	70	0.47	225	54	305.2	306.9	305.3
436.0	6634	-32.1	-34.2	82	0.49	224	57	305.6	307.3	305.7
420.0	6898	-33.1	-35.3	81	0.45	222	60	307.6	309.2	307.7
400.0	7240	-36.1	-38.6	78	0.34	220	64	308.0	309.2	308.1
397.0	7292	-36.5	-39.0	78	0.33	221	64	308.1	309.3	308.2
385.0	7503	-38.3	-41.7	70	0.26	224	63	308.5	309.4	308.5
370.0	7775	-39.9	-42.6	75	0.24	227	63	309.9	310.8	309.9
360.0	7960	-41.3	-44.4	72	0.21	230	62	310.4	311.2	310.4
344.0	8267	-43.7	-47.3	67	0.16	226	64	311.2	311.9	311.3
325.0	8645	-46.5	-49.0	76	0.14	222	65	312.5	313.0	312.5
319.0	8768	-47.3	-50.1	73	0.12	220	66	313.0	313.5	313.1
316.0	8830	-47.7	-50.7	71	0.12	220	66	313.3	313.8	313.4
300.0	9170	-50.5	-53.3	72	0.09	220	64	314.1	314.4	314.1
293.0	9324	-51.9	-54.6	73	0.08	220	64	314.2	314.5	314.2
280.0	9617	-53.7	-57.8	61	0.06	220	64	315.7	315.9	315.7
276.0	9710	-54.3	-58.8	57	0.05	221	65	316.1	316.4	316.1
250.0	10340	-58.1	-64.1	46	0.03	225	70	319.6	319.7	319.6
240.0	10597	-59.7	-65.7	45	0.02	225	70	320.9	321.0	320.9
225.0	10999	-62.1	-68.6	41	0.02	225	70	323.2	323.3	323.2
213.0	11340	-64.1	-71.1	38	0.01	230	66	325.2	325.2	325.2
202.0	11668	-61.5	-68.5	39	0.02	238	53	334.3	334.4	334.3
200.0	11730	-61.7	-68.7	39	0.02	240	51	334.9	335.0	334.9
197.0	11823	-61.9	-68.9	39	0.02	241	48	336.0	336.1	336.0

190.0	12048	-58.6	-66.5	36	0.03	245	41	344.9	345.0	344.9
189.0	12081	-58.1	-66.1	35	0.03	245	41	346.1	346.3	346.2
183.0	12283	-58.5	-67.5	30	0.02	242	43	348.7	348.8	348.7
178.0	12457	-58.1	-67.9	28	0.02	240	45	352.1	352.2	352.1
170.0	12746	-57.5	-68.5	23	0.02	253	43	357.8	357.9	357.8
169.0	12783	-57.6	-68.8	23	0.02	255	43	358.2	358.3	358.2
163.0	13009	-58.4	-70.8	19	0.02	260	31	360.6	360.7	360.6
156.0	13284	-59.3	-73.3	15	0.01	245	25	363.6	363.7	363.6
154.0	13365	-58.7	-73.0	14	0.01	240	23	366.0	366.0	366.0
150.0	13530	-57.5	-72.5	13	0.01	240	25	370.8	370.9	370.8
142.0	13878	-56.5	-73.5	10	0.01	246	27	378.4	378.5	378.4
132.0	14337	-60.5	-78.5	8	0.01	253	29	379.2	379.3	379.3
130.0	14433	-60.3	-78.7	7	0.01	255	29	381.3	381.4	381.3
127.0	14579	-59.9	-78.9	7	0.01	257	28	384.5	384.6	384.5
119.0	14984	-61.7	-81.7	5	0.00	264	23	388.4	388.5	388.4
113.0	15305	-61.1	-81.1	5	0.00	269	20	395.4	395.4	395.4
112.0	15360	-61.5	-81.5	5	0.00	270	19	395.7	395.7	395.7
107.0	15643	-63.3	-83.3	5	0.00	274	24	397.4	397.4	397.4
105.0	15759	-63.1	-83.4	5	0.00	275	25	400.0	400.0	400.0
100.0	16060	-62.5	-83.5	4	0.00	305	21	406.7	406.7	406.7
95.0	16373	-64.0	-84.5	5	0.00	315	14	409.8	409.8	409.8
89.7	16724	-65.7	-85.7	5	0.00	290	16	413.2	413.2	413.2
88.0	16840	-65.3	-85.7	4	0.00	295	17	416.3	416.3	416.3
85.7	17001	-64.7	-85.7	4	0.00	297	16	420.6	420.6	420.6
81.1	17336	-65.3	-85.3	5	0.00	302	14	426.1	426.1	426.1
77.3	17628	-64.7	-85.7	4	0.00	305	12	433.2	433.2	433.2
73.0	17976	-65.7	-85.9	5	0.00	310	10	438.1	438.2	438.1
72.3	18034	-65.9	-85.9	5	0.00	311	10	439.0	439.0	439.0
70.0	18230	-66.1	-86.1	5	0.00	315	12	442.6	442.7	442.6
56.7	19506	-66.5	-86.5	5	0.00	7	22	469.2	469.2	469.2
55.0	19691	-66.1	-86.4	4	0.00	15	23	474.3	474.3	474.3
52.1	20020	-65.3	-86.3	4	0.00	29	21	483.5	483.5	483.5
52.0	20032	-65.3	-86.3	4	0.00	30	21	483.7	483.7	483.7
50.0	20270	-65.7	-85.7	5	0.01	30	16	488.2	488.3	488.2
48.0	20515	-66.3	-86.3	5	0.00	0	14	492.4	492.5	492.4
41.0	21463	-68.8	-88.8	4	0.00	25	29	508.9	509.0	508.9
38.3	21872	-69.9	-89.9	4	0.00	25	33	516.2	516.2	516.2
36.0	22241	-69.9	-89.9	4	0.00	25	37	525.4	525.5	525.4
35.7	22291	-69.9	-89.9	4	0.00			526.7	526.7	526.7

Station information and sounding indices

```
                            Station number: 3354
                          Observation time: 010216/0000
                          Station latitude: 53.00
                         Station longitude: -1.25
                         Station elevation: 0.0
                           Showalter index: 11.68
                              Lifted index: 9.33
    LIFT computed using virtual temperature: 9.33
                                SWEAT index: 64.10
                                    K index: -21.50
                        Cross totals index: 1.10
                    Vertical totals index: 26.10
                      Totals totals index: 27.20
      Convective Available Potential Energy: 0.00
             CAPE using virtual temperature: 0.00
                      Convective Inhibition: 0.00
             CINS using virtual temperature: 0.00
                    Bulk Richardson Number: 0.00
          Bulk Richardson Number using CAPV: 0.00
  Temp [K] of the Lifted Condensation Level: 276.26
Pres [hPa] of the Lifted Condensation Level: 964.93
     Mean mixed layer potential temperature: 279.10
              Mean mixed layer mixing ratio: 4.99
              1000 hPa to 500 hPa thickness: 5392.00
Precipitable water [mm] for entire sounding: 9.24
```

Appendix 3: MODTRAN tape5 input cards

For the calculation of upwelled radiance and atmospheric transmission:

```
MM  7    3    1    0    0    0    3    3    3    3    1    1    0 268.150      0
ff  0f   0 365.00000        0.        0. f f f f       0.000
    5    2    2    0    0    0   6.00000   0.00000   0.00000   0.00000   0.00000
  107    0    0    Notts radiosonde
     0.000  1018.000     4.400     4.650     0.000     0.000ABC
     0.028  1016.000     5.600     4.930     0.000     0.000ABC
     0.258  1000.000     5.800     4.980     0.000     0.000ABC
     0.316   993.000     6.000     5.050     0.000     0.000ABC
     0.432   979.000     5.100     5.010     0.000     0.000ABC
     0.566   963.000     4.000     4.950     0.000     0.000ABC
     0.651   953.000     3.600     4.400     0.000     0.000ABC
     0.677   950.000     3.700     4.390     0.000     0.000ABC
     0.789   937.000     4.000     4.350     0.000     0.000ABC
     0.894   925.000     3.000     4.220     0.000     0.000ABC
     1.053   907.000     1.500     4.120     0.000     0.000ABC
     1.142   897.000     0.600     4.070     0.000     0.000ABC
     1.260   884.000     1.800     2.950     0.000     0.000ABC
     1.351   874.000     1.000     2.600     0.000     0.000ABC
     1.453   863.000     1.000     1.180     0.000     0.000ABC
     1.547   853.000     1.400     0.670     0.000     0.000ABC
     1.575   850.000     1.400     0.670     0.000     0.000ABC
     1.844   822.000    -0.300     0.450     0.000     0.000ABC
     2.119   794.000    -2.400     0.390     0.000     0.000ABC
     2.271   779.000    -3.500     0.350     0.000     0.000ABC
     2.383   768.000    -3.700     0.810     0.000     0.000ABC
     2.644   743.000    -4.500     0.590     0.000     0.000ABC
     2.718   736.000    -4.300     0.560     0.000     0.000ABC
     2.870   722.000    -4.900     0.490     0.000     0.000ABC
     2.990   711.000    -5.800     0.460     0.000     0.000ABC
     3.112   700.000    -6.700     0.430     0.000     0.000ABC
     3.157   696.000    -7.100     0.370     0.000     0.000ABC
     3.360   678.000    -7.700     0.280     0.000     0.000ABC
     3.372   677.000    -7.700     0.270     0.000     0.000ABC
     3.758   644.000   -10.900     0.500     0.000     0.000ABC
     3.987   625.000   -12.300     0.340     0.000     0.000ABC
     4.147   612.000   -13.700     0.710     0.000     0.000ABC
     4.184   609.000   -14.000     0.670     0.000     0.000ABC
     4.399   592.000   -15.500     0.470     0.000     0.000ABC
     4.749   565.000   -18.100     0.610     0.000     0.000ABC
     4.922   552.000   -19.300     0.460     0.000     0.000ABC
     5.058   542.000   -20.500     0.620     0.000     0.000ABC
     5.085   540.000   -20.700     0.600     0.000     0.000ABC
     5.363   520.000   -22.300     0.450     0.000     0.000ABC
     5.549   507.000   -23.900     0.450     0.000     0.000ABC
     5.621   502.000   -24.500     0.450     0.000     0.000ABC
     5.650   500.000   -24.700     0.450     0.000     0.000ABC
     5.767   492.000   -25.700     0.660     0.000     0.000ABC
     6.007   476.000   -26.900     0.280     0.000     0.000ABC
     6.191   464.000   -28.500     0.440     0.000     0.000ABC
     6.457   447.000   -30.700     0.470     0.000     0.000ABC
     6.634   436.000   -32.100     0.490     0.000     0.000ABC
     6.898   420.000   -33.100     0.450     0.000     0.000ABC
     7.240   400.000   -36.100     0.340     0.000     0.000ABC
     7.292   397.000   -36.500     0.330     0.000     0.000ABC
     7.503   385.000   -38.300     0.260     0.000     0.000ABC
     7.775   370.000   -39.900     0.240     0.000     0.000ABC
     7.960   360.000   -41.300     0.210     0.000     0.000ABC
     8.267   344.000   -43.700     0.160     0.000     0.000ABC
     8.645   325.000   -46.500     0.140     0.000     0.000ABC
     8.768   319.000   -47.300     0.120     0.000     0.000ABC
     8.830   316.000   -47.700     0.120     0.000     0.000ABC
     9.170   300.000   -50.500     0.090     0.000     0.000ABC
     9.324   293.000   -51.900     0.080     0.000     0.000ABC
     9.617   280.000   -53.700     0.060     0.000     0.000ABC
     9.710   276.000   -54.300     0.050     0.000     0.000ABC
    10.340   250.000   -58.100     0.030     0.000     0.000ABC
    10.597   240.000   -59.700     0.020     0.000     0.000ABC
    10.999   225.000   -62.100     0.020     0.000     0.000ABC
    11.340   213.000   -64.100     0.010     0.000     0.000ABC
    11.668   202.000   -61.500     0.020     0.000     0.000ABC
    11.730   200.000   -61.700     0.020     0.000     0.000ABC
    11.823   197.000   -61.900     0.020     0.000     0.000ABC
    12.048   190.000   -58.600     0.030     0.000     0.000ABC
    12.081   189.000   -58.100     0.030     0.000     0.000ABC
    12.283   183.000   -58.500     0.020     0.000     0.000ABC
    12.457   178.000   -58.100     0.020     0.000     0.000ABC
    12.746   170.000   -57.500     0.020     0.000     0.000ABC
    12.783   169.000   -57.600     0.020     0.000     0.000ABC
    13.009   163.000   -58.400     0.020     0.000     0.000ABC
```

```
    13.284   156.000   -59.300     0.010     0.000     0.000ABC
    13.365   154.000   -58.700     0.010     0.000     0.000ABC
    13.530   150.000   -57.500     0.010     0.000     0.000ABC
    13.878   142.000   -56.500     0.010     0.000     0.000ABC
    14.337   132.000   -60.500     0.010     0.000     0.000ABC
    14.433   130.000   -60.300     0.010     0.000     0.000ABC
    14.579   127.000   -59.900     0.010     0.000     0.000ABC
    14.984   119.000   -61.700     0.000     0.000     0.000ABC
    15.305   113.000   -61.100     0.000     0.000     0.000ABC
    15.360   112.000   -61.500     0.000     0.000     0.000ABC
    15.643   107.000   -63.300     0.000     0.000     0.000ABC
    15.759   105.000   -63.100     0.000     0.000     0.000ABC
    16.060   100.000   -62.500     0.000     0.000     0.000ABC
    16.373    95.000   -64.000     0.000     0.000     0.000ABC
    16.724    89.700   -65.700     0.000     0.000     0.000ABC
    16.840    88.000   -65.300     0.000     0.000     0.000ABC
    17.001    85.700   -64.700     0.000     0.000     0.000ABC
    17.336    81.100   -65.300     0.000     0.000     0.000ABC
    17.628    77.300   -64.700     0.000     0.000     0.000ABC
    17.976    73.000   -65.700     0.000     0.000     0.000ABC
    18.034    72.300   -65.900     0.000     0.000     0.000ABC
    18.230    70.000   -66.100     0.000     0.000     0.000ABC
    19.506    56.700   -66.500     0.000     0.000     0.000ABC
    19.691    55.000   -66.100     0.000     0.000     0.000ABC
    20.020    52.100   -65.300     0.000     0.000     0.000ABC
    20.032    52.000   -65.300     0.000     0.000     0.000ABC
    20.270    50.000   -65.700     0.010     0.000     0.000ABC
    20.515    48.000   -66.300     0.000     0.000     0.000ABC
    21.463    41.000   -68.800     0.000     0.000     0.000ABC
    21.872    38.300   -69.900     0.000     0.000     0.000ABC
    22.241    36.000   -69.900     0.000     0.000     0.000ABC
    22.291    35.700   -69.900     0.000     0.000     0.000ABC
     0.760     0.000   180.000     0.000     0.000
      1400     12400       100       100RMnext runN        0
    1
MM  7    3    1    0    0    0    3    3    3    3    1    0    0 270.150      0
ff  0f   0 365.00000        0.        0. f f f f       0.000
    5    2    2    0    0    0   6.00000   0.00000   0.00000   0.00000   0.00000
     0.760     0.000   180.000     0.000     0.000
      1400     12400       100       100RMnext runN        0
    1
MM  7    3    1    0    0    0    3    3    3    3    1    0    0 272.150      0
ff  0f   0 365.00000        0.        0. f f f f       0.000
    5    2    2    0    0    0   6.00000   0.00000   0.00000   0.00000   0.00000
     0.760     0.000   180.000     0.000     0.000
      1400     12400       100       100RMnext runN        0
    1
MM  7    3    1    0    0    0    3    3    3    3    1    0    0 274.150      0
ff  0f   0 365.00000        0.        0. f f f f       0.000
    5    2    2    0    0    0   6.00000   0.00000   0.00000   0.00000   0.00000
     0.760     0.000   180.000     0.000     0.000
      1400     12400       100       100RMnext runN        0
    1
MM  7    3    1    0    0    0    3    3    3    3    1    0    0 276.150      0
ff  0f   0 365.00000        0.        0. f f f f       0.000
    5    2    2    0    0    0   6.00000   0.00000   0.00000   0.00000   0.00000
     0.760     0.000   180.000     0.000     0.000
      1400     12400       100       100RMnext runN        0
    1
MM  7    3    1    0    0    0    3    3    3    3    1    0    0 278.150      0
ff  0f   0 365.00000        0.        0. f f f f       0.000
    5    2    2    0    0    0   6.00000   0.00000   0.00000   0.00000   0.00000
     0.760     0.000   180.000     0.000     0.000
      1400     12400       100       100RMnext runN        0
    1
MM  7    3    1    0    0    0    3    3    3    3    1    0    0 268.150      0
ff  0f   0 365.00000        0.        0. f f f f       0.000
    5    2    2    0    0    0   6.00000   0.00000   0.00000   0.00000   0.00000
     0.760     0.000   178.000     0.000     0.000
      1400     12400       100       100RMnext runN        0
    1
```

Pattern repeats with temperatures 268.150K to 278.15K for angles 180 to 150 degrees.

Final entry:

```
MM  7    3    1    0    0    0    3    3    3    3    1    0    0 278.150      0
ff  0f   0 365.00000        0.        0. f f f f       0.000
    5    2    2    0    0    0   6.00000   0.00000   0.00000   0.00000   0.00000
     0.760     0.000   150.000     0.000     0.000
      1400     12400       100       100RMnext runN        0
    0
```

For the calculation of downwelled radiance:

```
MM  7    3    1    0    0    0    3    3    3    3    1    1    0   0.000      1
ff  0f   0 365.00000        0.        0. f f f f       0.000
    5    2    2    0    0    0   6.00000   0.00000   0.00000   0.00000   0.00000
  107    0    0    Notts radiosonde
     0.000  1018.000     4.400     4.650     0.000     0.000ABC
     0.028  1016.000     5.600     4.930     0.000     0.000ABC
     0.258  1000.000     5.800     4.980     0.000     0.000ABC
     0.316   993.000     6.000     5.050     0.000     0.000ABC
     0.432   979.000     5.100     5.010     0.000     0.000ABC
     0.566   963.000     4.000     4.950     0.000     0.000ABC
     0.651   953.000     3.600     4.400     0.000     0.000ABC
     0.677   950.000     3.700     4.390     0.000     0.000ABC
     0.789   937.000     4.000     4.350     0.000     0.000ABC
     0.894   925.000     3.000     4.220     0.000     0.000ABC
     1.053   907.000     1.500     4.120     0.000     0.000ABC
     1.142   897.000     0.600     4.070     0.000     0.000ABC
     1.260   884.000     1.800     2.950     0.000     0.000ABC
     1.351   874.000     1.000     2.600     0.000     0.000ABC
     1.453   863.000     1.000     1.180     0.000     0.000ABC
     1.547   853.000     1.400     0.670     0.000     0.000ABC
     1.575   850.000     1.400     0.670     0.000     0.000ABC
     1.844   822.000    -0.300     0.450     0.000     0.000ABC
     2.119   794.000    -2.400     0.390     0.000     0.000ABC
     2.271   779.000    -3.500     0.350     0.000     0.000ABC
     2.383   768.000    -3.700     0.810     0.000     0.000ABC
     2.644   743.000    -4.500     0.590     0.000     0.000ABC
     2.718   736.000    -4.300     0.560     0.000     0.000ABC
     2.870   722.000    -4.900     0.490     0.000     0.000ABC
     2.990   711.000    -5.800     0.460     0.000     0.000ABC
     3.112   700.000    -6.700     0.430     0.000     0.000ABC
     3.157   696.000    -7.100     0.370     0.000     0.000ABC
     3.360   678.000    -7.700     0.280     0.000     0.000ABC
     3.372   677.000    -7.700     0.270     0.000     0.000ABC
     3.758   644.000   -10.900     0.500     0.000     0.000ABC
     3.987   625.000   -12.300     0.340     0.000     0.000ABC
     4.147   612.000   -13.700     0.710     0.000     0.000ABC
     4.184   609.000   -14.000     0.670     0.000     0.000ABC
     4.399   592.000   -15.500     0.470     0.000     0.000ABC
     4.749   565.000   -18.100     0.610     0.000     0.000ABC
     4.922   552.000   -19.300     0.460     0.000     0.000ABC
     5.058   542.000   -20.500     0.620     0.000     0.000ABC
     5.085   540.000   -20.700     0.600     0.000     0.000ABC
     5.363   520.000   -22.300     0.450     0.000     0.000ABC
     5.549   507.000   -23.900     0.450     0.000     0.000ABC
     5.621   502.000   -24.500     0.450     0.000     0.000ABC
     5.650   500.000   -24.700     0.450     0.000     0.000ABC
     5.767   492.000   -25.700     0.660     0.000     0.000ABC
     6.007   476.000   -26.900     0.280     0.000     0.000ABC
     6.191   464.000   -28.500     0.440     0.000     0.000ABC
     6.457   447.000   -30.700     0.470     0.000     0.000ABC
     6.634   436.000   -32.100     0.490     0.000     0.000ABC
     6.898   420.000   -33.100     0.450     0.000     0.000ABC
     7.240   400.000   -36.100     0.340     0.000     0.000ABC
     7.292   397.000   -36.500     0.330     0.000     0.000ABC
     7.503   385.000   -38.300     0.260     0.000     0.000ABC
     7.775   370.000   -39.900     0.240     0.000     0.000ABC
     7.960   360.000   -41.300     0.210     0.000     0.000ABC
     8.267   344.000   -43.700     0.160     0.000     0.000ABC
     8.645   325.000   -46.500     0.140     0.000     0.000ABC
     8.768   319.000   -47.300     0.120     0.000     0.000ABC
     8.830   316.000   -47.700     0.120     0.000     0.000ABC
     9.170   300.000   -50.500     0.090     0.000     0.000ABC
     9.324   293.000   -51.900     0.080     0.000     0.000ABC
     9.617   280.000   -53.700     0.060     0.000     0.000ABC
     9.710   276.000   -54.300     0.050     0.000     0.000ABC
    10.340   250.000   -58.100     0.030     0.000     0.000ABC
    10.597   240.000   -59.700     0.020     0.000     0.000ABC
    10.999   225.000   -62.100     0.020     0.000     0.000ABC
    11.340   213.000   -64.100     0.010     0.000     0.000ABC
    11.668   202.000   -61.500     0.020     0.000     0.000ABC
    11.730   200.000   -61.700     0.020     0.000     0.000ABC
    11.823   197.000   -61.900     0.020     0.000     0.000ABC
    12.048   190.000   -58.600     0.030     0.000     0.000ABC
    12.081   189.000   -58.100     0.030     0.000     0.000ABC
    12.283   183.000   -58.500     0.020     0.000     0.000ABC
    12.457   178.000   -58.100     0.020     0.000     0.000ABC
    12.746   170.000   -57.500     0.020     0.000     0.000ABC
    12.783   169.000   -57.600     0.020     0.000     0.000ABC
    13.009   163.000   -58.400     0.020     0.000     0.000ABC
    13.284   156.000   -59.300     0.010     0.000     0.000ABC
    13.365   154.000   -58.700     0.010     0.000     0.000ABC
    13.530   150.000   -57.500     0.010     0.000     0.000ABC
    13.878   142.000   -56.500     0.010     0.000     0.000ABC
    14.337   132.000   -60.500     0.010     0.000     0.000ABC
```

```
    14.433   130.000   -60.300     0.010     0.000     0.000ABC
    14.579   127.000   -59.900     0.010     0.000     0.000ABC
    14.984   119.000   -61.700     0.000     0.000     0.000ABC
    15.305   113.000   -61.100     0.000     0.000     0.000ABC
    15.360   112.000   -61.500     0.000     0.000     0.000ABC
    15.643   107.000   -63.300     0.000     0.000     0.000ABC
    15.759   105.000   -63.100     0.000     0.000     0.000ABC
    16.060   100.000   -62.500     0.000     0.000     0.000ABC
    16.373    95.000   -64.000     0.000     0.000     0.000ABC
    16.724    89.700   -65.700     0.000     0.000     0.000ABC
    16.840    88.000   -65.300     0.000     0.000     0.000ABC
    17.001    85.700   -64.700     0.000     0.000     0.000ABC
    17.336    81.100   -65.300     0.000     0.000     0.000ABC
    17.628    77.300   -64.700     0.000     0.000     0.000ABC
    17.976    73.000   -65.700     0.000     0.000     0.000ABC
    18.034    72.300   -65.900     0.000     0.000     0.000ABC
    18.230    70.000   -66.100     0.000     0.000     0.000ABC
    19.506    56.700   -66.500     0.000     0.000     0.000ABC
    19.691    55.000   -66.100     0.000     0.000     0.000ABC
    20.020    52.100   -65.300     0.000     0.000     0.000ABC
    20.032    52.000   -65.300     0.000     0.000     0.000ABC
    20.270    50.000   -65.700     0.010     0.000     0.000ABC
    20.515    48.000   -66.300     0.000     0.000     0.000ABC
    21.463    41.000   -68.800     0.000     0.000     0.000ABC
    21.872    38.300   -69.900     0.000     0.000     0.000ABC
    22.241    36.000   -69.900     0.000     0.000     0.000ABC
    22.291    35.700   -69.900     0.000     0.000     0.000ABC
     0.000     0.000     0.000     0.000     0.000
      1400     12400       100       100RMnext runN        0
    1
MM  7    3    1    0    0    0    3    3    3    3    1    0    0   0.000      1
ff  0f   0 365.00000        0.        0. f f f f       0.000
    5    2    2    0    0    0   6.00000   0.00000   0.00000   0.00000   0.00000
     0.000     0.000     1.000     0.000     0.000
      1400     12400       100       100RMnext runN        0
    1
MM  7    3    1    0    0    0    3    3    3    3    1    0    0   0.000      1
ff  0f   0 365.00000        0.        0. f f f f       0.000
    5    2    2    0    0    0   6.00000   0.00000   0.00000   0.00000   0.00000
     0.000     0.000     2.000     0.000     0.000
      1400     12400       100       100RMnext runN        0
    1
MM  7    3    1    0    0    0    3    3    3    3    1    0    0   0.000      1
ff  0f   0 365.00000        0.        0. f f f f       0.000
    5    2    2    0    0    0   6.00000   0.00000   0.00000   0.00000   0.00000
     0.000     0.000     3.000     0.000     0.000
      1400     12400       100       100RMnext runN        0
    1
MM  7    3    1    0    0    0    3    3    3    3    1    0    0   0.000      1
ff  0f   0 365.00000        0.        0. f f f f       0.000
    5    2    2    0    0    0   6.00000   0.00000   0.00000   0.00000   0.00000
     0.000     0.000     4.000     0.000     0.000
      1400     12400       100       100RMnext runN        0
    1
MM  7    3    1    0    0    0    3    3    3    3    1    0    0   0.000      1
ff  0f   0 365.00000        0.        0. f f f f       0.000
    5    2    2    0    0    0   6.00000   0.00000   0.00000   0.00000   0.00000
     0.000     0.000     5.000     0.000     0.000
      1400     12400       100       100RMnext runN        0
    1
MM  7    3    1    0    0    0    3    3    3    3    1    0    0   0.000      1
ff  0f   0 365.00000        0.        0. f f f f       0.000
    5    2    2    0    0    0   6.00000   0.00000   0.00000   0.00000   0.00000
     0.000     0.000     6.000     0.000     0.000
      1400     12400       100       100RMnext runN        0
    1
```

Pattern repeats for angles 0 to 90 degrees in 1-degree increments.

Final entry:

```
MM  7    3    1    0    0    0    3    3    3    3    1    0    0   0.000      1
ff  0f   0 365.00000        0.        0. f f f f       0.000
    5    2    2    0    0    0   6.00000   0.00000   0.00000   0.00000   0.00000
     0.000     0.000    90.000     0.000     0.000
      1400     12400       100       100RMnext runN        0
    0
```

For the calculation of broad band sky temperature:

```
MM  7    3    1    0    0    0    3    3    3    3    1    1    0   0.000      1
ff  0f   0 365.00000        0.        0. f f f f       0.000
    5    2    2    0    0    0   6.00000   0.00000   0.00000   0.00000   0.00000
  107    0    0    Notts radiosonde
     0.000  1018.000     4.400     4.650     0.000     0.000ABC
     0.028  1016.000     5.600     4.930     0.000     0.000ABC
     0.258  1000.000     5.800     4.980     0.000     0.000ABC
     0.316   993.000     6.000     5.050     0.000     0.000ABC
     0.432   979.000     5.100     5.010     0.000     0.000ABC
     0.566   963.000     4.000     4.950     0.000     0.000ABC
     0.651   953.000     3.600     4.400     0.000     0.000ABC
     0.677   950.000     3.700     4.390     0.000     0.000ABC
     0.789   937.000     4.000     4.350     0.000     0.000ABC
     0.894   925.000     3.000     4.220     0.000     0.000ABC
     1.053   907.000     1.500     4.120     0.000     0.000ABC
     1.142   897.000     0.600     4.070     0.000     0.000ABC
     1.260   884.000     1.800     2.950     0.000     0.000ABC
     1.351   874.000     1.000     2.600     0.000     0.000ABC
     1.453   863.000     1.000     1.180     0.000     0.000ABC
     1.547   853.000     1.400     0.670     0.000     0.000ABC
     1.575   850.000     1.400     0.670     0.000     0.000ABC
     1.844   822.000    -0.300     0.450     0.000     0.000ABC
     2.119   794.000    -2.400     0.390     0.000     0.000ABC
     2.271   779.000    -3.500     0.350     0.000     0.000ABC
     2.383   768.000    -3.700     0.810     0.000     0.000ABC
     2.644   743.000    -4.500     0.590     0.000     0.000ABC
     2.718   736.000    -4.300     0.560     0.000     0.000ABC
     2.870   722.000    -4.900     0.490     0.000     0.000ABC
     2.990   711.000    -5.800     0.460     0.000     0.000ABC
     3.112   700.000    -6.700     0.430     0.000     0.000ABC
     3.157   696.000    -7.100     0.370     0.000     0.000ABC
     3.360   678.000    -7.700     0.280     0.000     0.000ABC
     3.372   677.000    -7.700     0.270     0.000     0.000ABC
     3.758   644.000   -10.900     0.500     0.000     0.000ABC
     3.987   625.000   -12.300     0.340     0.000     0.000ABC
     4.147   612.000   -13.700     0.710     0.000     0.000ABC
     4.184   609.000   -14.000     0.670     0.000     0.000ABC
     4.399   592.000   -15.500     0.470     0.000     0.000ABC
     4.749   565.000   -18.100     0.610     0.000     0.000ABC
     4.922   552.000   -19.300     0.460     0.000     0.000ABC
     5.058   542.000   -20.500     0.620     0.000     0.000ABC
     5.085   540.000   -20.700     0.600     0.000     0.000ABC
     5.363   520.000   -22.300     0.450     0.000     0.000ABC
     5.549   507.000   -23.900     0.450     0.000     0.000ABC
     5.621   502.000   -24.500     0.450     0.000     0.000ABC
     5.650   500.000   -24.700     0.450     0.000     0.000ABC
     5.767   492.000   -25.700     0.660     0.000     0.000ABC
     6.007   476.000   -26.900     0.280     0.000     0.000ABC
     6.191   464.000   -28.500     0.440     0.000     0.000ABC
     6.457   447.000   -30.700     0.470     0.000     0.000ABC
     6.634   436.000   -32.100     0.490     0.000     0.000ABC
     6.898   420.000   -33.100     0.450     0.000     0.000ABC
     7.240   400.000   -36.100     0.340     0.000     0.000ABC
     7.292   397.000   -36.500     0.330     0.000     0.000ABC
     7.503   385.000   -38.300     0.260     0.000     0.000ABC
     7.775   370.000   -39.900     0.240     0.000     0.000ABC
     7.960   360.000   -41.300     0.210     0.000     0.000ABC
     8.267   344.000   -43.700     0.160     0.000     0.000ABC
     8.645   325.000   -46.500     0.140     0.000     0.000ABC
     8.768   319.000   -47.300     0.120     0.000     0.000ABC
     8.830   316.000   -47.700     0.120     0.000     0.000ABC
     9.170   300.000   -50.500     0.090     0.000     0.000ABC
     9.324   293.000   -51.900     0.080     0.000     0.000ABC
     9.617   280.000   -53.700     0.060     0.000     0.000ABC
     9.710   276.000   -54.300     0.050     0.000     0.000ABC
    10.340   250.000   -58.100     0.030     0.000     0.000ABC
    10.597   240.000   -59.700     0.020     0.000     0.000ABC
    10.999   225.000   -62.100     0.020     0.000     0.000ABC
    11.340   213.000   -64.100     0.010     0.000     0.000ABC
    11.668   202.000   -61.500     0.020     0.000     0.000ABC
    11.730   200.000   -61.700     0.020     0.000     0.000ABC
    11.823   197.000   -61.900     0.020     0.000     0.000ABC
    12.048   190.000   -58.600     0.030     0.000     0.000ABC
    12.081   189.000   -58.100     0.030     0.000     0.000ABC
    12.283   183.000   -58.500     0.020     0.000     0.000ABC
    12.457   178.000   -58.100     0.020     0.000     0.000ABC
    12.746   170.000   -57.500     0.020     0.000     0.000ABC
    12.783   169.000   -57.600     0.020     0.000     0.000ABC
    13.009   163.000   -58.400     0.020     0.000     0.000ABC
    13.284   156.000   -59.300     0.010     0.000     0.000ABC
    13.365   154.000   -58.700     0.010     0.000     0.000ABC
    13.530   150.000   -57.500     0.010     0.000     0.000ABC
    13.878   142.000   -56.500     0.010     0.000     0.000ABC
    14.337   132.000   -60.500     0.010     0.000     0.000ABC
```

```
    14.433   130.000   -60.300     0.010     0.000     0.000ABC
    14.579   127.000   -59.900     0.010     0.000     0.000ABC
    14.984   119.000   -61.700     0.000     0.000     0.000ABC
    15.305   113.000   -61.100     0.000     0.000     0.000ABC
    15.360   112.000   -61.500     0.000     0.000     0.000ABC
    15.643   107.000   -63.300     0.000     0.000     0.000ABC
    15.759   105.000   -63.100     0.000     0.000     0.000ABC
    16.060   100.000   -62.500     0.000     0.000     0.000ABC
    16.373    95.000   -64.000     0.000     0.000     0.000ABC
    16.724    89.700   -65.700     0.000     0.000     0.000ABC
    16.840    88.000   -65.300     0.000     0.000     0.000ABC
    17.001    85.700   -64.700     0.000     0.000     0.000ABC
    17.336    81.100   -65.300     0.000     0.000     0.000ABC
    17.628    77.300   -64.700     0.000     0.000     0.000ABC
    17.976    73.000   -65.700     0.000     0.000     0.000ABC
    18.034    72.300   -65.900     0.000     0.000     0.000ABC
    18.230    70.000   -66.100     0.000     0.000     0.000ABC
    19.506    56.700   -66.500     0.000     0.000     0.000ABC
    19.691    55.000   -66.100     0.000     0.000     0.000ABC
    20.020    52.100   -65.300     0.000     0.000     0.000ABC
    20.032    52.000   -65.300     0.000     0.000     0.000ABC
    20.270    50.000   -65.700     0.010     0.000     0.000ABC
    20.515    48.000   -66.300     0.000     0.000     0.000ABC
    21.463    41.000   -68.800     0.000     0.000     0.000ABC
    21.872    38.300   -69.900     0.000     0.000     0.000ABC
    22.241    36.000   -69.900     0.000     0.000     0.000ABC
    22.291    35.700   -69.900     0.000     0.000     0.000ABC
     0.000     0.000     0.000     0.000     0.000
       100      3000         2         2RMnext runw        0
    1
MM  7    3    1    0    0    0    3    3    3    3    1    0    0   0.000      1
ff  0f   0 365.00000        0.        0. f f f f       0.000
    5    2    2    0    0    0   6.00000   0.00000   0.00000   0.00000   0.00000
     0.000     0.000     1.000     0.000     0.000
       100      3000         2         2RMnext runw        0
    1
MM  7    3    1    0    0    0    3    3    3    3    1    0    0   0.000      1
ff  0f   0 365.00000        0.        0. f f f f       0.000
    5    2    2    0    0    0   6.00000   0.00000   0.00000   0.00000   0.00000
     0.000     0.000     2.000     0.000     0.000
       100      3000         2         2RMnext runw        0
    1
MM  7    3    1    0    0    0    3    3    3    3    1    0    0   0.000      1
ff  0f   0 365.00000        0.        0. f f f f       0.000
    5    2    2    0    0    0   6.00000   0.00000   0.00000   0.00000   0.00000
     0.000     0.000     3.000     0.000     0.000
       100      3000         2         2RMnext runw        0
    1
MM  7    3    1    0    0    0    3    3    3    3    1    0    0   0.000      1
ff  0f   0 365.00000        0.        0. f f f f       0.000
    5    2    2    0    0    0   6.00000   0.00000   0.00000   0.00000   0.00000
     0.000     0.000     4.000     0.000     0.000
       100      3000         2         2RMnext runw        0
    1
MM  7    3    1    0    0    0    3    3    3    3    1    0    0   0.000      1
ff  0f   0 365.00000        0.        0. f f f f       0.000
    5    2    2    0    0    0   6.00000   0.00000   0.00000   0.00000   0.00000
     0.000     0.000     5.000     0.000     0.000
       100      3000         2         2RMnext runw        0
    1
MM  7    3    1    0    0    0    3    3    3    3    1    0    0   0.000      1
ff  0f   0 365.00000        0.        0. f f f f       0.000
    5    2    2    0    0    0   6.00000   0.00000   0.00000   0.00000   0.00000
     0.000     0.000     6.000     0.000     0.000
       100      3000         2         2RMnext runw        0
    1
```

Pattern repeats for angles 0 to 90 degrees in 1-degree increments.

Final entry:

```
MM  7    3    1    0    0    0    3    3    3    3    1    0    0   0.000      1
ff  0f   0 365.00000        0.        0. f f f f       0.000
    5    2    2    0    0    0   6.00000   0.00000   0.00000   0.00000   0.00000
     0.000     0.000    90.000     0.000     0.000
       100      3000         2         2RMnext runw        0
    0
```

Appendix 4: Spreadsheet of inputs and outputs

	GIS analysis					Site survey			Materials properties		Weather data		Building data			Sensor model results										Building model results		
Address	**Digital number (1.1m buffer)**	**Distance from flight line**	**Building orientation**	**Building length (ridge)**	**Building width**	**Roof slope**	**Building type: 1=end 2=mid**	**Sky view factor**	**Spectral emissivity of roof material**	**Broad band emissivity**	**Ambient air temperature**	**Wind speed**	**Building internal temperature**	**Loft space air changes**	**From the council database**	**Sensor angle**	**Line of sight angle**	**Directional emissivity**	**At sensor radiance**	**Upwelled radiance**	**Atmospheric transmission**	**Downwelled radiance**	**Surface BB radiance**	**Roof surface temperature**	**Braodband sky temperature**	**Roof temp from council database**	**Difference**
	0-255	m	°	m	m	°	-	-	-	-	°C	m/s	C	hr^{-1}	mm	°	°	-	W/m^2	W/m^2	W/m^2	W/m^2	W/m^2	°C	K	K	K
7 NORTHWOOD	103.833	227	87	6.00	6.62	45.0	1	0.734	0.881	0.881	4.5	2.42	18.0	2.0	100	16.6	46.5	0.858	18.26	3.53	0.83	7.41	19.00	0.86	261.0	0.69	-0.17
16 NORTHWOOD	113.941	199	72	5.77	6.82	45.0	1	0.734	0.881	0.881	4.5	2.42	18.0	2.0	150	14.7	42.3	0.863	18.56	3.50	0.83	7.41	19.37	1.81	261.0	0.59	-1.22
18 NORTHWOOD	111.692	190	52	5.24	6.77	45.0	1	0.734	0.881	0.881	4.5	2.42	18.0	2.0	100	14.0	37.7	0.867	18.50	3.50	0.83	7.41	19.24	1.48	261.0	0.76	-0.72
21 NORTHWOOD	110.867	182	65	5.90	6.51	45.0	2	0.734	0.881	0.881	4.5	2.42	18.0	2.0	100	13.5	40.8	0.864	18.47	3.49	0.83	7.41	19.23	1.47	261.0	0.44	-1.02
31 NORTHWOOD	121.933	154	53	5.50	6.37	45.0	1	0.734	0.881	0.881	4.5	2.42	18.0	2.0	100	11.5	39.0	0.866	18.80	3.47	0.83	7.41	19.66	2.57	261.0	0.76	-1.81
57 NORTHWOOD	114.059	116	15	5.75	6.77	45.0	1	0.734	0.881	0.881	4.5	2.42	18.0	2.0	100	8.7	36.7	0.868	18.57	3.46	0.83	7.41	19.33	1.72	261.0	0.71	-1.02
64 NORTHWOOD	115.421	156	24	6.02	6.76	45.0	1	0.734	0.881	0.881	4.5	2.42	18.0	2.0	75	11.6	34.7	0.869	18.61	3.48	0.83	7.41	19.37	1.82	261.0	0.76	-1.06
65 NORTHWOOD	116.625	125	26	5.93	6.51	45.0	1	0.734	0.881	0.881	4.5	2.42	18.0	2.0	100	9.3	36.8	0.867	18.64	3.46	0.83	7.41	19.44	1.99	261.0	0.70	-1.28
73 NORTHWOOD	108.765	138	43	5.93	6.87	45.0	1	0.734	0.881	0.881	4.5	2.42	18.0	2.0	75	10.3	38.0	0.866	18.41	3.47	0.83	7.41	19.13	1.20	261.0	0.76	-0.44
8 ELTHAM	107.438	91	38	5.60	6.60	45.0	2	0.734	0.881	0.881	4.5	2.42	18.0	2.0	150	6.8	39.8	0.865	18.37	3.45	0.83	7.41	19.10	1.11	261.0	0.34	-0.77
12 ELTHAM	106.000	73	52	5.60	6.60	45.0	1	0.734	0.881	0.881	4.5	2.42	18.0	2.0	150	5.5	41.8	0.863	18.33	3.44	0.83	7.41	19.06	1.01	261.0	0.62	-0.39
18 ELTHAM	102.125	60	52	5.70	6.50	45.0	1	0.734	0.881	0.881	4.5	2.42	18.0	2.0	150	4.5	42.3	0.863	18.21	3.44	0.83	7.41	18.91	0.62	261.0	0.62	0.00
22 ELTHAM	107.786	43	37	5.70	6.30	45.0	2	0.734	0.881	0.881	4.5	2.42	18.0	2.0	150	3.2	42.4	0.862	18.38	3.43	0.83	7.41	19.14	1.21	261.0	0.36	-0.85
28 ELTHAM	97.813	38	53	5.70	6.40	45.0	1	0.734	0.881	0.881	4.5	2.42	18.0	2.0	150	2.9	43.3	0.862	18.08	3.43	0.83	7.41	18.75	0.19	261.0	0.62	0.43
34 ELTHAM	104.214	52	53	5.60	6.60	45.0	1	0.734	0.881	0.881	4.5	2.42	18.0	2.0	150	3.9	42.7	0.862	18.27	3.43	0.83	7.41	19.00	0.85	261.0	0.62	-0.23
38 ELTHAM	105.067	63	38	5.80	6.60	45.0	2	0.734	0.881	0.881	4.5	2.42	18.0	2.0	150	4.7	41.3	0.863	18.30	3.44	0.83	7.41	19.02	0.90	261.0	0.33	-0.58
40 ELTHAM	108.188	60	38	5.70	6.60	45.0	2	0.734	0.881	0.881	4.5	2.42	18.0	2.0	150	4.5	41.5	0.863	18.39	3.44	0.83	7.41	19.14	1.23	261.0	0.33	-0.89
52 ELTHAM	106.750	32	38	5.70	6.60	45.0	1	0.734	0.881	0.881	4.5	2.42	18.0	2.0	150	2.4	43.1	0.862	18.35	3.43	0.83	7.41	19.10	1.12	261.0	0.61	-0.51
41 ELTHAM	89.000	13	37	5.90	6.80	18.4	1	0.832	0.925	0.925	4.5	2.42	18.0	2.0	150	1.0	17.7	0.922	17.82	3.43	0.83	7.41	17.96	-1.88	261.0	0.21	2.10
56 ELTHAM	82.529	17	37	5.70	6.80	18.4	1	0.832	0.925	0.925	4.5	2.42	18.0	2.0	150	1.3	17.4	0.922	17.63	3.43	0.83	7.41	17.72	-2.56	261.0	0.23	2.79
59 ELTHAM	84.875	27	37	5.60	6.60	18.4	2	0.832	0.925	0.925	4.5	2.42	18.0	2.0	150	2.0	16.9	0.922	17.70	3.43	0.83	7.41	17.80	-2.32	261.0	-0.07	2.25
77 ELTHAM	76.667	62	37	5.90	6.50	18.4	2	0.832	0.925	0.925	4.5	2.42	18.0	2.0	150	4.7	15.0	0.923	17.45	3.44	0.83	7.41	17.48	-3.20	261.0	-0.08	3.11
78 ELTHAM	77.000	61	37	5.60	6.50	18.4	1	0.832	0.925	0.925	4.5	2.42	18.0	2.0	150	4.6	15.0	0.923	17.46	3.44	0.83	7.41	17.49	-3.16	261.0	0.27	3.43
82 ELTHAM	78.733	71	37	5.70	6.50	18.4	2	0.832	0.925	0.925	4.5	2.42	18.0	2.0	150	5.3	14.5	0.923	17.51	3.44	0.83	7.41	17.56	-2.99	261.0	-0.07	2.92
83 ELTHAM	72.600	76	37	5.70	6.70	18.4	2	0.832	0.925	0.925	4.5	2.42	18.0	2.0	150	5.7	14.3	0.923	17.33	3.44	0.83	7.41	17.32	-3.64	261.0	-0.09	3.55
108 ELTHAM	69.667	123	37	5.70	6.50	18.4	2	0.832	0.925	0.925	4.5	2.42	18.0	2.0	150	9.2	12.4	0.923	17.24	3.46	0.83	7.41	17.20	-3.97	261.0	-0.07	3.90
112 ELTHAM	88.643	132	37	5.30	6.60	18.4	1	0.832	0.925	0.925	4.5	2.42	18.0	2.0	150	9.9	12.1	0.924	17.81	3.46	0.83	7.41	17.93	-1.98	261.0	0.30	2.28
116 ELTHAM	82.000	139	37	5.90	6.50	18.4	2	0.832	0.925	0.925	4.5	2.42	18.0	2.0	150	10.4	11.9	0.924	17.61	3.47	0.83	7.41	17.67	-2.68	261.0	-0.08	2.59
122 ELTHAM	70.563	155	59	5.90	6.70	18.4	2	0.832	0.925	0.925	4.5	2.42	18.0	2.0	150	11.5	15.8	0.923	17.27	3.47	0.83	7.41	17.24	-3.86	261.0	-0.10	3.76
123 ELTHAM	78.810	250	62	5.60	6.60	18.4	1	0.832	0.925	0.925	4.5	2.42	18.0	2.0	150	18.2	18.6	0.922	17.51	3.55	0.83	7.41	17.55	-3.01	261.0	0.26	3.27
129 ELTHAM	89.333	268	54	5.70	6.40	18.4	2	0.832	0.925	0.925	4.5	2.42	18.0	2.0	150	19.4	17.0	0.922	17.83	3.56	0.83	7.41	17.95	-1.93	261.0	-0.06	1.87
132 ELTHAM	78.813	190	82	5.90	6.50	18.4	1	0.832	0.925	0.925	4.5	2.42	18.0	2.0	150	14.0	21.4	0.920	17.52	3.50	0.83	7.41	17.57	-2.95	261.0	0.23	3.18
155 ELTHAM	91.071	304	8	6.00	6.30	18.4	1	0.832	0.925	0.925	4.5	2.42	18.0	2.0	150	21.8	4.3	0.925	17.88	3.60	0.82	7.41	17.98	-1.84	261.0	0.24	2.07
1 FENWICK	105.643	163	25	5.35	6.60	45.0	1	0.734	0.881	0.881	4.5	2.42	18.0	2.0	200	12.1	34.3	0.869	18.32	3.48	0.83	7.41	18.98	0.80	261.0	0.60	-0.20

3 FENWICK	101.467	155	30	6.10	6.20	45.0	1	0.734	0.881	0.881	4.5	2.42	18.0	2.0	200	11.5	35.4	0.869	18.19	3.48	0.83	7.41	18.82	0.39	261.0	0.54	0.15
4 FENWICK	114.133	211	44	5.40	6.40	45.0	1	0.734	0.881	0.881	4.5	2.42	18.0	2.0	200	15.5	35.2	0.869	18.57	3.51	0.83	7.41	19.32	1.68	261.0	0.60	-1.08
6 FENWICK	105.200	207	44	6.00	6.40	45.0	2	0.734	0.881	0.881	4.5	2.42	18.0	2.0	200	15.2	35.3	0.869	18.30	3.51	0.83	7.41	18.96	0.76	261.0	0.27	-0.49
8 FENWICK	102.800	202	44	5.60	6.30	45.0	2	0.734	0.881	0.881	4.5	2.42	18.0	2.0	200	14.9	35.5	0.868	18.23	3.51	0.83	7.41	18.87	0.51	261.0	0.31	-0.20
9 FENWICK	107.000	147	21	5.70	6.20	45.0	2	0.734	0.881	0.881	4.5	2.42	18.0	2.0	200	10.9	35.0	0.869	18.36	3.47	0.83	7.41	19.04	0.96	261.0	0.31	-0.65
14 FENWICK	101.929	189	33	5.80	6.10	45.0	2	0.734	0.881	0.881	4.5	2.42	18.0	2.0	200	13.9	34.0	0.870	18.21	3.50	0.83	7.41	18.82	0.40	261.0	0.31	-0.09
15 FENWICK	110.867	141	4	5.80	6.30	45.0	1	0.734	0.881	0.881	4.5	2.42	18.0	2.0	200	10.5	34.5	0.869	18.47	3.47	0.83	7.41	19.19	1.35	261.0	0.56	-0.79
16 FENWICK	105.500	186	33	5.40	6.10	45.0	2	0.734	0.881	0.881	4.5	2.42	18.0	2.0	75	13.7	34.2	0.869	18.31	3.49	0.83	7.41	18.97	0.78	261.0	0.59	-0.18
17 FENWICK	113.308	140	4	5.80	6.30	45.0	2	0.734	0.881	0.881	4.5	2.42	18.0	2.0	200	10.5	34.6	0.869	18.55	3.47	0.83	7.41	19.29	1.60	261.0	0.29	-1.31
18 FENWICK	111.500	182	33	5.80	6.10	45.0	1	0.734	0.881	0.881	4.5	2.42	18.0	2.0	200	13.5	34.3	0.869	18.49	3.49	0.83	7.41	19.21	1.40	261.0	0.58	-0.83
21 FENWICK	106.500	140	4	5.80	6.30	45.0	1	0.734	0.881	0.881	4.5	2.42	18.0	2.0	200	10.4	34.6	0.869	18.34	3.47	0.83	7.41	19.02	0.90	261.0	0.56	-0.34
25 FENWICK	95.733	140	8	5.60	6.50	45.0	2	0.734	0.881	0.881	4.5	2.42	18.0	2.0	100	10.5	34.7	0.869	18.02	3.47	0.83	7.41	18.59	-0.22	261.0	0.47	0.69
26 FENWICK	110.929	173	18	5.70	6.40	45.0	1	0.734	0.881	0.881	4.5	2.42	18.0	2.0	200	12.8	33.0	0.870	18.47	3.49	0.83	7.41	19.18	1.32	261.0	0.57	-0.75
27 FENWICK	99.643	141	8	5.50	6.50	45.0	2	0.734	0.881	0.881	4.5	2.42	18.0	2.0	200	10.5	34.6	0.869	18.14	3.47	0.83	7.41	18.74	0.19	261.0	0.30	0.12
28 FENWICK	100.188	172	1	5.80	6.20	45.0	1	0.734	0.881	0.881	4.5	2.42	18.0	2.0	200	12.7	32.3	0.871	18.15	3.49	0.83	7.41	18.75	0.20	261.0	0.57	0.37
29 FENWICK	102.600	142	8	5.50	6.50	45.0	1	0.734	0.881	0.881	4.5	2.42	18.0	2.0	200	10.6	34.5	0.869	18.23	3.47	0.83	7.41	18.86	0.49	261.0	0.59	0.09
30 FENWICK	96.231	171	1	5.80	6.20	45.0	2	0.734	0.881	0.881	4.5	2.42	18.0	2.0	200	12.7	32.3	0.871	18.04	3.48	0.83	7.41	18.59	-0.22	261.0	0.30	0.52
31 FENWICK	103.000	144	24	5.60	6.30	45.0	1	0.734	0.881	0.881	4.5	2.42	18.0	2.0	200	10.8	35.4	0.868	18.24	3.47	0.83	7.41	18.88	0.55	261.0	0.59	0.04
33 FENWICK	98.000	147	24	5.60	6.30	45.0	2	0.734	0.881	0.881	4.5	2.42	18.0	2.0	100	10.9	35.3	0.869	18.09	3.47	0.83	7.41	18.68	0.03	261.0	0.48	0.46
34 FENWICK	104.786	172	1	5.40	6.20	45.0	1	0.734	0.881	0.881	4.5	2.42	18.0	2.0	200	12.8	32.3	0.871	18.29	3.49	0.83	7.41	18.93	0.67	261.0	0.61	-0.06
35 FENWICK	100.769	149	24	5.60	6.30	45.0	2	0.734	0.881	0.881	4.5	2.42	18.0	2.0	100	11.1	35.1	0.869	18.17	3.47	0.83	7.41	18.79	0.31	261.0	0.48	0.17
38 FENWICK	101.688	176	20	5.80	6.40	45.0	2	0.734	0.881	0.881	4.5	2.42	18.0	2.0	200	13.0	33.0	0.870	18.20	3.49	0.83	7.41	18.81	0.36	261.0	0.29	-0.08
39 FENWICK	97.923	156	24	5.60	6.40	45.0	1	0.734	0.881	0.881	4.5	2.42	18.0	2.0	200	11.6	34.7	0.869	18.09	3.48	0.83	7.41	18.67	0.01	261.0	0.58	0.58
40 FENWICK	103.667	178	20	5.60	6.40	45.0	2	0.734	0.881	0.881	4.5	2.42	18.0	2.0	200	13.2	32.9	0.870	18.26	3.49	0.83	7.41	18.89	0.57	261.0	0.30	-0.26
42 FENWICK	104.400	180	20	5.80	6.40	45.0	1	0.734	0.881	0.881	4.5	2.42	18.0	2.0	200	13.3	32.7	0.870	18.28	3.49	0.83	7.41	18.92	0.64	261.0	0.56	-0.08
44 FENWICK	101.071	185	33	5.40	6.40	45.0	1	0.734	0.881	0.881	4.5	2.42	18.0	2.0	100	13.7	34.2	0.869	18.18	3.49	0.83	7.41	18.79	0.32	261.0	0.77	0.45
45 FENWICK	106.000	200	59	5.60	6.60	45.0	1	0.734	0.881	0.881	4.5	2.42	18.0	2.0	200	14.7	39.1	0.866	18.33	3.50	0.83	7.41	19.02	0.92	261.0	0.57	-0.35
46 FENWICK	104.176	188	33	5.90	6.40	45.0	1	0.734	0.881	0.881	4.5	2.42	18.0	2.0	200	13.9	34.0	0.870	18.27	3.50	0.83	7.41	18.91	0.64	261.0	0.55	-0.09
47 FENWICK	102.571	208	67	5.70	6.60	45.0	1	0.734	0.881	0.881	4.5	2.42	18.0	2.0	200	15.3	41.0	0.864	18.22	3.51	0.83	7.41	18.90	0.60	261.0	0.56	-0.04
49 FENWICK	99.941	214	67	5.80	6.60	45.0	2	0.734	0.881	0.881	4.5	2.42	18.0	2.0	200	15.7	40.9	0.864	18.15	3.52	0.83	7.41	18.79	0.32	261.0	0.27	-0.05
51 FENWICK	95.438	219	67	5.80	6.60	45.0	2	0.734	0.881	0.881	4.5	2.42	18.0	2.0	200	16.1	40.9	0.864	18.01	3.52	0.83	7.41	18.61	-0.16	261.0	0.27	0.43
52 FENWICK	100.000	223	70	5.70	6.20	45.0	1	0.734	0.881	0.881	4.5	2.42	18.0	2.0	200	16.3	41.7	0.863	18.15	3.52	0.83	7.41	18.80	0.34	261.0	0.58	0.24
53 FENWICK	98.063	225	67	5.70	6.60	45.0	1	0.734	0.881	0.881	4.5	2.42	18.0	2.0	200	16.5	40.9	0.864	18.09	3.52	0.83	7.41	18.72	0.12	261.0	0.56	0.44
54 FENWICK	106.071	228	70	5.40	6.20	45.0	2	0.734	0.881	0.881	4.5	2.42	18.0	2.0	100	16.7	41.7	0.863	18.33	3.53	0.83	7.41	19.04	0.97	261.0	0.51	-0.47
55 FENWICK	97.625	234	89	5.50	6.50	45.0	1	0.734	0.881	0.881	4.5	2.42	18.0	2.0	200	17.1	47.2	0.857	18.08	3.53	0.83	7.41	18.76	0.22	261.0	0.59	0.36
57 FENWICK	101.375	240	89	5.80	6.50	45.0	2	0.734	0.881	0.881	4.5	2.42	18.0	2.0	200	17.5	47.3	0.857	18.19	3.54	0.83	7.41	18.91	0.62	261.0	0.28	-0.34
58 FENWICK	108.143	239	70	5.60	6.20	45.0	1	0.734	0.881	0.881	4.5	2.42	18.0	2.0	200	17.4	41.7	0.863	18.39	3.54	0.83	7.41	19.13	1.19	261.0	0.59	-0.59
59 FENWICK	93.308	246	89	5.60	6.50	45.0	2	0.734	0.881	0.881	4.5	2.42	18.0	2.0	200	17.9	47.4	0.857	17.95	3.54	0.83	7.41	18.58	-0.23	261.0	-0.34	-0.11
60 FENWICK	99.563	249	90	5.90	6.40	45.0	1	0.734	0.881	0.881	4.5	2.42	18.0	2.0	200	18.1	47.8	0.857	18.13	3.54	0.83	7.41	18.84	0.44	261.0	0.55	0.11
61 FENWICK	99.000	251	89	5.80	6.50	45.0	1	0.734	0.881	0.881	4.5	2.42	18.0	2.0	200	18.3	47.5	0.857	18.12	3.55	0.83	7.41	18.81	0.37	261.0	0.55	0.18
62 FENWICK	102.750	254	90	5.60	6.40	45.0	2	0.734	0.881	0.881	4.5	2.42	18.0	2.0	200	18.5	47.9	0.857	18.23	3.55	0.83	7.41	18.97	0.78	261.0	0.30	-0.47
64 FENWICK	100.250	260	90	5.70	6.40	45.0	2	0.734	0.881	0.881	4.5	2.42	18.0	2.0	100	18.9	48.0	0.857	18.16	3.55	0.83	7.41	18.87	0.51	261.0	0.47	-0.05
66 FENWICK	102.875	266	90	5.80	6.40	45.0	1	0.734	0.881	0.881	4.5	2.42	18.0	2.0	200	19.3	48.1	0.856	18.23	3.56	0.83	7.41	18.97	0.79	261.0	0.56	-0.23
67 FENWICK	100.214	273	97	5.70	6.60	45.0	2	0.734	0.881	0.881	4.5	2.42	18.0	2.0	200	19.8	50.5	0.854	18.15	3.57	0.83	7.41	18.89	0.58	261.0	0.28	-0.30
68 FENWICK	100.467	276	17	6.20	6.30	45.0	1	0.734	0.881	0.881	4.5	2.42	18.0	2.0	200	19.9	26.5	0.874	18.16	3.57	0.83	7.41	18.71	0.10	261.0	0.52	0.42
69 FENWICK	96.600	279	83	5.70	6.60	45.0	1	0.734	0.881	0.881	4.5	2.42	18.0	2.0	200	20.1	46.1	0.859	18.05	3.57	0.83	7.41	18.70	0.06	261.0	0.56	0.49
70 FENWICK	100.143	281	17	5.50	6.30	45.0	2	0.734	0.881	0.881	4.5	2.42	18.0	2.0	200	20.3	26.1	0.874	18.15	3.57	0.83	7.41	18.69	0.06	261.0	0.32	0.26
71 FENWICK	107.625	289	20	5.80	6.50	45.0	1	0.734	0.881	0.881	4.5	2.42	18.0	2.0	200	20.8	26.2	0.874	18.38	3.58	0.83	7.41	18.99	0.84	261.0	0.55	-0.29
72 FENWICK	95.857	287	17	6.00	6.30	45.0	2	0.734	0.881	0.881	4.5	2.42	18.0	2.0	200	20.7	25.8	0.875	18.02	3.58	0.83	7.41	18.52	-0.40	261.0	0.28	0.68
73 FENWICK	95.500	294	20	5.70	6.50	45.0	2	0.734	0.881	0.881	4.5	2.42	18.0	2.0	200	21.2	25.9	0.874	18.01	3.59	0.83	7.41	18.51	-0.44	261.0	0.29	0.73
74 FENWICK	97.067	292	17	5.50	6.30	45.0	1	0.734	0.881	0.881	4.5	2.42	18.0	2.0	200	21.0	25.5	0.875	18.06	3.59	0.83	7.41	18.57	-0.28	261.0	0.60	0.87
75 FENWICK	99.176	300	20	5.90	6.50	45.0	2	0.734	0.881	0.881	4.5	2.42	18.0	2.0	100	21.5	25.6	0.875	18.12	3.59	0.82	7.41	18.65	-0.06	261.0	0.44	0.50
77 FENWICK	96.000	305	20	5.40	6.50	45.0	1	0.734	0.881	0.881	4.5	2.42	18.0	2.0	200	21.9	25.3	0.875	18.03	3.60	0.82	7.41	18.52	-0.40	261.0	0.60	1.00
78 FENWICK	95.933	306	35	5.60	6.40	45.0	2	0.734	0.881	0.881	4.5	2.42	18.0	2.0	100	21.9	29.3	0.873	18.03	3.60	0.82	7.41	18.54	-0.35	261.0	0.47	0.83

79 FENWICK	98.063	315	26	5.90	6.60	45.0	1	0.734	0.881	0.881	4.5	2.42	18.0	2.0	200	22.5	26.3	0.874	18.09	3.61	0.82	7.41	18.61	-0.17	261.0	0.54	0.71
80 FENWICK	105.375	311	35	6.00	6.40	45.0	2	0.734	0.881	0.881	4.5	2.42	18.0	2.0	200	22.2	29.1	0.873	18.31	3.61	0.82	7.41	18.91	0.63	261.0	0.27	-0.36
81 FENWICK	94.600	320	26	5.60	6.60	45.0	1	0.734	0.881	0.881	4.5	2.42	18.0	2.0	200	22.8	26.1	0.874	17.99	3.61	0.82	7.41	18.47	-0.55	261.0	0.57	1.12
82 FENWICK	112.615	315	35	5.50	6.40	45.0	1	0.734	0.881	0.881	4.5	2.42	18.0	2.0	200	22.5	28.9	0.873	18.52	3.61	0.82	7.41	19.20	1.38	261.0	0.59	-0.79
84 FENWICK	96.583	323	45	5.80	6.30	45.0	1	0.734	0.881	0.881	4.5	2.42	18.0	2.0	200	23.0	32.2	0.871	18.05	3.62	0.82	7.41	18.58	-0.25	261.0	0.56	0.81
86 FENWICK	101.429	327	45	5.70	6.30	45.0	2	0.734	0.881	0.881	4.5	2.42	18.0	2.0	200	23.3	32.1	0.871	18.19	3.62	0.82	7.41	18.77	0.26	261.0	0.30	0.05
88 FENWICK	111.933	331	45	5.70	6.30	45.0	2	0.734	0.881	0.881	4.5	2.42	18.0	2.0	200	23.5	32.0	0.871	18.50	3.63	0.82	7.41	19.19	1.35	261.0	0.30	-1.05
90 FENWICK	111.400	335	45	5.70	6.30	45.0	1	0.734	0.881	0.881	4.5	2.42	18.0	2.0	200	23.8	31.9	0.871	18.49	3.63	0.82	7.41	19.17	1.29	261.0	0.57	-0.72